Universidade do Minho
Escola de Engenharia

Pedro Alexandre Marques Anacleto

Self-Folding 3D Micro Antennas For Implantable Medical Devices

julho de 2016

Universidade do Minho
Escola de Engenharia

Pedro Alexandre Marques Anacleto

Self-Folding 3D Micro Antennas For Implantable Medical Devices

Tese de Doutoramento em Engenharia Biomédica

Trabalho realizado sob a orientação do
Professor Doutor Paulo Mateus Mendes

julho de 2016

STATEMENT OF INTEGRITY

I hereby declare having conducted my thesis with integrity. I confirm that I have not used plagiarism or any form of falsification of results in the process of the thesis elaboration.

I further declare that I have fully acknowledged the code of ethical conduct of the University of Minho.

University of Minho, 21-07-2016

Full name: Pedro Alexandre Marques Anacleto

Signature: Pedro Alexandre Marques Anacleto

spiral out. keep going.

(Tool)

Acknowledgments

In first place I'd like to thank the *Anacleto Foundation*, namely to the main benefactors, Adélia and Manuel Anacleto, who since 1991 are asking "when will this end?" To the two of you, who never thought it was humanly possible to stay "in school", for so long, the most important "thank you".

The second heavy-weight acknowledgment goes to my supervisor, Professor Paulo Mateus Mendes (Minho University), for his unconditional support throughout this project, his enthusiasm and dedication to this cause of "difficult-to-see antennas", and the friendship that we have cultivated. Thank you very much. "Agora é que é!"

Another special thanks to Hugo Dinis, the young star of Minho University, for his friendship and for the work that we did together.

I want to thank Professor David Gracias (Johns Hopkins University) for receiving me at his research group. It was a beautiful and fulfilling experience that I will never forget. I'd like to thank Evin Gultepe, Rohan Fernandez, Mustapha Jamal and Shivendra Pandey, for your amazing friendship and mentorship throughout this time. Evin, a special thanks to you, for all your help and patience, you are a sweetheart.

The author, Pedro Alexandre Marques Anacleto, was supported by the Portuguese Foundation for Science and Technology (Programa Operacional Temático Fatores de Competitividade COMPETE) Grants: SFRH/BD/63737/2009 FCT; PTDC/EEA-TEL/65286/2006 FCT; PTDC/EEI-TEL/2881/2012; Fundo Comunitário Europeu FEDER and the National Science Foundation

Abstract

Recent advances in device miniaturization have been enabling smart and small implantable medical devices. These are often powered by bulky batteries whose dimensions represent one of the major bottlenecks on further device miniaturization. However, alternative powering methods, such as electromagnetic waves, do not rely on stored energy and are capable of providing high energy densities per unit of area, thus increasing the potential for device miniaturization. Hence, we envision an implanted medical device with an integrated miniaturized antenna, capable of receiving a radiofrequency signal from an exterior source, and converting it to a DC signal, thus enabling remote powering.

This thesis addresses the analysis, design, fabrication and characterization of novel 3D micro antennas that can be integrated on 500 × 500 × 500 μm^3 cubic devices, and used for wireless power transfer purposes. The analysis is built upon the theory of electrically small antennas in lossy media, and the antenna design takes into consideration miniaturization techniques which are compatible with the antenna fabrication process. For the antenna fabrication, a methodology that combines conventional planar photolithography techniques and self-folding was used. While photolithography allows the easy patterning of virtually every desired planar antenna configuration with reproducible feature precision, and the flexibility to easily and precisely change the antenna geometry and size, self-folding allows assembly of the fabricated planar patterns into a 3D structure in a highly parallel and scalable manner.

After fabrication, we characterized the fabricated antennas by measuring their S-parameters and radiation patterns, demonstrating their efficacy at 2 GHz when immersed in dispersive media such as water. This step required the development and test of multiple characterization setups based on connectors, RF probes and transmission lines and the use of an anechoic chamber. Moreover, we successfully show that the antennas can wireless transfer energy to power an LED, highlighting a proof of concept for practical applications. Our findings suggest that self-folding micro antennas could provide a viable solution for powering tiny micro devices.

Resumo

Os recentes avanços das tecnologias de miniaturização têm permitido o desenvolvimento de dispositivos médicos implantáveis inteligentes e mais pequenos. Estes são muitas vezes alimentados por baterias volumosas cujas dimensões limitam o nível de miniaturização alcançável por um microdispositivo. No entanto, existem formas alternativas de alimentar estes dispositivos que não dependem de energia armazenada, tais como ondas eletromagnéticas, que são capazes de providenciar uma elevada densidade de energia por unidade de área, aumentando assim o potencial de miniaturização dos dispositivos. Desta forma, visionamos um dispositivo médico implantado, com uma antena miniaturizada e integrada, capaz de receber um sinal de rádio frequência a partir de uma fonte externa, e convertê-lo num sinal DC, permitindo assim a alimentação remota do aparelho.

Esta tese apresenta a análise, desenho, fabrico e caracterização de micro antenas 3D, passíveis de integradas em dispositivo cúbicos de 500 × 500 × 500 μm^3, e utilizadas para fins de transferência de energia sem fios. A análise assenta na teoria das antenas eletricamente pequenas em meios com perdas, e o design da antena considera técnicas de miniaturização de antenas. Para o fabrico da antena foi utilizada uma metodologia que combina técnicas de fotolitografia planar e auto-dodragem (self-folding). Enquanto a fotolitografia permite a padronização de virtualmente todos os tipos de configuração planares de forma precisa, reprodutível, e com a flexibilidade para se mudar rapidamente geometria e tamanho da antena, o self-folding permite a assemblagem dos painéis planares fabricados numa estrutura 3D.

Depois do fabrico, as antennas foram caracterizadas medindo os seus parâmetros S e diagramas de radiação, demonstrando a sua eficácia a 2 GHz quando imersas num meio dispersivo, tal como água. Esta etapa exigiu o desenvolvimento e teste de várias setups de caracterização com base em conectores, sondas de RF e linhas de transmissão, e ainda o uso de uma câmara anecóica. Além disso, mostramos com sucesso que as micro antenas podem receber e transferir o energia para um LED acendendo-o, destacando assim esta prova de conceito para aplicações práticas. Os nossos resultados sugerem que estas micro antenas auto-dobráveis podem fornecer uma solução viável para alimentar micro dispositivos implantáveis muito pequenos.

Contents

Index of Figures

Index of Tables

List of Abbreviations

BW – Bandwidth

CPW – Coplanar Waveguide

DUT – Device under Test

EHS - Energy Harvesting Systems

ESA – Electrically Small Antenna

EM - Electromagnetic

FSLP – Free Space Loss Path

FDTD – Finite Difference Time Domain

FEM – Finite Element Method

HFSS – High Frequency Structural Simulator

IEEE - Institute of Electrical and Electronics Engineers

IMD – Implantable Medical Devices

LED – Light Emitting Diode

LP – Loss Path

MEMS - Microelectromechanical systems

NEMS - Nanoelectromechanical systems

MPE - Maximum Permissible Exposure

MoM – Method of Moments

PIFA - Planar Inverted-F Antenna

PMMA - Poly(methyl methacrylate)

PVA - Poly(vinyl acetate)

RFID - Radio Frequency identification

RF – Radiofrequency

SAR - Specific Absorption Rate

SEM – Scanning Electron Microscope

SMA – Sub Miniature version A

SU-8 – SU8 Photoresist

TL – Tissue Loss

VLSI - Very-Large-Scale Integration

VNA – Vector Network Analyzer

VSWR - Voltage Standing Wave Ratio

WPT – Wireless Power Transfer

WPTE - Wireless Power Transfer Efficiency

UV- Ultra Violet

1 Introduction

Due to the remarkable technological advances over the last decades, implantable medical devices (IMD) have experienced significant transformations, thus becoming extremely important tools, which are capable of soliciting, measuring and wirelessly communicate important physiological parameters. Such transformations are intimately related to the growing knowledge of the human body, and continuous progresses of material science, electronics and microfabrication techniques, which are enabling the development of small and smart devices capable of interacting with the human tissues at micro and nanoscales.

Small, implantable, low power, and wireless biomedical devices are a new technological trend with many possible applications and the potential to revolutionize modern medicine. In fact, the availability of newly implantable medical devices with wireless capabilities, and their reported potential for massification, has led an exponential market growth. In the past several years, the $125 billion medical device market has grown at a rate of 6% annually in the United States [1]**.** This growth is driven by factors such as the increasing elderly population and the associated increase in the prevalence of chronic degenerative diseases [2]. However, due to technological hurdles that still need to be addressed, ubiquitous implantable wireless medical devices that monitor, treat and prevent diseases, and guide our lifestyle habits are still ahead of us.

Some of the common challenges for implantable medical devices are their location within the body, how to access and operate them, their size, their dependence on battery technology and expected life time. Nonetheless, some of today's implantable medical devices (Figure 1.1) are equipped with advanced microelectronics and powering systems [2], unveiling life changing applications such as cochlear [3] and vision prosthesis [4], which aid patients to regain their hearing and sight, drug delivery systems that can change pharmacological therapies [5], glucose and blood pressure monitors [6-8] that facilitate diagnose and treatments decisions for diabetic and transplant patients, and neurostimulators for suppression of chronic pain [9]. Some can be implanted in very delicate areas such as arteries [10-11] eyes [4], and spinal cord [12], while others can be made with locomotion capabilities in fluid medium [13], and travel our entire intestinal tract while taking pictures and identifying tumors [14].

However, there is “plenty of room in the bottom” and a new generation of even smaller devices will enable the proliferation of unseen applications over previously inaccessible conduits of the human body, and hence allow better insight of pathologies and launch new medical solutions to treat patients with a high level of comfort and benefits.

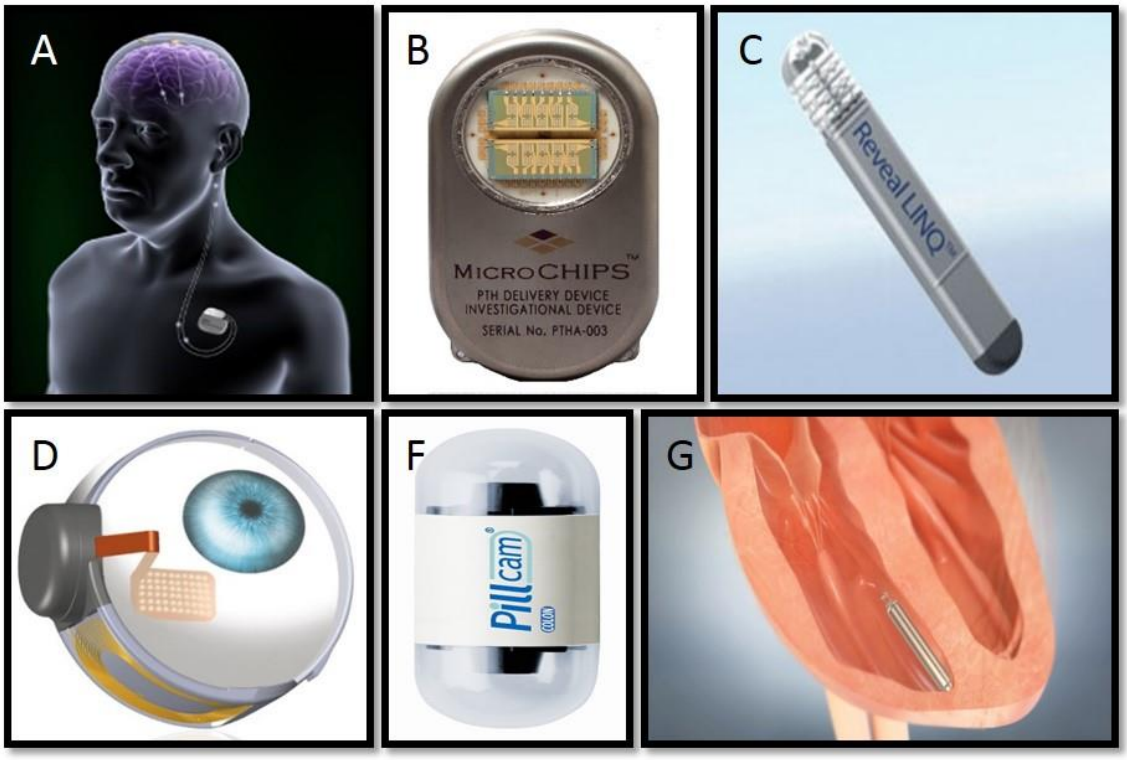

Figure 1.1 Commercially available implantable medical devices. A) A deep brain stimulator sends electrical impulses to the brain through implanted electrodes connected by leads. B) MicroCHIPS is an implantable drug delivery system suitable for patients who need frequent dosing or require regular injection in multiple therapeutic indications [5]. C) Insertable cardiac monitoring system helps doctors to diagnose and treat irregular heartbeats [15]. D) The Argus® II Retinal prosthesis system (also known as the bionic eye) is a retinal implant. It is intended to provide electrical stimulation of the retina, to induce visual perception in blind individuals [16]. E) PillCam endoscope capsule allow physicians to visualize the small bowel, esophagus and colon, and help diagnosing disorders of the gastrointestinal tract [17]. F) The Nanostim is a leadless pacemaker that does not require a surgical pocket for implantation [18].

1.1 Ultra-miniaturized Implantable Medical Devices

Since Feynman's 1959 lecture "*There's Plenty of Room at the Bottom*", researchers predicted that advances in materials science, and in micro and nanotechnologies would enable smart and integrated structures, and finally miniaturized devices, that would open up new possibilities for modern medicine. In fact, emergent areas of medical innovation include the development of wireless and tetherless tools, which are sufficiently small to be deployed inside the human body through its natural orifices or by minimally invasive techniques. This way, miniaturized tools can pass through the various small and hard-to-reach conduits of the human body, such as the gastrointestinal tract and the circulatory system, thus replacing current medical tools and implants (cf. Figure 2.11).

To utilize these devices in three-dimensional environments within the body, it is advantageous to develop them with 3D profiles as seen in implantable medical devices such as stents [10], and embolic coils [19] to treat aneurisms and blockages. The recent developments in microtechnology can enable 3D fabrication and integration for certain applications, but are typically limited in throughput. Such methods include microscale machining, wafer bonding, direct write techniques and stereolithography. One cost-effective approach for high throughput 3D fabrication and integration at the micro and nanoscale, is the combination of photolithography with self-assembly and self-folding techniques. In fact, these combined techniques have already produced ultra-small tools, suitable for medical applications on the millimeter scale and below (Figure 1.2). Examples range from microfluidic devices for vascularized systems with nutrient and waste transport [20], to micro containers appropriate for drug delivery systems, cell encapsulation and bioartificial pancreas [21-22], micro grippers for colon biopsy and cell gripping [23-24], and microdrillers for remotely controlled minimally invasive surgery [25].

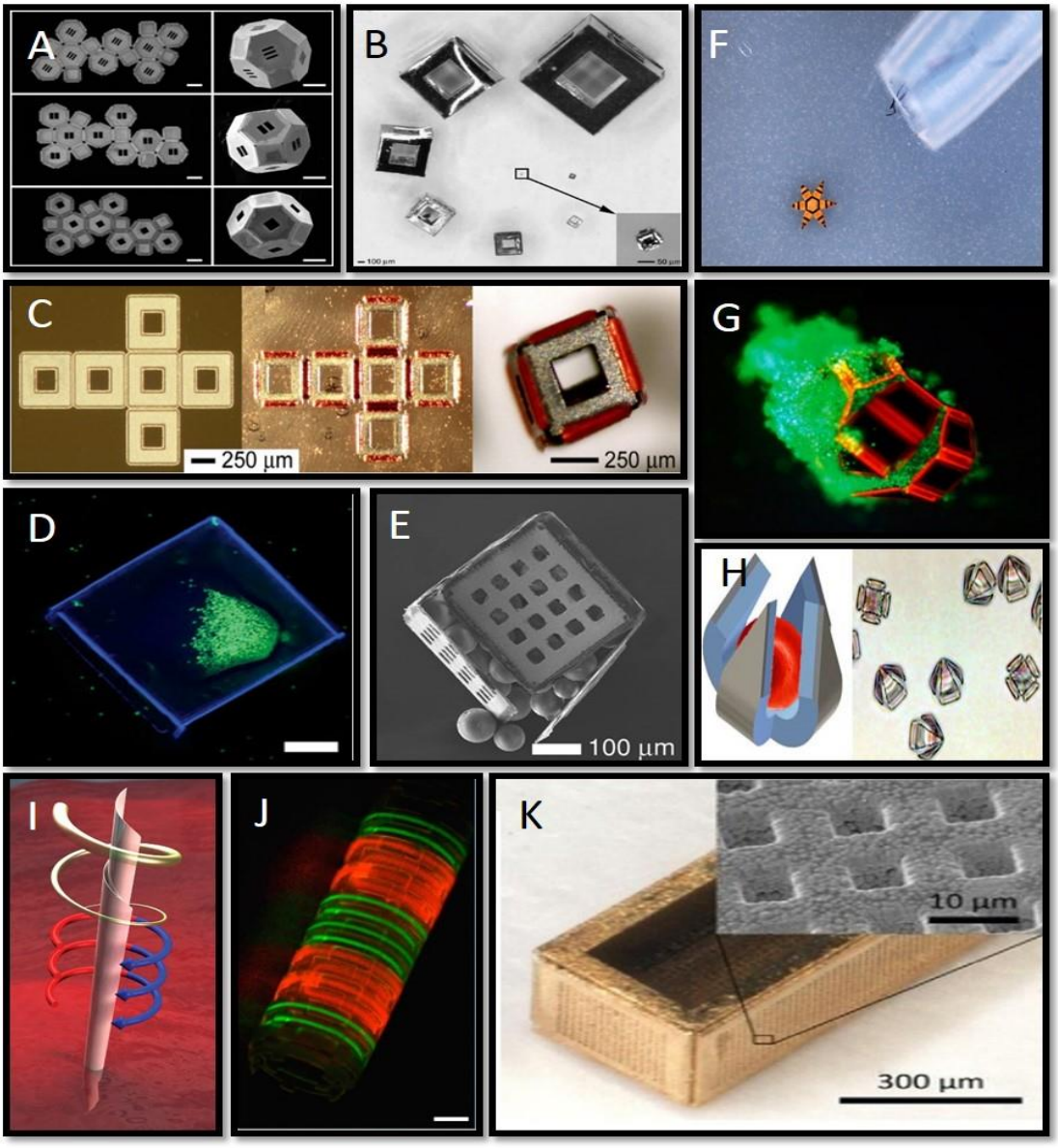

Figure 1.2 Ultra-small biomedical tools fabricated by self-assembly and self-folding. A) Self-folded hollow octahedra and their 2D net template precursors. Scale bar: 300 µm [26]. B) Self-assembled cubic containers over two orders of magnitude in size, from 2 mm to 50 µm. Scale bars: 100 µm (left) and 50 µm (right) [21]. C) Lithographically patterned 2D templates (left) with liquefiable hinges (center) that upon heating fold into hollow polyhedral containers (right). Scale bars: 250 µm [21]. D) Fibroblast cells encapsulated within a self-folded polymeric micro container. The green color indicates that the cells are alive. Scale bar: 250 µm [27]. E) Metallic micro container loaded with glass microbeads. Scale bar: 100 µm [28]. F) Open micro-gripper next to a plastic pipette tip (with a maximum dimension of 300 µm when closed, and 1.5 mm tip-to-tip when open) [23]. G) Microgripper capturing and moving a piece of biological tissue: scale bar 200 µm [29]. H) Single cell microgripper with captured cells within the arms of 50 µm grippers [24]. I) Schematic of self-folded magnetic microtools with sharp ends, directed at enabling drilling and incision operations of tissues (5 x 20 μm^2) [25]. J) Self-assembled microfluidic device with dual channels. Scale bar: 500 µm[20]. K) Au-coated capsule of a bioartificial endocrine pancreas prototype with micropores. Scale bar: 300 µm [22].

1.2 Powering Implantable Medical Devices

The functionalities, performance and reliability of modern implantable medical devices that can deliver real-time in-vivo stimulation, data collection, and high speed wireless communications are on the rise. However, this increased device complexity is requiring more power, and certain applications have seen their implementation restricted due to their high power consumption, and the unavailability of sustainable and sufficiently small powering methods [30-32]. Examples can be seen in cochlear implants, where increasing the temporal resolution and the number of channels can improve the perceived sound quality in deaf patients, but it in turn requires an increase in the data rate, which consequently results in high power consumption [33]. Also in intraocular retinal prostheses, where the number of electrodes and encoding resolution are also constrained by the achievable data rate, which is also dependent on the available power [34]. Power can be provided by on-board batteries, energy harvesters or external sources such as electromagnetic waves. However, batteries, whose bulky size is in many cases the most important factor limiting a device's achievable level of miniaturization, are still the first choice for power hungry implantable medical implants.

1.2.1 Batteries

At present, batteries are the still the standard method for powering portable electronics and most commercially available IMDs due to their portability, reliability, and long shelf lives, and overall convenience [32][35]. Nonetheless, batteries often account for an important percentage of the device's total volume and weight, making them big and heavy, and thus harder to implant. Figure 1.3 presents several implantable devices and their batteries, where it can be seen that in some cases the battery can take more than 50% of the device's total available volume. This aspect alone points to the fact that an important strategy for further device miniaturization may lie in the replacement of batteries by alternative and much smaller power sources. In addition, besides size and weight issues, batteries also have limited capacities and lifespans [33][35].

One of the major inconveniences of battery powered implanted IMDs lies in the fact that once implanted, devices will have to be surgically retrieved for battery

replacement. For instance, the expected battery lifetime of a modern pacemaker is of 5 to 10 years. When the battery drains, the patient will undergo another surgery to replace the battery, which translates into serious economic and health burdens.

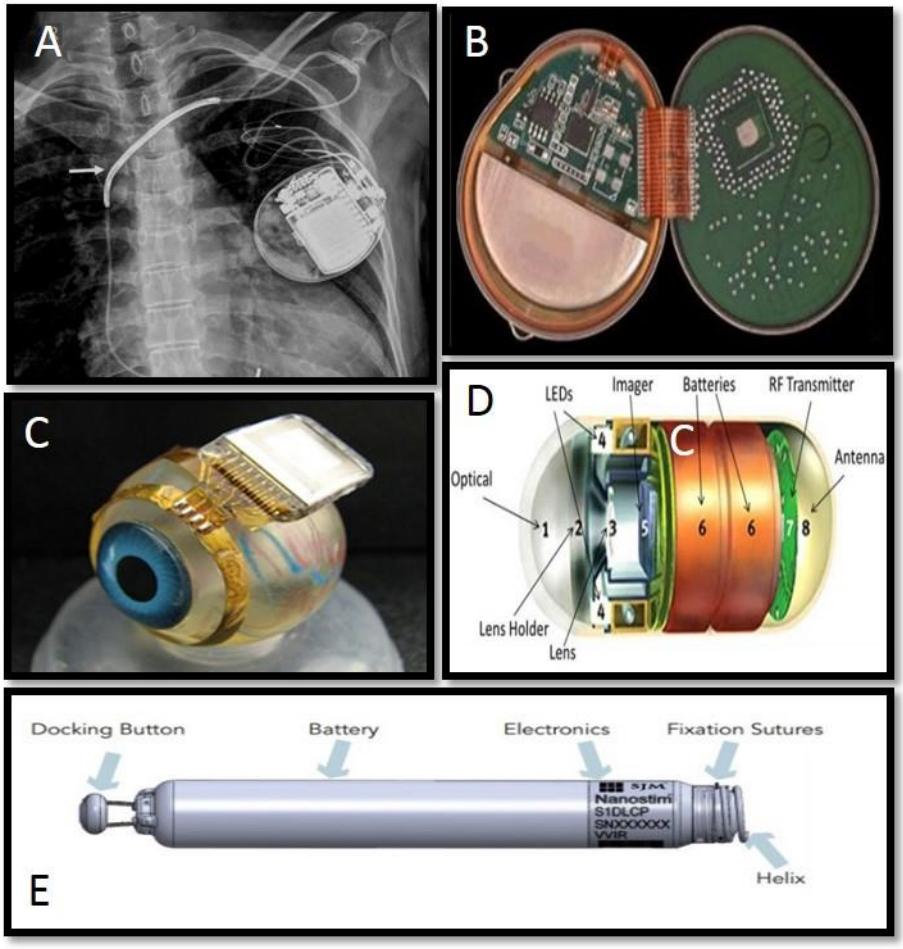

Figure 1.3 Batteries of commercially available medical devices. A) A pacemaker with a battery occupying more than 50% of the device's total volume [36]. B) Battery of an earlier model of a MicroCHIPS drug delivery system [5]. C) Retinal prosthesis with a bulky battery [37] D) Main components of a PillCam endoscopic capsule with the battery occupying 40% of the whole device's volume [17]. E) The Nanostim leadless pacemaker whose battery occupies roughly 80% of the device's total volume [38].

Another important concern of battery powered IMDs is battery leakage and the high risk of infection. To solve this problem, biodegradability has emerged as an important property of emerging battery technologies, allowing for temporary implantable device's batteries to benignly degrade at the end of the life cycle without toxic byproducts/residues. Efforts have also been made to develop flexible batteries for

implantable applications since that in many cases the implant has to conform to the curvature of the human body or a specific organ [39].

It is noteworthy that advances in materials science and microfabrication have made possible miniaturized batteries that may be extremely important for future biomedical tools. Figure 1.4A presents a 3D printed micro battery (occupying a volume of 2.1 × 2.1 × 1.5 mm^3 after packaging) capable of providing a power density of 2.7 mW/cm^2 [40], and Figure 1.4B displays another micro battery (boxed in a 6 mm^3 package), capable of providing a power density of 0.675 W h/ml [41]. However, in spite of being incredibly small batteries, both require packaging systems that relegates them to the millimeter scale, and therefore make impractical for sub-millimeter applications. At the centimeter scale, Figure 1.4C, D and E show 3D biodegradable [42], and thin flexible [43-44] batteries, that in spite of being too big for sub-millimeter IMDs, still represent some of the newest trends in battery technology, suitable for body adaptable devices due to their thin, planar and flexible profiles. Nonetheless, these small batteries show equally small energy densities, which may be insufficient for the devices' power requirements.

The necessary packaging makes batteries bulky, and despite having experienced notable levels of miniaturization, reduced toxicity, biodegradability and improved flexibility, their overall size remains as a main bottleneck in further device size reduction [40][43][45][46]. Though, replacing batteries by alternative and/or complementary power-supply systems that do not rely on stored energy is still an important challenge looking for solutions.

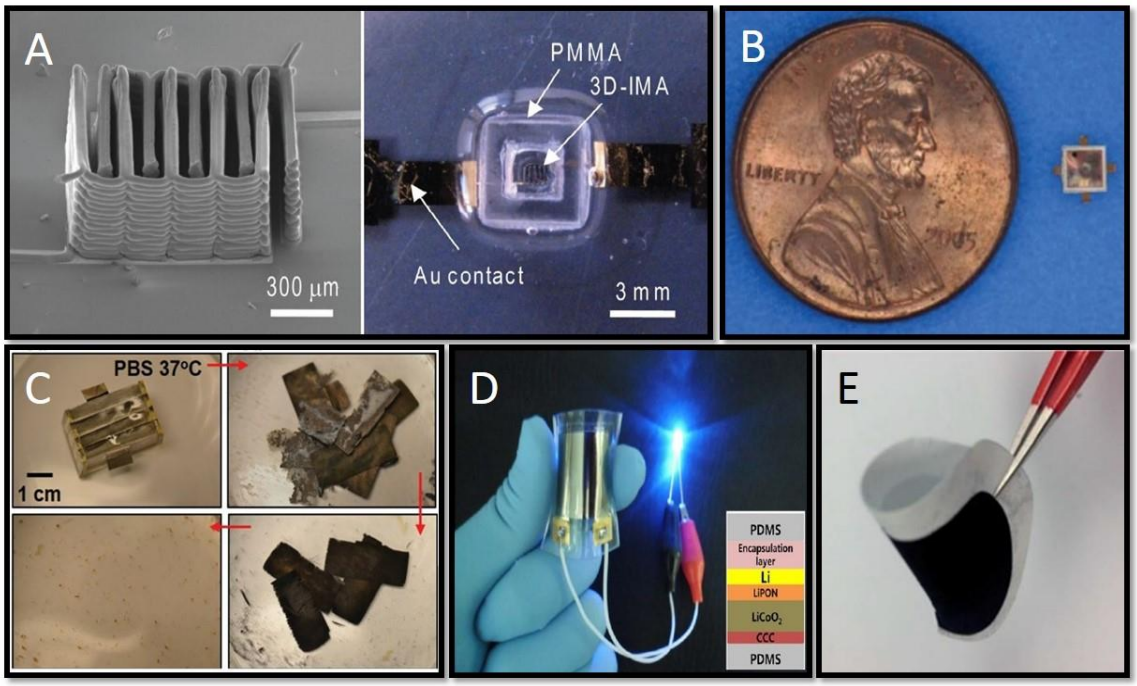

Figure 1.4 State-of-the-art miniaturized batteries. A) 3D printed interdigitated Li-Ion microbattery before packaging (left), after packaging (right) (2.1 × 2.1 × 1.5 mm^3 after packaging) [40]. B) Ultra high energy density lithium rechargeable microbattery (3 × 3 × 0.7 mm^3) [41]. C) Fully biodegradable primary battery dissolution process (energy density: 0.1mA/cm^2) [42]. D) Bendable inorganic thin-film battery (2.54 × 2.54 × 0.2 cm^3, energy density: 106 µA h/cm^2) [43]. E) Flexible cellulose based carbon nanotube films for bio-compatible zinc batteries (1 × 1 cm^2, energy density: 60 mA/cm^2) [44].

1.2.2 Antennas

Most implantable medical devices have strong size restrictions that make impractical the use of on-board stored energy. Moreover, if the target devices are in the sub-millimeter scale, batteries can be completely dismissed due to size incompatibilities. Hence, considering alternative powering methods, radiofrequency is the one providing the highest power density per unit area [32], thus being a strong candidate to be utilized in sub-millimeter implantable applications that need continuous and steady power [35][47]. Consequently, there is now a major focus on the design and implementation of efficient miniaturized antennas for the powering of small implantable devices. However, antennas are, alongside with batteries, typically one of the device's largest components, and can in turn act as a bottleneck on further device miniaturization.

Currently, most integrated, on-chip, and sub-millimeter antennas are inherently planar due to ease of lithographic fabrication and low cost [32][48][49]. While efficient

planar antennas usually require large cross-sections which are not suitable for small form factor devices [21][23][50], three dimensional (3D) antennas make use of most of a given volume and can exhibit a relatively long length and high efficiency. Also, 3D geometries are able to form hollow structures that can be used for packaging of electronic components and batteries, and storage of liquids and cells [21]. The literature suggests that certain geometries can be useful for performance enhancement and optimization of small antennas, where 3D designs have been used to overcome some of the limitations of planar geometries namely their large cross-sections, small bandwidth and low radiation efficiency [32][51][52][53].

In fact, a variety of 3D geometries have already been used in several antenna applications (Figure 1.5) such as implanted stent-based antennas [10], dome-shaped antennas [54-55], reconfigurable origami antennas [56], helical antennas for smart dental applications [57], 3D printed bionic ears with an infused inductive coil antenna [58], terahertz responsive helical shaped and copper-coated microalgae [59], and μTags delivered into living cells [52]. Currently, the relevant fabrication methods of 3D antennas and other RF applications include: manual assembly [56][60][61][62], 3D printing [54][63], metallic inks on paper [64], direct transfer patterning of metallic patterns [55], thin film roll up [57], self-assembly [65], self-folding [66-67], wafer stacking [68-69], biotemplating [59], transfer printing [70] and compressive buckling [71]. However, all the aforementioned methods are either time consuming, unsuitable for mass production, strongly dependent on a few selected material types or have relatively low feature resolution and shape control, and therefore are not truly appropriate for sub-millimeter antenna structures fabrication.

While most electronic components scale down (bounded by some limits) without significant performance impairment, antenna miniaturization is usually attained at the expense of its performance degradation (bandwidth, efficiency, and gain). Also, when miniaturized antennas are used inside the human body there are additional challenges that need to be overcome, such as RF signal attenuation in the tissues and reflection at the air-skin, and tissue-tissue interfaces. However, recent research [72-73] has found that the optimal operating frequency of antennas in human tissues lies in the low GHz range (up to 10 GHz), opening doors for the use of miniaturized antennas for implantable applications. Since the antenna size scales inversely with its resonant

frequency, lower operating frequencies require a larger antenna size, which translates to a larger device size. As a result, since it is necessary to decrease the antenna resonant frequency without increasing the total occupied volume, the design of miniaturized antennas should consider a careful balance between the smallest possible antenna size and the highest efficiency. One possible solution to achieve a small volume occupied by the antenna while decreasing its frequency is to modify its shape [53][74][75][76].

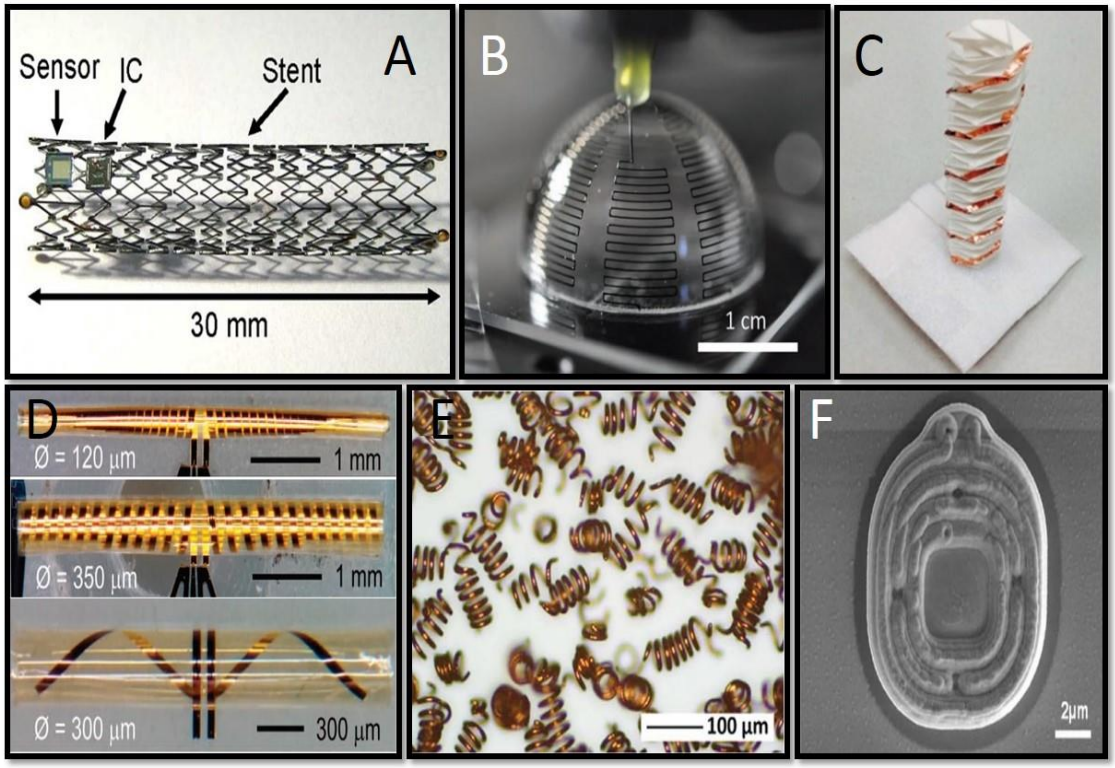

Figure 1.5 3D antenna geometries. A) Stent-antenna prototype with wireless powering capabilities [77]. B) A 3D printed meander line based conformal antenna [54]. C) Hand manufactured origami helical antenna where the whole structure can collapse to change its resonance frequency [66]. D) Thin film helical antennas for dental applications [57]. E) Spirulina-templated microstructures which are coated with metal unveiling spiral terahertz responsive micro structures [59]. F) Inductive and capacitive structures deployed into a living cell for potential passive RF identification tags [52].

1.3 Motivation

The motivation behind this work lies in the fact that a new generation of ultra-miniaturized wireless/theterless biomedical tools (presented in Figure 1.2) needs efficient powering schemes. These tools have reached dimensions that have not yet been accompanied by battery technology, and alternative powering method whose implementation does not further add to the device's size would be desirable. In fact, this can be achieved using electromagnetic waves in the radiofrequency range, to wirelessly power small devices equipped with equally small antennas. One of the main advantages of using radiofrequency signal as a powering method, lies in the fact that high power densities per unit of area can be achieved, hence facilitating further device miniaturization [13][32][78][73].

So far, a powering strategy for sub-millimeter tools had not yet been proposed, mostly due to size restrictions [21]. Therefore, this work aims at the development of a sub-millimeter antenna structure for wireless power transfer applications, without increasing the host device's size. This can be accomplished by utilizing micro antennas, which are conformal with the geometry of the host device, or by making the device's own structure itself an antenna. This approach represents a major advantage even over other alternative powering methods, such as energy harvesters, which require the use of additional bulky components that further add to the device's total size.

These micro antennas can be made utilizing advanced materials and applying microfabrication techniques. This thesis will pursue the possibility of wirelessly power an implantable sub-millimeter device ($500 \times 500 \times 500\ \mu m^3$), whose dimensions are a key factor to enable new sites of implantation, and new medical strategies for diagnose and treatment. In fact, micro cubic containers with small form factor and high aspect ratio have been proposed for drug delivery and cell encapsulation, since their geometry allows hollow structures with high integration and packaging capabilities. The devices were loaded with gels, cells and drugs, and further release-on-demand was mediated by remote heating with electromagnetic fields [21][79]. This composition makes obvious the need for external power and wireless communications, giving birth to the vision of a wireless implantable sub-millimeter cubic device, with an integrated microantenna as shown in Figure 1.6.

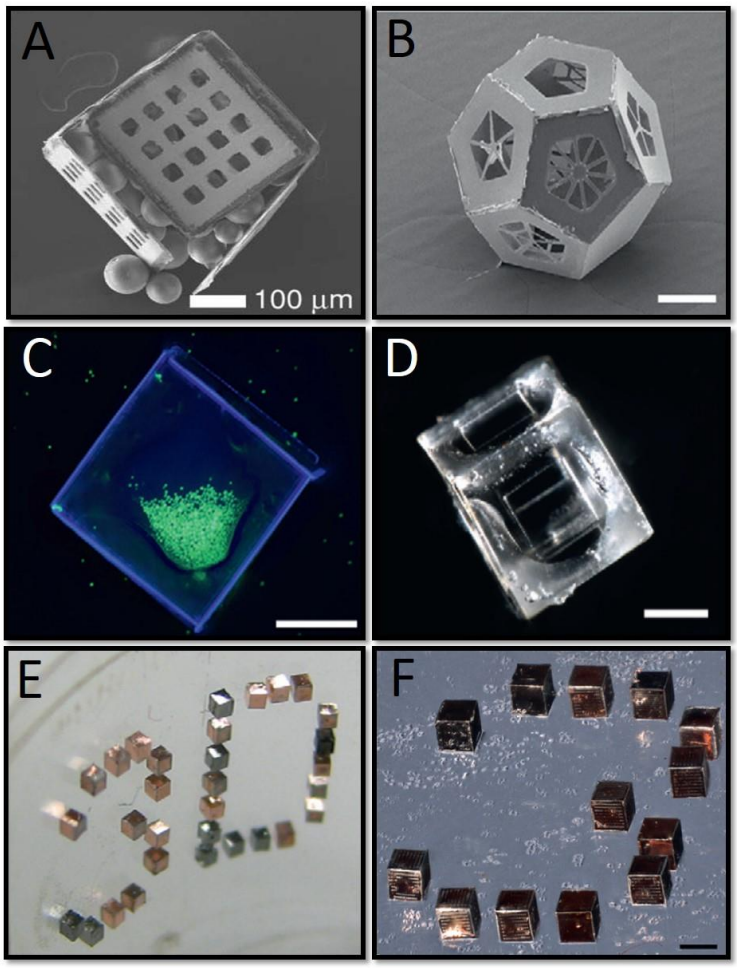

Figure 1.6 A) Self-loaded micro container overfilled with 150 mm glass beads (scale bar: 100 um) B) Dodecahedral shaped hollow metallic container featuring surface patterning of slits (scale bar: 250 um). C) Container made of SU8 panels with live fibroblast cells inside (scale bar: 250 um). D) SU8 container and biodegradable polycaprolactone hinges (scale bar: 500 um). E – F) Ordered self-folded cubic microwell arrays composed of gold coated containers [79].

1.4 Goals and Challenges

One of the main goals of this work is the development of a methodology that enables the fabrication of 3D micro antennas, which operate in the low gigahertz range when embedded in dispersive media. Prior to fabrication, it is intended to characterize the antennas by measuring their S-parameters and radiation properties. Finally we intend to demonstrate a wireless power transfer application. Here, a water immersed micro antenna will receive a RF signal from an external antenna, and convert it into DC signal, and by lightening up an LED, it will demonstrate that power was successfully transferred.

Due to the dimensions of the host device, it is required to develop an extremely small antenna, and this particular feature instantly posed an enormous challenge. First, sub-millimeter structures had to be fabricated using microfabrication technologies. To do so, we adopted a methodology that combines conventional planar photolithography and self-folding methods. The microstructures were fabricated starting with silicon wafer substrates, followed by thin film deposition, photolithography, electrodeposition and etching techniques. Secondly, small antennas have naturally high operating frequencies, which consequently induce high losses in the wireless path due to dispersive media such as the human body. Strategies had to be found in order to reduce the operating frequency while keeping the antenna parameters within practical and workable values. Lastly, the fabricated antennas are extremely hard to manipulate and to characterize. The available instrumentation such as connectors, transmission lines, and probes are often bigger than the antenna, making very difficult to precisely measure the antenna parameters, such as the radiation pattern, and to clearly understand what is actually being measured.

1.5 Main Contributions

The contributions described in this work address the topic of wireless powering of miniaturized devices, introducing a methodology to fabricate 3D sub-millimeter antenna structures, and discussing how this methodology can be used for a wireless power transfer application for ultra-small implantable devices. The development of such structures requires a multidisciplinary effort, by studying and bringing together the knowledge from several fields such: as human tissue physiology, for the comprehension of the underlying concepts of RF interaction with biological media; 3D modeling and RF simulation for the design of valid models; material science and microfabrication techniques for the development of the antenna structures; and RF measurement methods for the antenna characterization. In summary the key contributions of this work are summarized as follows:

- Introduction of the smallest ever 3D antenna structure for the powering of ultra-small implantable devices.

- A methodology to use antennas that usually operate in the high gigahertz in the low gigahertz range (Figure 1.7A).
- Application of self-folding as both an antenna fabrication and miniaturization technique.
- The development of extremely small antenna characterization and measuring setups (Figure 1.7 B, C, D).
- Demonstration of wireless power transfer setup where a micro antenna immersed in dispersive media is used to receive an RF signal from an RF source in order to power an LED (Figure 1.7E, F, G).

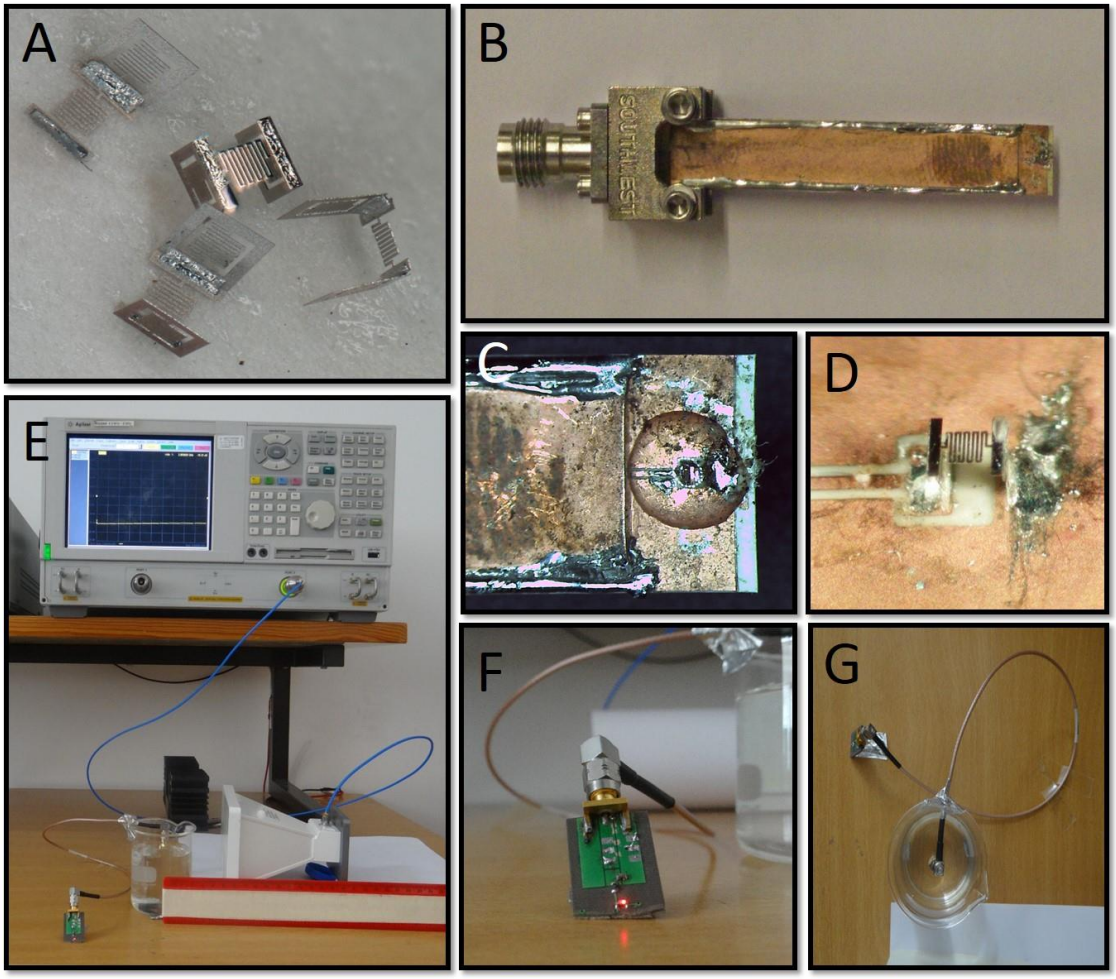

Figure 1.7 A) Fabricated micro antennas. B) Antenna characterization setup composed of an end launch connector and a transmission line. C) Transmission line with a micro antenna and dispersive media. D) Close-up view of the micro antenna on the transmission line. E) Wireless power transfer setup composed of transmitting horn antenna and receiving micro antenna immersed in water. F) Rectifying circuit with and LED showing that power was successfully received by the fabricated micro antenna. G) Top view of the passive system composed of the immersed micro antenna and rectifying circuit.

List of papers:

P. Anacleto, E. Gultepe, D. Gracias, J. H. Correia, P. M. Mendes. "*Antenna operating frequency selection for energy harvesting on nano biomedical devices*". 41st European Microwave Conference (EuMC), 2011.

P. Anacleto, P. M. Mendes, E. Gultepe, D. H. Gracias. *"3D small antenna for energy harvesting applications on implantable micro-devices"*. Loughborough Antennas and Propagation Conference (LAPC), 2012.

P. Anacleto E. Gultepe, D. H. Gracias P. M. Mendes. "*Energy Harvesting For Self-Folding Micro Devices*". International Conference on Biomedical Electronics and Devices Proc. BIODEVICES, 2012.

P. Anacleto, P. M. Mendes, E. Gultepe, D. H. Gracias. "*Micro antennas for implantable medical devices*". IEEE 3rd Portuguese Meeting in Bioengineering (ENBENG), 2013.

S. Gomes, J. Fernandes, P. Anacleto, P. M. Mendes, E. Gultepe, D. Gracias. "*Ultra-small energy harvesting microsystem for biomedical applications*". 44th European Microwave Conference (EuMC), 2014.

F. Rodrigues, S. Gomes, P. Anacleto, J. Fernandes, P.M. Mendes, "*RF CMOS wireless implantable microsystem for sacral roots stimulation with on-chip antenna and far-field wireless powering*", European Microwave Conference (EuMC), 2015.

H. Dinis, P. Anacleto, J. Fernandes, P.M. Mendes, "*Characterization of chip-size electrically-small antennas for smart wireless biomedical devices*", 9th European Conference on Antennas and Propagation (EuCAP), 2015.

M. Zamith, J. Magalhaes, P. Anacleto, P.M. Mendes. "*60 GHz on-chip antenna array with efficiency improvement using 3D microfabrication technology*", 9th European Conference on Antennas and Propagation (EuCAP), 2015.

P. Anacleto, E. Gultepe, S. Gomes, P.M. Mendes, D. Gracias. "*Self-folding microcube antennas for wireless power transfer in dispersive media*", Technology. 2016. (Accepted).

Patent:

P. Anacleto, E. Gultepe, P.M. Mendes, D. Gracias. "*THREE DIMENSIONAL SELF-FOLDED MICROANTENNA*", United States Patent Application 20140320378, 2014.

1.6 Thesis Outline

In this first chapter, introductory notes concerning the main drivers pushing for the miniaturization of implantable medical devices are discussed. Here are presented several ultra-miniaturized biomedical tools that may greatly contribute to the birth of a new generation of implantable devices that will enable new medical applications. Since all IMDs need to be powered, we then discuss the common and alternative powering methods, pointing out why batteries are often impractical for implantable applications and how radiofrequency energy is a suitable candidate to power ultra-small devices.

Chapter two starts with a brief historical context of the first implantable medical devices. A description of the essential building blocks of IMD is presented, followed by a discussion on the introduction of wireless capabilities into IMDs and its impact on modern medicine. Then we discuss alternative IMD powering technologies. Here, an overview of some of the well-known energy harvesting technologies such as fuel cells, piezoelectric transduction and radiofrequency waves is given. Since radiofrequency powering methods offer wireless and continuous power, we will examine wireless power transfer techniques with emphasis on near and far-field applications such as inductive coupling and radiative transfer. Finally, we will review the state-of-the-art of antenna technology for centimeter and millimeter scale applications.

In chapter three the discussion will be centered on implanted antennas and the interaction between electromagnetic waves and lossy media, in order to understand the loss mechanism that is responsible for the attenuation of radiofrequency waves in biological tissues. We will also study the operating frequency of very small implantable antennas and its relationship with tissue attenuation and antenna efficiency. Here, the fundamental aspects of antenna miniaturization are presented, highlighting geometry modification, dielectric loading with high permittivity materials, and the full use of the volume circumscribing the antenna. Finally, we will focus on electrically small antennas, their performance constrains and the fundamental limitations imposed by their size.

In chapter four, the design considerations and the methods used for the antenna project are described. Several antenna designs are discussed and a careful explanation is given in order to better understand what structural changes (and results)

lead to the final antenna design. An extended antenna geometry parametric analysis is also presented.

Chapter five is reserved to the micro antenna fabrication process. Here the fundamental principles behind self-folding are introduced. A summary of the fabrication process is shown, followed by the design rules and fabrication steps, detailed fabrication protocol, and concluded with the final results, *i.e.* the fabricated micro antennas.

Chapter six is dedicated to antenna measurements and the development of a wireless power transfer application using the fabricated micro antennas. Throughout this chapter, the different steps/iterations that lead to the final characterization setup are discussed in order to give an insight on how demanding it is to accurately measure and characterize sub-millimeter antennas. The several experimental setups used for antenna characterization and radiation pattern measurement are discussed as well as the materials and methods involved in the WPT application.

Chapter seven will be reserved for final conclusions, and prospects of future work related with this research.

2 Smart and Small

The arrival of microfabrication techniques, which allowed increased device complexity within small form volumes, was extremely important for the development of IMDs. Furthermore, with the inclusion of wireless capabilities, another significant technological leap was given, as devices are now capable of communication, hence providing continuous and relevant data that can be easily accessed by physicians for quicker and more accurate medical diagnose. However, the scaling down of implantable devices raises the problem of how to power them, as batteries don't scale down in the same way and may become too big to be used on. Consequently, alternative sources that do not rely on stored energy are emerging. Energy harvesting methods have been proposed but many such technologies are still premature or provide insufficient power. Yet, other alternative methods, which rely on the use of radiofrequency, have been proposed and presented as a viable source of uninterrupted power.

This chapter starts with a brief historical perspective of the development of implantable medical technologies, followed by a review of the IMD essential building blocks, and a discussion on wireless connectivity and how it plays a key role in the new medical paradigm of personalized health. Then, we will focus on the IMDs alternative powering methods, such as energy harvesters and radiofrequency power sources, which promise to bring great benefits to IMDs by replacing batteries, and thus facilitating further device miniaturization. In the path of RF power, we will review the wireless power transfer concepts and methods, while focusing our attention into near and far-field applications, which have proven to be key for many implantable applications.

2.1 Implantable Medical Systems

The first implantable medical devices were developed in the 1930's when the initial attempts of nerve and muscle electrical stimulation were performed [32]. Between 1950 and 1970, telemetry systems were developed mostly for tracking purposes. These were modest systems composed by a battery, a coil antenna and sensor, and their capabilities remained restricted to sensing pH levels, intestinal

contractions, temperature and pressure. The first stimulation systems were also developed for stimulation of the peripheral and central nervous systems. Small electric currents were used to produce nerve signals transmission or blockage (pain suppression). Also in this period, the first attempts to develop cardiac defibrillators, visual prosthesis and brain stimulators for emotional control were made. Between 1970 and 1990 the implants matured. With the first microelectronics and integrated circuits, device miniaturization was possible and new generations of sensors and cameras were used. Micromechanical elements, chemical, physical, and biological actuators were incorporated, and new miniaturized telemetry systems uncovered a new world of implantable solutions. It was in the same period that the first dedicated journals in the field of transducers and MEMS emerged. From 1990 to the present day, the development of very large scale integrated circuits (VLSI) and application specific integrated circuit (ASIC), as well as the miniaturization of physical, chemical, and biological transducers, MEMS and NEMS cleared many technical barriers and widened the applications of implantable systems in medical and life sciences research. These devices are now able to mitigate lost functions, treat health disorders and monitor biological parameters, and promise to improve health care and reduce the cost of diagnostics [32][80].

2.1.1 IMDs Applications

Starting with the first ever implanted cardiac pacemaker in 1953, the therapeutic applications of IMDs are intended for active treatment and diagnostic applications. Active treatment devices can be found in assistive/artificial organs such as cardiovascular assistive devices, heart pacemakers, respiratory pacers, artificial kidneys and lungs, urinary control systems, artificial vocal cords; drug delivery systems, cancer treatment or pain relieve drug infusion devices; neural recorders and stimulators for epilepsy treatment, Parkinson's disease and pain suppression; middle ear and cochlear implants for the hearing impaired and vision prosthesis for the blind. The diagnostic applications make use of the body's physiological signals to monitor blood pressure, blood oxygen level, blood glucose, ECG, temperature and inner ocular pressure. Devices that monitor organ functions, transplanted organs, disease progression, and cancer

growth are also available, as well as dwelling devices in the esophagus, digestive channel, and other body cavities [30][32][78].

2.1.2 Essential Blocks of Implantable Medical Devices

Modern IMDs are biomedical instruments that can sense, actuate, gather information and/or solicit a reaction within a living organism from a location external to the body through a wireless communication link [32]. The system is usually surgically implanted inside the body or is placed inside body cavities. The essential parts of an implantable system are presented in Figure 2.1, where the implant is linked to external equipment by a wireless link for telemetry (sensing) or stimulation (actuation). When both are linked together, it is called a closed-loop control system.

The system can be fully electronic or can have mechanical, chemical or biological parts. In implantable telemetry systems, the sensors convert the biological parameters into electric signals, which are processed by the interface and are transmitted to an external receiver using a radiofrequency link (or other wireless means such as optical or ultrasound). In implantable actuation systems, the external unit makes use of the wireless link to send command signals, driving the actuators to solicit certain actions. The actuators are the electrical stimulators that send electrical current to muscles or nerves through stimulating electrodes. In closed-loop control systems, the telemetry and stimulating units are linked together to control a specific body function where the telemetry component acts as a feedback unit [30][32][78].

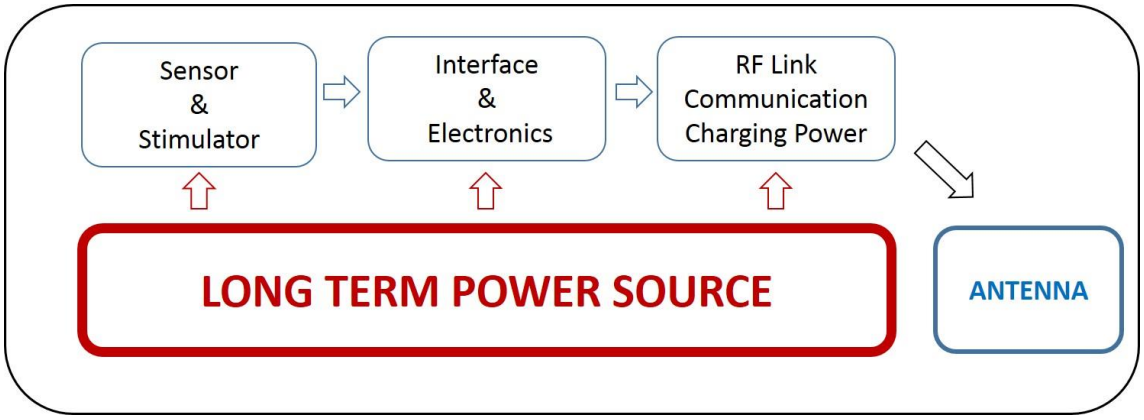

Figure 2.1 Conceptual diagram of the essential parts of an implantable system.

2.1.3 Wireless Capabilities

In the early development stages of IMDs, telemetry was not available, but as technology evolved and our understanding of the biological interaction between radiofrequency and human tissues matured, the benefits of RF use in biomedical applications surpassed the implementation challenges, thus becoming more widespread [78]. IMDs are now capable of bidirectional RF telemetry applications between a remote or inaccessible location within the human body and an external receiving station. This feature is a key factor for the new medical paradigm of personalized health care and a must-have for the most recent medical implants [78]. The ability to communicate with, to control, and to wirelessly power an implanted device can provide unprecedented access to the human body and personal health data without interruptions. With remote monitoring, physicians and patients could be provided with continuous health condition status updates, and be permanently aware of the state of their well-being, and hence potentially prevent diseases and favor home hospitalization as depicted in Figure 2.2.

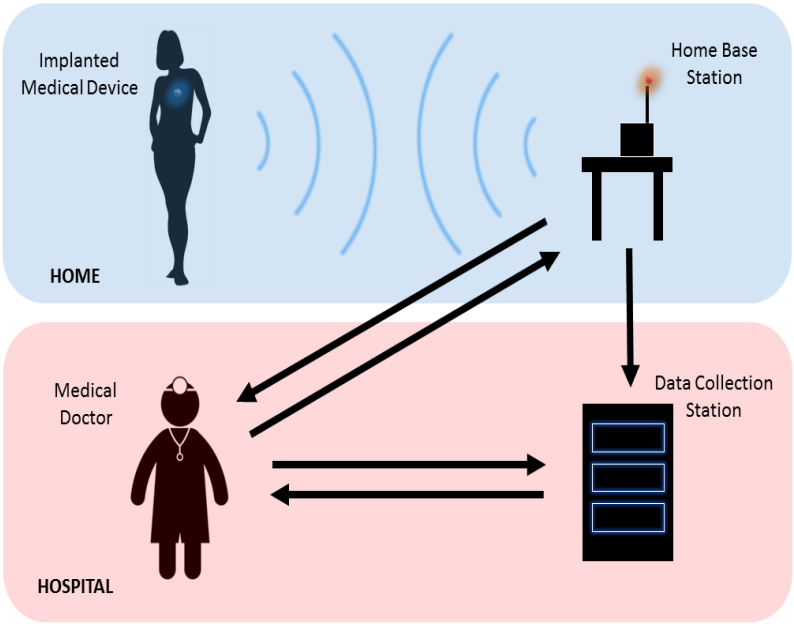

Figure 2.2 IMD communication path with a home based station and a medical facility. The IMD communicates with a home base station, which in turn can communicate with the physician at the hospital. A data collection station keeps the physician updated with the patient's clinical information and instructions (drug dosage, stimulus, etc.), that can be transmitted from the physician to the patient's IMD at home. The home base station can also power the IMD through electromagnetic radiation.

Besides the instant benefits to patients and healthcare providers that arise from this feature, economic benefits are also extremely relevant. Personal health records can be created and direct access to cellular or fixed networks and to the internet can offer remote monitoring of patients, hence decreasing hospital visits. Recent studies suggest that physicians who access medical devices through remote monitoring can offer a reduction of 40% in hospital visits and the cost per visit reduced by $1,800 [32][80].

2.2 Alternative Powering Methods

Most implantable medical devices are currently powered by batteries, which periodically have to be recharged or replaced, and therefore the need for alternative power methods is becoming more evident. Furthermore, these power sources must be small, inexpensive and highly reliable. This need has given rise to a new field of research and engineering practices frequently referred to as “energy harvesting”. This term generally denotes devices or systems that capture (or harvest) energy in the environment and convert it to a useful form. Well-known examples of large-scale and renewable power generation are solar arrays, wind farms, and ocean wave generators. However, energy harvesting is usually used to describe or define technologies, devices, and systems that capture ambient energy to replace the batteries, carrying with them the theoretical promise of perpetual, maintenance-free power sources with long lifetimes and high reliability while being competitive on size and cost.

It is noteworthy that the overall dimensions of energy harvesting systems for biomedical applications are usually in the millimeter or centimeter range, and only the transducers are in fact in the microscale. In the available literature the term “micro” usually refers to the parallel fabrication techniques common to the semiconductor and MEMS industries. In practice, some of the devices will be macroscale devices that are moving toward microscale implementations.

In this section, we will review some alternative powering technologies and methods that can provide power to implantable medical devices. Since IMDs have to be small, reduced size is also a pre-requisite for implantable energy harvesting systems (EHS). However, most EHS have overall dimensions in the centimeter and millimeter scales and generate power in the microwatt range (10-100 μW). Many energy

harvesting sources (and methods) have been presented in the literature [81-84], and among them biological [85], thermal [86], piezoelectric [87], and electromagnetic sources [67] have been proposed for powering of IMDs. Here, special attention will be given to fuel cells, thermoelectric generators and piezoelectric materials and electromagnetic sources.

2.2.1 Fuel Cells

Fuel cells convert the electrochemical energy of a fuel into electricity using catalytic oxidation/reduction reactions. Glucose and enzymatic biofuel cells are an interesting solution for implantable medical applications due to their high energy density and power [85][88]. Although having been proven feasible *in vivo* [89] (Figure 2.3A), several issues such as the long-term *in vivo* performance and safety still have to be addressed for fuel cells to be considered for implantable applications [90].

2.2.2 Thermoelectric Generators

Thermoelectric generators [91] are solid-state devices that directly convert the thermal energy of a temperature gradient into electrical energy. Their attractive features, such as high reliability, durability, and compactness are appealing since the human body is an abundant source of thermal energy. Thermoelectric generators can be used in very low-power implantable applications such as supporting a clock circuit inside a rabbit [91] (Figure 2.3B). However, they suffer from low conversion efficiencies and even very low power circuits need a temperature gradient of several Kelvin, and such gradients are difficult to attain inside the human body [92].

2.2.3 Piezoelectric Transduction

Piezoelectric transduction has also been proposed as a way of powering IMDs. The working principle is based on the ability of piezoelectric materials to produce an electrical voltage when subjected to mechanical deformation. These materials have proven to enable mechanical-to-electrical energy conversion from the natural contractile and relaxation motions of arteries [93], heart, lung, and diaphragm to power a pacemaker [87] (Figure 2.3C), and can also exist in the form self-powered

nanosystems [94]. The main challenges of piezoelectric power sources for IMDs relies on the variable, and usually small output energy levels, thus making the design of power management circuits a challenging task that needs to be further investigated.

2.2.4 Radio Frequency

Energy transfer from electromagnetic waves to IMDs has also been proposed [95] (Figure 2.3D). Among the different alternative powering techniques, RF energy is the one providing the highest energy density per unit area, thus having the highest potential for miniaturization [13][32][73][78]. Since the transducer in RF energy transfer is an antenna, its miniaturization is key. However, and as we will see in chapter three, antenna miniaturization is a challenging task that requires a compromise between antenna size and its overall performance. With the increasing use of wireless communications, the opportunities for wireless energy transfer are growing. In the next section we will discuss wireless powering approaches such as inductive coupling systems, making use of coils, and radiative transmission, by means of antennas, have been investigated as methods of wirelessly transferring energy to implantable medical devices [67][73][77][96].

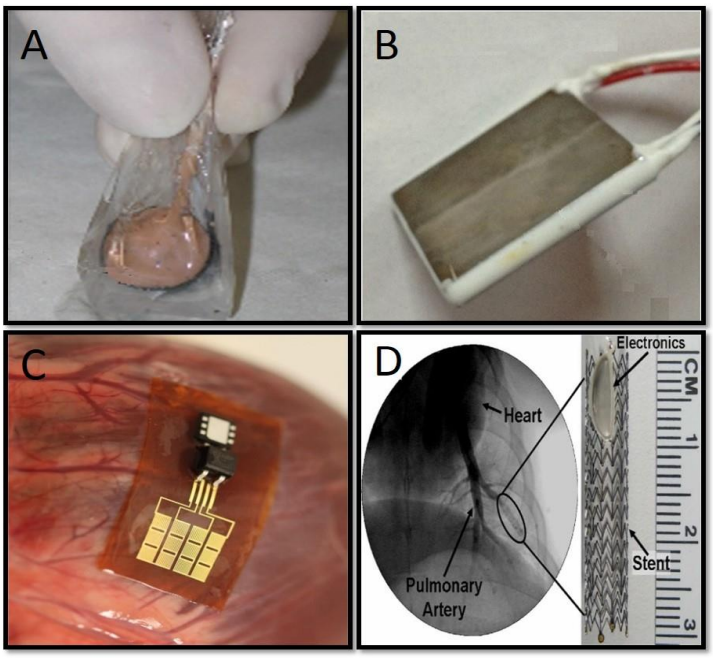

Figure 2.3 Alternative powering methods for implantable applications. A) A glucose biofuel cell for rat implantation [89]. B) Implantable thermoelectric generator [91]. C) A piezoelectric system capable of harvesting

energy from the natural contractile and relaxation motions of the heart, lung, and diaphragm and used to power a pacemaker [87]. D) Implantable stent in the pulmonary artery [95].

2.3 Wireless Power Transfer

Transferring power wirelessly over a distance is a major technologic breakthrough as it can provide devices with virtually unlimited energy, thus improving the overall device features. As a result, in recent years, wireless powering technologies have emerged as solid options for the powering of biomedical applications (Figure 2.4).

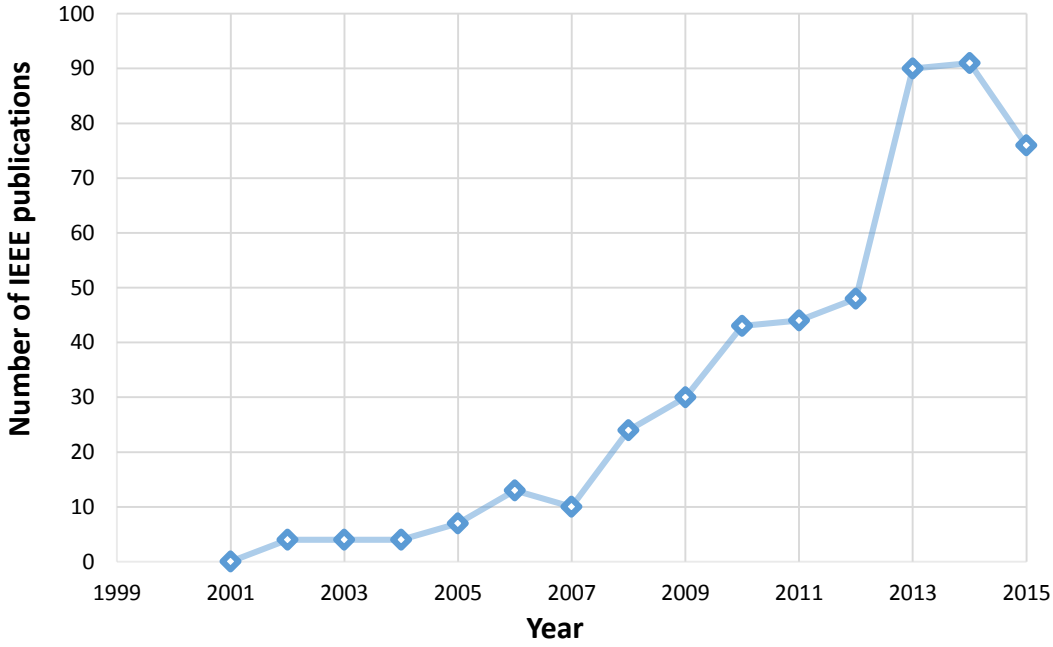

Figure 2.4 The rapid development of the WPT applied in biomedical applications, the number is indexed by using key words "Wireless Power Transfer and Biomedical" in IEEE Xplore (adapted from [97]).

Among them, mostly the inductive and radiative methods have been proposed for the powering of implantable medical devices. In this thesis we will focus on the antenna near-field and far-field transfer regions, which describe specific areas within an electromagnetic field formed around an antenna.

The space surrounding an antenna is usually subdivided into three regions, designated to identify the field structure in each one of them. These are the reactive near-field, the radiating near-field and the far-field, as shown in Figure 2.5. The

transitions between these regions are not distinctive, although various criteria have been established and are commonly used to identify them.

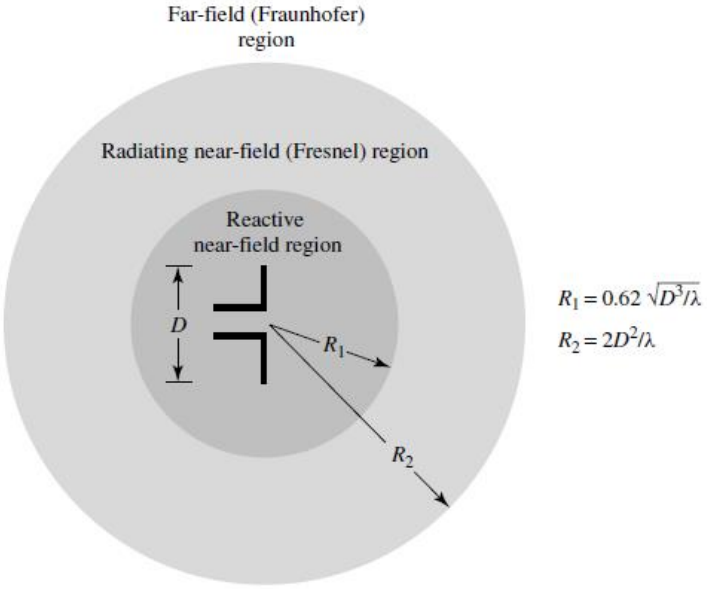

Figure 2.5 Field regions of an antenna [98].

The reactive near-field is defined as that portion of the near-field region immediately surrounding the antenna, wherein the reactive field predominates. It means the E and H fields are out of phase, by 90 degrees, to each other (for propagating or radiating fields, the fields are orthogonal but are in phase). For most antennas, the outer boundary of this region is commonly assumed at a distance $R < 0.63$ from the antenna surface (λ is the wavelength and D the largest dimension of the antenna).

The radiating near-field (Fresnel) region is defined as that between the reactive near-field and the far-field regions, wherein radiation fields predominate. If the antenna has a maximum overall dimension which is very small compared to the wavelength, this field region may not exist. The inner boundary is assumed to be $R \geq 0.63\sqrt{D^3/\lambda}$, and the outer boundary $R < 2D^2/\lambda$.

The far-field (Fraunhofer) region is defined as that region of the field of an antenna where the angular field distribution is essentially independent of the distance from the antenna. The inner boundary is taken to be the radial distance $R > 2D^2/\lambda$ and the outer one at infinity [98].

Both near-field and far-field electromagnetic fields decrease inversely with distance from the antenna. The reactive near-field attenuates as waves travel away from the antenna with distance dependency of $1/r^3$, while the radiating near-field attenuates with a dependency of $1/r^2$. The far-field attenuates with a distance dependency of $1/r$.

The near-field and far-field transfers have their own subtypes, as seen in Table 2.1. The near-field transfer includes inductive and capacitive coupling, while the far field transfer includes the propagating electromagnetic. The characteristics of the five kinds of transfers are summarized in the table below.

Table 2.1 A comparison between wireless power transfer methods.

WTP type	*Frequency*	*Directivity*	*Range*	*Penetrability*	*Efficiency*
Inductive Coupling	Low Hz-MHz	Low	Short	Strong	High
Capacitive Loading	Low Hz-MHz	Low	Short	Strong	High
Propagating	MHz	Medium	Medium	Medium	Medium
Electromagnetic	THz	High	High	Low	Low

Several authors [97] argue that due to weak directivity, strong tissue penetrability and high efficiency, wireless power transfer by means of inductive coupling is the best option for implantable medical applications. However, as we will see in the next section, inductive coupling presents a series of drawbacks when used for wireless power transfer, which can be surpassed by a using radiative transfer instead.

2.3.1 Inductive Coupling

In inductive coupling, an alternating current in a transmitting coil generates an alternating magnetic field, which passes through, and couples to a secondary coil. The generated alternating fields induce an electromotive force in the receiving coil that can be used to power a load as seen in Figure 2.6. Unlike RF systems that communicate by means of propagating plane waves in free space, inductive coupling relies on setting up a quasi-static magnetic field around the transmitting coil. When a second coil is introduced into that field, the incident time varying magnetic flux density on that coil

induces a voltage on its windings. The modulated voltage can then be processed and data can be transmitted. Data and power can be transmitted over short distances, and applications using this principle have been the preferred energy transferring method when it comes to implantable medical devices [13][73][99][100].

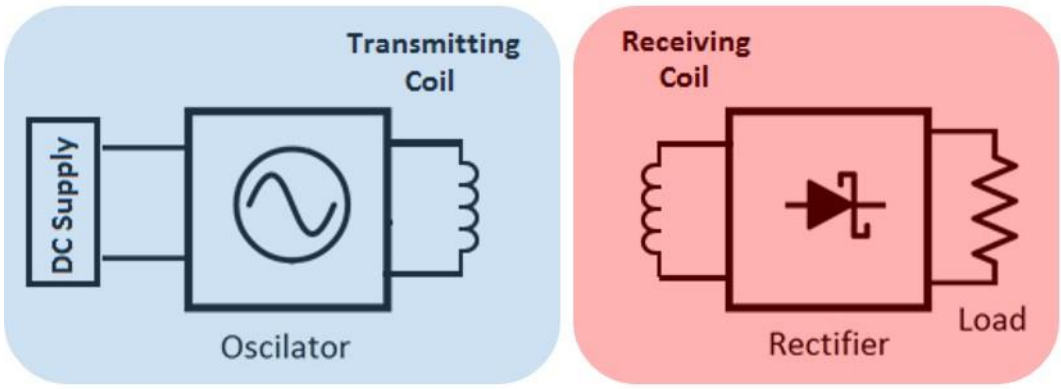

Figure 2.6 Schematic of the inductive coupling transfer setup.

Since inductive coupling mostly exploits low frequencies, such as the 13.56 MHz industrial, scientific, and medical (ISM) band, it becomes very practical for the powering of IMDs due to low signal attenuation in the human tissues. However, regardless of its popularity, near-field methods are not free of challenges. Among them, the week coupling between coils is a common one. Several reasons for this have been reported but coil misalignment is usually a major issue, causing low power transfer efficiencies and low data transfer [101-103]. In fact, this method requires precise positioning between coils, which can be very difficult to achieve specifically if the subject is expected to be moving [104]. Moreover, there are coupling difficulties for devices implanted in dissipative and heterogeneous tissues. Also, inductive coupling is limited by exponential decay, as it is a near field phenomenon, and thus the external coil has to be in close proximity to the implant, which limits the comfort and freedom to perform daily live activities.

2.3.2 Radiative Transfer

As future implantable devices are expected to be ubiquitous and fully compatible with the subject lifestyle, there's an obvious technological drive to proceed

towards the development of solutions that do not require users to carry, or to be in close proximity of, a signal-reading and/or powering station as in inductive coupling systems [105-106]. In this way, it is important to increase the distance at which implantable devices can communicate and be wirelessly powered. This can be accomplished by using RF antennas exploiting radiative transfer, where communication and wireless powering are performed utilizing propagating electromagnetic waves.

To power small devices with small integrated antennas, the electromagnetic wavelengths are typically in the microwave range. These microwaves are generated by an RF source which is connected to an antenna. The energy radiates outwards in all directions, in the form of an electromagnetic wave that leaves the transmitting antenna, and is intercepted by a receiving one located at a distance (Figure 2.7). The received RF signal is then rectified and transferred to a load.

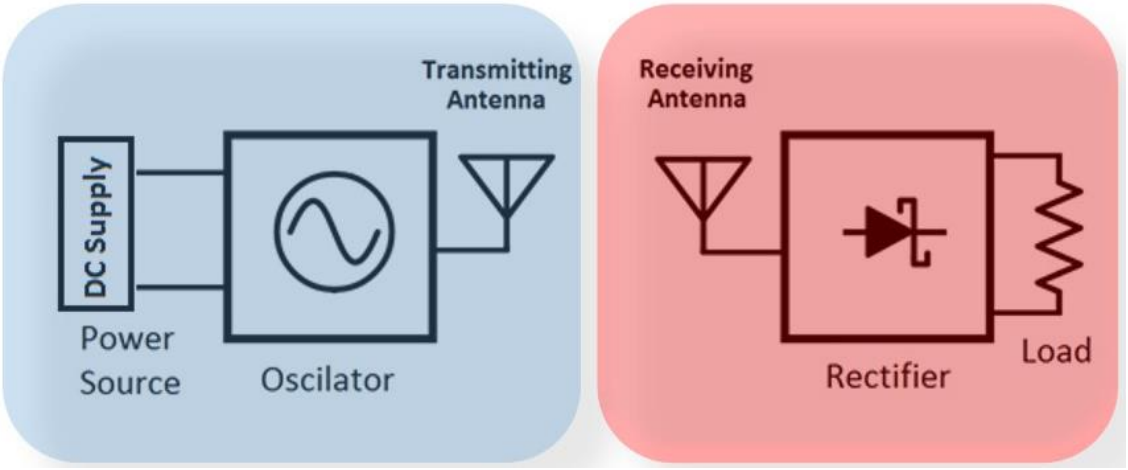

Figure 2.7 Schematic of the radiative transfer setup.

Unlike in inductive coupling, this type of transfer, usually performed in the radiating far-field, is not strongly restricted to short distance operation, nor by the strict positioning and alignment between the transmitting and receiving coils, and can be used to transmit energy to multiple receivers. This desensitization of transmit and receive antennas to relative alignment and orientation means that implants with integrated antennas can operate more robustly in the far field, and with the uncertainty of the implant's position and orientation in respect to the external source.

2.4 Antennas for Implantable Medical Devices

Currently, the majority of commercially available IMDs make use of inductive coupling, i.e., magnetic induction, for data and power transfer, mostly due to the fact that inductive coupling operates at low frequencies and therefore signal losses in the tissues are low. Some examples of IMD that make use of inductive coupling are the microCHIPS drug delivery implant for osteoporosis treatment [5], CardioMEMS pulmonary artery pressure sensor [107], and the Argus® II retinal prosthesis system from Second Sight Medical Products Inc. [4][16] (Figure 2.8).

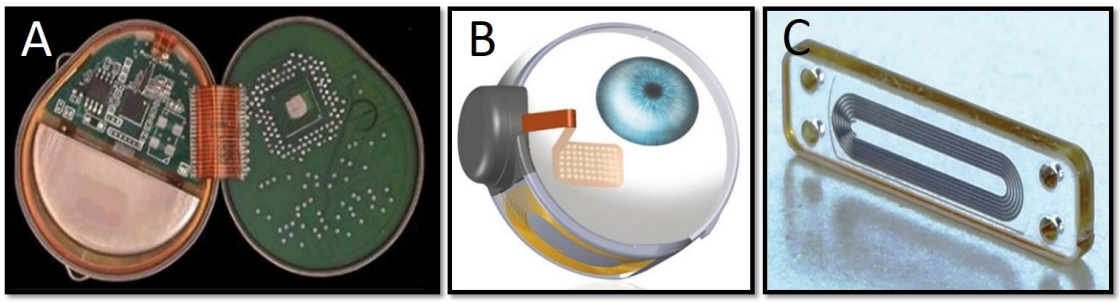

Figure 2.8 Commercially available IMDs that make use of inductive coupling for data or power transfer. A) MicroChips implantable drug delivery device [5]. B) The Argus® II Retinal Prosthesis System [16]. C) Implantable aorta pressure sensor [107-108].

However, many patents of IMDs with integrated antennas have been recently filed by major medical device companies such as Medtronic. Inc. and Boston Scientific, Inc. This new trend is supported by the increasing capabilities and functionalities of modern implantable devices that collect, manage, and quickly transmit high volumes of data. Inductive coupling systems are known for their low data transfer rates and hence some providers are making efforts to equip their products with RF antennas for quicker wireless data links and power. Patents have been filed for cardiac pacemakers, defibrillators, intracranial devices, and neurostimulators [109-116]. Nevertheless, literature on antennas for implantable applications is rich and growing, and the need for high data links over larger distances is fueling new antenna designs and applications. Table 2.2 presents some of the most recent antenna designs proposed for IMDs. These antennas are suitable for wireless power transfer purposes, in-body telemetry, monitoring and sensing, and found in key implantable technologies, as seen in intraocular, neural, cardiovascular, drug delivery and endoscopic devices.

2.4.1 Antennas on Centimeter Scale Devices

Antennas come in many forms and shapes such as flexible spiral [109], wire [110], inverted E [111], stacked in high dielectric substrates [115], fractals [114], and 3D configurations[112-113]. Most antennas used in miniaturized devices are of planar geometry due to ease of fabrication and low cost [48-49], and examples can be seen on single spirals, meander lines, dipoles, slots, PIFA, loops, and fractal antennas. Even, to fit on centimeter scale devices, the antennas have to be miniaturized, and a common way of doing it is to alter its geometry [74-76]. In fact, antenna miniaturization can be achieved in many ways such as bending a dipole [117], printing radiating elements on both sides of a substrate [118], capacitive loading and slit formation [119], slot creation [120], and layer stacking [121-122] (Figure 2.9).

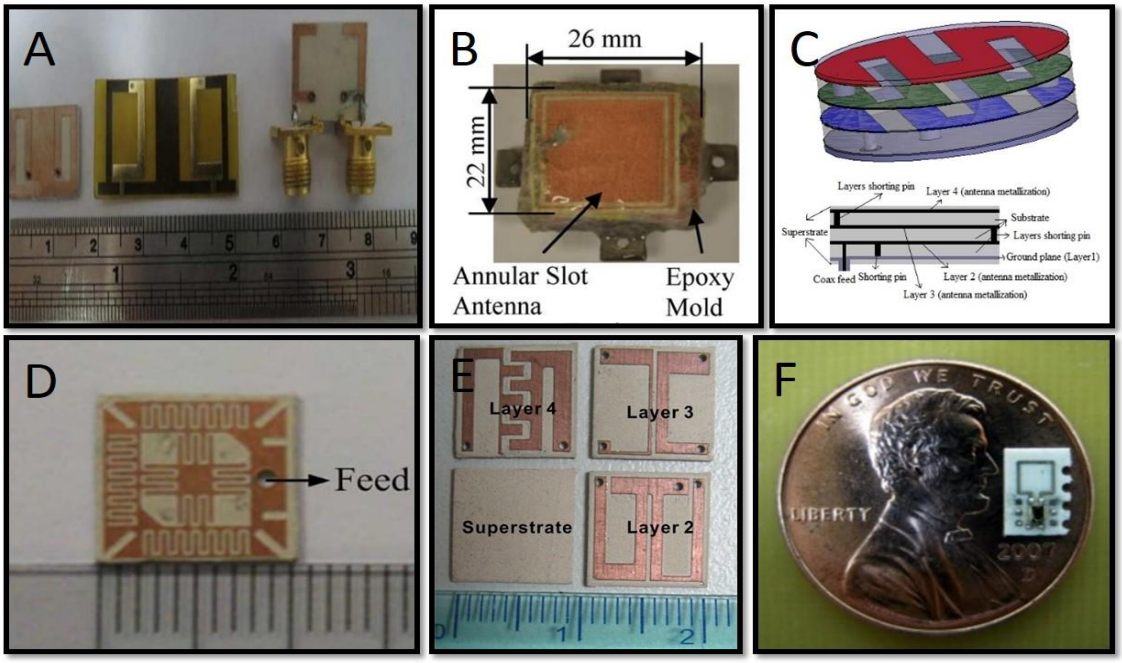

Figure 2.9 Planar antennas proposed for IMDs. A) Flexible planar dual-band implantable antenna for endoscopy capsule [118]. B) Annular slot antenna for intracranial pressure sensor [120]. C) Multi-layer implantable antenna for a brain stimulation system [121]. D) Capacitive loaded patch antenna for biomedical applications [119]. E) Implantable triple-band implantable antenna with a spiral and stacked structure [122]. F) Self-propelled implantable device with loop antenna [13].

Other miniaturized antennas adopt 3D typologies in order to efficiently use most of a given three dimensional space, in order to produce larger antennas (Figure 2.10). 3D antenna designs have been utilized as an relevant tactic for antenna performance

enhancement and optimization, thus overcoming some of the limitations of planar antenna, namely their large cross-sections, low bandwidth and low radiation efficiency [32][51][52][53]. Examples range from folded antennas for dental implants [131] and cochlear implants [123], conformal antennas for central venous catheter [124], a monopole on-chip antenna for an intraocular pressure monitor device [125], and an implanted stent antenna for pulmonary failure detection [10]. Frequently, the packaging requirement have priority over the antenna, which lead to solenoid radiator geometries. These geometries are very common in in-dwelling devices for gastrointestinal applications such as in endoscopic capsules where 3D antenna designs are used [126-127]. Non-solenoid antenna geometries have also been proposed as seen in [128-130].

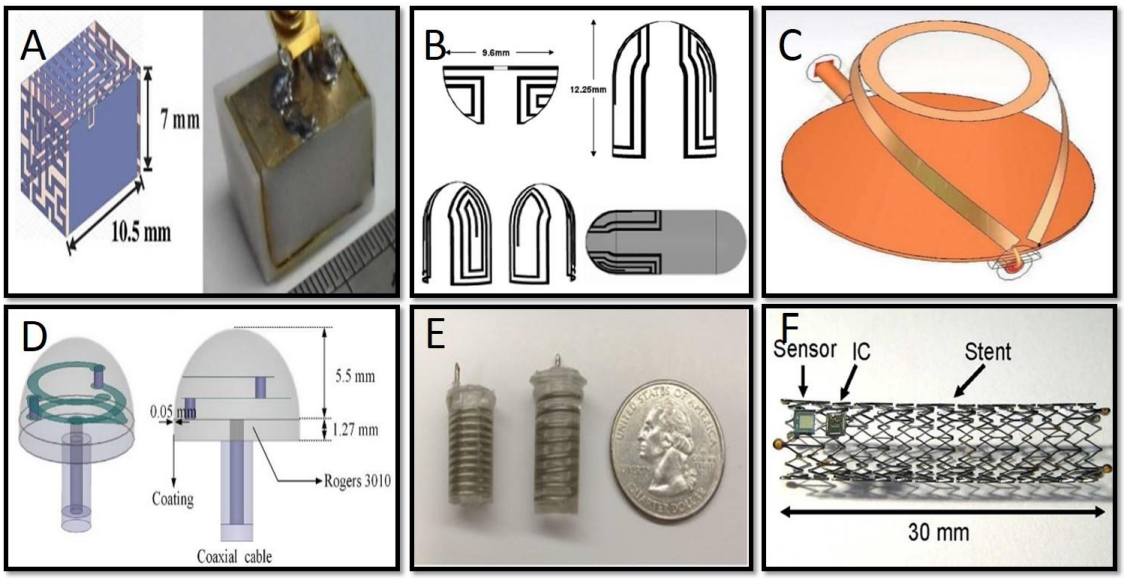

Figure 2.10 3D Antennas proposed for IMDs. A) 3D folded antenna for dental implants [131]. B) Conformal meandered dipole antenna for ingestible capsule endoscope [128]. C) 3D conformal monopole antenna for central venous catheter [124]. D) Low-profile cylindrical helical antenna for ingestible endoscopy capsule [127]. E) RFID tag helix antenna sensors for wireless drug dosage monitoring [130]. F) Stent antenna for heart failure detection by monitoring internal pressure measurements of the pulmonary artery [10].

2.4.2 Antennas for Millimeter Scale Applications

Until now we have seen centimeter scale antennas for centimeter scale devices. However, if devices are intended to be implanted in the tiny openings and vessels of the human body, not only the devices' dimensions have to be drastically reduced, but their antennas as well. Figure 2.11A presents a centimeter scale double action biopsy spoon

forceps, used to grasp and collect tissue from the colon walls and, in between the forceps, it can be seen a microgripper. Both tools, being utilized for colon biopsy, are introduced via the anus. While the forceps retrieve colon tissue samples every 10 cm, the microgrippers, which can be deployed in by the thousands, covering a much wider area of the colon, and collect many more tissue samples, thus increasing the probability of finding cancerous cells. Figure 2.11C presents a centimeter scale drug delivery device, which is implanted under the skin, while in Figure 2.11D and E, present two micro containers suitable for drug delivery *in situ*, which can be deployed in the narrow conduits of the human body.

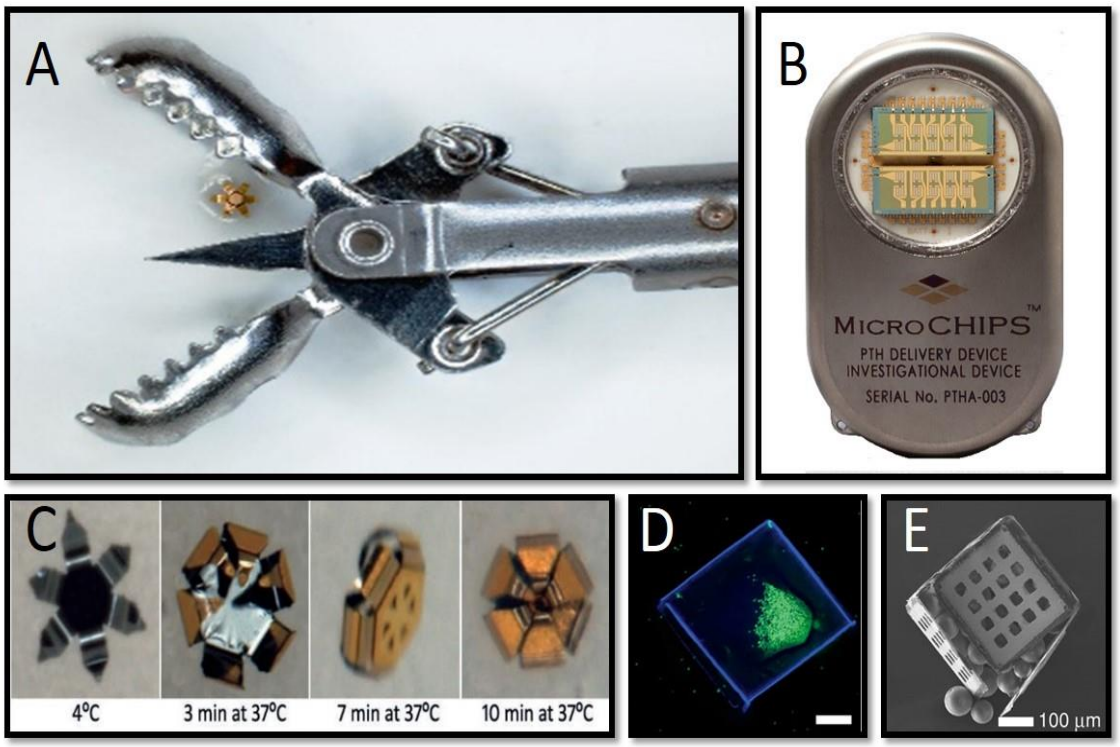

Figure 2.11 A) double action biopsy forceps and a microgripper [23]. B) MicroCHIPs drug delivery implantable device [5]. C) The microgrippers are activated thermally when inside the colon. The sequence shows the thermal actuation of the microgrippers at 37° C within 10 min. D) Self-folded polymeric micro container and E) Metallic micro container, both suitable for drug delivery and cell encapsulation purposes.

In both cases, an ultra-miniaturized version of a centimeter scale tool requires some sort of external triggering or activation, which could be provided with a radiofrequency signal [21]. The realization of extremely small antennas for sub-millimeter devices is not very common and the literature is also scarce. A few examples can be seen in micro coil arrays for nuclear magnetic resonance [132], micro helixes

arrays for remote imaging [133], metal coated spirulina for terahertz responsive structures [59], and micro tags delivered into living cells containing inductive and capacitive structures for potential passive radio-frequency identification applications [52] (Figure 2.12). Several reasons can be pointed out for the scarcity of more ultra-small implantable tools making use of sub-millimeter antennas, and the main one being the fact that radiofrequency losses in human tissues increase with frequency, thus resulting in low power transfer efficiency. Nonetheless, with the possibility of transferring power in the low-gigahertz range, such losses can be diminished, which may encourage further research on this subject.

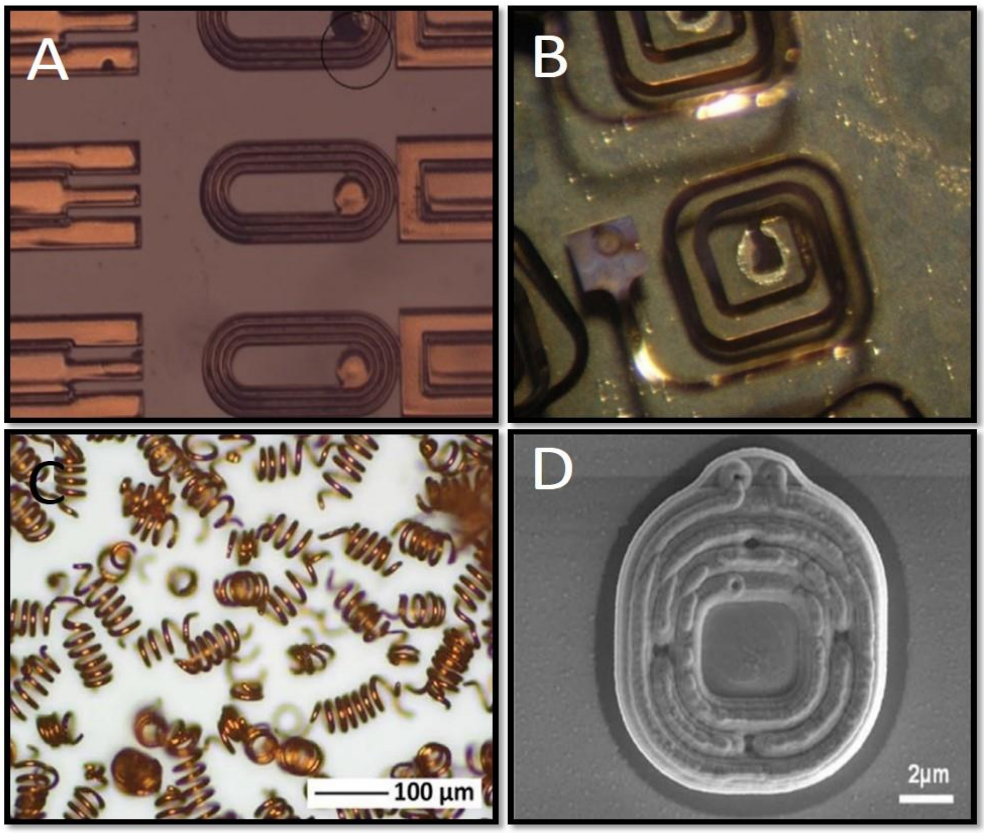

Figure 2.12 Micro coil antennas (1000 × 500 µm^2) for a nuclear magnetic resonance application [132]. B) Micro-helix antenna array prototype for a remote imaging application [133]. C) Spirulina-templated microstructures which are coated with metal unveiling spiral terahertz responsive micro structures [59]. D) Micro tag into living cell [52].

Table 2.2. Antennas for implantable medical devices: State of the Art.

Type	Dimensions	Frequency	BW	Applications	Range	Year
Loop	2 mm^2	1.86 GHz		Energy Harvesting	5 cm	2012 [13]
Monopole	1.5 x 3.2 mm^2	5.2 GHz		Intraocular Energy Harvesting	10 cm	2013 [125]
Fractal	20 ×20 ×1.6 mm^3	2.4 GHz / 5.8 GHz		Energy Harvesting	25 cm	2014 [134]
Patch Capacitive	10 x 10 x 1.27 mm^3	2.4 - 2.48 GHz	7.74%	Neuro Implant Telemetry	< 7 m	2014 [119]
Loop	2 x 2 x 2 mm^3	300 MHz	Narrow	Brain Machine		2013 [135]
Annular Slot	6.5 x 6.5 mm^2	2.4 GHz ISM	26 %	Intracranial Pressure Sensor		2013 [120]
3D folded fractal	245mm^2	MedRadio	4.8 MHz	Telemetry Dental Device	3 m	2013 [131]
Patch Spiral Dipole	204 mm^3	402-405 MHz (MICS)		In body Telemetry	40 cm	2013 [136]
	300 mm^3				138 cm	
Folded Dipole	20 x 0.8 x 0.8 mm^3	0.951 – 0.956 GHz		In body Telemetry		2013 [137]
3D conformal	10 x 10 x 16 mm^3	401–406 MHz	273 MHz	Telemetry		2014 [124]
Flexible PIFA	13.4 x 16 x 0.835 mm^3	402-405 MHz 2.4 GHz	23 % 21 %	Telemetry	10 cm	2014 [118]
Spiral Dipole	10 x 10 x 0.675 mm^3	MICS ISM	47.5 % 31.6 %	Telemetry		2014 [117]
Folded Dipole	36mm × 1.6mm mm^3	924 MHz	225 MHz	Telemetry	10 m	2013 [129]
Folded Loop	38 x 38 x 2.2 mm^3	2.37–2.58 GHz	210 MHz	Telemetry Cochlear	10-50 mm	2014 [123]
Stent Antenna	3394 mm^3	2.4 GHz	555 MHz	Cardiovascular Stent Telemetry		2009 [10]
Spiral	393 mm^3	500 MHz	21 %	Capsule Endoscope Telemetry	150 mm	2011 [126]
Meander Dipole	60×60×0.127m^3	1.4 GHz	20 %	Capsule Endoscope Telemetry		2009 [128]
Helix	1332 mm^3	2.4 GHz	110 MHz	Drug Dosage Monitoring		2014 [130]
Helical	Π x $(5.5)^2$ x 3.81 mm^3	2.4-2.48 GHz ISM	26%	Capsule Endoscope Telemetry	150 mm	2014 [127]
Loop	5 mm radius 5um thick	1.8 GHz		Glucose Sensor	15 cm	2012 [6]

3 Small Antennas for Implantable Medical Devices

Unlike conventional antennas, typically used for communication in free space, implanted antennas are subjected to special conditions that hinder their performance. First, they are typically embedded in high loss media, such as the human tissues, that affect the propagation of the electromagnetic waves, attenuating them. Second, due to size requirements, they have to be miniaturized, which is usually achieved at the expense of the antenna performance degradation, namely its efficiency, and gain. Furthermore, and as we will explain, these two special conditions are related. Due to its dielectric properties, the human body can be seen as a low pass filter, where the biological tissues allow low frequency electromagnetic signals to pass through them, but strongly attenuate any high frequency ones. On the other hand, since the antenna operating frequency is inversely proportional to its size, it means that an implanted miniaturized efficient antenna will operate at a high frequency [72], resulting in high tissue attenuation. This fact alone could discourage the use of high frequency antennas on IMDs. In fact, most of today's commercially available IMDs make use of low frequency links based on inductive coupling, for communication and wireless power transfer. In contrast, the use of low frequency electromagnetic signals would represent a serious drawback since it requires large receiving antennas and consequently larger devices.

However, recent research [138] has shown that there is a desirable frequency range, located in the low gigahertz (1-10 GHz), where the electromagnetic signals losses due to tissue attenuation might not be too intense, thus opening the way for small antennas to communicate with, and power IMDs. At this point, several relevant questions may arise: "is it possible to wirelessly power an implantable device with a small antenna", "how severe are the losses due to issues attenuation", "how small can an antenna be and still remain of practical use and what are their specific characteristics and limitations?" To answer these questions, we will review some important notions regarding the interaction between electromagnetic waves and lossy media, and discuss a power budget model, in an attempt to assess how much power would be possible to provide to a small implanted antenna. Then, we will study the fundamental limitations

imposed by antenna size reduction, showing how it affects the antenna efficiency and gain. Finally, since implantable antennas have to be miniaturized, several miniaturization techniques and the important aspects of making an antenna small will be described. Emphasis is given on how to change the antenna geometry in order to keep its frequency low by means of antenna geometry modification, use of dielectric loading, full use of the volume circumscribing the antenna, and optimization of the current distribution within the antenna structure.

3.1 Electromagnetic Field Interaction with Materials

In this section we will discuss the interaction of electromagnetic fields with the materials they propagate in. Since the interactions of **E** and **B** with materials are complex and hard to explain, three parameters are defined to account for these interactions: Permittivity ε (Farad/m), or *dielectric constant*, describes how much induced polarization and partial alignment of permanent electric dipoles occurs for a given applied **E**. *Relative permittivity* (unitless), defined as $\varepsilon_r = \varepsilon/\varepsilon_0$, is the permittivity relative to that of free space; *Conductivity* σ (Siemens/m), describes how much conduction current density a given applied **E** will produce; *Permeability* μ (Henry/m), defines how much partial alignment of permanent magnetic dipoles occurs for a given applied **B**. *Relative permeability* (unitless) is defined as $\mu_r = \mu/\mu_0$. For most applications, the human body is so weakly magnetic that we can assume $\mu = \mu_0$, so $\mu_r = 1$. Table 3.1 presents the dielectric properties of some human body tissues. Skin, fat and muscle are frequently mentioned in the literature since many implantable medical devices are designed for either subcutaneous or deep tissue implantation. It is noticed that increasing frequency affects the tissues dielectric properties by increasing their conductivity and decreasing their permittivity.

Table 3.1 Dielectric properties of body tissues: muscle, skin and fat [139].

Frequency	**1 GHz**			**10 GHz**			**100 GHz**		
Tissue	**σ**	**ε**	**$\tan\delta$**	**σ**	**ε**	**$\tan\delta$**	**σ**	**ε**	**$\tan\delta$**
Muscle	0.972	54.81	0.320	10.626	42.764	0.446	62.499	8.630	1.301
Skin	0.899	40.93	0.395	8.0138	31.29	0.460	39.433	5.598	1.266
Fat	0.053	5.447	0.176	0.5852	4.602	0.228	3.562	2.889	0.221

EM waves change their propagation behavior due to the interaction with biological material. Its energy is retained in the lossy material (lossy if σ ≠ 0), causing loss to the propagating wave and the material to heat up. Introducing Ampere's law:

$$\nabla \times B = \mu\left(J + \varepsilon\frac{\partial E}{\partial t}\right) \tag{1}$$

using Maxwell's magnetic field strength or magnetic field intensity definition $H = B/\mu$, where H (A/m) (with B and H being often referred to simply as magnetic fields):

$$\nabla \times H = (J_c + j\omega\varepsilon E) \tag{2}$$

where J_c is the conduction current. $J_c = \sigma_c E$, and σ_c represents the mobility of free electrons in the material. The permittivity is a complex number:

$$\varepsilon = \varepsilon_{real} - j\varepsilon_{imaginary} \tag{3}$$

$$\nabla \times H = \sigma_c E + j\omega\left(\varepsilon_{real} - j\varepsilon_{imaginary}\right)E \tag{4}$$

Combining the conduction term with the imaginary part of the permittivity (since both are in phase with the electric field) gives:

$$\nabla \times H = \left(\sigma_c + \omega\varepsilon_{imaginary}\right)E + j\omega\varepsilon_{real}E \tag{5}$$

The term $\left(\sigma_c + \omega\varepsilon_{imaginary}\right)E$ represents the current that produces a loss (heat) and it is defined as effective conductivity σ_{eff}, or as also seen in the literature simply σ:

$$\sigma_{eff} = \sigma_c + \omega\varepsilon_{imaginary} \tag{6}$$

The term $j\omega\varepsilon_{real}$ in (5) is the displacement current, which represents the lossless portion of the oscillation. The higher the frequency ω, the larger the displacement current as well as the loss due to $\omega\varepsilon_{imaginary}$ in (6).

3.1.1 Electromagnetic Wave Interaction with Biological Material

Often, antenna problems consider the imaginary part of (3) to be negligible. However, when EM waves propagate in biological media this imaginary part accounts for an important part of the interaction. This complex permittivity is then defined as:

$$\varepsilon_{complex} = \varepsilon' - j\varepsilon'' = \varepsilon_0(\varepsilon_r' - \varepsilon_r'') \quad (7)$$

Here ε' represents the lossless component of the material properties and $\boldsymbol{\varepsilon''}$ represents the combined components of the material interaction that leads to loss. In the same way, complex permeability can be defined as:

$$\mu_{complex} = \mu' - j\mu'' = \mu_0(\mu_r' - j\mu_r'') \quad (8)$$

where μ_0 is the permeability of free space and the quantity $(\mu_r' - j\mu_r'')$ is the complex relative permeability. μ' describes the lossless interaction between the magnetic field and the material magnetic dipoles, while μ'' represents any loss associated with aligning the magnetic dipoles.

For most applications, the human body is so weakly magnetic that we can assume $\mu_{complex} = 0$, so $\mu_r' = 1$, $\mu_r'' = 0$. The ratio between ε' and ε'' describes the degree of loss in the material. This ratio is called the loss tangent $\left(tan\,\delta = \varepsilon''/\varepsilon' = \sigma_{eff}/\omega\varepsilon'\right)$ or the dissipation factor. Data banks [139] of materials' electrical properties usually provide the loss tangent $(tan\,\delta)$ and relative permittivity ε_r'. When the loss tangent is large, the material is very lossy.

3.1.2 Electromagnetic Wave Attenuation in Biological Material

In a lossy material, the effective conduction current creates a loss in the material as the wave propagates, and the magnitude of the wave decreases exponentially as [140]:

$$E(z,t) = E_0 e^{-\alpha z} sin(\omega t - \beta z - \phi) \quad (9)$$

The attenuation constant α (Neper/m) shows how fast the wave is attenuated as it propagates. The field inside the body can be expressed as a function of the propagation distance by $E_0 e^{-\alpha z}$ where E_0 is the incident field at the body surface, and z is the propagation distance.

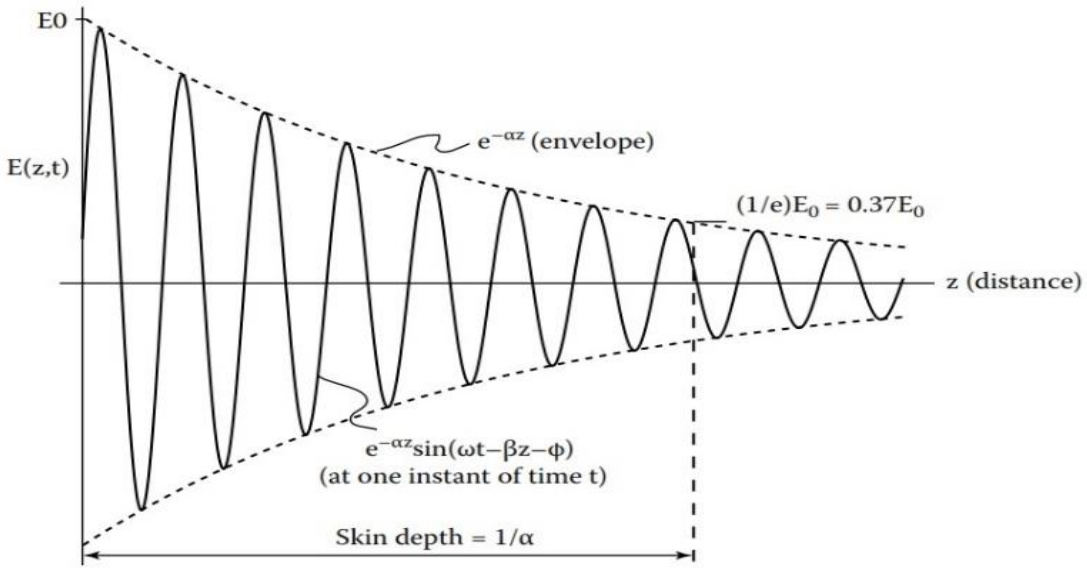

Figure 3.1 Propagating wave $E(z,t)$. The peak magnitude of this wave in a lossy material decreases exponentially as a function of distance traveled. Its envelope is given by $e^{-\alpha z}$ [140].

The attenuation constant α is then dependent of frequency and the material's permittivity and conductivity, and can be calculated as [140]:

$$\alpha = \omega \left\{ \frac{\mu' \varepsilon'}{2} \left[\sqrt{1 + \left(\frac{\sigma_{eff}}{\omega \varepsilon'} \right)^2} - 1 \right] \right\}^{\frac{1}{2}} (Np/m) \qquad (10)$$

Most biological tissues are nonmagnetic, so $\mu' = \mu_0$. It is clear now that increasing the effective conductivity or the frequency, increases the losses and therefore the attenuation. The attenuation can be used to determine a parameter called skin depth, which is given by *1/α* (m), which is the distance the wave propagates before its magnitude is dropped to 1/e = 0.37, or about 1/3 of its original value (Figure 3.1).

3.1.3 Specific Absorption Rate

When radio frequency waves reach and propagate in biological tissues, their power is absorbed and dissipated within the lossy media. This power dissipation causes the tissues to heat up, which could be hazardous. The specific absorption rate (SAR) has consequently been used as a measure of the rate at which energy is absorbed by the biological tissues when exposed to a radio frequency wave, in order to estimate the tissue heating and potential harmful effects. The SAR is defined as the power absorbed per mass of tissue, or watt per kilogram (W/Kg), and it is averaged either over the whole human body or over a small sample volume (1 g or 10 g of body tissue).

The SAR is dominated by the induced electric field (E) inside the homogenous tissue and can be defined as:

$$SAR = \frac{\sigma |E_{rms}|^2}{\rho} \tag{11}$$

where σ is the conductivity and ρ is the density of the medium under the electromagnetic exposure [141]. The spatial average SAR at any point can be determined by averaging the values enclosed in a region R, with a given mass M in a volume V as:

$$SAR = \frac{1}{M(V)} \int \frac{\sigma_e'(r)|E(r)|^2}{2} dv \tag{12}$$

where $\frac{\sigma_e'|E|^2}{2}$ is the average power density absorbed at the point of observation r. According to the IEEE standard for maximum human exposure to RF electromagnetic fields, the tissue SAR should not exceed 1.6 W/kg (1 g averaging) and 2 W/Kg for (10 g averaging) for safe operation [141]. For RF frequencies below 10 MHz, the induced electric field should also be considered to avoid unwanted stimulation of the tissue [142]. There are also some safety standards that limit the maximum permissible exposure (MPE) in terms of incident electric and magnetic fields to the human tissue [143]. However, MPE is only considered when the distance between the power source and the tissue is bigger than 20 cm, which is not the case for inductive power

transmission to IMDs based on near-field coupling but can be important in far field applications [141].

So far we have discussed the EM wave interaction with materials and lossy media, the first of the two special conditions that constrain the performance of implanted antennas. In the next section our discussion we will focus on electrically small antennas, and the limitations imposed by antenna size reduction on its performance.

3.2 Electrically Small Antennas

An electrically small antenna (ESA) is conventionally defined as one having dimensions much smaller than the wavelength. Wheeler, one of the pioneers of the study of ESAs, defined it as an antenna whose maximum dimension can be circumscribed by a radian sphere with a radius of one radian in length [144]. Later, Best [60] provided a more reasonable definition for an ESA, as an antenna having the length in terms of $ka \leq 0.5$ where k is the wave number $k = 2\pi/\lambda$ and a is the radius of sphere circumscribing the antenna (Figure 3.2).

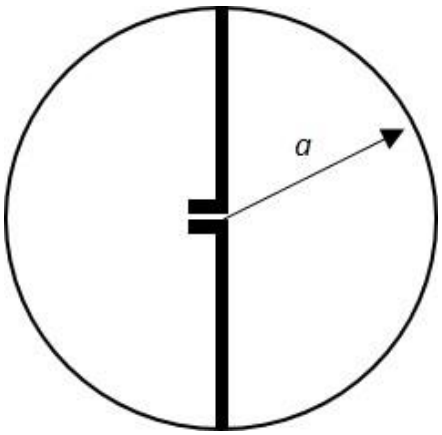

Figure 3.2 Electrically small dipole antenna within the radian sphere of radius *a.*

3.2.1 Performance of Electrically Small Antennas

Small antennas have specific characteristics that differ from those whose size is comparable to the wavelength. First of all, the input impedance of a small electric (magnetic) dipole antenna is highly capacitive (inductive), while its resistive component is very small, making it difficult to perfectly match to a 50 Ω load. Its radiation pattern tends to look like the classical vertical dipole one, omnidirectional in the azimuth plane with a figure-of-eight pattern in the elevation plane, or a donut shape Figure 3.3. This feature can be particularly interesting as omnidirectionality can be advantageous for applications that need to be independent of orientation, like in wireless sensor networks, implantable medical devices, and power transfer applications

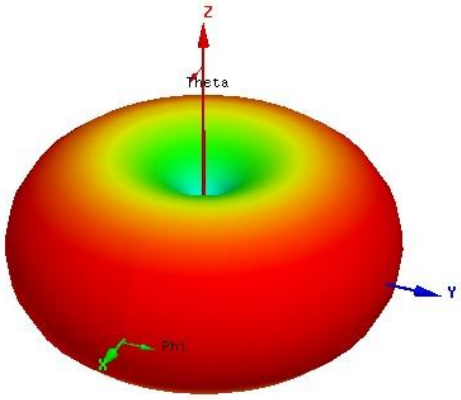

Figure 3.3 Simulated radiation pattern of a 3.2 mm monopole antenna in free space resonating at 35 GHz.

3.2.2 Input Impedance

Generally the input impedance of small antennas is typically characterized by low resistance and high reactance. As the antenna size becomes smaller the radiation resistance decreases causing antenna reactance to dominate. Usually, a matching circuit is used to improve the small antenna efficiency. Nevertheless, that imposes the challenge of designing an equally small matching circuit. Therefore, it is important to design a self-resonant antenna with high radiation resistance that can be connected to a standard transmission line. This issue will be addressed further ahead in this chapter in the “Antenna Miniaturization” section, as well as in the next chapter, where antenna design strategies will be implemented to promote a higher input resistance.

3.2.3 Bandwidth and Antenna Quality factor

The antenna bandwidth (BW) can be seen as the range of frequencies within which the antenna performance, with respect to some characteristic, conforms to a specified standard [98]. It can be defined as the difference between the highest frequency f_{high} and the lowest frequency f_{low}, both specified at a certain value of a parameter such as VSWR, or Return Loss, thus determining the frequency range over which the antenna can properly radiate or receive energy. The antenna quality factor *Q*, relates the antenna ability to store energy with its ability to dissipate it as follows:

$$Q = \frac{\omega P_{react}}{P_{rad}} \tag{13}$$

where P_{react} is the reactive power stored in the antenna and P_{rad} is the radiated power from the antenna. A low *Q* antenna shows increased losses through radiation i.e. higher radiation resistance with correspondingly higher radiation efficiency. On the other hand, a high *Q* antenna shows increased stored energy and hence less losses through radiation. Another important characteristic of *Q* is that it is (approximately) inversely proportional to antenna bandwidth. A common approximation between *Q* and the 3 dB fractional bandwidth is:

$$Q \approx \frac{1}{BW} \ (for\ Q \gg 1) \tag{14}$$

Frequently, small antennas have high Q, meaning that there are not good radiators. They also have a small bandwidth, which might not be favorable for communication, but relatively unimportant for wireless power transfer purposes. However, the attainable *Q* value or bandwidth are limited by the antenna size. These fundamental limitations have been discussed by many researchers, first by Wheeler, Chu, and others. Wheeler (1947) first noticed that antenna size reduction imposes a fundamental limitation on bandwidth [144]. He showed that it directly limits the "radiation power factor" - a ratio of the radiated power to the reactive power - implying that radiation efficiency is constrained by the antenna size. He indicated that the

"radiation power factor" equals the reciprocal of *Q*, thus antenna size reduction limits *Q* and the relative bandwidth. Wheeler derived *Q* for the most limiting case as:

$$Q = \frac{1}{(ka)^3} \tag{15}$$

where *Q* is inversely proportional to the antenna size, thus the antenna size imposes a fundamental limitation for the attainable bandwidth. In 1948, Chu also studied the limitations of small antennas [145], and derived the minimum possible antenna Q. Many other authors such as Collin and Rothschild [146], Hansen [147], McLean [148], Thal [149], Hansen and Collin [150], Gustafsson [151], Yaghjian and Stuart [152] improved upon the previously given theory thus obtaining new expressions of *Q*.

S. Best also discussed the quality factor of electrically small antennas. Based on the concept that the Q of a resonant electrically small dipole antenna can be minimized with an antenna geometry that fully utilizes the spherical volume of the radian sphere surrounding the antenna. Best demonstrated a self-resonant four-arm folded spherical dipole that may have been the lowest *Q* ever realized with a practical antenna [153]. So far, Chu's limit has been assumed the lowest achievable *Q* for a given antenna size, which in turn, is impossible to achieve in practice. The design of small antennas is an exercise of finding new techniques to approach Chu's limitations as closely as possible, where the main issues would be the study of the antenna shape, the current distributions and their relations with radiation efficiency [154].

3.2.4 Gain and Directivity

The antenna gain, *G*, shows how efficiently an antenna transforms the available power at its input terminal into radiated power. It is defined as the ratio of the radiation intensity in a given direction, to the radiation intensity that would be obtained if the power accepted by the antenna was radiated isotropically. Although the gain of the antenna is closely related to its directivity, a measure that accounts for the antenna efficiency as well as its directional capabilities. The radiation intensity corresponding to the isotropically radiated power is equal to the power accepted (input) by the antenna divided by 4π. It can be expressed as [98]:

$$G = 4\pi \frac{radiation\ intensity}{total\ input\ (accepted) power} = \frac{4\pi U(\theta, \phi)}{P_{in}} \quad (16)$$

The antenna directivity is defined as the ratio of the radiation intensity in a given direction to the radiation intensity averaged over all directions. The directivity of a nonisotropic source is equal to the ratio of its radiation intensity in a given direction over that of an isotropic source and it is given by [98]:

$$D = 4\pi \frac{radiation\ intensity}{total\ radiated\ power} = \frac{4\pi U(\theta, \phi)}{P_{rad}} \quad (17)$$

The maximum obtainable gain was first presented by Chu [145]. A more recent analysis by Geyi [155] who also discussed physical limitations of small antennas and derived the normal gain (Figure 3.4A) and the ratio of maximized *G*/*Q* (Figure 3.4B) for omnidirectional and directional antennas, given by equation (18) and equation (19) respectively.

$$max \frac{G}{Q} \approx \frac{6(ka)^3}{2(ka)^2 + 1} \quad (18)$$

$$max \frac{G}{Q} \approx \frac{3(ka)^3}{2(ka)^2 + 1} \quad (19)$$

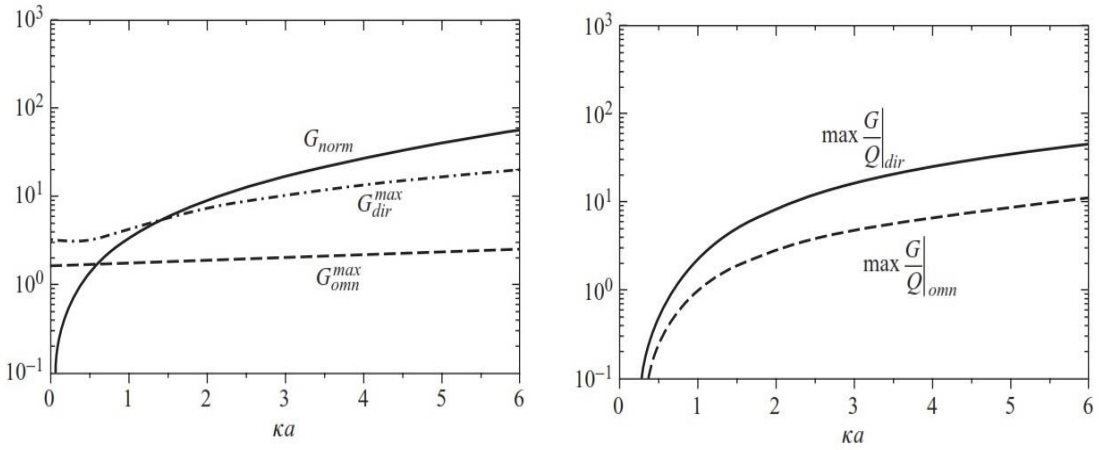

Figure 3.4 A) Geyi's normal gain and maximum obtainable gain for directional and omnidirectional antennas. B) Geyi's maximum obtainable G/Q for directional and omnidirectional antennas [155].

3.2.5 Radiation Efficiency

The radiation efficiency, η, is the ratio of the power radiated by the antenna to the power delivered to its input terminals, and it is often seen in the antenna gain expression [154]:

$$G = \eta(1 - |\Gamma|^2)D \tag{20}$$

where G is the realized gain. This expression includes the mismatches between the source and the matching network, which we will assume to be lossless. Apart from the radiation, the losses in the antenna are given by R_{loss}, and the radiation efficiency can be given by:

$$\eta = \frac{R_{rad}}{R_{rad} + R_{loss}} = \frac{R_{rad}}{R_a} \tag{21}$$

where R_a is the total antenna input impedance, $R_a = R_{rad} + R_{loss}$. It was mentioned previously that as the antenna size decreases, the R_{rad} also decreases, leaving the resistance R_{loss} to dominate the efficiency expression while the antenna efficiency drops. This was well explained by Harrington [74] showing that the antenna losses are very severe for smaller ka values.

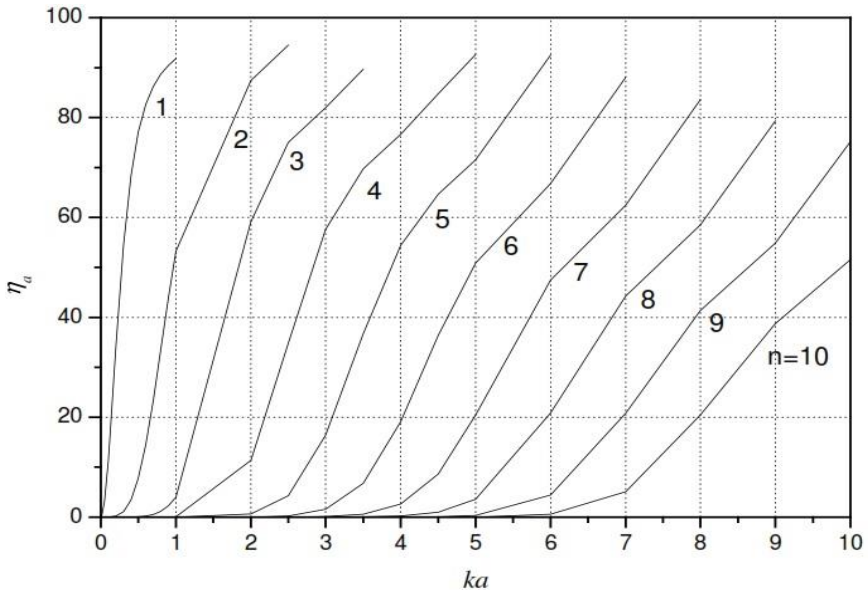

Figure 3.5 Antenna efficiency for different values of *ka* [156].

As shown in Figure 3.5, the antenna *ka* value can be seen as the most important factor in determining its efficiency. Figure 3.6 [156] shows three parameters such as the antenna gain, quality factor and efficiency at the fundamental mode, with variable *ka*, clearly stating that all antenna parameters improve as the antenna dimension increases.

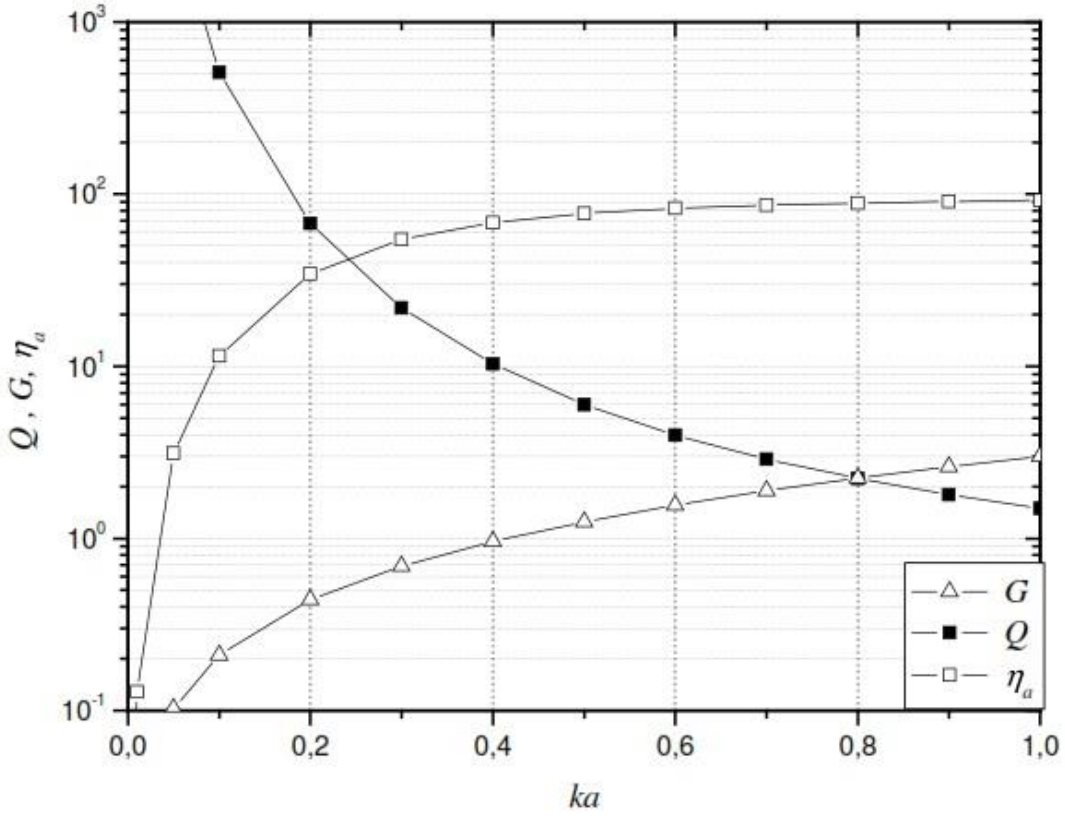

Figure 3.6 Antenna gain, quality factor and efficiency for the fundamental mode for a variable *ka* [156].

We started this chapter mentioning that the performance of implanted miniaturized antennas is conditioned by the nature of the lossy media they're implanted in, and the fundamental limitations inherent to their small dimensions. Now that these mechanisms have been explained, we will proceed to the characterization of a power budget model, in an attempt to assess how much power would be possible to provide to a small antenna implanted in human muscle tissue.

3.3 Power Budget

A radiofrequency (RF) signal emitted by an RF source will experience some sort of attenuation from the moment it leaves the source until it reaches the receiving antenna.

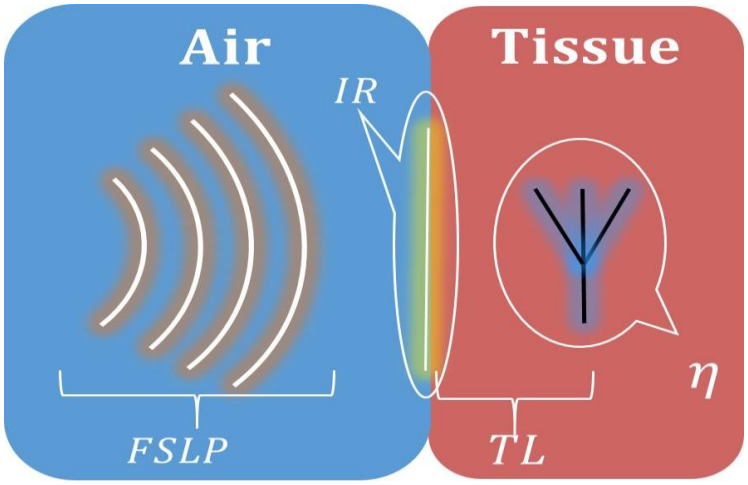

Figure 3.7 Electromagnetic wave loss path between a radiofrequency source and a tissue implanted antenna.

In the case of implantable devices, the EM signal will undergo several loss stages. The first stage occurs in the free space loss path (FSLP) between an external radiofrequency source and the human body (usually air), as seen in Figure 3.7. Here, the attenuation is low when compared to that in the human body. A second loss mechanism occurs at the air-tissue interface, where the incident EM wave will suffer some interface reflections (IR), due to the impedance mismatch between two propagation environments [78][157]. This is followed by another loss stage, the tissue losses (TL), in path between the air-tissue interface and the implanted antenna. As IMDs can be transdermal or implanted several centimeters deep inside human tissues, the losses will depend on the implantation depth.

In a wireless powering application, the total power received by the implanted device, or power budget, can be modeled accordingly to Figure 3.7. The total power received by the implanted device (P_r), depends on several parameters such as: the initial transmitted power by a radiofrequency source (P_t), the power reduction that occurs in the free space path loss (FSPL); the power reflected/transmitted at the

interface air-tissue (IR); the power reduction due to tissue losses (TL); and the power the antenna is able to accept in regards to the available power, or antenna efficiency η. Thus, the power received by an implanted antenna can be given as:

$$Pr = Pt \times FSPL \times IR \times TL \times \eta \tag{22}$$

3.3.1 Free Space Path Loss

The free-space path loss (FSPL) expresses the loss of an EM wave travelling through free space (usually air) without reflection or refraction events. The FSPL is proportional to the square of the distance between the transmitter and receiver and to the square of the signal frequency:

$$FSPL = \left(\frac{4\pi d}{\lambda}\right)^2 = \left(\frac{4\pi df}{c}\right)^2, \qquad FSPL(dB) = 10log_{10}\left(\frac{4\pi df}{c}\right)^2 \tag{23}$$

λ is the signal wavelength, f the signal frequency, d the distance from the transmitter and c is the speed of light in vacuum. Due to the finite size of a receiving antenna's aperture only a portion of the transmitted energy can be picked up a certain distance away. Given a certain receive antenna size, the ratio of received power to transmitted power as a function of distance, assuming the far-field approximation, is given by:

$$\frac{P_{Rx}}{P_{Tx}} = \frac{A_{eff}}{4\pi d^2} \tag{24}$$

where A_{eff} is the effective receive antenna aperture area and d is the distance between the antennas. For an isotropic antenna, this area is $\lambda^2/4\pi$, but for an implanted antenna, the determination of this wavelength value (λ) is not trivial as it is dependent on the dielectric properties of the surrounding biological tissues. Incorporating the gains of the receiving and transmitting antennas results in Friis transmission equation:

$$\frac{P_{Rx}}{P_{Tx}} = G_{Tx}G_{Rx}\left(\frac{\lambda_{eff}}{4\pi d^2}\right)^2 \quad (25)$$

where λ_{eff} is the effective wavelength of the wave that is seen at the receive antenna and equals the wavelength in free space divided by the square root of the effective permittivity (ε_r). After travelling through the free space path, and experiencing the resulting attenuation, the electromagnetic wave will face the air-tissue interface where part of it will be reflected and another part will be transmitted to the tissues.

3.3.2 Electromagnetic Waves at the Interface

Here we will discuss the EM wave reflection at an interface between two different dielectric layers. The E-field boundary conditions dictate that the sum of incident and reflection waves on one side of the interface is equal to the transmission wave on the other side of the interface:

$$\overrightarrow{E^i} + \overrightarrow{E^r} = \overrightarrow{E^t} \quad (26)$$

For a propagating plane wave and an air-skin interface, the ratios of transmission-to-incident power ($P_{t/i}$) and reflection-to-incident power ($P_{r/i}$) are given by [158]:

$$P_{r/i} = \frac{\left|S_{1(air)}{}^r\right|}{\left|S_{1(air)}{}^i\right|} = R_{air-skin}{}^2 \quad (27)$$

$$P_{t/i} = \frac{\left|S_{2(skin)}{}^t\right|}{\left|S_{1(air)}{}^i\right|} = \frac{T_{air-skin}{}^2\eta_{1(air)}}{\eta_{2(skin)}} \quad (28)$$

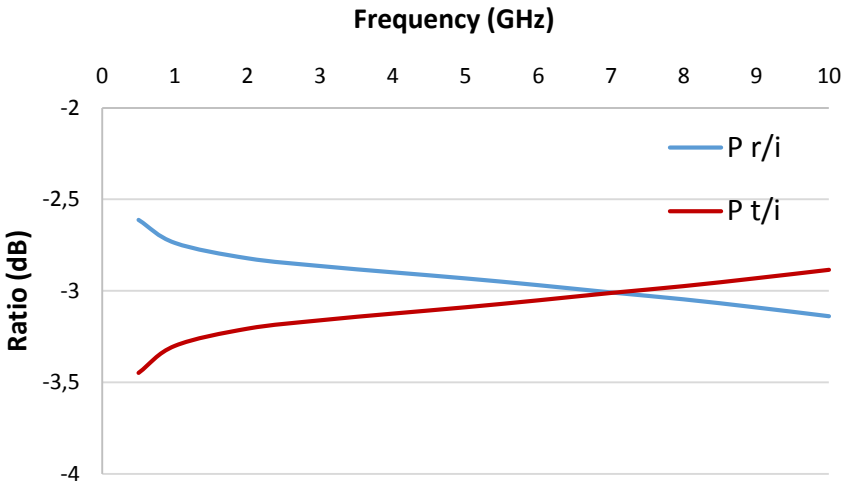

Figure 3.8 Ratios of transmitted and reflected power at an air-skin interface.

The ratios of transmission-to-incident power ($P_{t/i}$) and reflection-to-incident power ($P_{r/i}$) considering an air-skin interface, from 0.5 – 10 GHz (Figure 3.8), reveal that from 0.5 – 7 GHz, more than half of the incident power is reflected back. At 7 GHz, half of the incident power (-3 dB) is reflected, and the other half is transmitted to the tissue. Above 7 GHz, more than half of the incident power is transmitted to the tissue. It is worth mentioning that, due to the multi-material nature of the human body, several EM wave reflection stages are expected to occur in the EM wave path towards the implanted antenna, thus the power of EM signal will be further reduced if several tissues are to be considered.

3.3.3 Losses in Biological Tissues

Following the FSPL and the air-tissue interface, the transmitted EM wave faces another lossy path as it travels through the biological tissue. The human body can be seen as an irregular dielectric, with frequency dependent conductivity and permittivity. It is partially conductive and composed of materials with different dielectric constants, thicknesses and characteristic impedances, thus it is not the ideal media for radiofrequency signal propagation [159]. The tissues will attenuate the electromagnetic waves, reflecting and absorbing them. The degree of the absorption effects varies with the tissue characteristics, which is largely based on water and ionic content, and the frequency of the incoming signal [160]. When the signal's wavelength is significantly larger than the cross-section of the human body, the electromagnetic waves can easily pass through it with very little effect on them. These wavelengths occur at frequencies below 4 MHz. Above this frequency, the absorption of RF energy increases and the human body may be considered to be essentially dense until roughly 1 GHz. From this point on, the dielectric properties of the tissues begin to introduce a scattering effect on the electromagnetic waves [95]. Therefore, in establishing a reliable wireless link between an external RF source and an implanted device, a good characterization of the biological media electrical properties is necessary. To this end, two important databases [139][161] that provide the dielectric properties of many human tissues and liquids (between 10 Hz and 100 GHz), were extremely useful throughout this work as well as in other tissue path loss models described in the literature [162-163]. The attenuation (power loss in dB) in a given tissue, and at a given implantation depth *z*, can be then determined using:

$$PL_{db} = 20Log_{10}(e^{\alpha z}) \tag{29}$$

Where *z* represents the penetration depth (in meters). The dielectric properties of body tissues such as skin, fat, muscle were computed into eq. (10) and the α values were extracted. These calculations were performed considering an antenna implanted 2.5 millimeter deep (implantation depth, *z = 0.0025 m*).

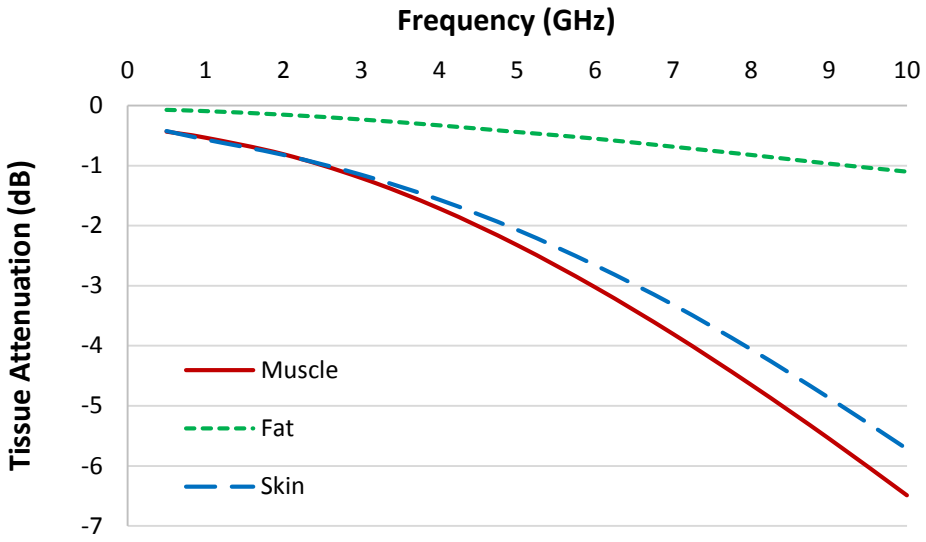

Figure 3.9 Power attenuation due to tissue loss in dry skin, fat and muscle for an implantation depth of 2.5 mm.

As seen in Figure 3.9, fat induces the lowest attenuation due to its low water content. In opposition, muscle tissue has the highest water content, and consequently induces an intense attenuation of EM waves. As seen in Table 3.1, muscle tissue has the highest effective conductivity and consequently the highest loss and induced attenuation. The effect of frequency on increasing loss is clear, as with increasing frequency, tissue attenuation is more intense, as well as the power loss.

So far we have seen how to calculate the FSLP, the IR and the TL. As seen in equation (22), antenna efficiency η is the last variable in determining the expected amount of power received by an implanted antenna. In the next section we will study the efficiency of small antenna implanted in muscle tissue.

3.3.4 Antenna Efficiency

In this section we will determine the last term of equation (22), the antenna efficiency. We consider a muscle tissue implanted micro antenna, whose maximum dimension is confined in a 500 µm diameter sphere, and calculate the efficiency for different *ka* values, where *k* is the wave number ($k = 2\pi/\lambda$) and *a* is the radius of radiansphere circumscribing the antenna, which we will keep constant at 250 µm. We will calculate the antenna efficiency for the 0.5 – 10 GHz frequency window accordingly to Harrington [74]:

$$efficiency = \frac{100}{1+D} \quad (30)$$

D is the dissipation factor, which can be calculated for different *ka* values as follows:

$$D(\beta r) = \frac{R_e(\eta_c)}{2\eta}[|U_n(\beta r)|^2 - 2] \quad (31)$$

$$\eta_c = (1+j)\sqrt{\frac{\omega\mu}{2\sigma}} \quad (32)$$

This antenna efficiency calculation method was derived by Harrington for antennas in free space. However, here we will use it as an approximation to derive the efficiency of an antenna implanted in dispersive media (human muscle tissue). Therefore, we will consider the surrounding medium as an isotropic, homogeneous dielectric with negligible magnetic properties, with impedance given by:

$$\eta_{muscle} = \sqrt{\frac{\mu}{\varepsilon}} = \sqrt{\frac{\mu.\mu_0}{\varepsilon.\varepsilon_0}} = \frac{Z_0}{\sqrt{\varepsilon_r}} \approx \frac{377}{\sqrt{\varepsilon_r}}\ \Omega\ ,\ \eta_0 = 120\pi \quad (33)$$

It is worth mentioning that $\beta = \frac{2\pi}{\lambda} = k$. Therefore, the $U_n(\beta r)$ values are extracted from [74], assuming (n=1), are in fact $U_n(ka)$ since r is the radius of the sphere. Figure 3.10 [156] is an updated version of the original graph shown in Harrington's paper, and $\beta r = ka$. The efficiency results were calculated for gold, nickel and copper antennas at different *ka* values as seen in Table 3.2.

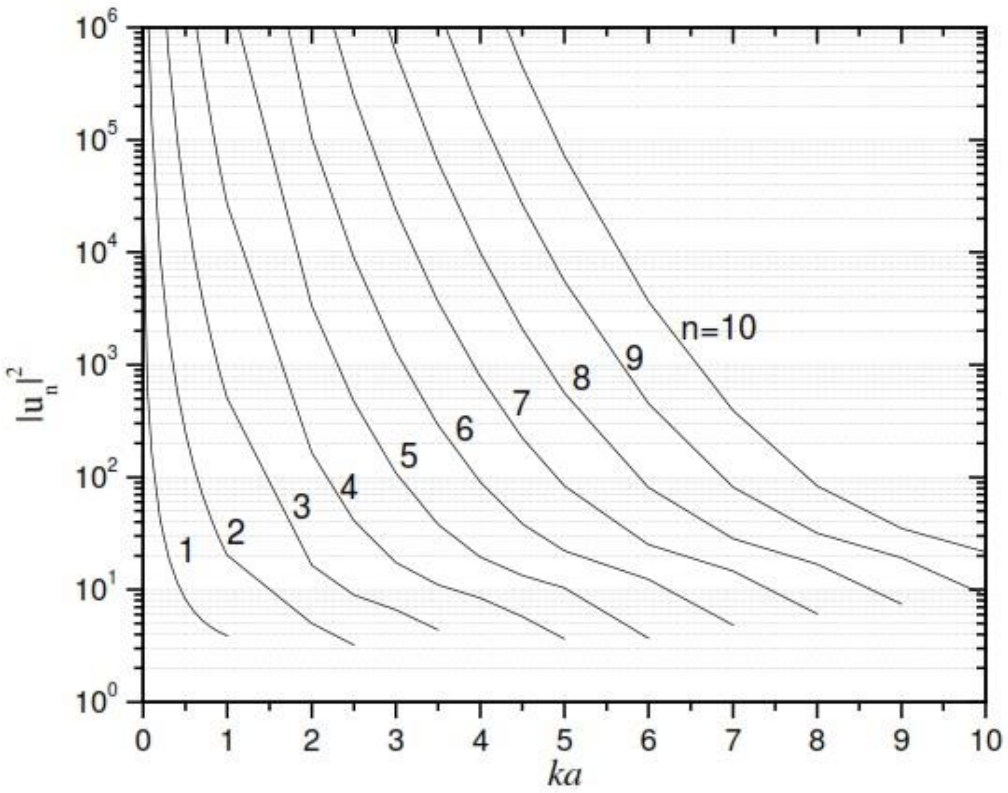

Figure 3.10 Functions $|U_n|^2$ [156].

Table 3.2 Efficiency of a muscle tissue implanted antenna confined in 500 µm diameter sphere for varying *ka*.

		copper		*gold*		*nickel*	
Ka	**Freq (GHz**	**Eff. (%)**	**Eff. (dB)**	**Eff. (%)**	**Eff. (dB)**	**Eff. (%)**	**Eff. (dB)**
0.019	0.5	0.05	-32.8	0.04	-33.6	0.02	-35.8
0.038	1	0.06	-32.0	0.05	-32.7	0.03	-35.0
0.076	2	0.05	-32.5	0.04	-33.3	0.027	-35.5
0.113	3	0.05	-32.9	0.04	-33.6	0.025	-35.9
0.149	4	0.07	-31.4	0.06	-32.1	0.04	-34.4
0.184	5	0.16	-27.8	0.13	-28.6	0.08	-30.8
0.218	6	0.30	-25.2	0.25	-25.9	0.15	-28.2
0.250	7	0.94	-20.2	0.79	-21.0	0.47	-23.2
0.282	8	1.07	-19.7	0.90	-20.4	0.53	-22.6
0.313	9	1.28	-18.9	1.07	-19.6	0.64	-21.9
0.342	10	1.64	-17.8	1.38	-18.5	0.83	-20.8

As predicted by the theory [74], and as seen in Table 3.2, for a fixed *a* (*a* = 250 µm), the efficiency of a muscle tissue implanted antenna is very poor at low frequencies, while higher efficiencies are only possibly by exploiting higher operating frequencies (and higher ka).

3.3.5 Tissue Losses and Antenna Efficiency

Figure 3.11 presents the antenna efficiency and tissues losses of a micro antenna (for different antenna materials) embedded in muscle tissue. The 0.5 – 10 GHz frequency window can be divided in three sections, the first from 0.5 – 4 GHz, characterized by relatively low antenna efficiency and tissue loss; a second from 4 – 7 GHz, characterized by increasing efficiency and somewhat stable tissue losses; and a final section from 7 – 10 GHz, where efficiency is relatively higher but so are the tissue losses. The results evidence a tradeoff between antenna efficiency and tissue attenuation which may indicate a preferable frequency range to communicate with, or to wirelessly power a micro device. This analysis suggests that the operating frequency of a small antenna whose maximum dimension fits inside a 500 µm sphere, could lay on the range of 0.5 – 7 GHz. It is then clear that for higher frequencies, tissue attenuation dominates over the antenna efficiency, and in opposition, for lower frequencies, losses will be dominated by antenna efficiency.

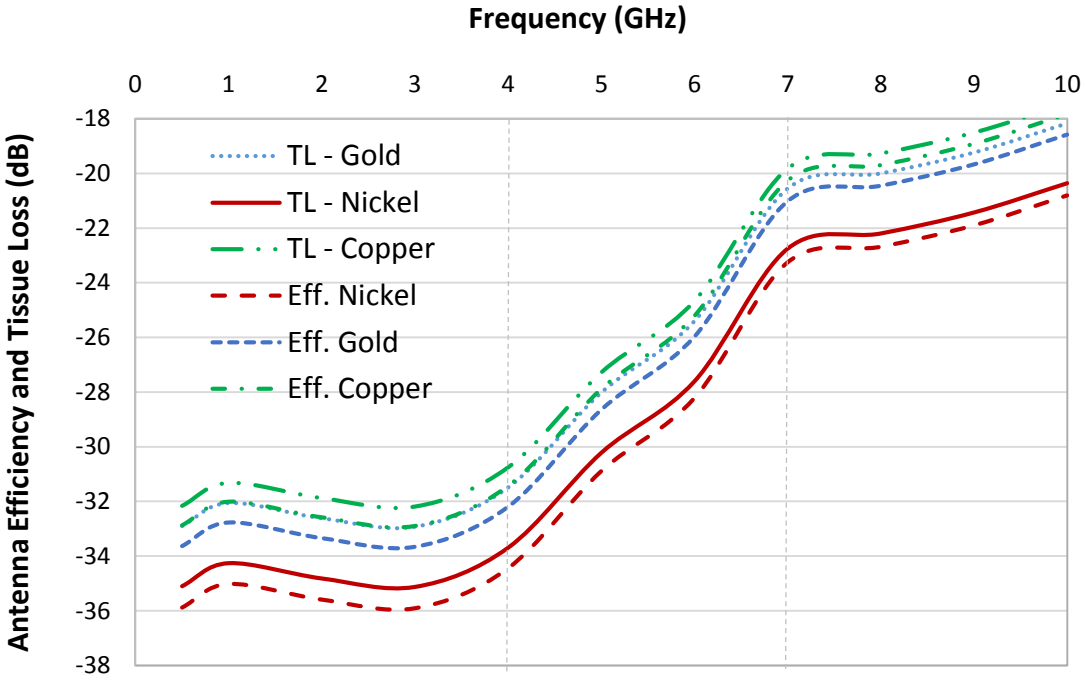

Figure 3.11 Efficiency and Tissue Losses of different material antennas implanted in muscle tissue, 2.5 mm deep. (TL - Tissue Loss, Eff. – Efficiency).

Others [73][138], despite the fact of having analyzed the optimal frequency for wireless power transfer using RF coils and inductive coupling, also conclude that the

optimum operating frequencies for implantable medical devices lies in the low gigahertz range. Nevertheless, the obtained results still represent a good approximation to those of other publications.

It is important to bear in mind that the analysis done in this section considered human muscle tissue as the operating medium. As we will see in the next section, loading an antenna in a high permittivity material (such as muscle tissue) can be used as an antenna miniaturization technique, and as a way of improving the antenna efficiency. As the power requirements of tiny implantable medical devices are inherently small, we believe that equally small and low efficiency antennas, could be used in a wireless power transfer application at a relatively low implantation depth.

In the next section some important and widely used antenna miniaturization techniques are presented. These are methods that were used during the micro antenna project (chapter 4), in order to achieve a miniaturized antenna that fits in 500 x 500 x 500 μm^3 volume.

3.4 Antenna Miniaturization

"The art of antenna miniaturization is an art of compromise: one has to design the smallest possible antenna that is still suitable for a given application with regard to its radiation characteristics. Or in other words, one looks for the best compromise among volume, bandwidth and efficiency. And the best compromise is usually obtained when most of the allotted volume participates in the radiation" [75].

The aim of miniaturization is to create an antenna with dimensions much smaller than the wavelength while keeping its key characteristics the same as, or as close as, before its downsizing. In this section we will address some well-known methods to achieve electrically small antennas such as the creation of periodic structures, the modification of the antenna geometry, the full use of volume/space circumscribing the antenna, and the arrangement of current distributions.

3.4.1 Periodic Structures

Periodic structures can be modified arrangements from the same linear wire precursor of length L_0 to form helixes, meander lines, zigzags and fractal structures (Figure 3.12). These structures are advantageous for small antenna design since they are low cost and of relatively simple fabrication. They easily achieve self-resonance thus helping to mitigate antenna matching issues which are typical of small antennas.

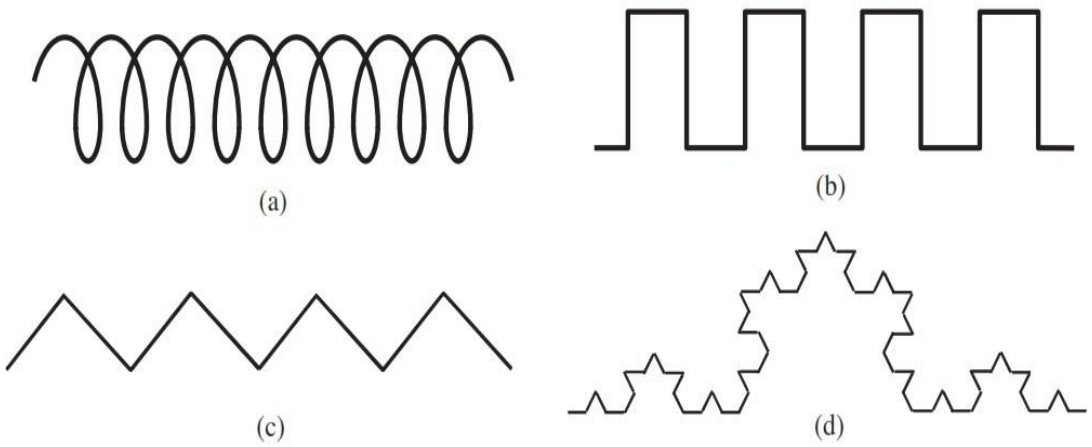

Figure 3.12 Examples of periodic structures [154]. A) Helix. B) Meander. C) Zig-zag. D) Fractal.

Figure 3.13 shows a wave travelling through a wire antenna of length L_0 and the same wave travelling a meandered wire antenna of length L. The wave travelling time t_p on the antenna of length L, is longer than t_0, on the wire of length L_0. Thus, the velocity $v = L_0/t_p$ is smaller than $c = L_0/t_0$, implying that the wave propagates more slowly on the antenna with the meander line [154].

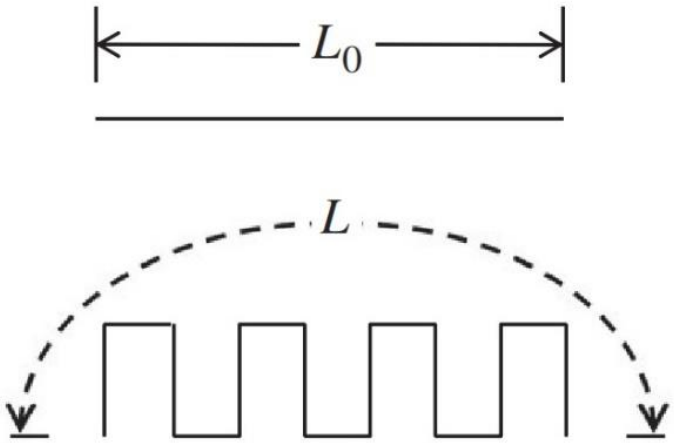

Figure 3.13 Linear wire of length L_0 and meander line of length L [154].

The meander line periodic structure is of particular interest in this thesis since it was chosen as one of the miniaturization techniques for the antenna design project. Rashed-Mohassel [164] present a good miniaturization example, where a straight standand dipole, within a 2π × 6 cm sphere and resonating at 1.73 GHz, was then modified into a meander line. The new meandered structure, within the same sphere, operates at 543 MHz showing a 70% size reduction. The same study shows that a meandered triangular shaping avoids current cancellation, which might happen between two close parallel sections that in turn could lead to lower resistance values. Also noteworthy is the fact that slight modifications to the meander line structure can lead do input impedance change. The triangular shape of Figure 3.14B has an input impedance R_{in} = 120 Ω, while the square meander line of Figure 3.14A shows R_{in} = 26.5 Ω. Sinusoidal meandering of Figure 3.14C allows higher miniaturization, with a resonant frequency of 325 MHz (81% size reduction) but R_{in} = 5.36 Ω.

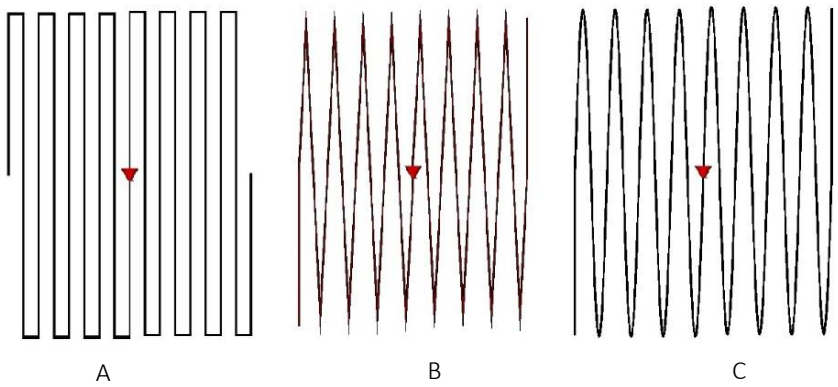

Figure 3.14 Meander lines structures A) Rectangular. B) Triangular. C) Sinusoidal [164].

Table 3.3 Parameters of different meander line structures [164].

Antenna	f_o(MHz)	$R_{rad}(\Omega)$	Q	*ka*
A	543	26.52	59.8	0.499
B	548	120	59	0.498
C	325	5.36	74.6	0.296

3.4.2 Modification of the Antenna Geometry

Geometry modification is probably the most extensively used technique in antenna miniaturization [75][154][165], creating electrically longer antennas in small areas and volumes. This technique is also widely used for multiband operation where multiple resonant frequencies can be accomplished, corresponding to the different lengths of the current path. Common examples are slot or notch formation (also called lumped loading) [166], bending [60] or folding [48][67], short circuiting and grounding, and the aforementioned periodic structures. Slots consist of openings within a metal patch thus blocking the current's natural path, while notches are cuts made at the edge of a patches producing the same effect. Both make a wave travel through a longer path as seen in Figure 3.15, increasing the antenna electrical size and reducing its resonant frequency [75][154].

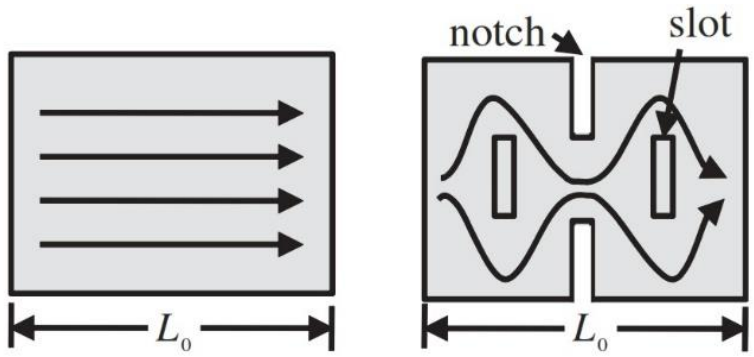

Figure 3.15 Current path extension on an antenna structure by introducing a slot and notch [154].

Bending, folding, short circuiting and the use of ground planes are simple and effective antenna miniaturization techniques to make an antenna smaller, and yet keeping its resonant features. In Figure 3.16, a classic example of a monopole bent into an inverted-L-antenna, which, upon short-circuiting to a ground plane turns into an inverted-F-antenna is shown.

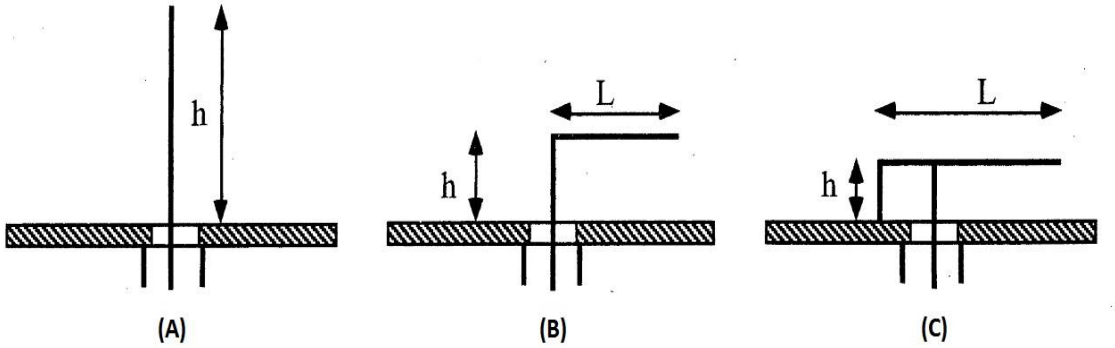

Figure 3.16 Antenna miniaturization by bending and short circuiting to the ground plane. A) Monopole before bending. B) Inverted-L-antenna after bending. C) Inverted-F-antenna after short circuiting to ground plane [75].

This technique can be explained with the example of the monopole compared to the dipole. To be resonant the dipole must have roughly a half wavelength length. This dimension can be halved by replacing one dipole arm by a ground plane which will in turn create a virtual dipole arm according to image theory. This principle can be easily extended to planar antenna designs, where the planar inverted-F-antenna (PIFA) design is a classic example widely used in telecommunications and implantable medical devices [48][167][168].

3.4.3 Material Loading of Antenna Structure

Loading the antenna structure with dielectric or magnetic materials is a good strategy to achieve antenna tuning of self-resonance. The operating wavelength becomes shorter in a high permittivity media and therefore the antenna becomes electrically smaller. Steven Best [169] shows an example of antenna miniaturization by loading a dipole antenna with high permittivity materials. Typically, the addition of lossy dielectric materials around the antenna would add to the total losses thus reducing the overall radiation efficiency. Nevertheless, Best argues that at many frequencies, such dielectric loading increases the antenna's radiation resistance and thus improving the antenna efficiency.

3.4.4 Full Use of the Volume Circumscribing the Antenna

The full use of the spherical volume circumscribing the antenna to improve its parameters has been discussed as a technique to improve the performance of miniaturized antennas [51][54][55]. In practice, this is an idealized concept since the antenna never fully occupies the whole volume of a sphere in which it is contained. Nevertheless, efforts can be made to use most of the available space with the antenna design. Meander lines, fractal and helical geometries are examples that effectively provide some occupied volume optimization. Many authors [51][60][75][98][145][147] describe how the antenna performance can be improved if it efficiently utilizes the volume of the sphere of radius a, circumscribing the antenna. A well-known example is Best's [51] four arm helical antenna design, which efficiently occupies the spherical volume as seen in Figure 3.17. More recent antennas designs have shown interesting geometries that make an extremely good use of the available volume unveiling three dimensional electrically small antennas with enhanced bandwidth and efficiency as seen in conformal printing of metallic inks in the form of meander lines [54] and direct patterning of metallic patterns in the shape of a spherical helix [55] onto hemispherical surfaces.

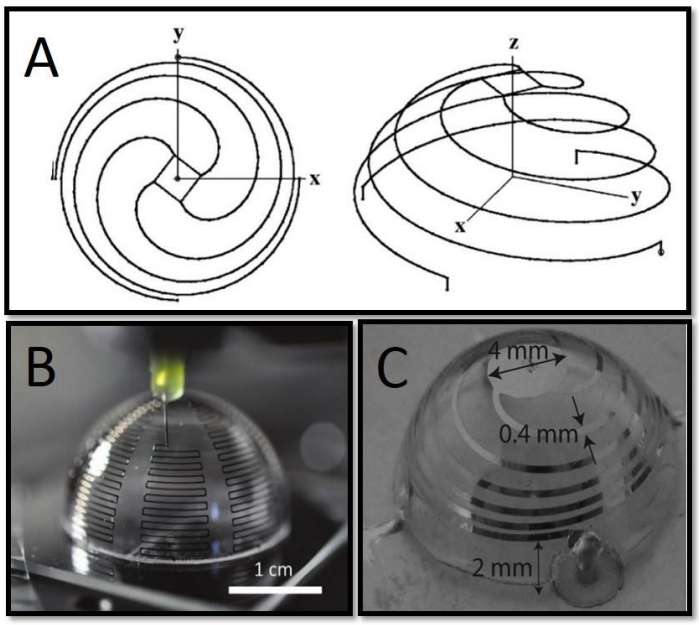

Figure 3.17 Examples the full use of the volume circumscribing the antenna. A) Four arm helical antenna [51]. B) meander line antenna [54]. C) spherical helix antenna [55].

3.4.5 Arrangement of Current Distribution Uniformly

This is a similar concept to the full use of space/volume but here the goal is to arrange the current distribution uniformly within the antenna structure. Nevertheless, uniform distribution can never be realized by a small antenna [165]. On a small dipole, the current distribution tends to zero toward the end of the element and with maximum value at its center presenting a triangular shape (Figure 3.18). This current distribution is expected to be triangular with a maximum at the feed point and zero at the end.

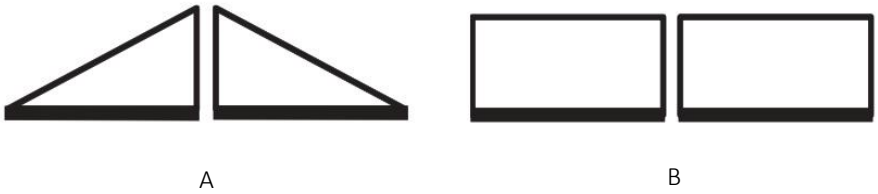

Figure 3.18 Current distribution on a small dipole. A) Triangular shape. B) Uniform (ideal case) [154].

With a small dipole antenna, the current distribution can be more uniformly distributed by means of capacitive loading. With a capacitive plate at the end of the dipole the antenna gain can be maximized [154].

4 Micro Antenna Project

As seen in previous chapters, the massification of small wireless implantable medical devices is still limited by some technological challenges, such as the miniaturization of their integrated antennas and the development of powering schemes that do not rely on stored energy. These issues become even more noticeable when the dimensions of a device are set to a sub-millimeter cubic volume (500 x 500 x 500 μm^3). Within such volume, an integrated antenna will be obviously small, and operate at high frequencies which is undesirable for implantable applications due to severe electromagnetic wave attenuation in the human tissues. However, with proper antenna design strategies and miniaturization techniques, allied to the dielectric loading effect caused by the high permittivity nature of body tissues, it is possible to implement a small antenna which operates in the desired low gigahertz range (1-10 GHz).

The design of micro antennas can be greatly improved by using software tools, which can quickly predict the antenna's radiation characteristics and input parameters, ultimately freeing us from the slow trial-and-error methods. Usually, simulation tools are capable to create and test virtually any antenna geometry and its surrounding environment. Parametric analysis can be quickly conducted, and the designed structures can be studied with great level of detail, thus unveiling the antenna's capabilities and limitations. During the design phase, one must consider that after fabrication, the antennas have to be characterized using microwave equipment. So, issues such as the antenna feeding method and integration schemes must be assessed during this stage. It is of extreme importance for the antenna geometry to be designed in compatibility with the fabrication methods, materials and available equipment.

The utilized simulation software was Ansys HFSS, which proved to be a fundamental tool as it provided fast 3D model design, quick structural modification and fine tuning of the antenna characteristics over a multitude of different media, which was crucial for the understanding of the antenna performance. Throughout this chapter we will look at the micro antenna design and project, discuss how the results gathered from several design iterations, and how these were critical for the process of shaping and achieving the final antenna design.

4.1 Antenna Analysis Techniques

Due to their reduced size it is naturally hard to experimentally analyze the performance and characteristics of sub-mm antennas. Performance constrains are felt when the antenna size is very small comparatively to the radiated wavelength, when the radiation resistance becomes too small to be accurately determined, or when the antenna size is very small that a precise measurement becomes extremely difficult to make. To overcome these challenges, we can now rely on electromagnetic (EM) simulators to rigorously design and test virtually every antenna geometry and implement reliable surrounding environments. Highly specialized computer-aided antenna design and analysis has replaced the lengthy process of iterative experimental modification of the past as EM simulators are now virtually ubiquitous.

Recently we have witnessed the miniaturization of small hand held, wearable and implanted devices which hold miniaturized built-in antennas. These antennas are frequently surrounded by materials such as casings, human tissues, and water that directly affect antenna performance, which is expected to remain unchanged or even improved. This is when EM simulators play a key role as they can offer remarkable physically reliable interpretations of antennas and their properties [78][156].

4.2 The Finite Element Method

HFFS is a high performance full wave electromagnetic field simulator for arbitrary 3D volumetric passive modeling that integrates simulation, visualization, solid modeling, and parameter automation. It employs the finite element method (FEM) dividing the full problem space into thousands of smaller regions and representing the field in each sub-region (element) with a local function. The geometric model is divided into a large number of tetrahedra where a single tetrahedron is represented by a four-sided pyramid, and the pool of tetrahedra is referred to as FEM mesh.

Due to the size of the antenna proposed in this project, it is of good practice to use an EM simulator. Here, the user must bear in mind that valid solutions derive from carefully designed models, accurate geometries, correct materials and well-defined boundary conditions.

4.3 Micro Antenna Design

The inspiration to design an antenna which can be integrated on a 500 x 500 x 500 μm^3 volume arose from the works of Gracias *et al.*, which stress the need of wireless control and powering for ultra-small tools, such as micro containers suitable for drug delivery applications, among others [170]. The challenge was to apply the same techniques used to fabricate the micro structures shown in Figure 4.1 in order to create a small radiating structure, which could fit in, or become a micro device itself.

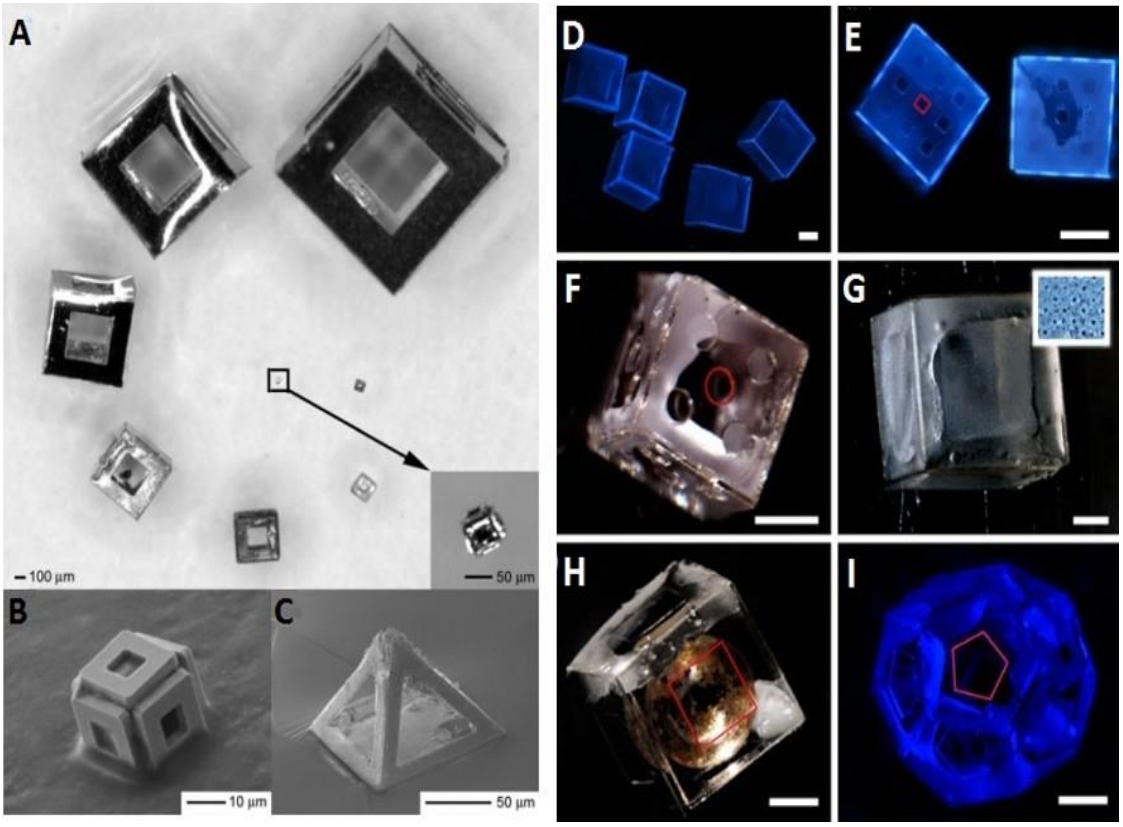

Figure 4.1 Gracias Lab micro structures fabricated by combining photolithography with self-folding methods [21][27] A) Self-folded containers fabricated with a wide range of sizes all the way from 2 mm to 50 µm. B) 10 µm cube. C) 50 µm square pyramid. D - G) Polymeric containers (500 µm – 1 mm). H) 1 mm sized container with a single square 500 µm pore and with a single microbead encapsulated within. I) Self-folded 500 µm sized dodecahedron with a single 250 µm sized pentagonal pore on each face.

Two strategies aiming for the development of a micro antenna that fits on a 500 x 500 x 500 μm^3 volume were initially adopted. One involved the patterning of a metallic strip on a planar cruciform SU-8 template that, upon folding, turns into a cube, while the metallic strip structure becomes a square loop antenna inside of it (Figure 4.2A). The second approach makes use of a planar cruciform metallic template that, upon folding, becomes a cube. In this case, the structure of the metallic cube acts itself as the antenna (Figure 4.2B).

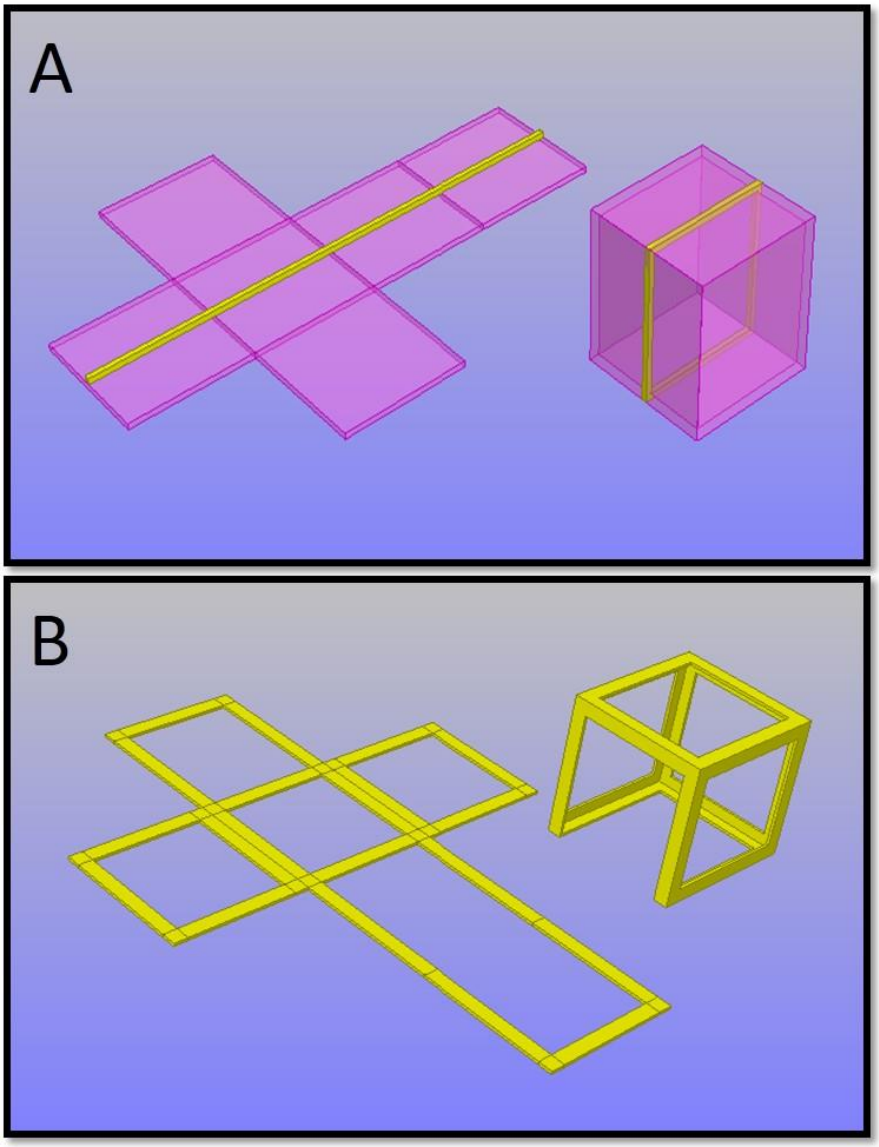

Figure 4.2 A) HFSS model of An unfolded (left) polymeric template composed of six 500 x 500 μm^2 panels with a patterned metallic strip, and a folded (right) square loop antenna inside an SU-8 cube. B) HFSS model of a unfolded (left) planar metallic template composed of six 500 x 500 μm^2 panels and a folded (right) cube antenna.

4.3.1 Square Loop Antenna

A square loop antenna geometry was the first attempt of having a micro antenna within the 500 x 500 x 500 μm^3 volume. The design proposed in Figure 4.2A was simulated and analyzed with Ansoft HFSS to study the behavior of the antenna and polymeric cube within biological media. The model is composed of layer representing the biological tissues, and the 500 x 500 x 500 μm^3 polymeric cube with patterned metal strips, which upon folding becomes a square loop, as seen in Figure 4.3. Gold was chosen as the antenna material. The square loop antenna has a total length of 1.98 mm and a 20 x 20 μm^2 cross-section. The SU-8 cube is 20 µm thick, with a ε_r = 4, electric, and tan δ = 0.08. A 20 x 20 μm^2 lumped port, placed in the middle of the loop structure, determines the system's excitation. The biological tissue layer was programmed with the dielectric properties (relative permittivity, electrical conductivity and loss tangent) of dry human skin, muscle and fat, with values taken from [139].

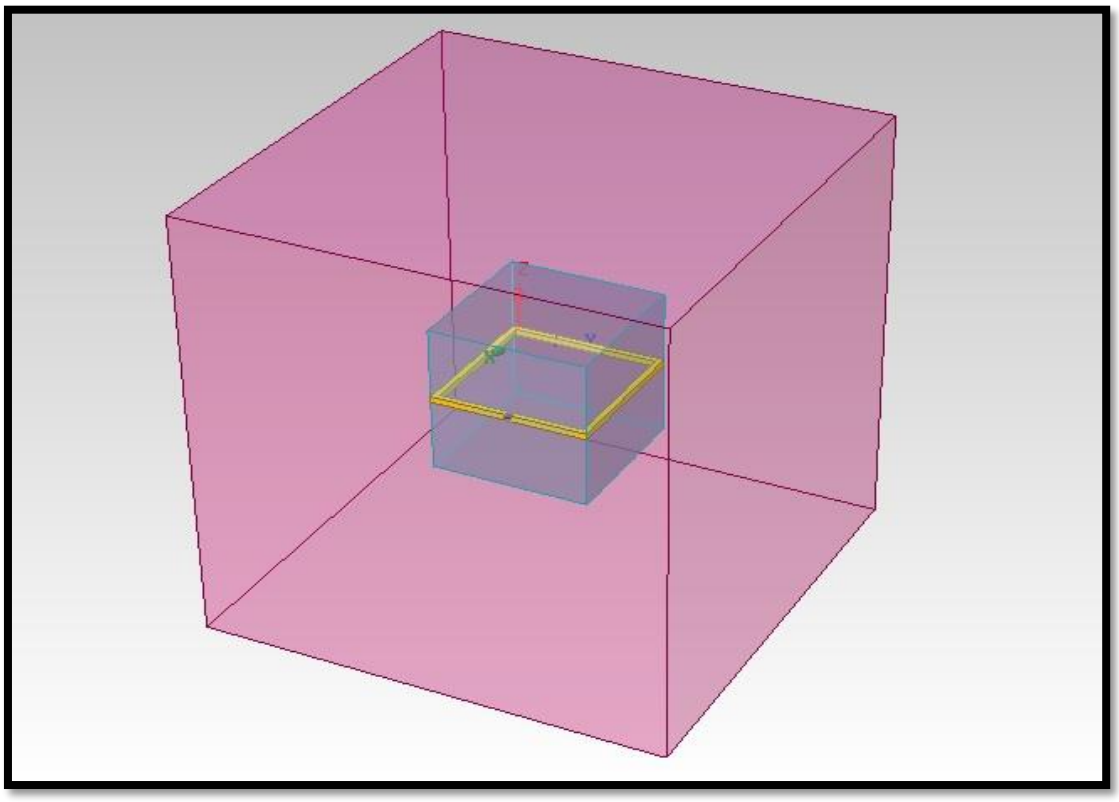

Figure 4.3 HFSS model of a square loop antenna within a 500 × 500 × 500 μm^3 polymeric cube, in the geometrical center of a 5 × 5 × 5 mm^3 layer of biological tissue (the biological tissue layer is not shown accordingly to its real size).

Simulations were performed in order to study the performance of the micro antennas when surrounded by biological tissue, and to determine what operating frequency should be adopted as the working frequency. Hence, for two tissue layers with different volumes (5 x 5 x 5 mm^3 and 10 x 10 x 10 mm^3), simulations were performed from 1 to 10 GHz. In order to select the work frequency band and the tissue volume to be used, HFSS's radiation efficiency was the selected parameter to help us determine these two variables. Since HFSS's radiation efficiency parameter provides not only the antenna efficiency, but also information about the losses that occur in the surrounding tissues, it can be used to discriminate the antenna performance when embedded in different tissues (dielectrics), as well as what frequencies induce higher losses. The radiation efficiency is therefore a very good indicator to decide if the antenna performance, within certain conditions, is acceptable or not.

Simulations revealed that higher radiation efficiencies were obtained in the frequency band of 1-10 GHz, when the tissue box volume was set to 5 x 5 x 5 mm^3. Figure 4.4 shows that for both skin and muscle tissue, the minimum attenuation values lie around 5 GHz, while for fat tissue, those values lie around 10 GHz. Compared with skin and muscle, fat tissue has a lower water content and therefore different dielectric properties. Nevertheless, the attenuation in fat tissue at 5 GHz is relatively closer to that of skin and muscle tissues, and thus an operating frequency of 5 GHz was assumed as the work frequency for future simulations. This frequency lies in the optimal frequency range discussed in chapter three.

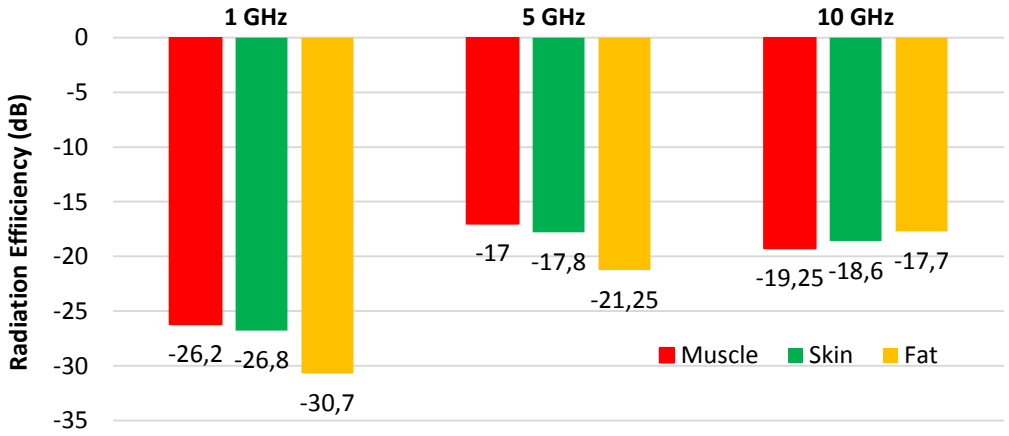

Figure 4.4 The square loop antenna simulated radiation efficiencies at 1 GHz, 5 GHz and 10 GHz, when embedded in a 5 x 5 x 5 mm^3 volume of human muscle, skin and fat.

4.3.2 Cubic Antenna

The cubic antenna approach was inspired in the self-folded metallic cubes of Figure 4.1A. However, instead of patterning a metallic strip in the middle of a polymeric cube, the self-folded metallic cube was used as the resonant element. As the cubic geometry is larger than the square loop, is it expected for the antenna electrical size to be increased and, therefore, the resonant frequency to decrease. Also, this geometry improves the antenna's occupied volume within the radian sphere surrounding the 500 x 500 x 500 μm^3 cube. In the cubic antenna case, the 500 x 500 μm^2 panels have a 10 x 50 μm^2 cross-section and the lumped port length was increased to 400 µm. Aside the antenna geometry, all simulation model parameters were kept the same as in the square loop antenna example.

4.3.3 Square Loop and Cubic Antennas: Performance Analysis

As seen in chapter three, small antennas are expected to operate at high frequencies when in free space (air). Simulation results show that the square loop and cubic antennas have operating frequencies of approximately 0.7 THz (700 GHz) and 0.25 THz (250 GHz), respectively (Figure 4.5).

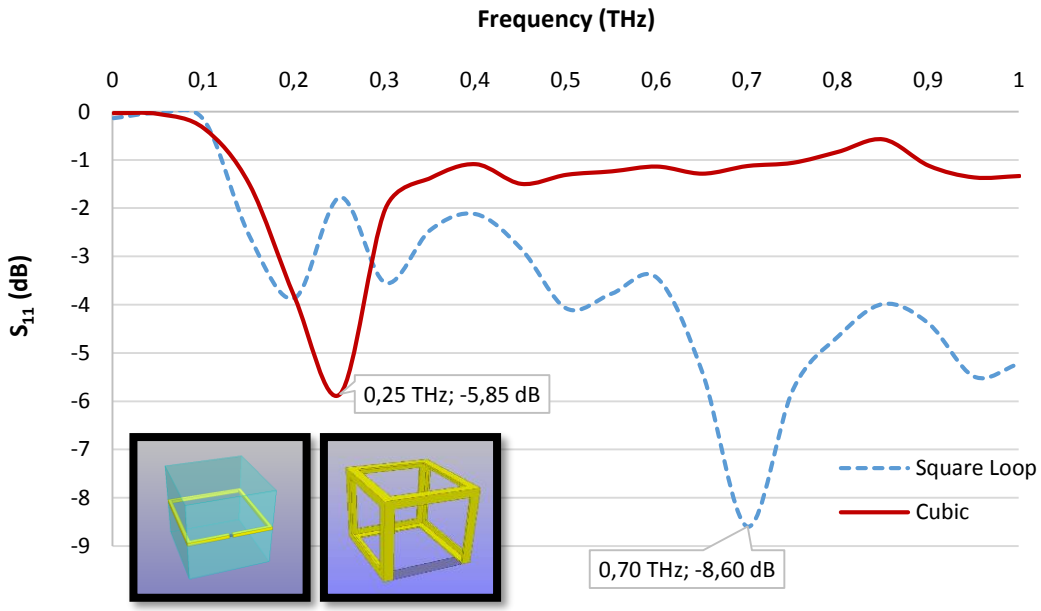

Figure 4.5 Simulated S_{11} of the square loop and cubic antennas in air.

However, when embedded in a biological tissue (e.g. muscle tissue) and at the specified work frequency of 5 GHz, (muscle tissue: ε_r = 49.5, σ = 4.04 at 5 GHz), the performance of both antennas was not satisfactory. Despite the dielectric loading induced by the high permittivity nature of human muscle, both the square loop and the cubic antenna fail to operate at low frequencies. Simulations show that at 5 GHz, both antennas have extremely low resistance (around 1 Ω) and relatively high reactance (Figure 4.6). Therefore, in order to operate within the biological tissue, the antennas have to be impedance matched by changing the feeding source resistance and capacitance.

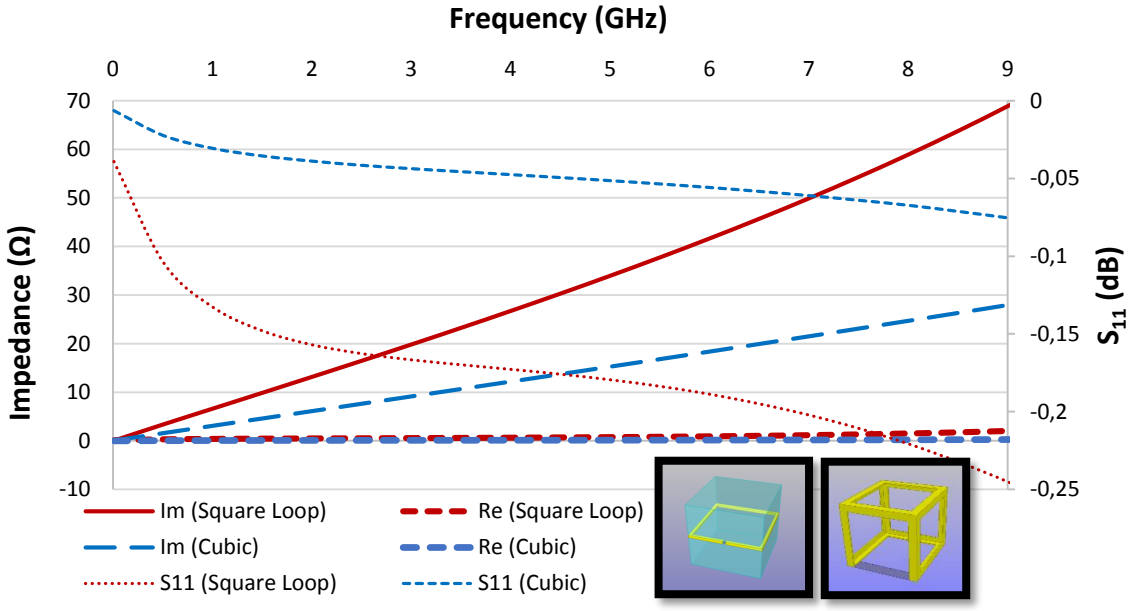

Figure 4.6 Square loop and cubic antennas simulated impedance and S_{11} embedded into a layer of muscle tissue.

Another perspective to the analysis can be given by the antenna surface current distribution, and by the radiation pattern (Figure 4.7). On both antennas, it is noticed that the surface currents do not stream along most of the antenna's structure. In the square loop antenna, the current distribution is confined within just one antenna small section, on the vicinity of the feeding port (Figure 4.7A). The cubic antenna, despite having a geometry that enables alternative current paths, it does not seem to significantly improve the current distribution, since it circulates only through the four

500 µm sections adjacent to feeding port, two in the X axis and two in the Z axis (Figure 4.7B).

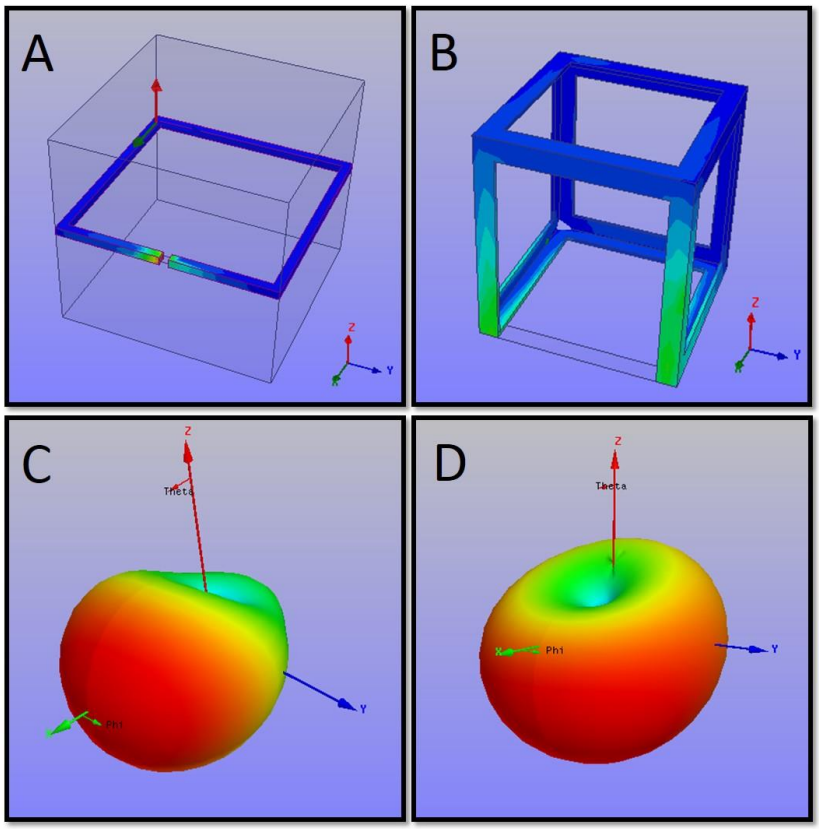

Figure 4.7 A) Current distribution on the surface of the square loop antenna at 5 GHz. B) Current distribution on the surface of the cubic antenna at 5 GHz. C) 3D simulated radiation pattern of the square loop antenna. D) 3D simulated radiation pattern of the cubic antenna.

Both antennas have very low gains (-45 dB for the square loop and -47 dB for the cubic antenna). Their radiation patterns (Figure 4.7C and D) evidence some directionality, which seems to be related to the poor current distribution over the antenna structures (Figure 4.7A and B). In both cases, the preferable direction of radiation is restricted to just a fraction of the antenna's structure, in the vicinities of their respective feeding ports. Hence, this performance analysis suggests that a new design strategy is needed for higher gain, better current distribution, a more isotopic radiation pattern, and to match the antenna's input impedance.

4.4 U-Shaped Antenna

The performance analysis of the square loop and cubic antennas helped to identify some critical design issues that needed be solved. Here, instead of a cruciform shape that folds into a cube, the antenna's is a simple 2D three-panel template that, upon folding, turns into a U-shaped 3D structure (Figure 4.8).

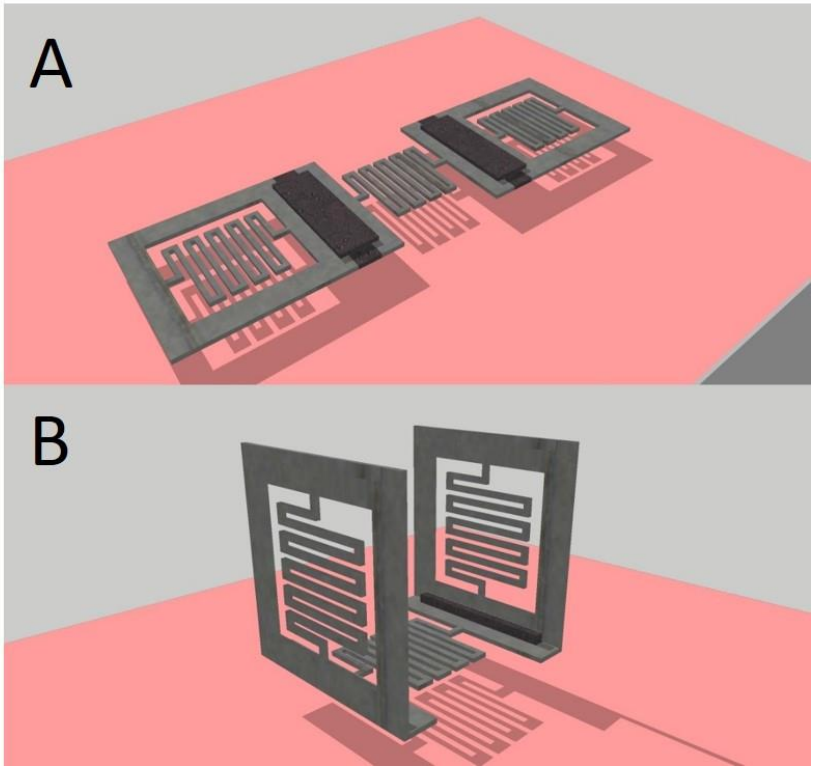

Figure 4.8 A) Unfolded 2D antenna structure. B) U-shaped 3D antenna after folding.

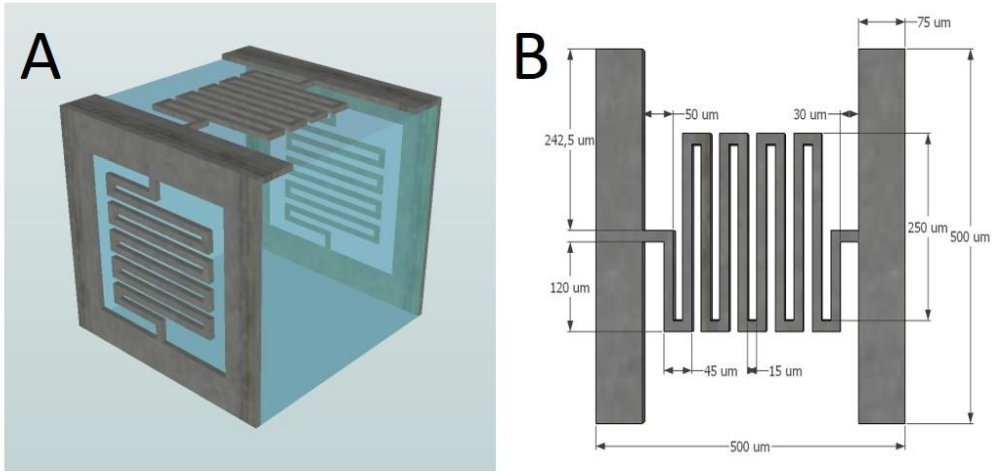

Figure 4.9 A) U-shaped antenna on a 500 × 500 × 500 μm^3 hypothetical device. B) U-shaped antenna top panel and features' dimensions.

This geometry is based on several antenna miniaturization techniques such as structure folding/bending, and the creation of periodic structures such as meander lines (Figure 4.9). This approach induces electrical currents to travel along one single and longer path, from one end of the antenna to the other, avoiding surface current concentration in one specific area. It was noticed that this strategy alone helps increasing the antenna input resistance. Nevertheless, in order to achieve a 50 Ω input impedance, further design optimization was required. As mentioned in chapter three, meander line structures were introduced as an antenna miniaturization technique.

Simulations were carried out to study the U-shaped antenna performance in air, and dispersive media such as muscle tissue (Figure 4.3). Figure 4.10 shows the S_{11} of the U-shaped antenna (in air) comparatively to previous designs. As the electrically smaller antenna, the square loop antenna has naturally the highest operating frequency, around 0.7 THz. The cubic geometry, represents an electrically longer antenna when compared to the square loop, and thus it operates at a lower frequency, around 0.25 THz. Finally, the U-shaped antenna geometry resonates around 0.08 THz (80 GHz), indicating that successful antenna miniaturization was achieved within the 500 x 500 x 500 μm^3 volume.

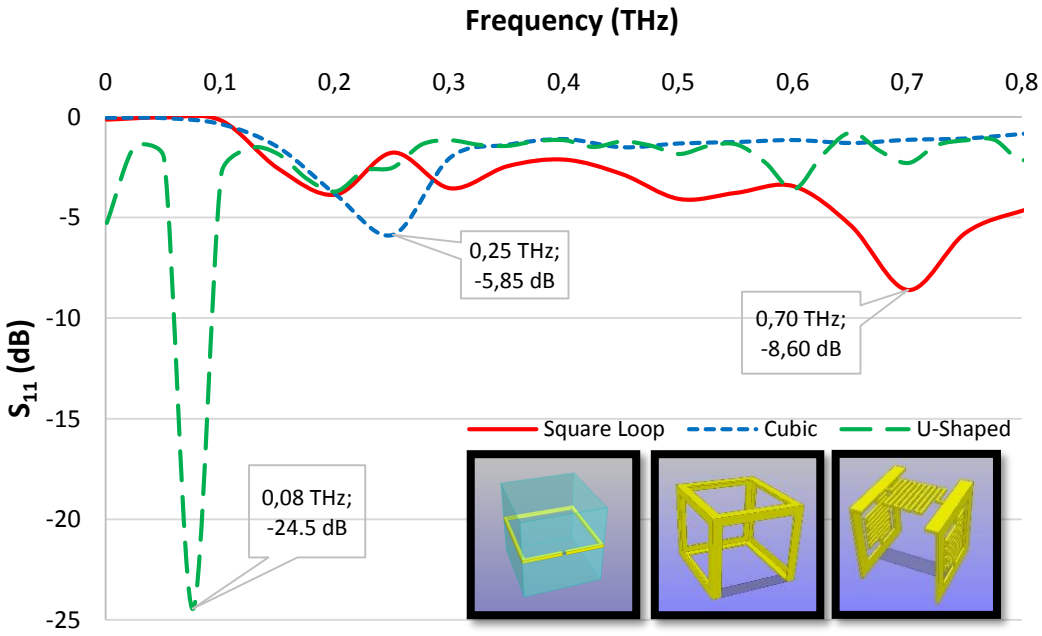

Figure 4.10 Square loop, cubic and U-shaped antennas simulated S_{11} in air.

When embedded in biological media, the U-shaped antenna operating frequency shifts to lower frequencies due to the effect of dielectric loading with high permittivity material. HFSS simulations show that, when embedded in muscle tissue, the U-shaped antenna operates around 3.3 GHz (Figure 4.11).

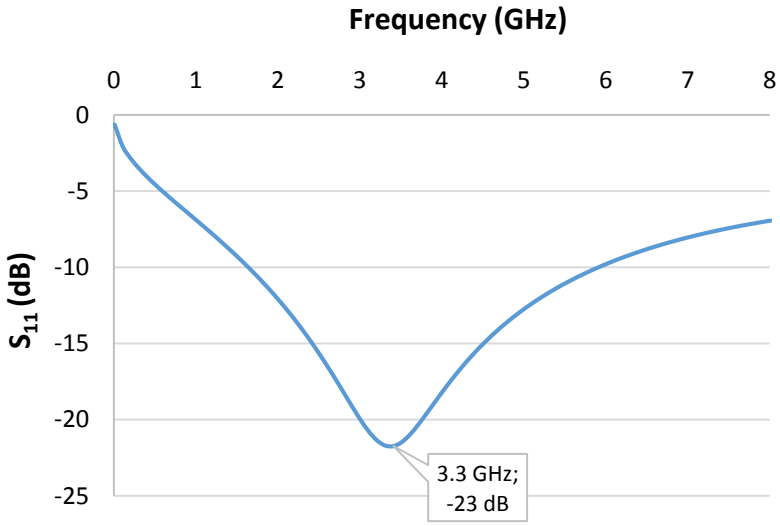

Figure 4.11 Simulated S_{11} of a U-Shaped antenna embedded in muscle tissue.

Figure 4.12 shows the result of the antenna geometry optimization of the current distribution and the 3D radiation pattern. As it can be seen in Figure 4.12A, the current distribution is no longer confined to a small antenna section, in fact, it now flows over most of the antenna structure. The U-shaped has a gain of -36 dB with a donut-shaped radiation pattern as seen in Figure 4.12B.

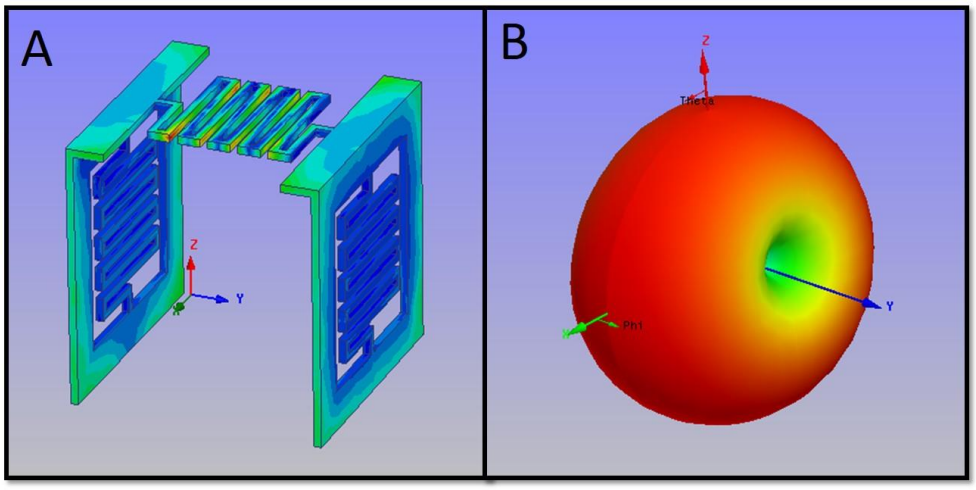

Figure 4.12 U-shaped antenna: A) Current distribution. B) Simulated radiation pattern.

4.5 Antenna Geometry Modification

The simulations suggest that regular structures, such as meander lines help to reduce the antenna resonance frequency and to adjust the input impedance. Next we show how some antenna parameters can be fine-tuned by means of small structural modifications.

4.5.1 Meander Line Number of Turns

Simulations show that increasing the meander line number of turns (Figure 4.13A - Figure 4.13 D), can affect the antenna operating frequency, decreasing it (Figure 4.13E). Essentially this modification makes the antenna electrically longer. It also affects the antenna input impedance (Figure 4.13F), making it more resistive, bringing it closer to 50 Ω as the number of turns increases.

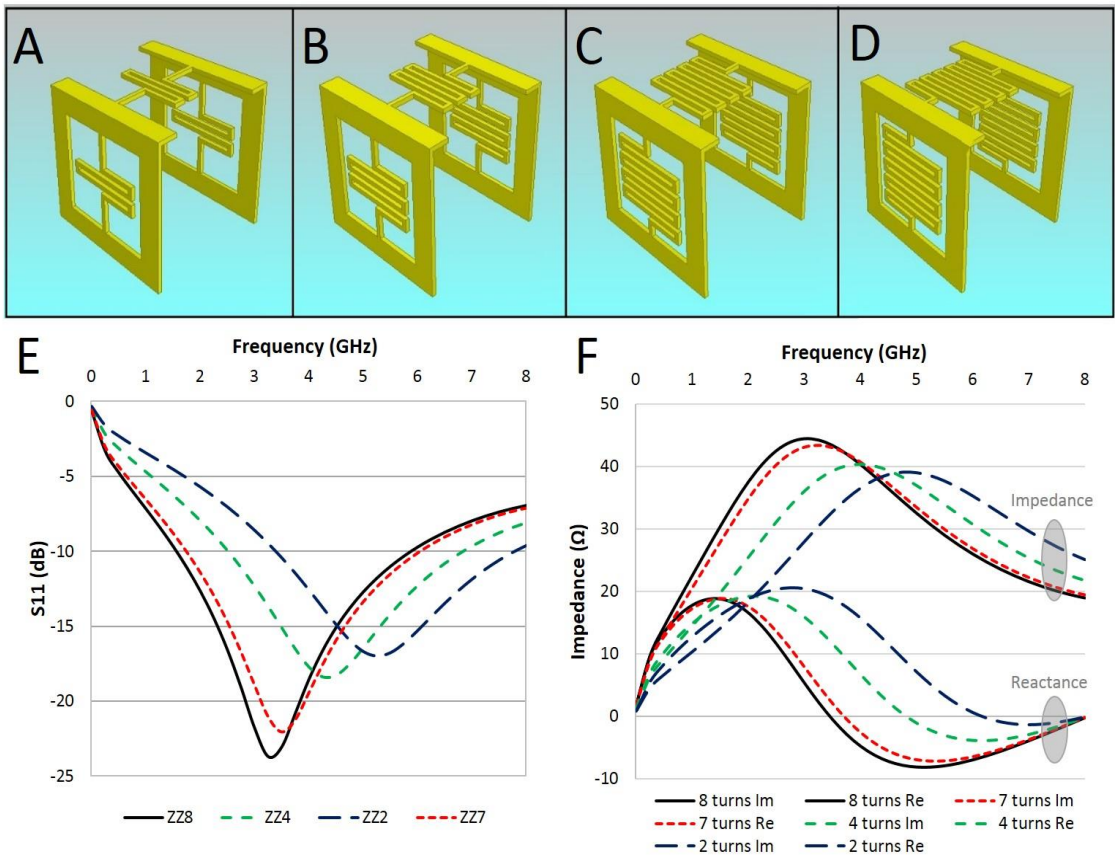

Figure 4.13 Variation of the meander line number of turns. U-shaped antenna with A) 2-turns. B) 4-turns. C) 7-turns D) 8-turns meander line. E) S-parameter. F) input impedance.

4.5.2 Meander Line Length with Constant Number of Turns

We simulated four antenna designs, where the only geometry of the top panel was modified (the antenna side panels geometry was kept constant with an 8 turn meander line). The top panel number of meander line turns was kept constant (8 turns), and the longitudinal length was varied (Figure 4.14A to Figure 4.14D). Figure 4.14B represents the control geometry whose dimensions as shown in Figure 4.9B. In comparison, Figure 4.14A shows a 20% increment in meander line length, while Figure 4.14C and D present decrements of 25% and 50%, respectively. The results show that, and similarly to those of Figure 4.13, the meander line length has a strong impact on both the antenna operating frequency and input impedance. This is basically another method of making an antenna electrically longer. As seen in Figure 4.14E, increasing the meander line length decreases the antenna operating frequency while increasing the resistive impedance (Figure 4.14F). The antennas operating frequencies range from 4.26 GHz to 2.26 GHz, with input impedances varying from 40 Ω to exactly 50 Ω, for the antenna design of Figure 4.13A.

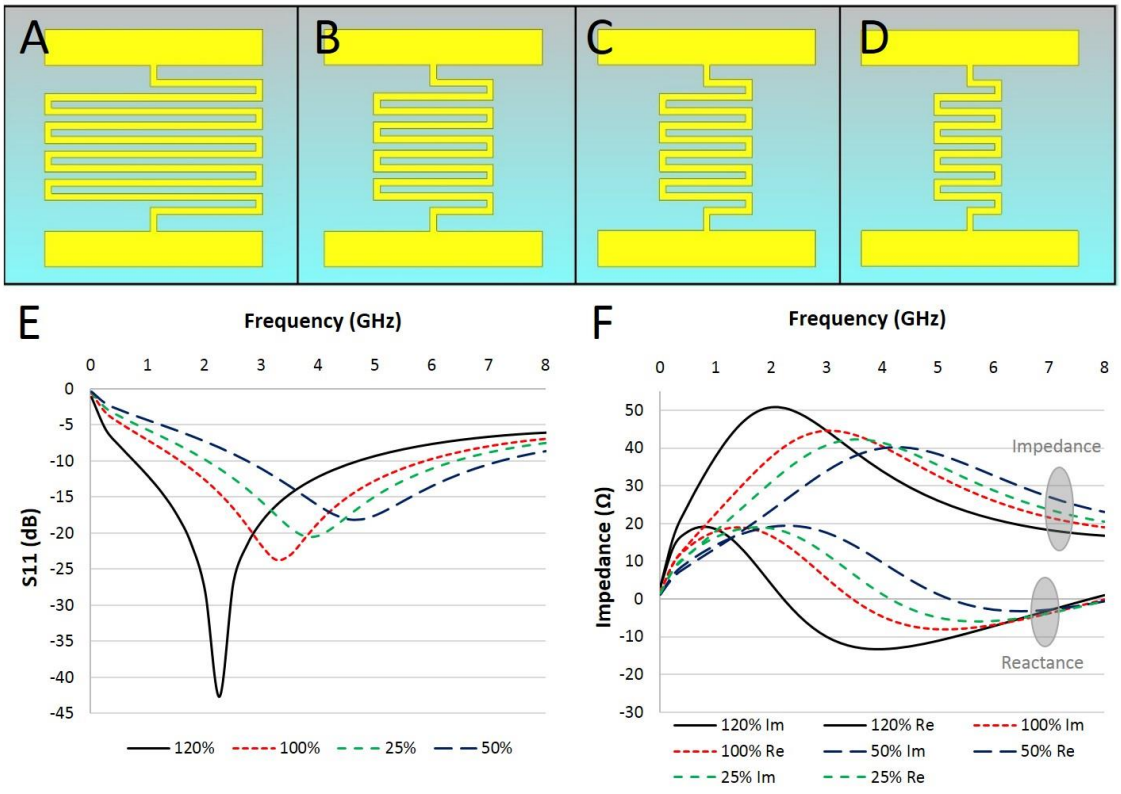

Figure 4.14 Variation of the meander line length under a fixed number of turns. U-shaped antenna top panel with A) 120% B) 100% C) 50% D) 25% meander line lengths. E) S-parameter. F) input impedance.

4.5.3 Meander Line Pitch

The effect of varying the meander line pitch (the distance between two consecutive meander lines arms) is presented in Figure 4.15. The top views of different meander line pitches (Figure 4.15A – Figure 4.15C), denominated as *low*, *medium* and *high* are presented. Again, the antenna side panels are kept with 8-turn meander lines, whose dimension are shown in Figure 4.9.The simulations show that the pitch variation has a small effect over the antenna resonant frequency. The low pitch antenna design exhibits a resonant frequency of 4.5 GHz, while the design with the highest pitch works at 4.26 GHz. In the same manner, varying the meander line pitch produces small, but more noticeable changes in the input impedance (Figure 4.15E), where a higher pitch promotes the increase of the antenna input impedance.

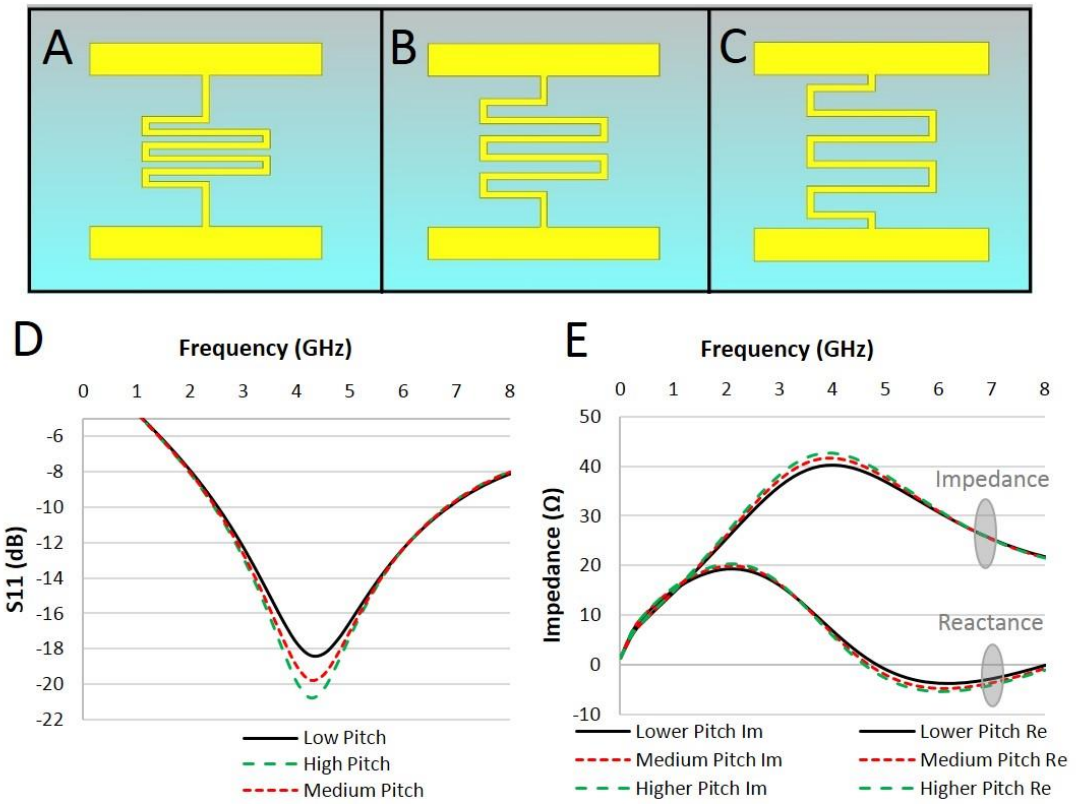

Figure 4.15 Variation of the meander line pitch. U-shaped antenna top panel with A) low B) medium C) high meander line pitch. D) S-parameter. E) Input impedance.

In summary, the results show that the modification of the meander line by manipulating the number of turns (Figure 4.13), the length of a line with a fixed number of turns (Figure 4.14), the meander line pitch (Figure 4.15), promotes the

general lengthening of the current paths, increasing the antenna electrical size and decreasing the resonant frequency. Overall, the three presented techniques effectively promote resonant frequency reduction and input impedance control.

4.5.4 Antenna Side Panel Geometry

After realizing that the antenna top panel has an important influence over the antenna's performance, we will now study the effect of manipulating the geometry of the U-shaped antenna side panel. Figure 4.16 presents five antenna designs with different side panel geometries. In all of them, the antenna's top panel geometry is kept unchanged, and its dimensions are shown in Figure 4.9.

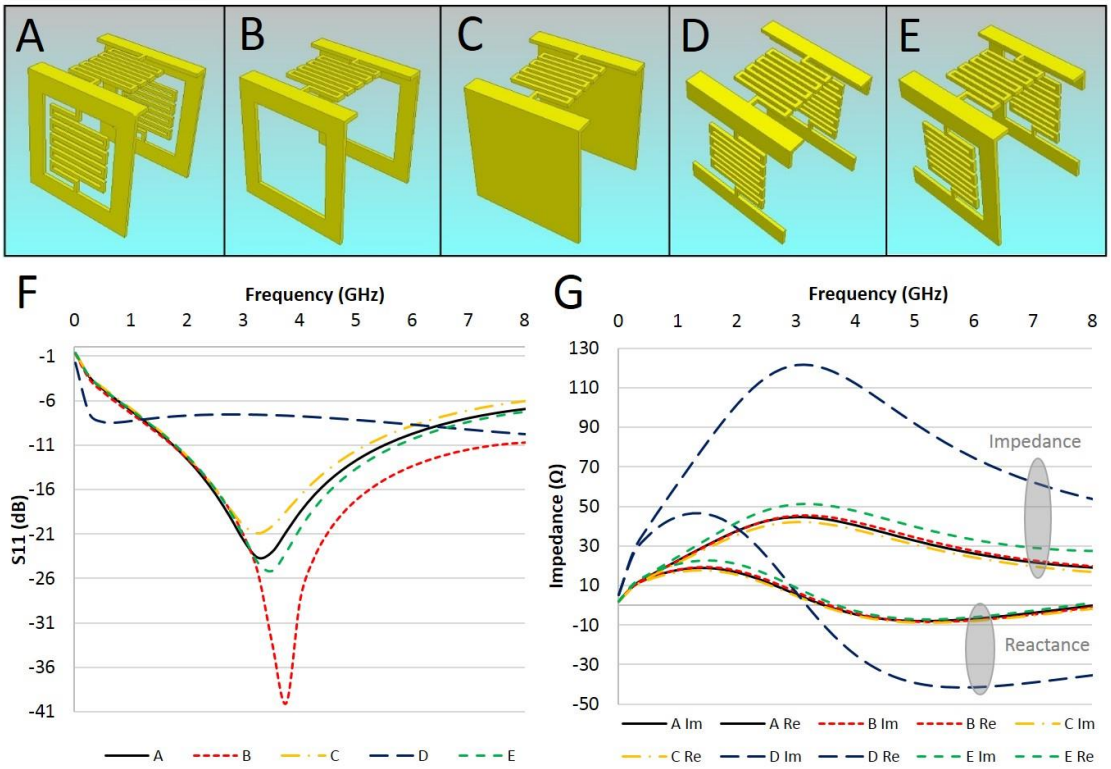

Figure 4.16 Variation of the antenna side panel geometry. U-shaped antennas with different side panel geometries. A) Side panel with meander line. B) Side panel without meander line. C) Filled side panel. D) Side panels without both side columns. E) Anti-Symmetric side panels without one column. F) S-parameter. G) Input impedance.

The antenna design of Figure 4.16A represents the control geometry, with an S_{11} of -23 db at 3.4 GHz. To better understand the effect of the side panel's shape, we started by simulating an antenna without it (Figure 4.16B). It presents an S_{11} of -25 dB at 3.5 GHz, with a slight frequency shift (0.24 GHz) when compared to the control

geometry. This frequency shift can be explained by the fact that the side panel's meander line promotes an alternative current path, making the antenna slightly electrically larger, thus operating at a higher frequency. On the other hand, the design of Figure 4.16C has two solid, completely filled side panels. In this case the operating frequency didn't significantly alter when compared to the control. However, the S_{11} value increased to -20.9 dB, since square surfaces offer less resistance to the current flow, and hence decreasing the antenna input impedance, which in turn decreases the antenna S_{11}. Other antenna design, composed of three equal panels (Figure 4.16D), was also simulated. The two side panel's columns were cut, originating a structure where the current path is made exclusively through the meander line. Looking at the input impedance graph (Figure 4.16G) it can be seen that the antenna is extremely resistive throughout the analyzed spectra, since the current flows through three consecutive meandered paths, which greatly increase resistivity. In order to reduce the excessive resistivity of the previous design, we simulated an antenna whose side panels have a meander line structure and one column on the side as seen in Figure 4.16E. With this design the antenna operates at 3.76 GHz with an impedance of 49 Ω, showing that it is possible to control the antenna impedance, reaching a nearly 50 Ω value by manipulating its geometry.

4.5.5 Antenna Side Panel Separation Distance

In this section, the separation distance between the two antenna side panels is studied. The control geometry (Figure 4.17A) has a panel separation distance of 470 µm while the separation distance of the antenna design of Figure 4.17B is 940 µm. The number of the meander line turns was kept constant to 8 turns. The simulation shows that doubling the distance between panels does not prove to be advantageous in terms of decreasing the antenna operating frequency since it does work at 3.76 GHz, however it does improve the S_{11} by 2.5 dB. Nonetheless, this strategy can be useful for antenna impedance adjustment to a desired value.

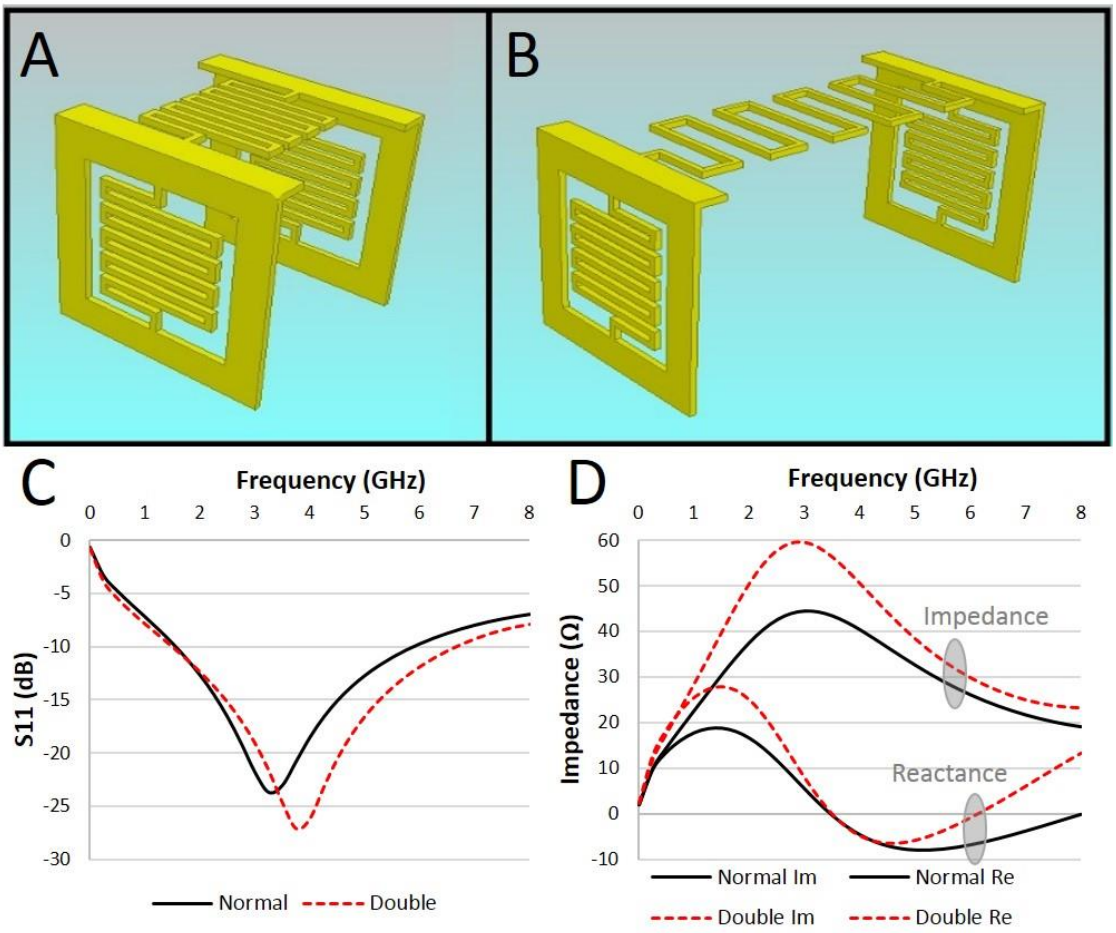

Figure 4.17 Increasing the antenna side panel distance. U-shaped antenna with A) normal meander line. B) Doubled meander line. C) S-parameter. D) Input impedance.

The meander line's design parameters (number of turns, separation, with and length) were optimized for this specific case. A total of 8 turns were used to attain resonance with an input impedance of nearly 50 Ω (with an almost null reactive component), with no impedance matching. It is worth mentioning that the U-shaped antenna design considers the antenna feeding to be performed between the two outermost panels, which after folding, distance 470 µm from each other. Also, the antenna features, such as thickness and the meander line width, were defined accordingly to the capabilities and precision of the available fabrication methods.

The promising results given by HFSS simulations show that a U-shaped antenna may be a viable candidate for a 500 x 500 x 500 μm^3 device. In the next chapter we will discuss the antenna fabrication by means of photolithography combined with self-folding method.

5 Antenna Fabrication

Several methods for the fabrication of three dimensional antennas have been reported in the literature. These methods include manual folding [60-61], 3D printing of metallic inks [54], metallic inks on paper [64], direct transfer patterning of metallic patterns [55], self-folding [66-67], manual assembly [62], self-assembly [65], and wafer stacking [68-69]. Other complex three dimensional architectures suitable for other electromagnetic applications can be fabricated by 3D printing [63], lithography [170], biotemplating [59], transfer printing [70], and compressive buckling [71]. However, most of these methods are time consuming, not suitable for antenna mass production, strongly dependent on a few selected material types, do not allow electronic component integration, have relatively low feature resolution and control over the antenna geometry, and are unfitting for the fabrication of sub-millimeter 3D structures.

In this chapter it is described an alternative method to fabricate sub-millimeter 3D micro antennas, based on patterned metallic 2D templates that self-fold due to the minimization of surface energy of liquefied hinges. Here it is utilized a methodology that combines conventional planar photolithography techniques and self-folding, wherein physical forces derived from surface tension, are used to fold planar structures into 3D ones. By doing so, it is then possible to produce precisely patterned static and reconfigurable sub-millimeter antennas that are challenging to manufacture, and able to overcome the aforementioned limitations of other methods. In this fabrication process, photolithography allows the easy patterning of virtually every desired planar configuration with reproducible feature precision, and the flexibility to easily and precisely change the antenna geometry and size. Self-folding allows the fabricated planar patterns to fold into the final 3D structure in a highly parallel and scalable manner. This combined method offers ease of mass production, extreme control of size and shape, material versatility, and the ability to integrate electronic modules, as well as the flexibility to easily and precisely change the antenna geometry and size.

5.1 Surface Tension-Driven Self-Folding

One of the main challenges of fabricating 3D submillimeter-scale objects lies in the inherent two dimensionality of fabrication techniques which are capable of patterning top and bottom faces but are incapable of patterning side ones. A few techniques such as stereolithography, laser micromachining, and ion beam milling can overcome this challenge but are too expensive and time-consuming [170]. However, a strategy called self-assembly (which is reminiscent of the ancient Japanese art of paper folding, called origami), based on folding of a 2D template to form a 3D structure, has recently been suggested for the fabrication of submillimeter-scale objects. Several strategies for self-assembly based on folding have been explored, including the use of electroactive polymers, magnetic forces, stress-induced forces, and surface forces. Among these, the use of surface forces is particularly attractive since it does not require active actuation. The highlight of this self-assembly process is that it retains all of the advantages of conventional microfabrication while enabling 3D fabrication in a highly parallel and cost-effective manner.

5.1.1 The Self-Folding Technique

The process of self-folding is outlined in Figure 5.1, which captures the essential function of the folding hinges that play a critical role in forming a folded structure. Here, two adjacent square faces are held together by a single folding hinge. One face is assumed to be fixed, and the other is allowed to rotate freely around the solder hinge. In the 2D template, the folding hinge solder is in the form of a T-shaped right prism. On reflow, the solder liquefies and forms a rounded contour (Figure 5.1C). Because of the high interfacial tension of the liquid solder there is a strong driving force to minimize the exposed interfacial area between the molten solder and the surrounding fluidic liquid. This driving force causes the solder to ball up, which results in the rotation of adjacent faces. The fold angle is primarily controlled by the solder volume. Different solder volumes generated underfolded (Figure 5.1D), correctly folded (Figure 5.1E), or overfolded structures (Figure 5.1F). Experimentally, the solder volume that determines the equilibrium folding angle is manipulated by controlling the height of the electrodeposited solder for a given hinge geometry.

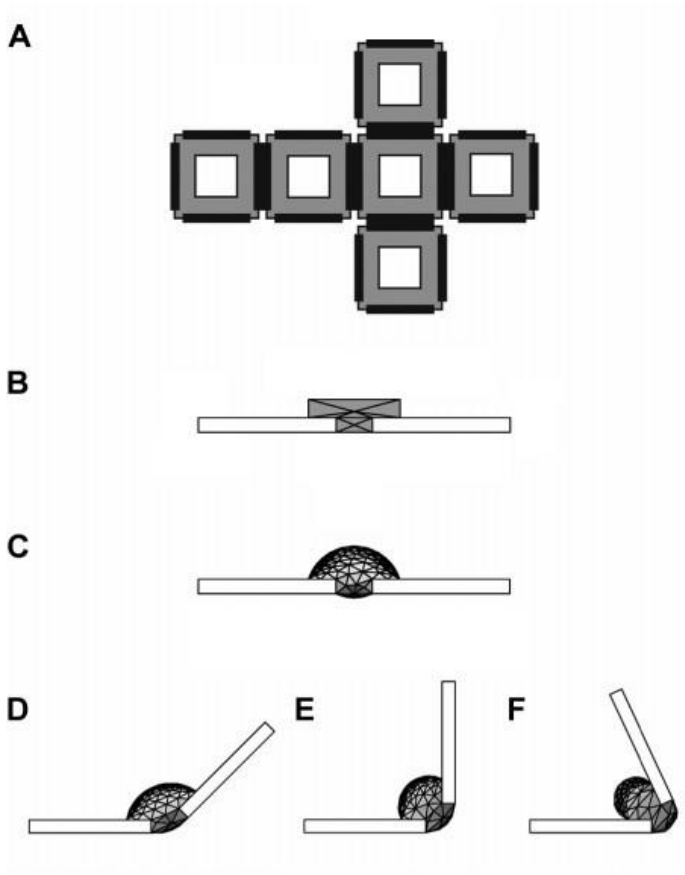

Figure 5.1 The self-assembly process. A) Top view of a 2D template used to self-assemble a cubic structure. B) Side view of a patterned solder hinge. C) Side view of a solder hinge at the onset of reflow of the folding hinge. D) Under folded panels. E) Right-angle folded panels. F) Overfolded panels [170].

5.1.2 Fabrication Summary

A schematic illustration of a cubic structure self-folding process is shown in Figure 5.2. The micro antennas are fabricated on silicon wafer substrates, where a polymeric sacrificial layer and conductive chromium and copper thin films layers are deposited (Figure 5.A). The antenna body is made of electroplated nickel (Figure 5.2B) and folding hinges are made out of solder (Figure 5.2C). The panels and hinge materials should be chosen so that the hinge material has a lower melting point than the panels, and hence the panels remain rigid while the hinges are melted. The conductive and sacrificial layers are etched and dissolved to lift-off the antennas from the substrate (Figure 5.2D). Folding occurs (Figure 5.2E) when the released structures are heated above the melting point of the hinge material using a high-boiling point solvent, and finally fold into 3D structures.

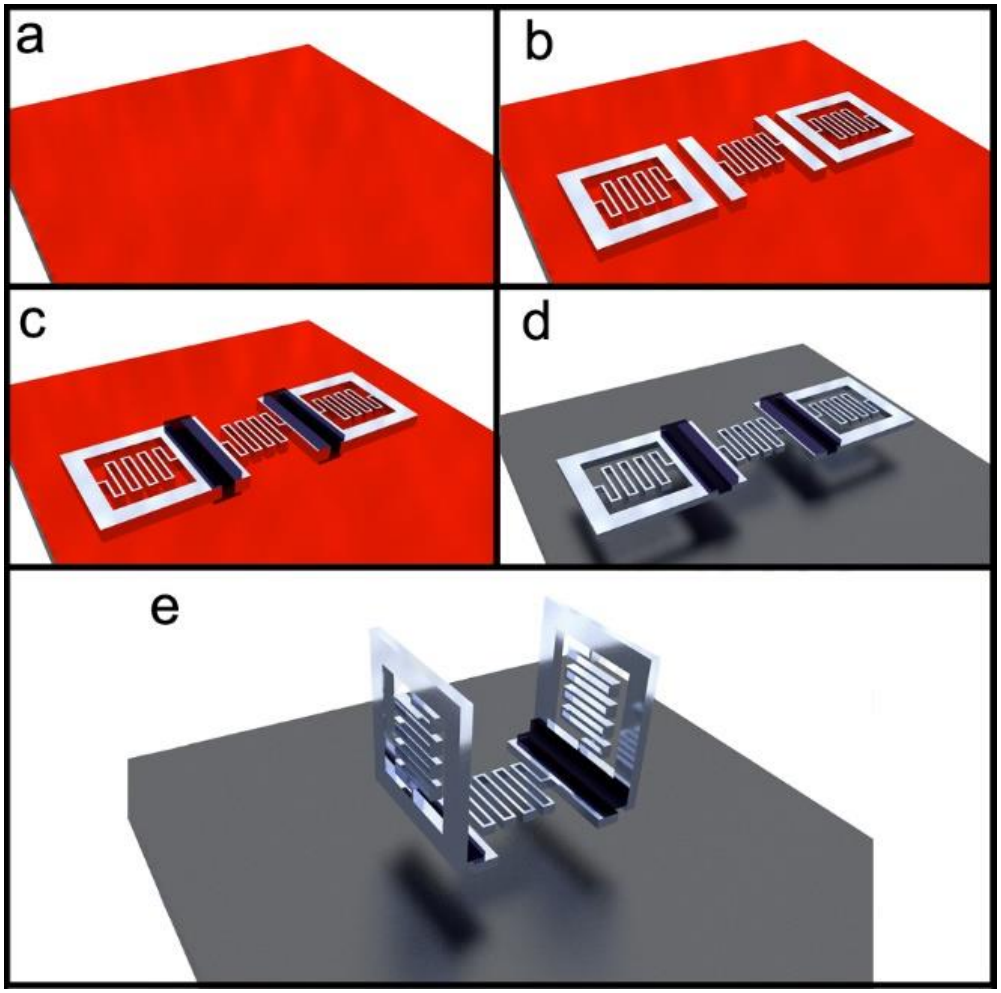

Figure 5.2 Relevant fabrication steps of the U-shaped antenna.

5.2 Fabrication Workflow

In this section we will present the 3D micro antenna fabrication process in detail discussing the utilized materials, techniques and equipment providing an understandable protocol (please see Appendix 1 for more details), allowing others to precisely reproduce the fabricated antennas.

5.2.1 Mask Design Rules

For the fabrication process, two photomasks are required, one for rigid 2D antenna panels and the other for the hinges. The masks are designed using two dimensional vector graphics software programs such as AutoCAD (Figure 5.3). The successful fabrication of the micro antennas starts with careful application of mask design rules such as the positioning and size of the antenna panels and solder hinges. In

the antenna panels mask, the individual 500 x 500 μm^2 panels that compose the antenna should be drawn as nets, and the adjacent panels should be spaced by a gap of width that is approximately 0.1L (L = 500 µm). In the folding hinges mask, the rectangular structures should have lengths of 0.8L and widths of 0.2L. Figure 5.3 shows an antenna prototype with multiple nickel patterns and hinges.

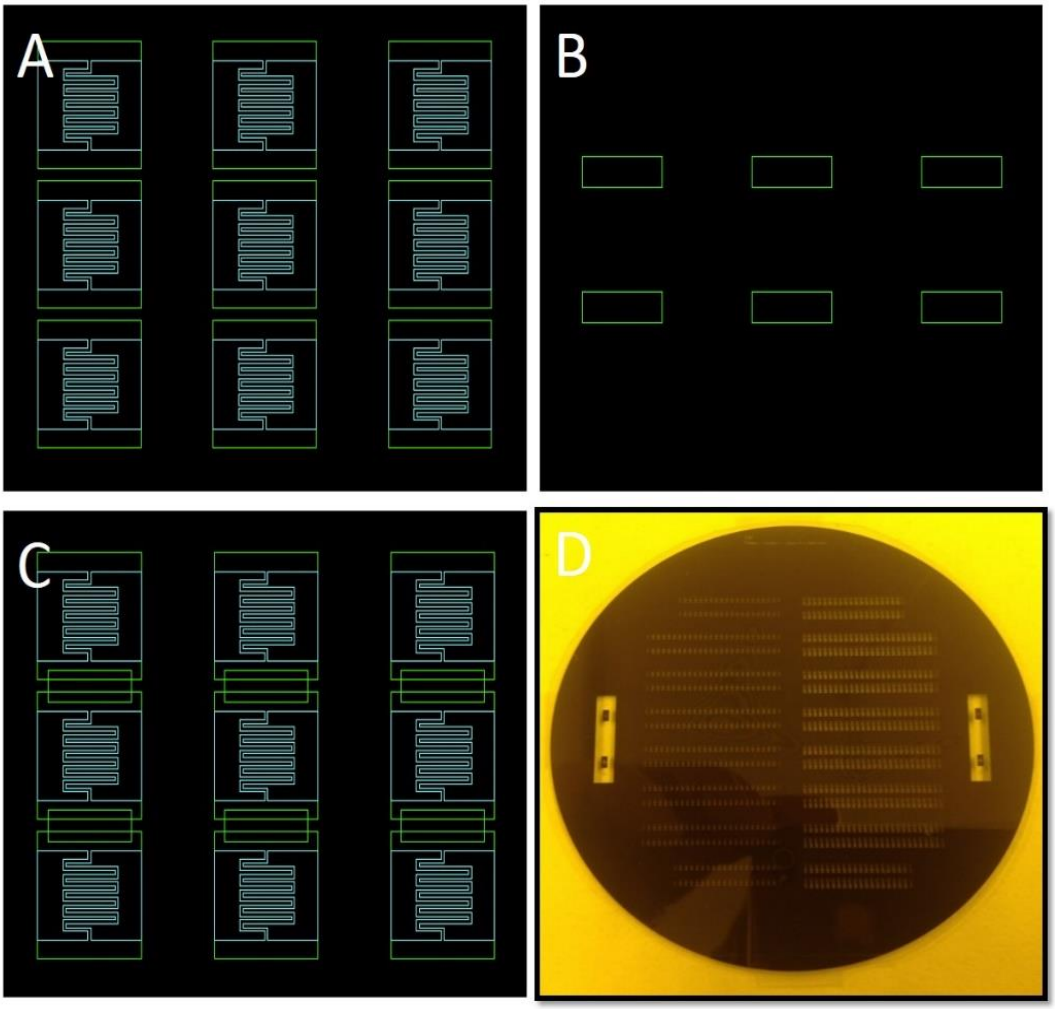

Figure 5.3 Autocad design of the micro antenna structures and solder hinges for the photomask used in the lithography process. A) Antenna panels. B) Folding hinges. C) Antenna panels and hinges. D) Printed photomask.

5.2.2 Substrate, Sacrificial, and Conductive Layers Preparation

In this fabrication process, flat substrates such as silicon wafers are used. Also, for good adhesion purpose, it is important to clean and dry the substrates. It is generally sufficient to clean the substrates with methanol, acetone and isopropyl alcohol (IPA), dry them with nitrogen (N_2), and then heat them with a hot plate or in an oven at

150 °C for 5-10 min. In order to release the 2D templates from the substrate after patterning, sacrificial layers are required. A variety of films composed of metals (*e.g.*, copper), dielectrics (*e.g.*, alumina), or polymers (*e.g.*, PMMA, PVA) can be used. In this work, a 5 µm thick layer of PMMA will be removed subsequently with an adequate solvent. Hence, we spin coat a 5 µm thick layer of 950 PMMA A11 at 1000 rpm on the silicon wafers. Then we wait for 3 min to let the PMMA even out on the wafer and afterward bake it at 180 °C for 60 sec.

The silicon substrate must have a proper conductive layer, as this layer will be important during the electroplating process, which will allow the patterning of metallic templates and hinges. When choosing a conductive film, important considerations are the ease of deposition and dissolution of the material, and the etch selectivity. For the micro antenna fabrication, a 15 nm-thick chromium layer was used as an adhesion promoter and 100 nm of copper as a conductive layer. Both films were deposited onto the silicon wafer by thermal evaporation, first the chromium and then the copper using the setup shown in Figure 5.4.

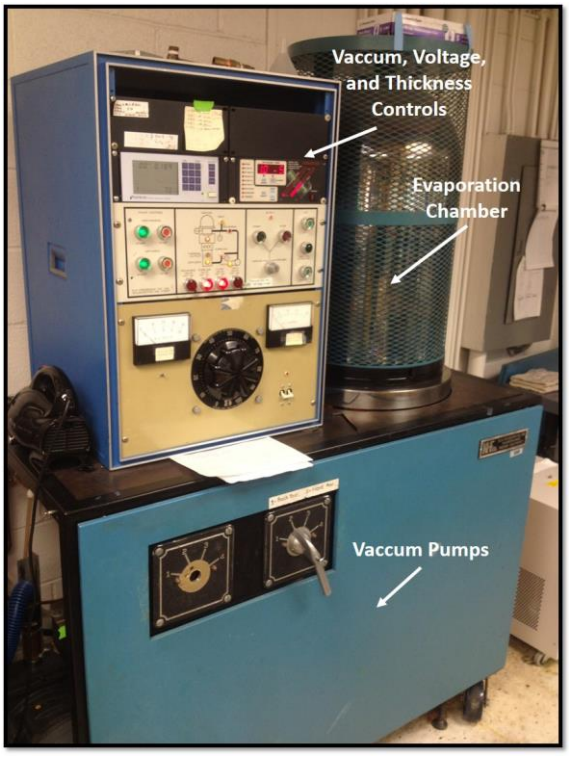

Figure 5.4 Thermal evaporation setup composed of an evaporation chamber, the vacuum, voltage, and layer thickness controls and monitors, and the necessary vacuum pumps.

5.2.3 Patterning the Panels

The panels are patterned (Figure 5.5) using typical photolithography consisting on coating a substrate with a photoresist layer (SPR220), baking, exposing, and developing. Photoresists such as SPR, AZ or SC series can be used. Depending on the choice of photoresist, thickness and therefore spin speed, exposure time and development time will need to be adjusted accordingly. After photolithography, depending on the size of metallic 2D templates, thick panels can be formed by electroplating. Faraday's laws of electrodeposition and the efficiency of the bath should be used to calculate the electroplating current based on the total exposed surface area of the panels. Typical current densities for nickel (Ni) and solder (Pb-Sn) plating are between 1-10 mA/cm^2 and 20-50 mA/cm^2, respectively. In this work, the antenna body was made out of 10-12 µm electroplated nickel.

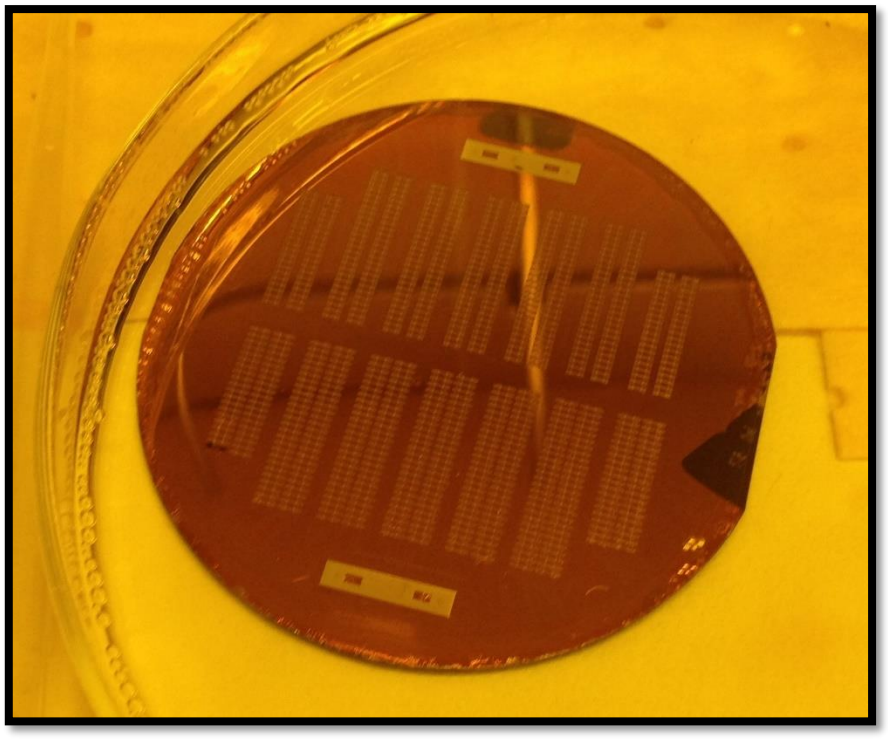

Figure 5.5 Silicon wafer with electroplated nickel panels.

5.2.4 Patterning the Hinges

In order to pattern the hinges (Figure 5.6), a second round of photolithography needs to be done using the hinge mask. For surface tension driven assembly, the panels and hinges materials should be chosen so that the hinge material has a lower melting point than the panels and hence the panels remain rigid while the hinges are melted. Assembly occurs when the templates are heated above the melting point of the hinge material. For example, in case of metallic particles with Ni panels, we electrodeposit Pb-Sn solder on the hinges which melts at ~200 °C, and prompts the folding. The process works best when the hinge material is restrained within the hinge region during reflow, *i.e.*, it does not spread all over the panels and does not completely dewet from the panel. This holding can be achieved by the selection of materials with appropriate wetting characteristics and viscosity. After many attempts, the optimum thickness for the hinge pads was found to be of 15 μm.

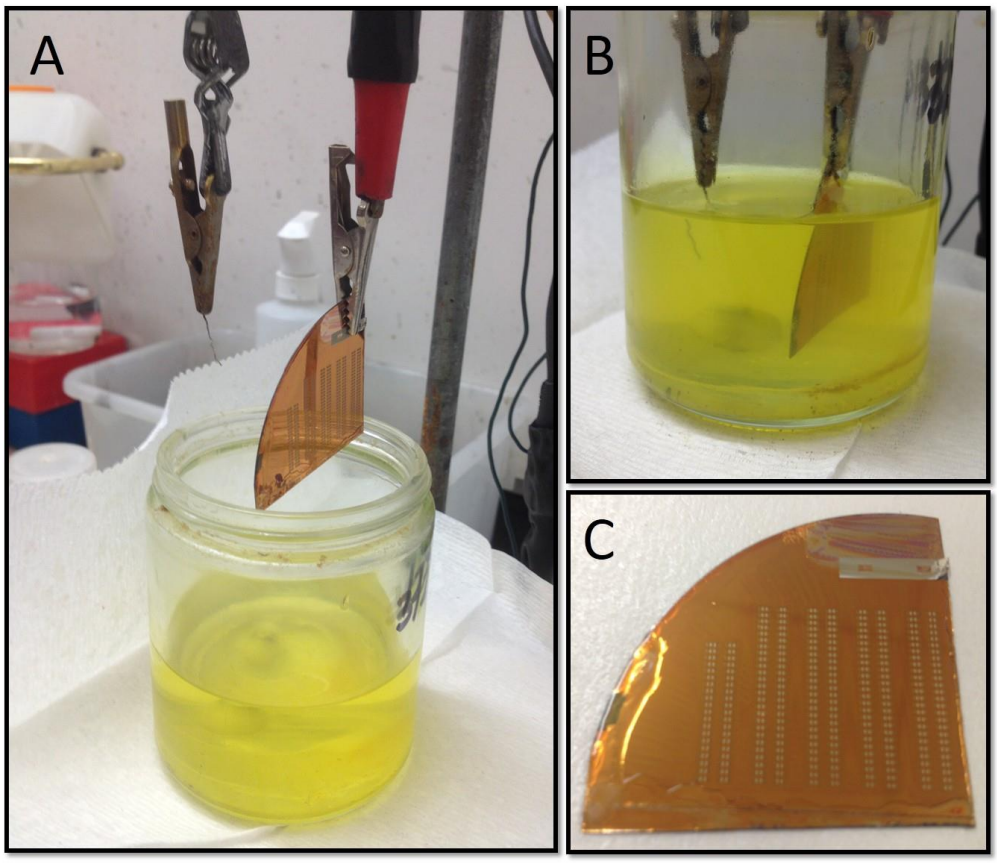

Figure 5.6 Electroplating setup. A) A commercial solder plating solution with the anode (left) and cathode (right) ready for solder electroplating. B) The submerged solder anode and quarter silicon wafer. C) A quarter silicon wafer with electroplated hinges ready for photoresist strip.

5.2.5 Releasing the Templates from the Substrate and Folding

To release the patterned 2D templates, the sacrificial layer needs to be dissolved by appropriate etchants for chromium and copper (Figure 5.7). The released 2D templates are transferred to a folding solution in a petri dish where they are heated above the hinge material melting point. Upon heating, the hinges get liquefied and the precursors assemble into the appropriately shaped particles. A small amount of Indalloy flux 5RMA was added to the solvent to clean and dissolve any oxide layers on the solder and thereby ensure good solder reflow. For the fabrication of cubic shaped antennas, the locking hinges grant the precise folding. In the case of U-shaped antennas, this step has to be carefully timed to avoid the structure over-folding, since locking hinges are not used.

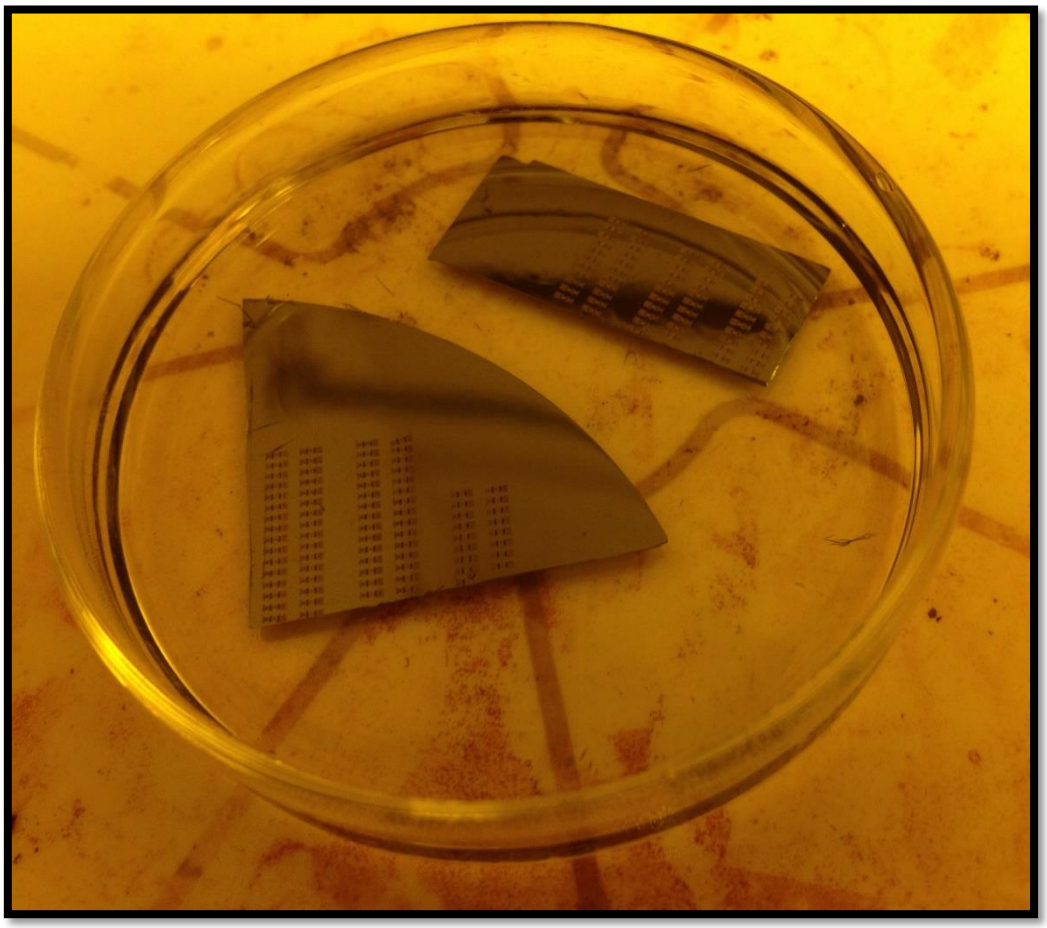

Figure 5.7 Pieces of silicon wafers without chrome and copper layers, with unfolded antennas attached to it ready for the releasing step.

5.3 Results

Figure 5.8 presents the fabricated 3D antenna structures from planar faces (Figure 5.8A) that self-fold with temperature to create the final U-shape of the micro antennas with 90° angles (Figure 5.8B). Scanning electron microscopy pictures were also taken (Figure 5.9).

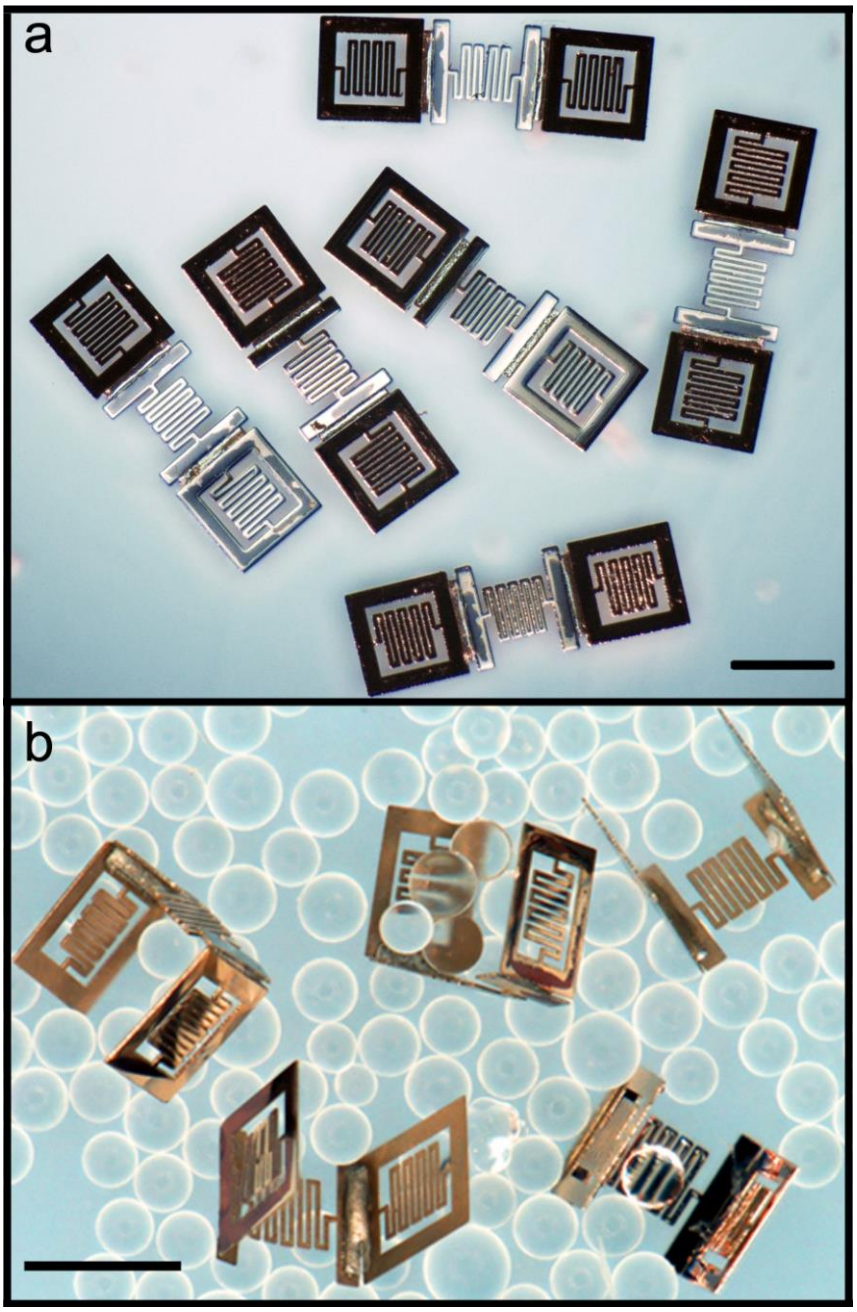

Figure 5.8 The fabricated micro antennas: A) Released structures before folding. B) After folding. Silica beads added into the medium to emphasize the 3D structure of the antennas. Scale bars: 500 µm.

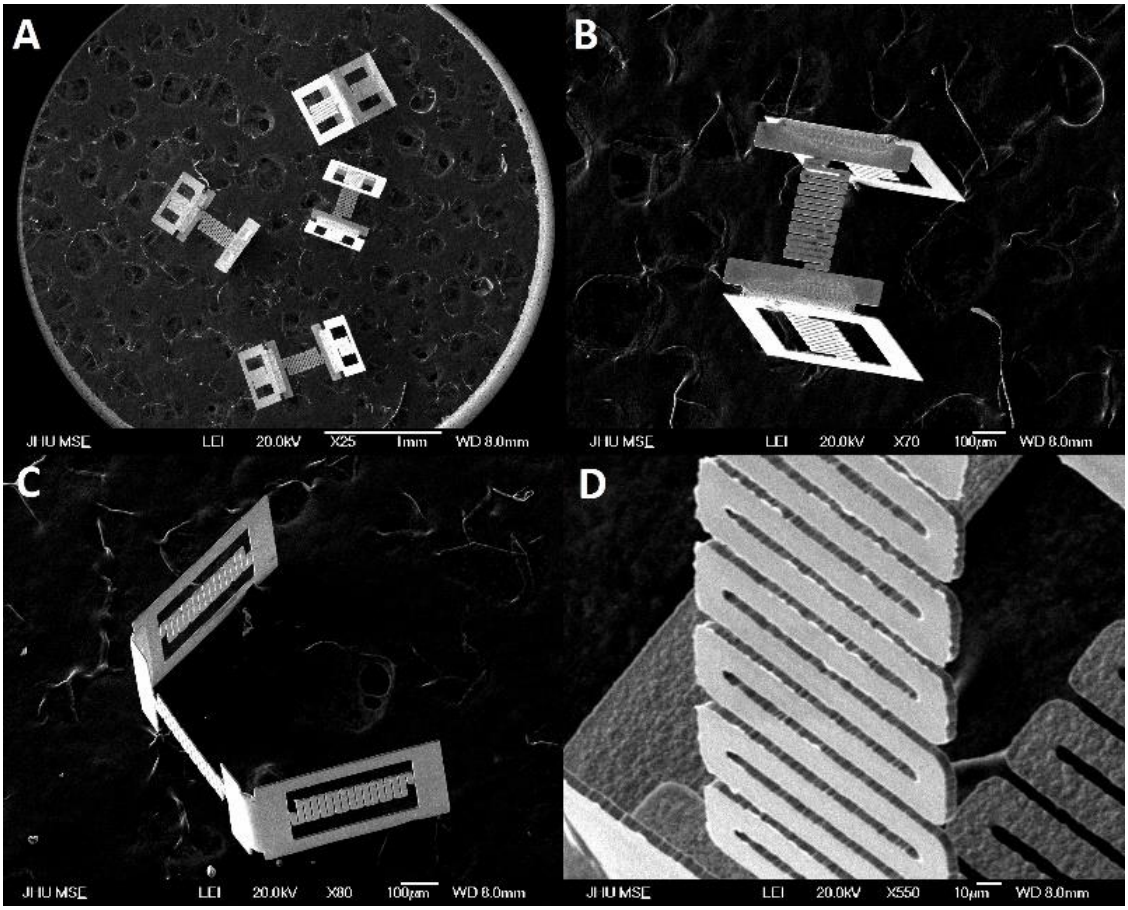

Figure 5.9 Scanning electron microscopy images of folded micro antennas. A) Underfolded and overfolded antennas. B) Perfectly folded antenna with 90º angles. C) Under folded antenna. D) Antenna's meander line.

As the figures above show, the U-shaped micro antennas were successfully fabricated. Though, these results were only achieved after a great deal of optimization at any given fabrication step. The most critical step was antenna panel folding since not all structures will fold perfectly, with a 90° angle. Figure 5.9A displays under folded and over folded antennas. The cause for this may be related with the disposition of the structures on the folding dish placed on the hotplate. It was noticed that different hotplate areas have different temperatures and hence some structures fold faster or slower than others. Another possible cause for this can be related with the hinge electroplating, as it was often noticed thought microscope inspection that structures on the edge of the wafer could have less electroplated material. Since higher folding yields varied from batch to batch, it can be said that the folding time is somehow governed by the hinges electroplating. Hence, at each batch, control experiments should be performed in order to evaluate the folding time.

6 Development of a Characterization Setup & Experimental Results

Throughout the antenna project stage, simulation results provided valuable insights of how the antenna would perform in air and when surrounded by dispersive media such muscle tissue. Nevertheless, despite of HFSS's high level of trust, the implemented models need to be validated via experimental measurements. Hence, after the antenna project and fabrication, it is necessary to characterize the obtained structures. Some of the most commonly measured antenna features are the S-parameters, the radiation pattern and gain. In this chapter, we will describe the several experiments conducted in the effort of measuring the antenna S-parameters and radiation pattern. It is important to take into consideration that the fabricated antennas are extremely small, and that fact has important consequences over their handling and the engineering of the characterization setups. Also, as seen in chapter three, the antenna gain is expected to be very low which makes it challenging to measure.

For the characterization, the proposed micro antenna has to be connected to a carrier structure, serving as an interface between the antenna and a vector network analyzer (VNA). Different approaches were investigated and tools such as SMA and end launch connectors, transmission lines, and RF probes were utilized. All these approaches demonstrated to be somewhat useful for S-parameter measurement, however most of them are not suitable for the antenna radiation pattern measurement, as we will see further ahead. Once found the best interface structure, we proceeded to the measurement of the antenna radiation pattern. Finally, a wireless power transfer practical application is presented. Here, a horn antenna is used to wirelessly transfer power to the fabricated micro antenna immersed in dispersive media, where the micro

antenna is connected to a rectifying circuit which turns the received radiofrequency into DC power and an LED is lighten up to prove the setup feasibility.

6.1 Characterization Setup

Following the antenna fabrication, it is necessary to measure its input characteristics, such as the S-parameters. These can be obtained using a VNA to which the antennas are generally connected to via a specific connector attached to a coaxial cable. Commonly, connectors are centimeter scale structures with millimeter scale feeding pins. However, the fabricated antennas have sub-millimeter dimensions and their feeding is intended to happen in between their side panels, approximately a 500 µm gap. Thus, it was necessary to engineer an interface structure to which the micro antennas can be connected to. In the following sections we will present and discuss the performance of the several strategies utilized to this end.

As seen on the micro antenna project chapter, the U-shaped antenna was simulated when embedded in human muscle tissue. Since muscle is a high water content medium, in the current chapter we will use fresh water in our experiments, as a first approximation phantom, to mimic a high permittivity medium such as muscle tissue. The U-shaped antenna was simulated when embedded in fresh water (ε_r = 81 and σ = 0.01), also high permittivity medium, capable of inducing dielectric loading and decreasing the antenna operating frequency to the low gigahertz range. Simulated S-parameters show that when the U-shaped antenna is immersed in fresh water, it operates at 2 GHz (Figure 6.1). For comparison purposes, the U-shaped antenna was also simulated when immersed in muscle tissue, but at the same frequency of the water embedded antenna. Therefore, the muscle dielectric properties at 2 GHz (ε_r = 53 and σ = 1.453) were extracted from [139]. In these conditions, the S-parameters indicate that the antenna operates at 2.7 GHz (Figure 6.1). The simulated gains for the water and muscle embedded antennas are similar, -35.4 dB and -35.8 dB respectively, and both radiation patterns have donut shaped around the X-axis (Figure 6.2). The radiation pattern of the U-shaped antenna embedded fresh water is shown in Figure 6.3. Since the simulated operating frequencies and gains are not drastically different between the two tested media, fresh water was considered as an acceptable characterization

medium and, therefore, it will be use as a first approach phantom, emulating human muscle tissue throughout this experiment.

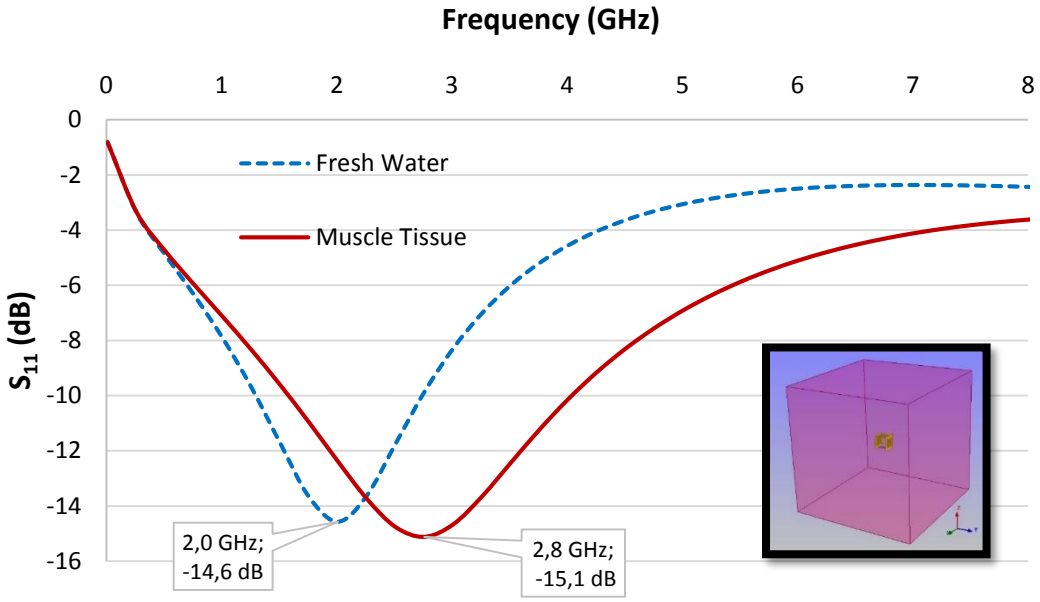

Figure 6.1 Simulated S_{11} of the U-shaped micro antenna embedded in dispersive medium (fresh water and muscle tissue). The inset figure shows a representation of the micro antenna embedded in a 5 x 5 x 5 mm^3 box.

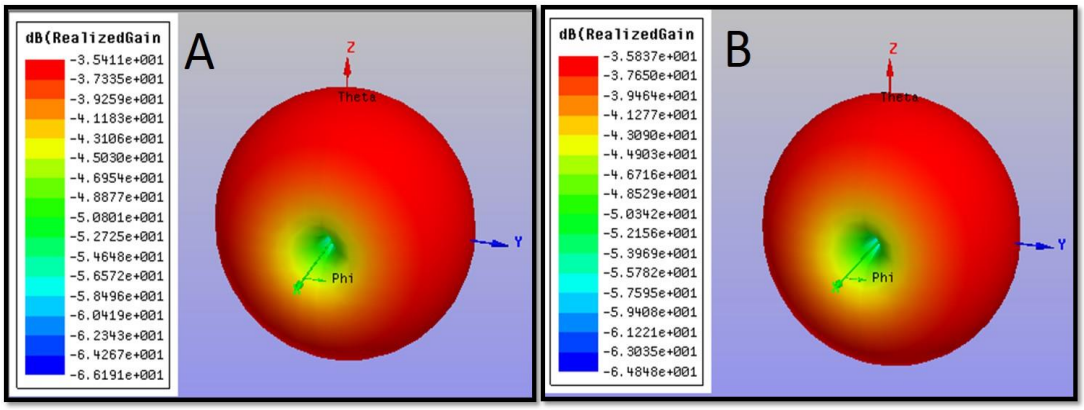

Figure 6.2 Simulated gain of the micro antenna embedded in A) Fresh water. B) Muscle tissue.

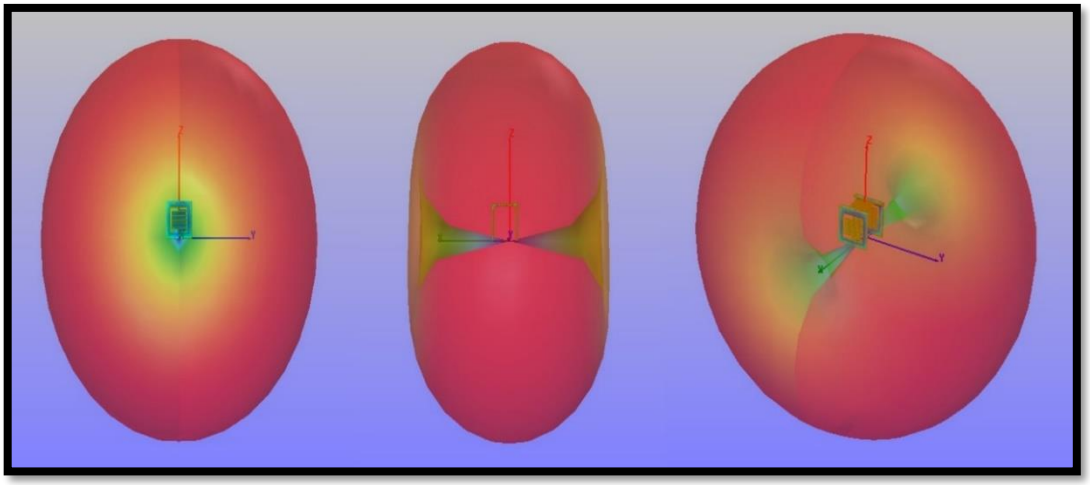

Figure 6.3 Simulated 3D radiation pattern of the U-shaped antenna embedded in water.

6.1.1 SMA Connector

The first attempt to measure the antenna's S-Parameters was accomplished by utilizing an SMA connector to which the micro antenna is soldered to. A regular SMA connector has four ground pins that distance several millimeters from the central feeding one. Thus, in order to solder the micro antenna to it, the SMA connector had to be modified. Three of the four connector's ground pins were removed, while the remaining one was carefully bent towards the central pin, leaving a distance of almost 500 μm between them, and the antenna soldered as shown in Figure 6.5.

Since the micro antenna is intended to operate inside the human body (where tissues are mostly constituted of water), a water droplet was used as a first approach to a muscle tissue phantom, serving a double purpose: the model validation and the study of the ability of the water droplet to terminate the SMA connector by itself, hence allowing the structure to radiate without the presence of the antenna. If the second is verified, it would mean that the structure is not suitable for antenna characterization, as it would be impossible to determine what part of the radiation was due to the antenna, and what part came from the water phantom that surrounds it. In Figure 6.5 the model built for the simulation is presented.

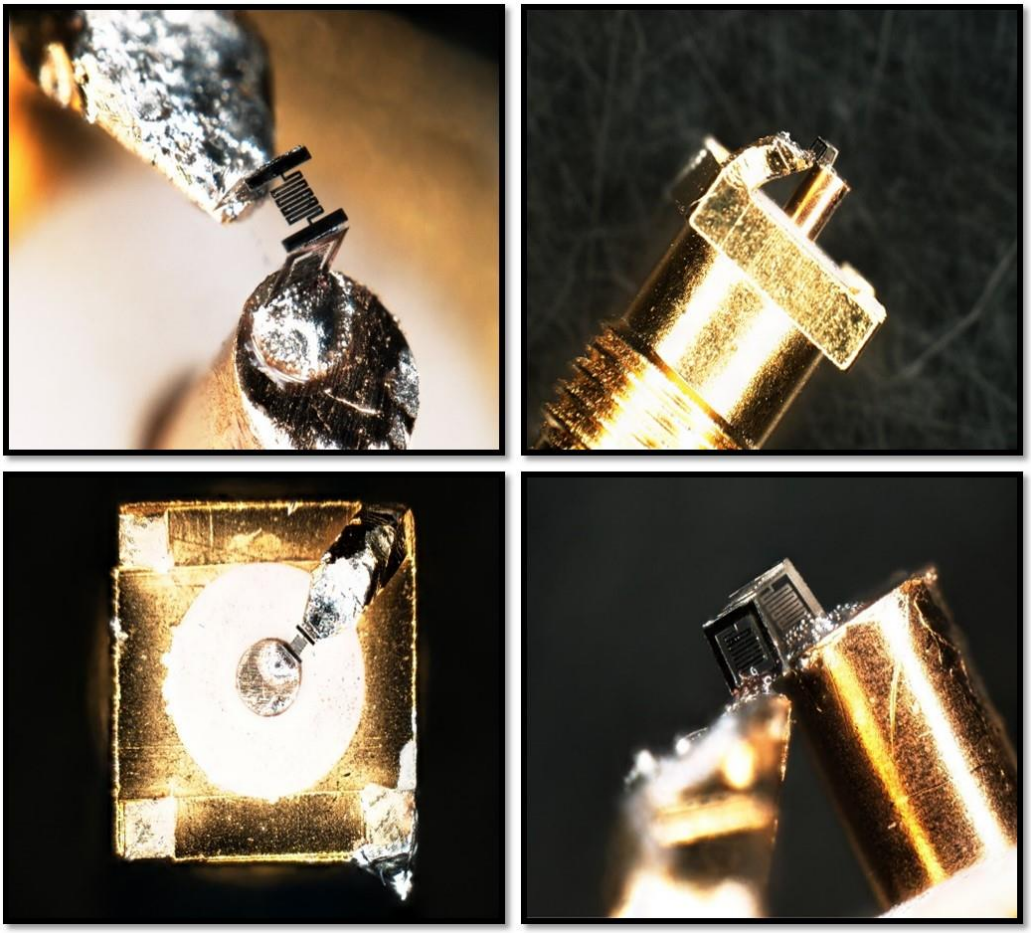

Figure 6.4 Micro antenna soldered to a modified SMA connector.

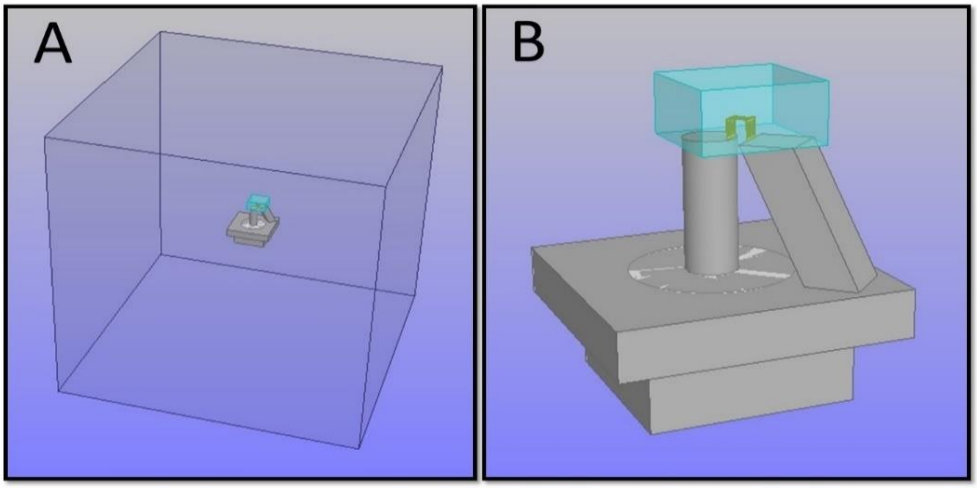

Figure 6.5 A) HFSS model composed of the SMA connector, the micro antenna and a water phantom. B) Close-up view of the SMA connector and micro antenna model.

6.1.1.1 S-Parameters

The S-parameters were initially simulated with HFSS and then experimentally measured. First, control experiments were performed, which consisted of measuring the S_{11} of the SMA connector without the micro antenna, and then with the water phantom placed in between the feeding and ground pins (Figure 6.6). Following the control experiments, the antenna was placed on the SMA connector and the measurements were performed with the antenna surrounded by air and water (Figure 6.7).

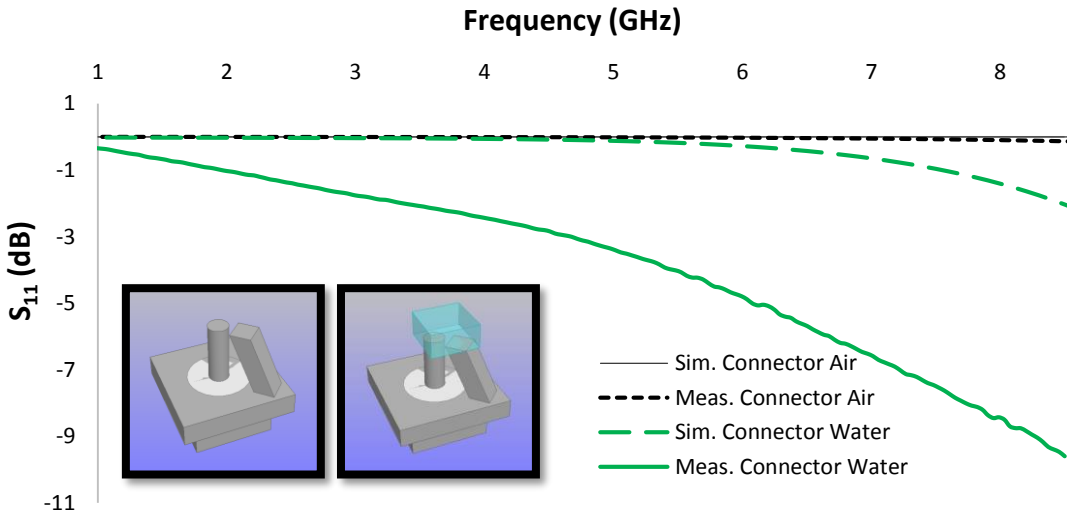

Figure 6.6 Simulated and measured S_{11} of the SMA connector (control experiments).

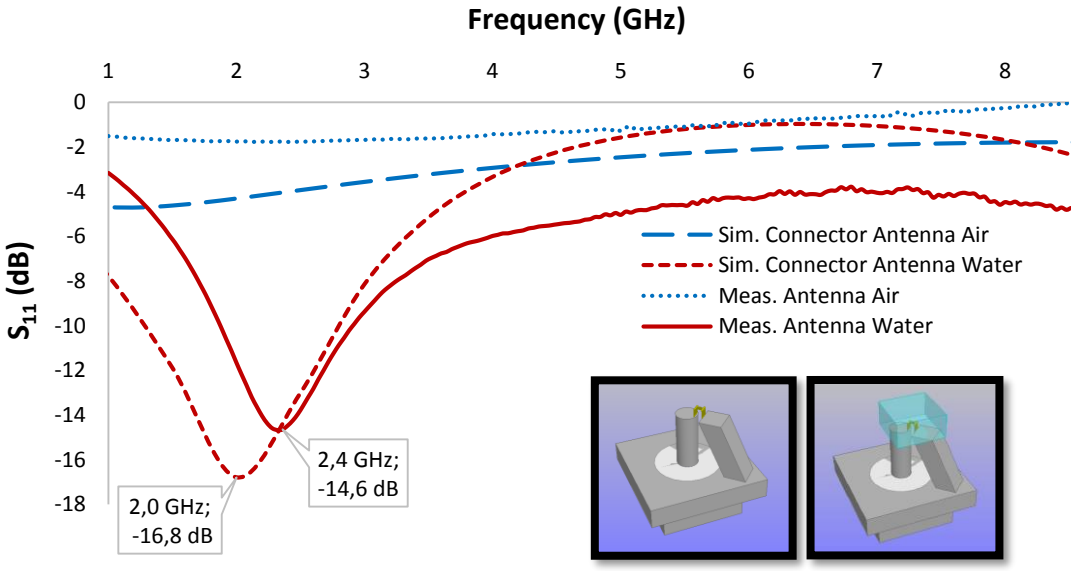

Figure 6.7 Simulated and measured S_{11} of the SMA connector and antenna system, with and without the water phantom.

The simulated and experimental results demonstrate good agreement. As the control experiments reveal, when there is no water phantom on the connector all of the injected power is reflected back, as the S_{11} value remains flat at 0 dB over the analyzed frequency band. Nonetheless, by adding the antenna to the system, it is noticed that some of the injected power is accepted and less power is reflected back. In air, there's no longer a flat S_{11} line around 0 dB, meaning that the system could be accepting power at higher frequencies. When the water phantom is added, the antenna is then able to accept he injected power as seen in the simulated (2.0 GHz, -16.8 dB) and measured (2.4 GHz, -14.7 dB) S_{11} curves. The 400 MHz and a 2.1 dB difference between simulated and measured results is considered acceptable.

6.1.1.2 Antenna Radiation Pattern

In this section we present the simulated antenna 3D radiation patterns and gains. Since simulations suggest that the system composed of the micro antenna on the SMA connector accepts most of the injected power at around 2 GHz, then the results shown in Figure 6.8 and in Table 6.1 were computed for the same frequency.

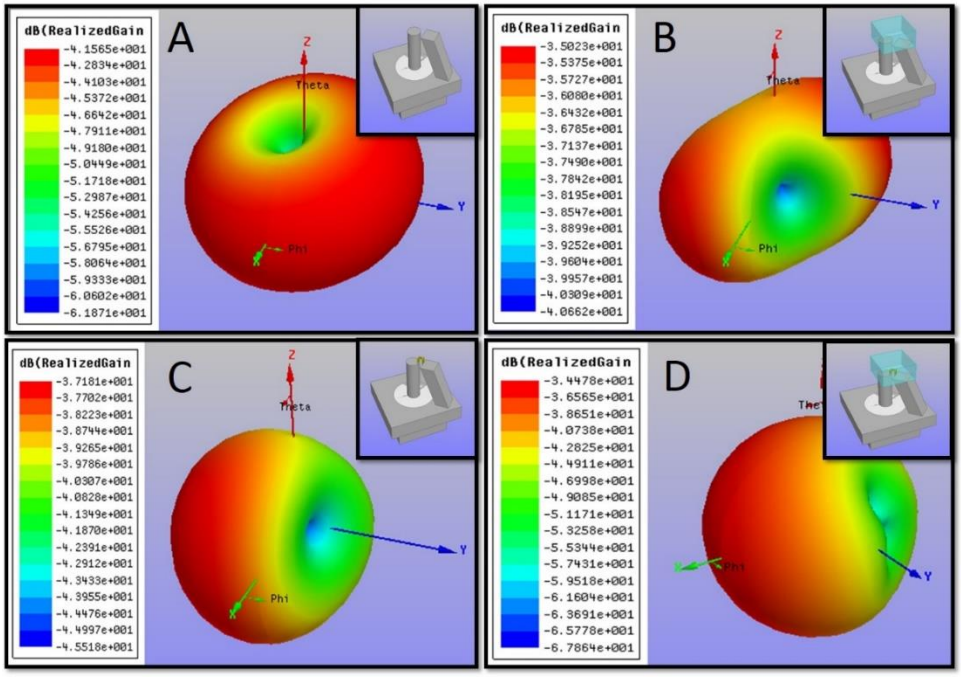

Figure 6.8 Simulated 3D radiation pattern of the SMA connector and micro antenna model. (The inset figures have the same axis orientation as their respective main figures).

Table 6.1 Simulated max. realized gains of the SMA connector and micro antenna system.

Tested Conditions	Max. gain (dB)
A) Connector (on air)	-41.5
B) Connector (on water)	-35
C) Connector + Antenna (on air)	-37.1
D) Connector + Antenna (on water)	-34.4

Analyzing the 3D radiation patterns of Figure 6.8, it can be seen that none of the tested conditions have a donut-shaped pattern around the X-axis (Figure 6.2A). The standalone SMA connector presents a donut-shaped radiation pattern around the Z-axis, while the other iterations (B, C and D) produced 3D patterns that translate the combined effect of the SMA connector, water phantom and antenna, and none of is similar to the 3D radiation pattern of Figure 6.3. Analyzing the maximum gains (Table 6.1), it is noticed that the system composed of the connector, antenna and water phantom, has a gain value (-34.4 dB) similar to the one simulated for the micro antenna embedded in water (-35.4 dB). However, the 3D radiation pattern does not have a donut shape nor does it circle around the X-axis (Figure 6.9), demonstrating that the SMA connector interface might not the most appropriate structure for the radiation pattern measurement.

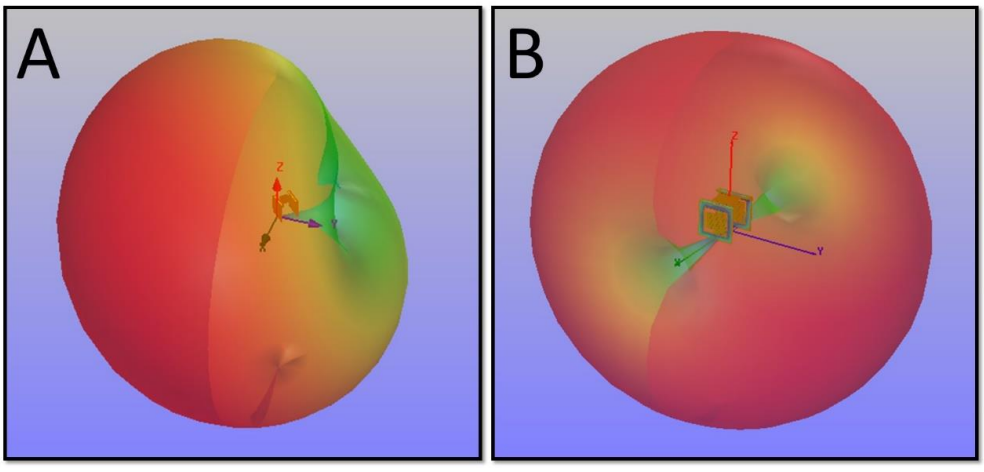

Figure 6.9 Simulated 3D radiation patterns. A) SMA connector, micro antenna and water phantom system. B) Standalone micro antenna embedded in muscle tissue.

It is also worth mentioning that the proposed setup was difficult to use as it was rather difficult to solder the antenna and to control the water volume around it. Therefore a different interface structure is required in order to overcome these difficulties.

6.1.2 Coplanar Waveguide

In order to ease the antenna mounting and to gain some control over the water volume surrounding the antenna, a coplanar waveguide (CPW) interface was used since its flat shape eases the antenna soldering and helps the control over the water droplet phantom. A CPW is a type of electrical transmission line (which can be fabricated using printed circuit board technology) consisting of a thin metallic film strip on the surface of a dielectric substrate and two ground electrodes running parallel to the strip. Unlike other types of electrical transmission lines such as the microstrip line, which has a ground plane located on the opposite side of the dielectric substrate and thus not easily accessible, the CPW has the ground plane right next to the central feeding strip which is very convenient in this case [171]. CPWs can have different types of discontinuities such as open-end, short-end, gap, and step among others as seen in Figure 6.10 [172].

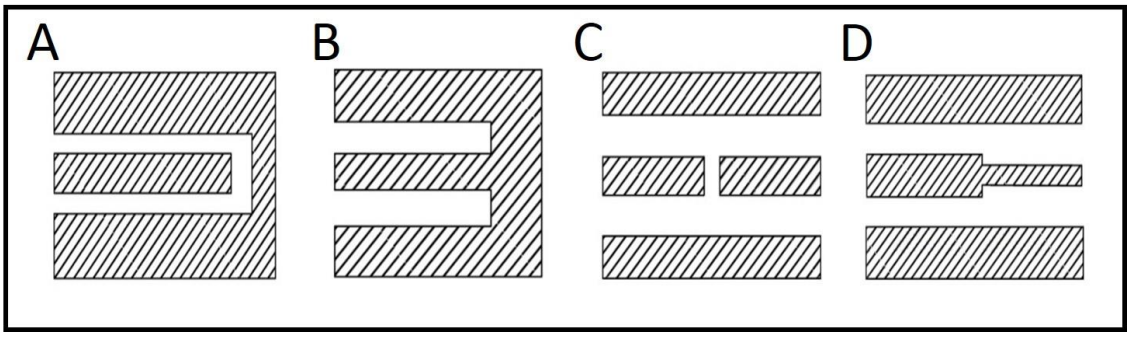

Figure 6.10 Examples of different types of CPW discontinuities [172]. A) Open-end. B) Short-end. C) Gap. D) Step.

The open-end geometry demonstrated to be appropriate for this project since it allows the antenna to be conveniently placed between the CPW's central strip and the ground plane. Moreover, this configuration allows an SMA connector to be easily soldered to the CPW structure (cf. Figure 6.13A). When used for antenna communication, the CPW requires proper dielectric material selection and adequate line dimensions. Also, possible energy losses must be calculated. Radiation losses imply that part of the signal injected in the waveguide is further radiated into space by the

CPW itself and, consequently, not delivered to the load, *i.e.,* antenna in this case. These losses are heavily dependent on the waveguide geometry and usually occur in transmission lines with finite resistivity dielectrics. Since all power is intended to be delivered to the antenna, dielectric and radiation losses in the CPW should be minimized. Therefore, the dielectric material must have high permittivity and small dielectric loss tangent [173]. The selected dielectric material was Rogers R03010, which has a 10.2 dielectric constant and a 0.0023 loss tangent. The CPW parameters (Figure 6.11) were calculated in order to achieve a 50 Ω impedance, accordingly to [174].

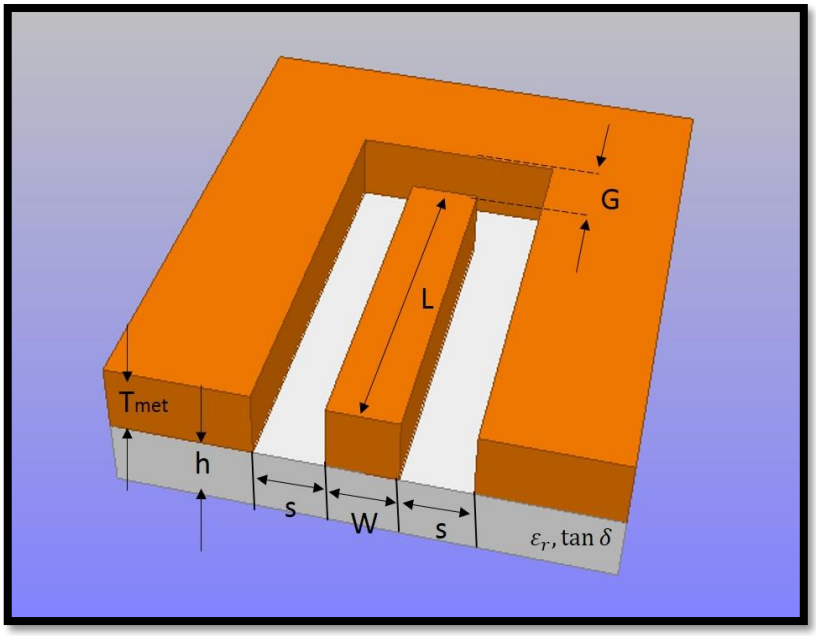

Figure 6.11 Open-end coplanar waveguide schematics and parameters: trace length *L*, metal width *W*, metal spacing *S*, substrate thickness h, gap g, metal thickness T_{met}, substrate dielectric constant ε_r, substrate loss tangent tanδ.

The final dimensions were trimmed by simulation and are presented below. The CPW was composed of a $20 \times 20 \times 1.27\ mm^3$ dielectric layer of the RO3010 laminate with a 17 µm thick copper clad on top. The CPW *h*, *w* and s parameters were 1.27 mm, 1.25 mm and 0.45 mm respectively. Having the CPW properly dimensioned, simulations were performed with HFSS in order to access its performance.

The antenna was placed between the central strip and the ground plane (Figure 6.12). To model interface completely, the system excitation was provided via an

SMA connector model with circular lumped port and a radiation boundary was applied to an air box surrounding all the structures.

Erro! A origem da referência não foi encontrada. The CPW was fabricated using a p hotomask to pattern the metallic profile onto a 17 µm copper clad laminate RO3010 substrate. The exposed copper was etched using ferric chloride to create the feed line and ground plane. The micro antenna was soldered to the CPW using solder paste and an SMA connector was soldered to it (Figure 6.13).

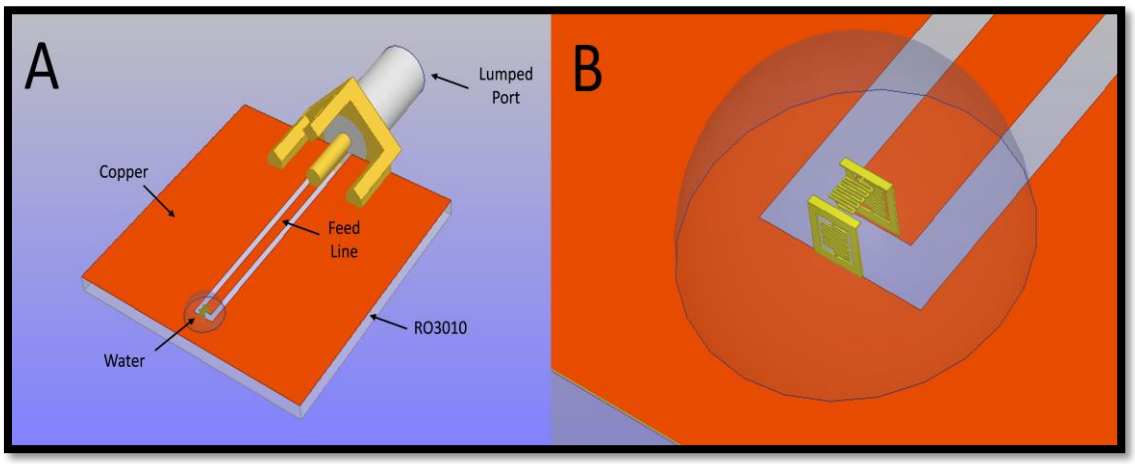

Figure 6.12 A) HFSS model of an open-end coplanar waveguide with an antenna. B) Close up view of the antenna connecting the central strip and the ground plane.

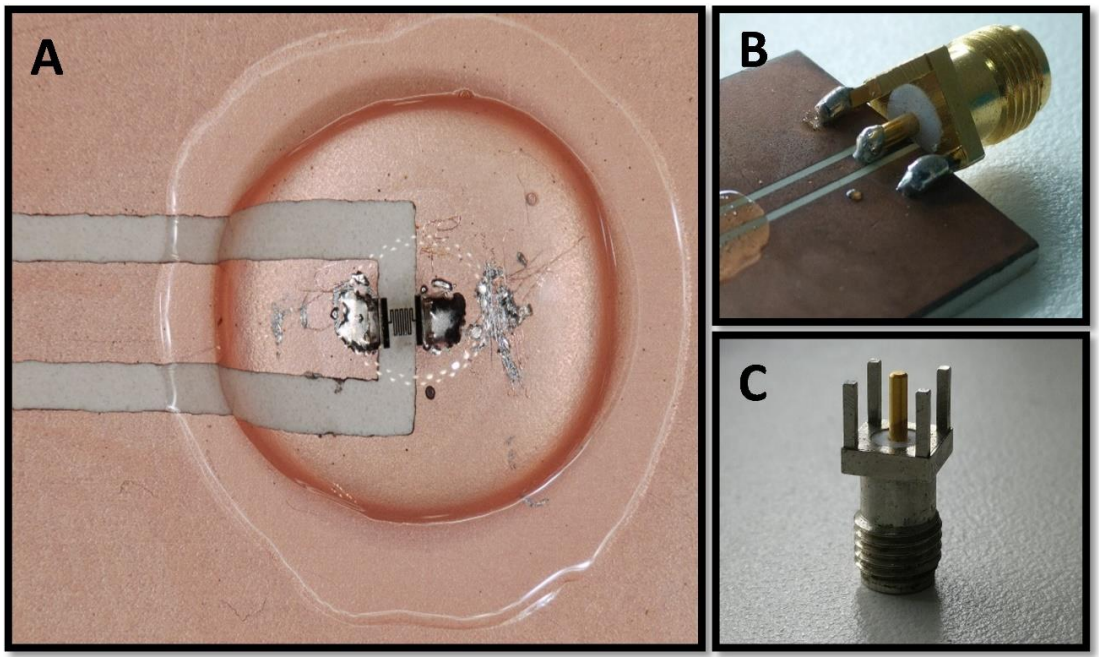

Figure 6.13 Fabricated coplanar waveguide. A) Antenna soldered to the CPW and embedded in droplet of water which is maintained steady within a hydrophobic nail polish barrier. B) SMA connector soldered to the CPW. C) SMA connector used to connect the CPW to the coaxial cable.

6.1.2.1 S-Parameters

After the CPW design and fabrication, simulations and experimental measurements for the standalone CPW in air, and then with a water droplet on the open-end CPW discontinuity. Next, the antenna was added to the system, and measurements were repeated accordingly. Figure 6.14 and Figure 6.15 display the control simulated and measured S_{11} parameters.

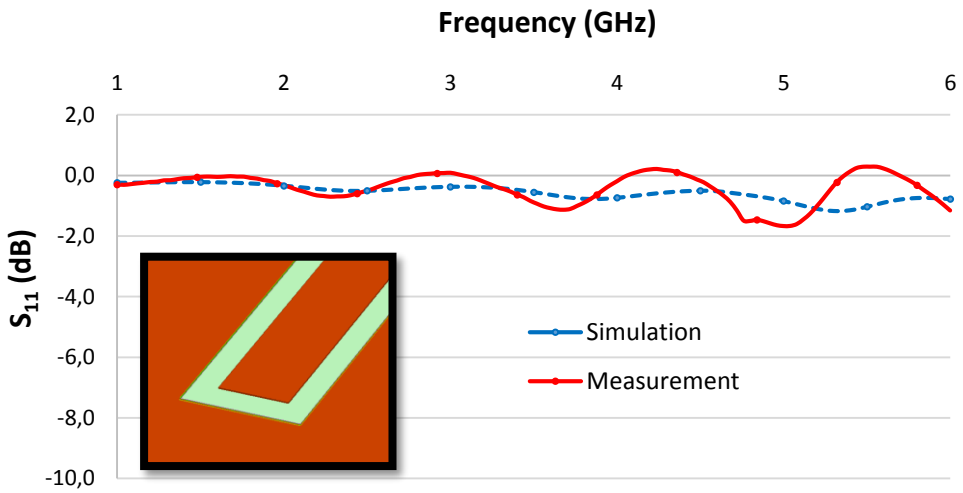

Figure 6.14 Control simulated and measured S_{11} of the fabricated CPW in air.

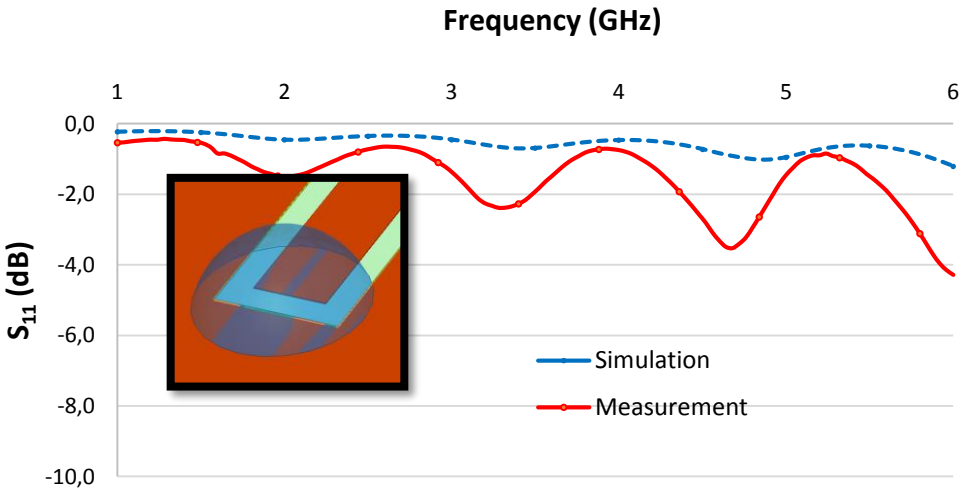

Figure 6.15 Control simulated and measured S_{11} of a CPW with a water droplet on its termination.

The standalone CPW analysis (Figure 6.14) shows a fair correspondence between simulated and measured results, specifically between the S_{11} maximum and minimum values, where the 0.5 dB difference between them, shows that both models were correctly implemented, accurately reproducing the measured results. The S_{11} values indicate that the waveguide is not capable of efficiently delivering energy as is, due to its inexistent line termination, as S_{11} values are close to 0 dB, meaning that most of the injected power is reflected to the source.

It is worth mentioning that some measured S_{11} values are above 0 dB. This is usually seen as impossible in a passive device, since the reflected signal could never be larger than the injected one. However, it has been shown that it may occur for certain load terminations. It has been demonstrated [175] that even though the reflection coefficient may be bigger than 0 dB, the power conservation law is always respected, *i.e.*, the reflected power is never bigger than the injected power.

Then, a water droplet was added onto the termination between signal line and ground plane (Figure 6.15), and again a good agreement between simulated and experimental results was verified, thus confirming the models' validity for the S-parameters. When comparing the results of Figure 6.14 and Figure 6.15, it can be seen that the water phantom induced a slight displacement of the S_{11} peaks. This was expected since a new dielectric material (other than air) was on the CPW termination, thus affecting its operation. Finally, it is verified that the S_{11} parameter never comes close to -10 dB, therefore letting us conclude that a waveguide terminated with a water droplet can't properly guide energy, as most of it is reflected back to the source.

However, by adding the micro antenna to the system, and thus connecting the strip line to the ground plane, the system's response is expected to change. The simulated and measured results are shown in Figure 6.16. Again, the HFSS model seems adequate since there is a good agreement between the simulated and measured results.

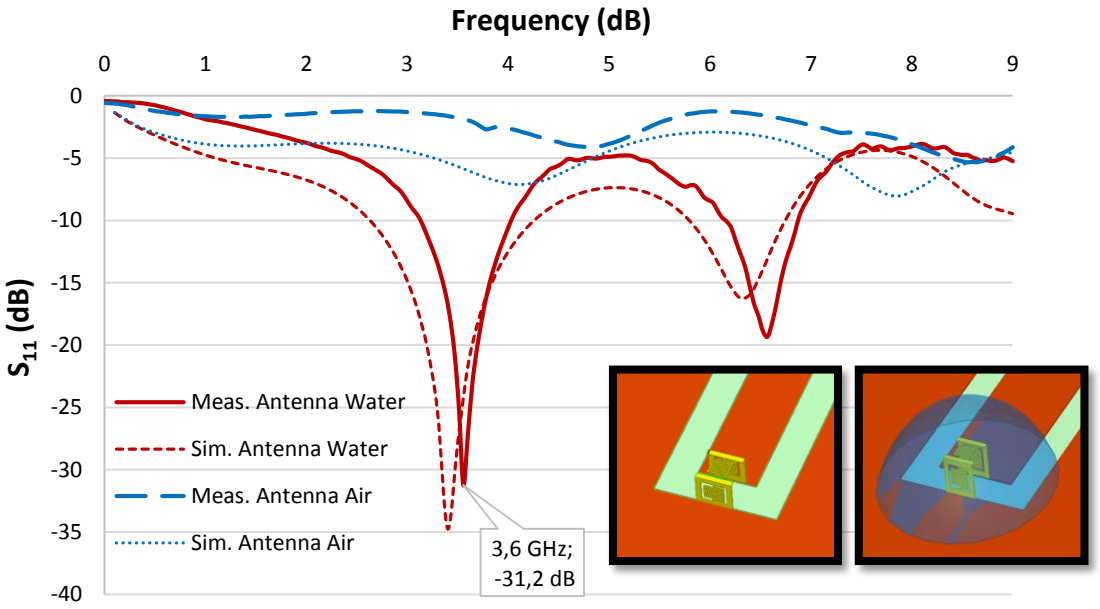

Figure 6.16 Simulated and measured S_{11} of the CPW and antenna system, with and without the water phantom.

For the CPW and antenna system in air, at no point the S_{11} values go below -10 dB, meaning that the antenna does not accept injected signals efficiently. However, that is not the case when water is added to the system as shown by the simulated (3.4 GHz, -34 dB) and measured (3.6 GHz, -31.2 dB) S_{11} values (Figure 6.16). Again, when the line is terminated by the micro antenna and a water droplet, the system is capable of accepting most of the injected power. These results were expected since the antenna was designed to operate in the low gigahertz range (1-10 GHz) when surrounded by dispersive media such as muscle tissue or water, opposite to the range of 50-70 GHz when surrounded by air.

6.1.2.2 Antenna Radiation Pattern

In this section we present and discuss the simulated antenna gain and 3D radiation pattern of the previously tested conditions. As seen previously, simulations suggest the CPW and antenna system accepts most of the injected power at around 3.6 GHz. Therefore, the results shown in Figure 6.17 and in Table 2 were extracted for the same frequency.

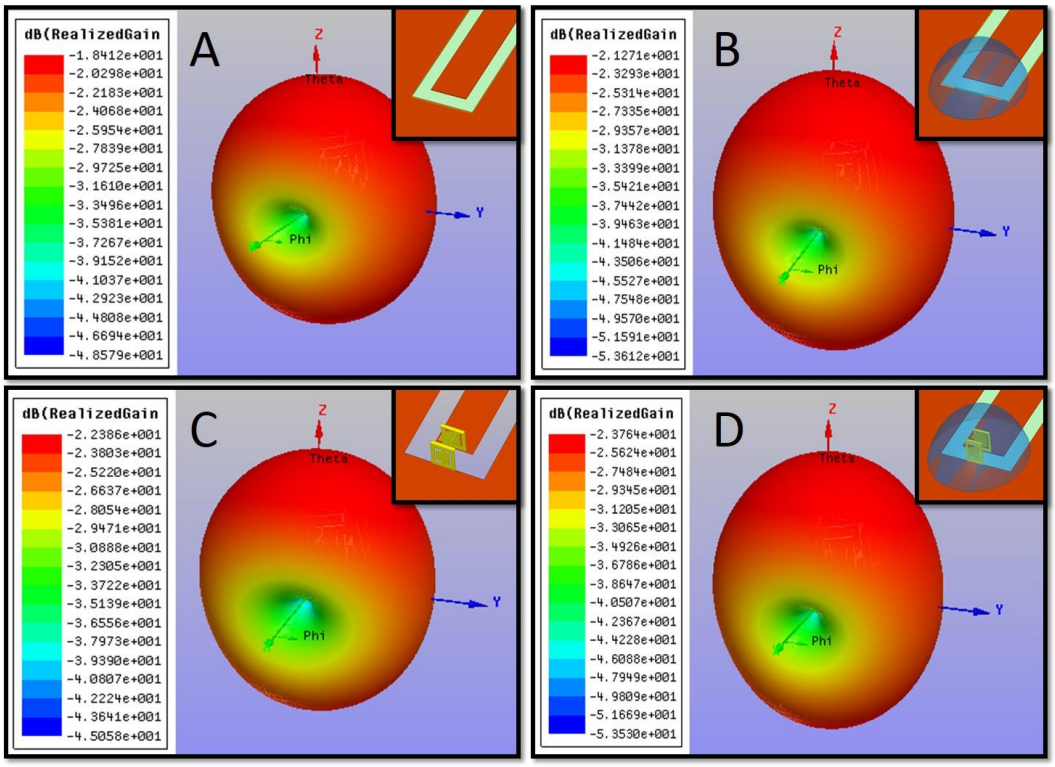

Figure 6.17 Simulated 3D radiation patterns of the CPW and micro antenna models.

Table 6.2 Simulated max. realized gains of the CPW and micro antenna system.

Tested Condition	Max. gain (dB)
A) CPW (on air)	-18.4
B) CPW (on water)	-21.2
C) CPW + Antenna (on air)	-22.4
D) CPW + Antenna (on water)	-23.8

Among the tested conditions, the standalone CPW (condition A) has the highest gain. Due to this, the CPW must be discarded as a viable antenna interfacing structure for the radiation pattern measurement since its higher gain masks the gain of all the other conditions. Simulations show that adding a water droplet to the system does not improve the maximum achievable gain. Instead, when water is added to the standalone CPW or to the CPW with an antenna, the gain decreases. Adding the antenna to the system also decreases the gain. However, all radiation patterns are very similar among each other with a donut-shape radiation pattern.

6.1.3 Modified CPW

The gain analysis showed that a standalone CPW itself has a better gain than the CPW and micro antenna system. In an attempt to solve this problem, a modified CPW (finite ground CPW) was designed with widths comparable to those of the micro antenna to avoid the masking effect seen in the previous CPW design. Hence, they were projected and modeled with HFSS to have an impedance of approximately 50 Ω. In order to do so, a CPW with 50 µm wide lines separated by 30 µm distance, were designed on a 100 µm thick Rogers RO3850HT substrate (ε_r = 3.14). The antenna was placed in between them (Figure 6.18B), and the lines were in turn connected to a three point (signal-ground-signal) 40A-GSG-100-DP CPW probe (Figure 6.18C).

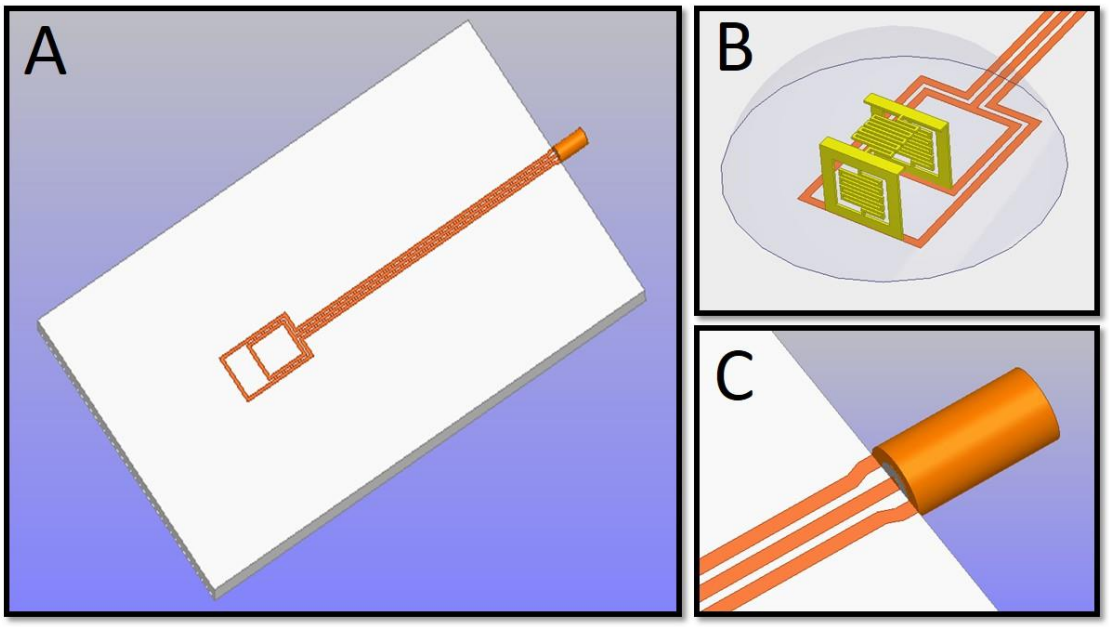

Figure 6.18 A) Modified CPW on a RO3850HT substrate. B) Micro antenna mounted on the termination of the designed 50 Ω modified CPW. C) Modified CPW connected to a probe.

The new CPW was fabricated in the same manner as the previous one, resorting to mask design, photolithography and etching techniques (Figure 6.19). The simulations and measurements were carried in the same way as in the previous steps. These lines can also be used with the fabrication and "on-wafer" antenna self-folding technique proposed in [176], establish a link between the antennas and any circuitry in an implantable wireless microdevice.

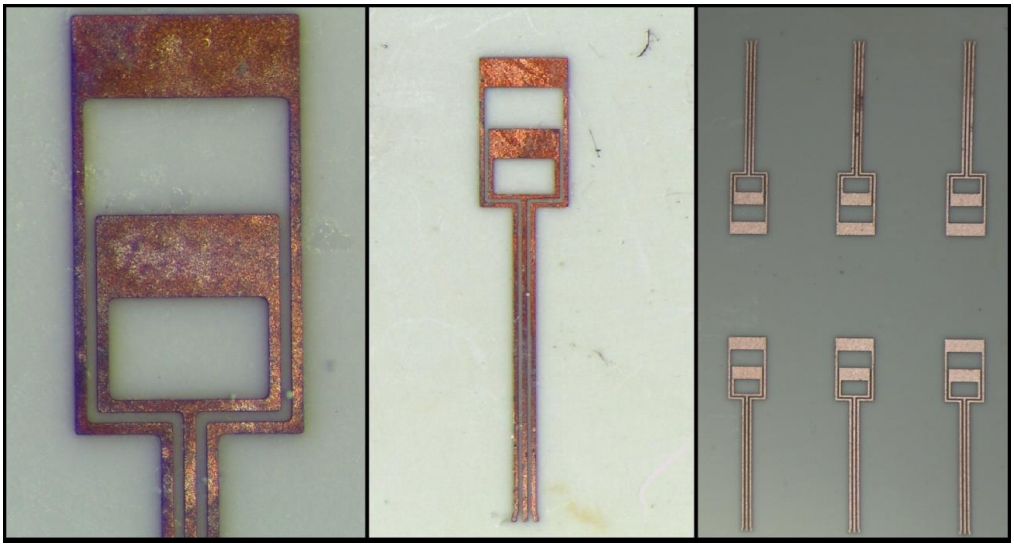

Figure 6.19 Fabricated CPW with 50 µm wide lines.

Figure 6.20 Three point probe connected to the VNA, touching the modified CPW.

6.1.3.1 S-Parameters

Figure 6.21 shows the simulated and measured S_{11} of the modified CPW, with and without the water phantom. Ideally, without the antenna, the S_{11} should be close to zero since the injected power should have no way to be radiated. This would mean that most of the injected power was being reflected back. However, since the S_{11} values are not zero, it means that some of the injected power may be radiated by the CPW itself or lost in the substrate. When the water droplet is added to the system, it acts as a terminating load, as shown by the S_{11} e.g. -19 db at 7 GHz. The simulated and measured results do not really agree on this point. Looking at the simulation results, it is possible to identify a small dip around 6.5 - 7 GHz but clearly not as intense as displayed in the measurements.

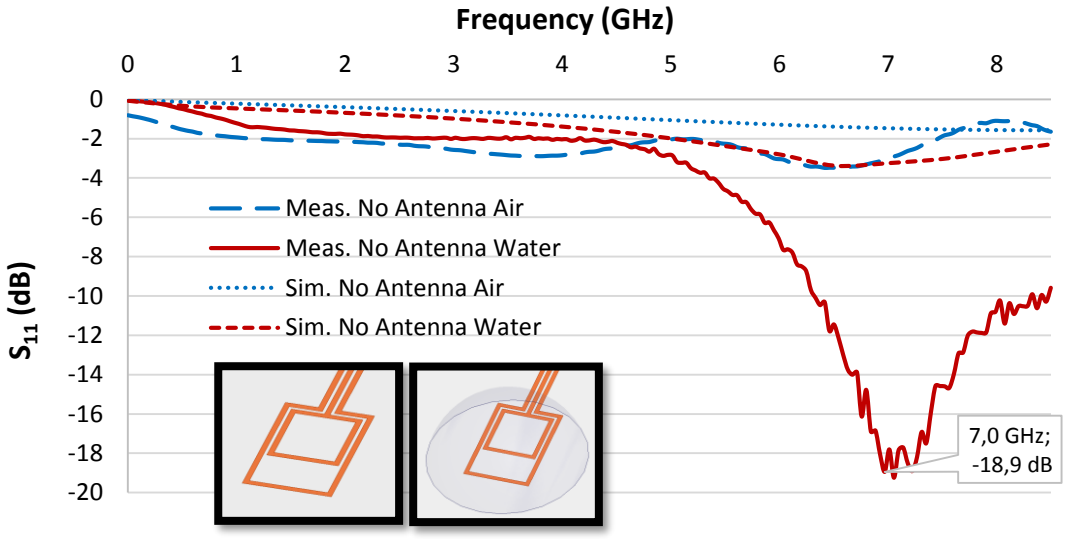

Figure 6.21 Simulated and measured S_{11} of the modified CPW with and without the water phantom.

The results of the modified CPW and micro antenna system are presented in Figure 6.22. In air, the system performs in the same way as for the SMA connector and previous CPW examples, with the high S_{11} values indicating that most of the injected power is being reflected back to the source. On the other hand, when the water is added to the system, the micro antenna accepts most of the power and radiates at 1.7 GHz with S_{11} of -14 dB (Figure 6.22). However, the S_{11} measurements show that the modified CPW geometry does have some relevant influence over the system's

operating frequency, decreasing it even further, beyond 2 GHz in this case as we can see in Figure 6.22.

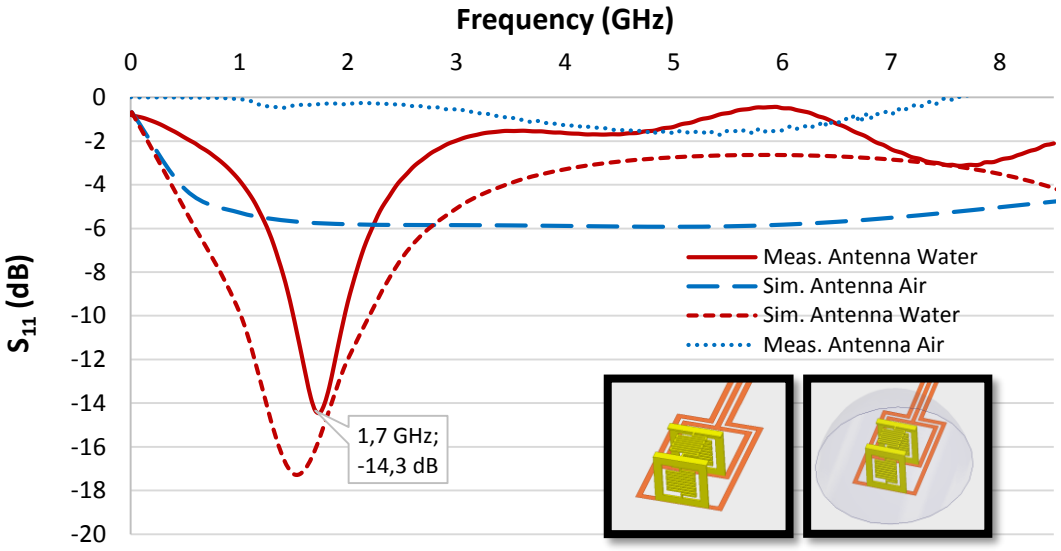

Figure 6.22 Simulated and measured S_{11} of the modified CPW and the antenna system, with and without the water phantom.

6.1.3.2 Antenna Radiation Pattern

As the simulations suggest the modified CPW and antenna system accepts most of the injected power at around 1.7 GHz, therefore the simulated radiation patterns (Figure 6.23) and maximum gains (Table 6.3) were extracted for the same frequency.

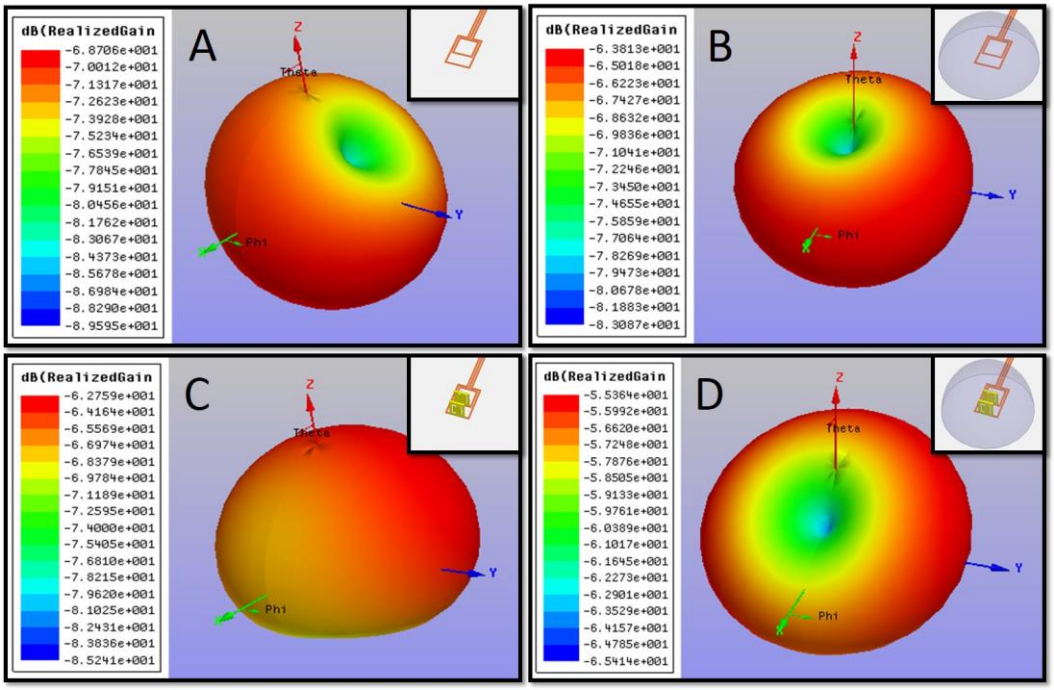

Figure 6.23 Simulated 3D radiation patterns of the modified CPW and micro antenna system.

Table 6.3 Simulated max. realized gains of the modified CPW and micro antenna system.

Tested Condition	Max. Gain (dB)
A) Mod. CPW (on air)	-68.7
B) Mod. CPW (on water)	-63.8
C Mod. CPW + Antenna (on air)	-62.7
D) Mod. CPW + Antenna (on water)	-55.3

As presented in Table 6.3 the highest gain was verified for the modified CPW and micro antenna embedded in water system, while the lowest gain for the standalone modified CPW case. This case, and in opposition to the first CPW design, the gains are very low and the 3D radiation patterns significantly differ from the one of Figure 6.3. Therefore, these structures were also dismissed as an alternative for the radiation pattern measurement.

Throughout this experiment, the length of CPW lines was questioned. Suspicions came from the fact that the S_{11} did drop below 2 GHz and by the presence of a S_{11} deep at 7 GHz when water terminates the CPW line (Figure 6.21). It was thought that due to the length of the CPW lines, they could interfere with the antenna and maybe justify the S_{11} peak at 1.7 GHz. Thus, the CPW line length was shortened, by simply cutting the

pre-existing copper lines and bringing the RF probe closer to the structure as seen Figure 6.24. The measurement results are shown in Figure 6.25

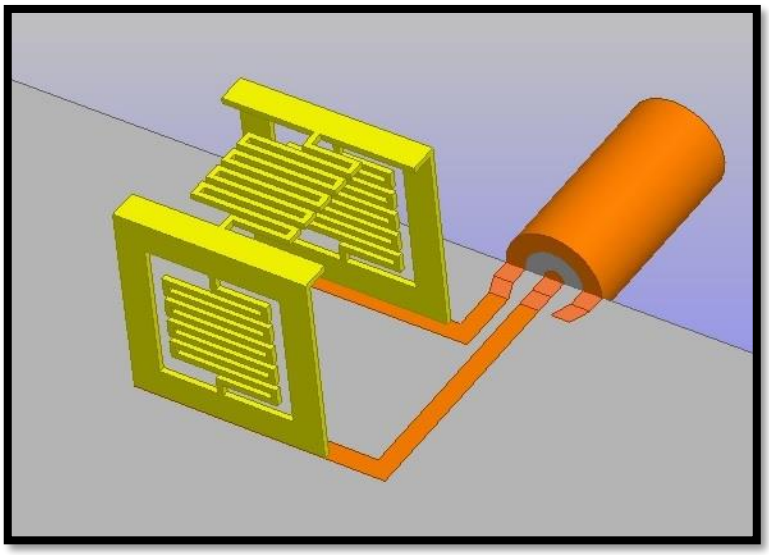

Figure 6.24 HFSS model of the shortened CPW.

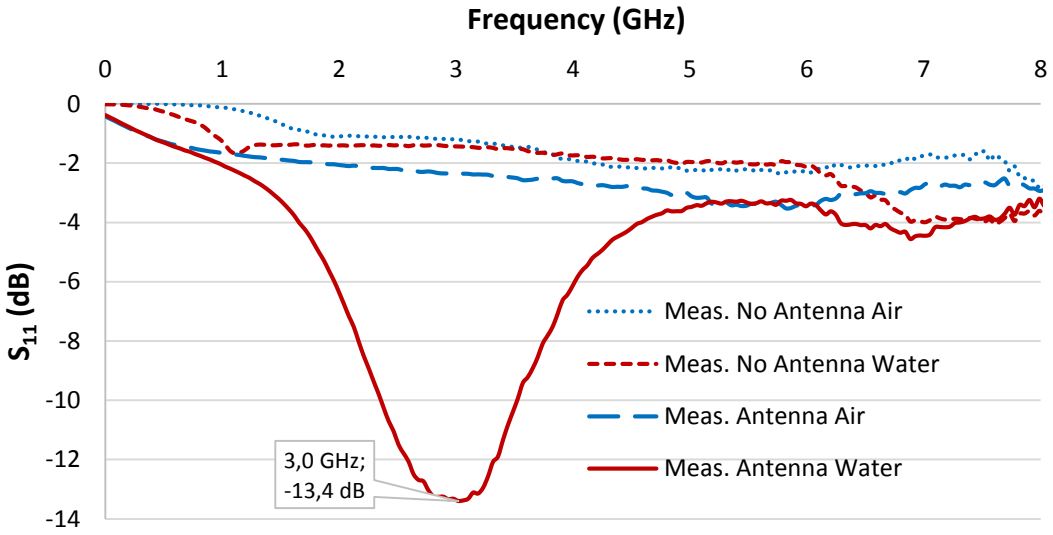

Figure 6.25 Measured and simulated S_{11} of the shortened CPW.

The measurements of the shortened version of the modified CPW, showed a 1.3 GHz shift from the previously seen S_{11} peak at 1.7 GHz, to 3 GHz. This suggests that the copper lines were performing radiating structures, thus influencing the S-parameter measurements. Also, the S_{11} peak previously seen at 7 GHz (Figure 6.21), and caused by the water droplet on the antenna termination is gone. This resonance phenomenon is

caused by the CPW length of 1 cm, and at 7 GHz, λ/4 = 1 cm, thus explaining the S_{11} peak.

Throughout this experience were encountered some challenges that made difficult the correct measurement of the S-parameters. Using the RF probe proved to be quite challenging, as the probe terminations often touch the water phantom surrounding the micro antenna, thus affecting the measurements. Another major and constant challenge was to solder the micro antenna to the thin metallic lines, which, proved to be an incredibly extenuating task.

Up until this point, all the tested antenna carrier structures revealed some important fragilities. First, all of them demonstrated to be hard to use, mostly due to the micro antenna fixation issues. Secondly, the interfaces interfere with the antenna S-parameters, and lastly, none of the gain analysis studies provided confident results in order to proceed to the experimental radiation pattern measurement. Yet, and keeping in mind the challenges found in all tested interface structures, another attempt was made and in the next section we will discuss the use of a different type of connector and transmission line.

6.1.4 End Launch Connector and Transmission Line

An end launch connector (from Southwest Microwave, Inc.) can be used with single or multi-layer printed circuit boards (Figure 6.26). This type of connector was chosen due to its low return loss (S_{11}), low insertion loss (S_{21}), throughout a wide frequency range as well as low leakage current. Since it does not allow the direct interconnection with the antenna structure, we must use a transmission line where the micro antenna is soldered to. Here the transmission line's central strip joins to the connector's feeding pin and the ground connections are made by direct contact between the connector and the transmission line's top and bottom ground planes. HFSS models of the end launch connector and a transmission line were developed (Figure 6.27).

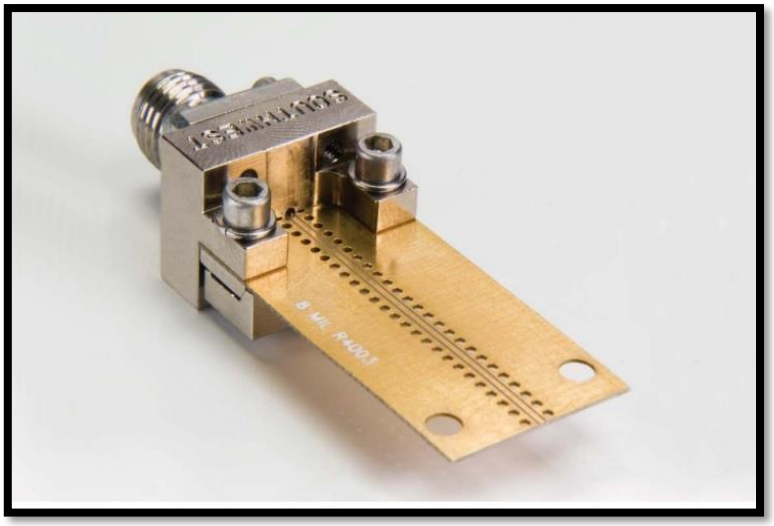

Figure 6.26 Southwest microwave End launch connector.

A new transmission line geometry with an open-end termination, with a 3.9 mm long and 125 µm wide central feeding line was developed to fit on the end launch connector. At the end of the line, a 600 x 300 μm^2 pad was created to facilitate the antenna soldering. The distance between the soldering pad and the ground plane ahead is of 400 µm so that the antenna can be properly soldered in between. The ground plane has a U-shaped geometry in order to precisely fit the connector. The dielectric used was a 100 µm thick 6.7 x 4.9 mm^2 Rogers 3850HT, with and 9 µm copper clad, and $\varepsilon_r = 3.14$.

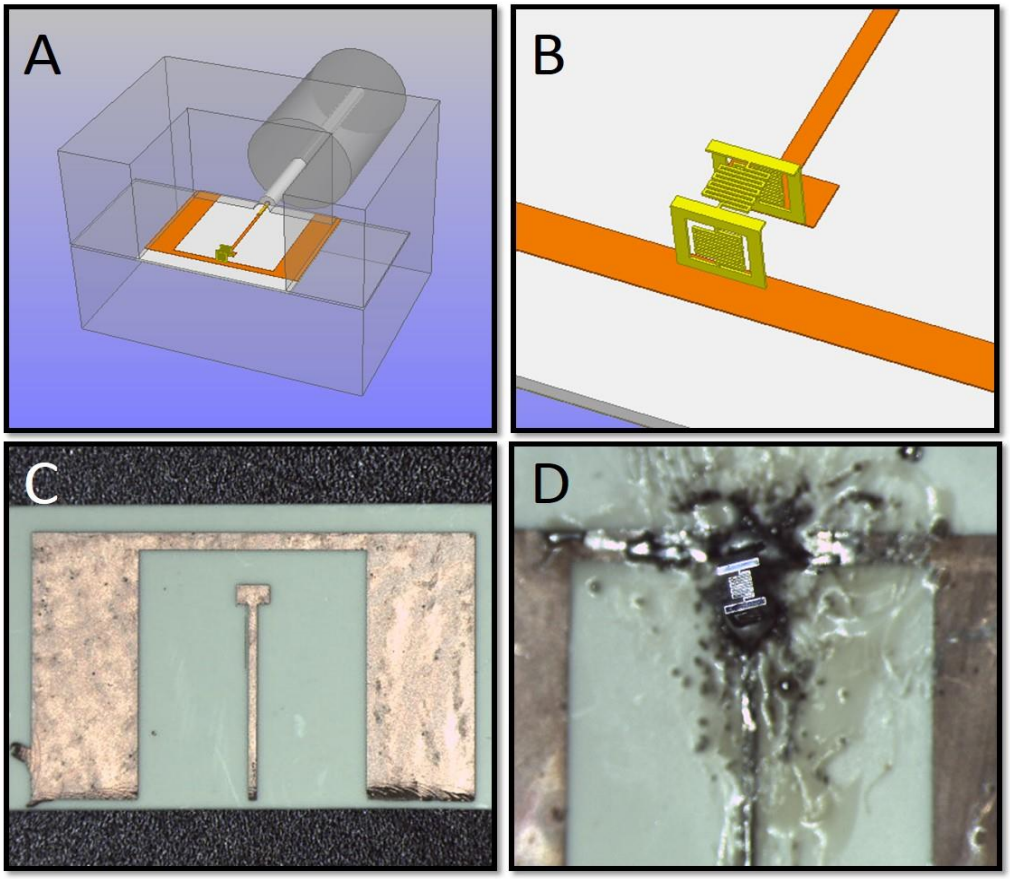

Figure 6.27 End launch connector and transmission line system. A) HFSS model of the system composed of the end launch connector, the transmission line and micro antenna. B) Close-up view of the HFSS micro antenna model on the transmission line. C) Fabricated transmission line. D) Antenna soldered to the transmission line.

6.1.4.1 S-Parameters

Here, as in the previous iterations, control experiments were done to study the new connector and transmission line system. Like in previous cases, the water droplet on the CPW (without the antenna) causes an S_{11} peak at higher frequencies. However, non-overlapping measured and simulated S_{11} deeps are observed. When placed on top of the dielectric, the water's molecular adhesion and cohesion forces seem to weaken, most likely due to the substrate's roughness, and the drop slightly spreads over the substrate. This makes difficult to control the volume of the water phantom, and that is especially true in the case of the Rogers substrate when copper clad was etched. Such may explain the observed 2 GHz difference between the simulation and measurements (Figure 6.28).

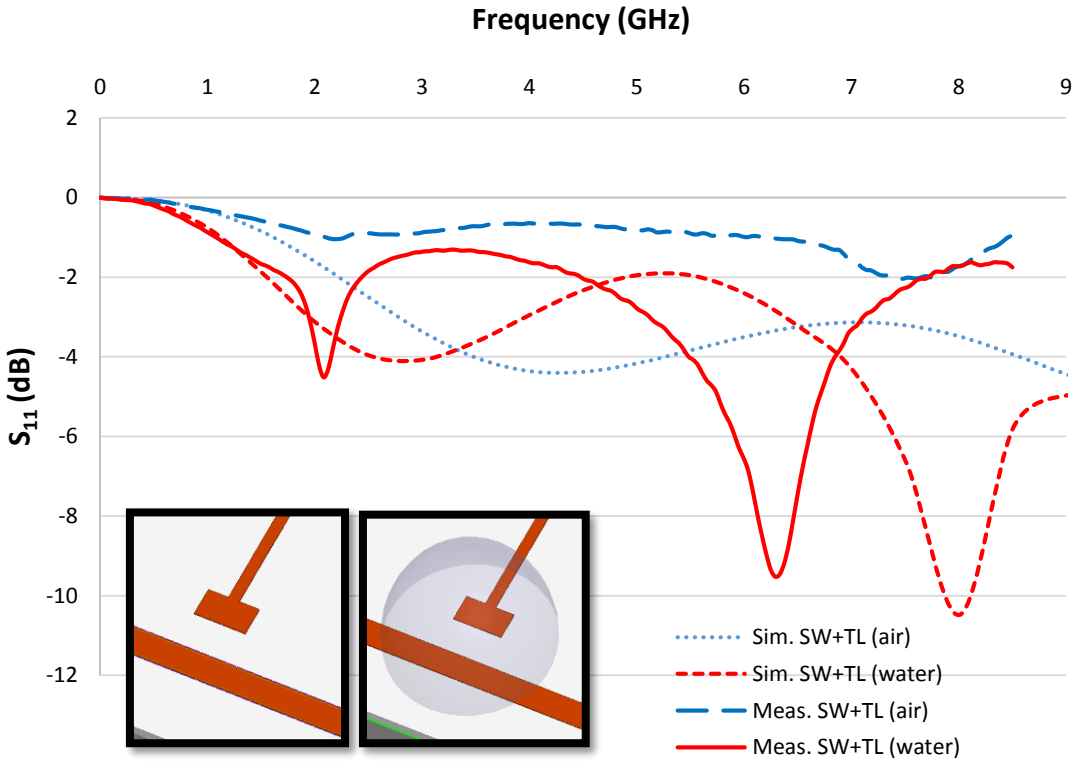

Figure 6.28 Simulated and measured S_{11} of the connector and transmission line system, with and without water. (SW – Southwest end launch connector, TL – Transmission line).

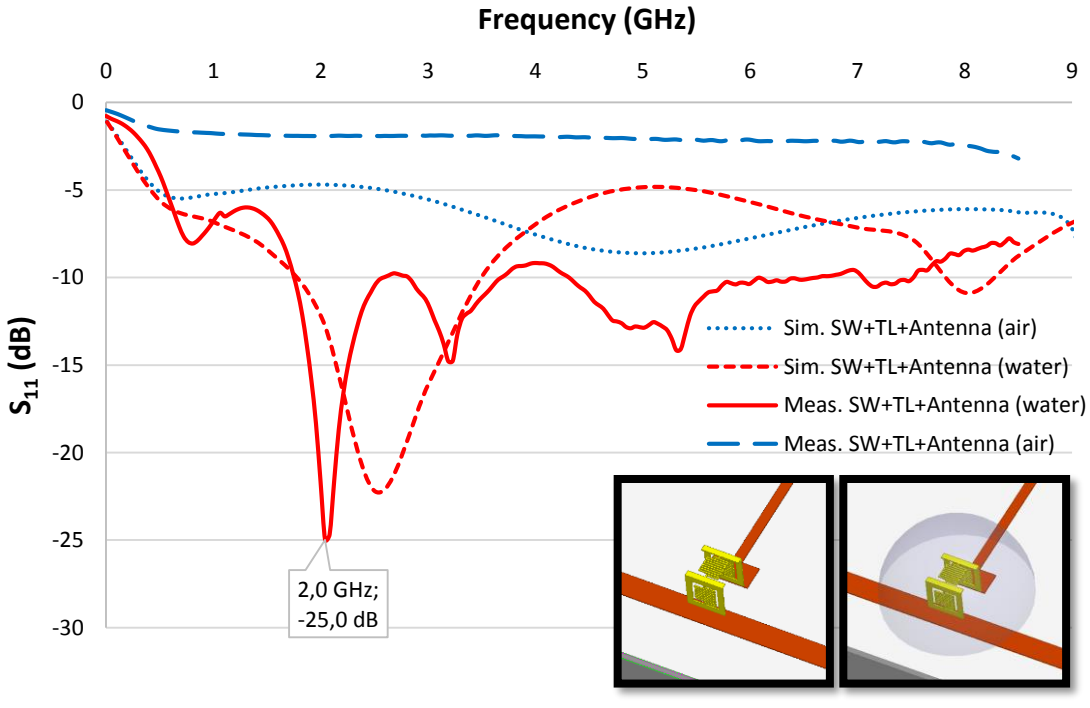

Figure 6.29 Simulated and measured S_{11} of the connector and transmission line system with the micro antenna, with and without water. (SW – Southwest end launch connector, TL – Transmission line).

Adding the micro antenna to the system (Figure 6.29), the results are similar to those of the previously analyzed cases. The dielectric loading effect caused by the water droplet sets the antenna operating frequency at 2 GHz with an S_{11} of -25 dB. Again, when the water is absent, the antenna is expected to operate in the high gigahertz range. The S-parameter measurement results revealed to be very similar to those observed in the case of the SMA connector, the CPW and the transmission lines and probe system. In the next section, we will study the validity of this setup for the radiation pattern measurements.

6.1.4.2 Antenna Radiation Pattern

First, the gain of the end launch connector was determined as a control measure. From Figure 6.30 it can be seen a donut shape radiation pattern, caused by the relatively long monopole-like feeding line structure, starting at the very beginning of the connector and ending at the feeding pin. Simulation results show a very low gain of -71 dB. Compared to the previously used mounting structures, the end launch connector has a much lower gain, which is extremelly important to determine the antenna gain without any masking effects.

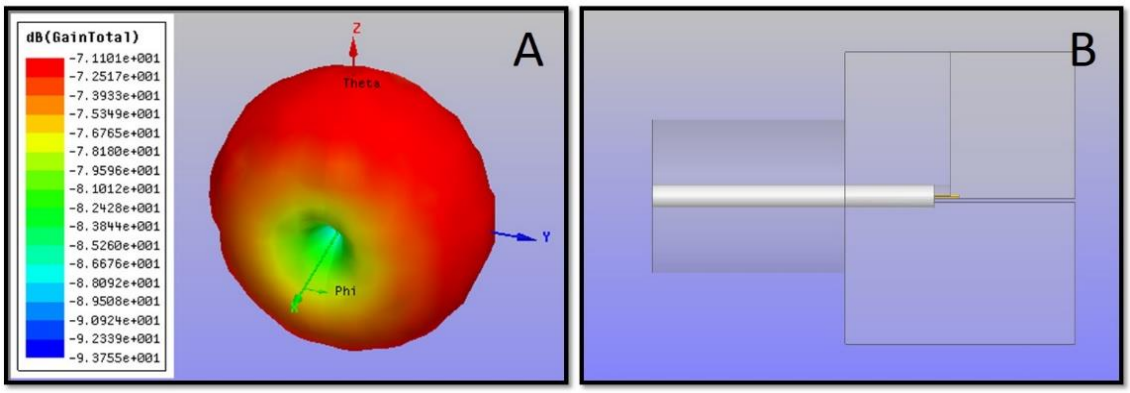

Figure 6.30 A) End launch connector radiation pattern. B) Connector's side view (XZ plane) showing the feeding pin.

Since the system accepts most of the injected power at 2 GHz, the simulated gains were extracted at that frequency. The 3D radiation patterns are shown in Figure 6.31 and the maximum gains in Table 6.4.

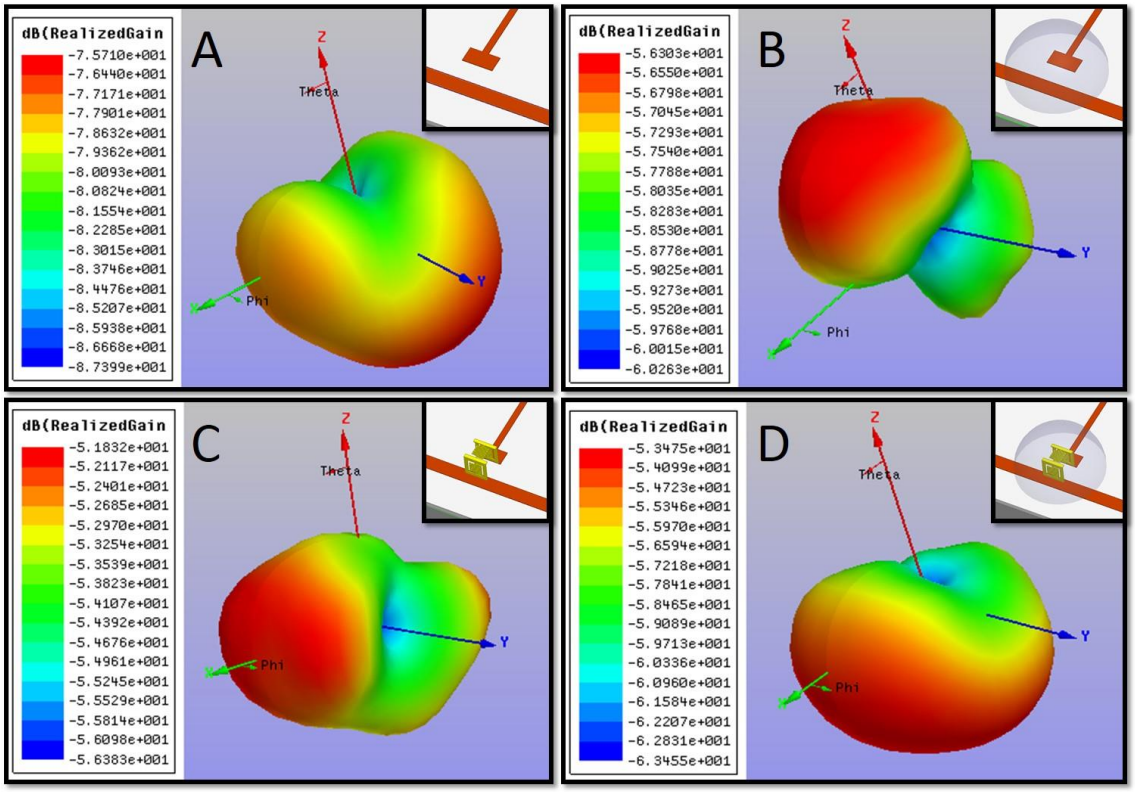

Figure 6.31 Simulated 3D radiation patterns of the end launch connector, transmission line and micro antenna system.

Table 6.4 Simulated max. realized gains of the end launch connector, transmission line and micro antenna system. (SW – Southwest end launch connector, TL – Transmission line)

Tested Condition	Max. Gain (dB)
A) SW Standalone	-71
B) SW + TL (on air)	-75.7
C) SW + TL (on water)	-56.3
D) SW + TL + Antenna (on air)	-51.8
E) SW + TL + Antenna (on water)	-53.4

The results given by the simulated radiation patterns and gain analysis indicate that the proposed setup is not suitable for the antenna radiation pattern measurement. A viable solution must guarantee that the connector and transmission line system (without antenna nor water phantom) does not have a higher gain than the system composed of the connector, transmission line, antenna, and water phantom, and that

does not happen in this case. As seen in Table 6.4, the minimum gain of -75.7 dB is observed for the end launch connector and transmission line system (condition B). This means the gain is further decreased when the transmission line is attached to the connector. Also, the gain of condition E is lower than condition D, when the opposite was expected. Moreover, as elements are added, the shape of the simulated radiation patterns vary significantly for each iteration, with none of them providing the expected donut shape pattern. The 3D radiation patterns of Figure 6.31 also suggest that the transmission line length might not be adequate. As the micro antenna stands on, and is surrounded by the connector structure, a "boxing effect" may be disturbing the expected donut-shaped radiation pattern.

Hence a new transmission line configuration much be found, one assuring that condition E of Table 6.4 has the highest gain. Also, a new design must avoid the boxing effect cause by proximity between the antenna and the connector, and that can be easily achieved by increasing the transmission line's length.

6.1.5 End Launch Connector and Buried Transmission Line

After many iterations, a new transmission line configuration was achieved. The main aspects of this optimization were the optimization of the line's length, the *s* and *w* parameters, and the use of an extra dielectric layer on top of the existing one. The line length was increased to 40 mm, keeping the antenna structure away from the connector, avoiding the boxing effect. The *s* and *w* parameters were recalculated accordingly to the line's length, and were both set to 100 µm. To solve this issue, several designs were tested and it was concluded that an extra dielectric layer had to be added on top of the existing substrate to prevent the line from radiating. The new transmission line scheme, with the metallization layer embedded between two dielectric layers with a top and bottom ground, is shown in Figure 6.32 and Figure 6.33.

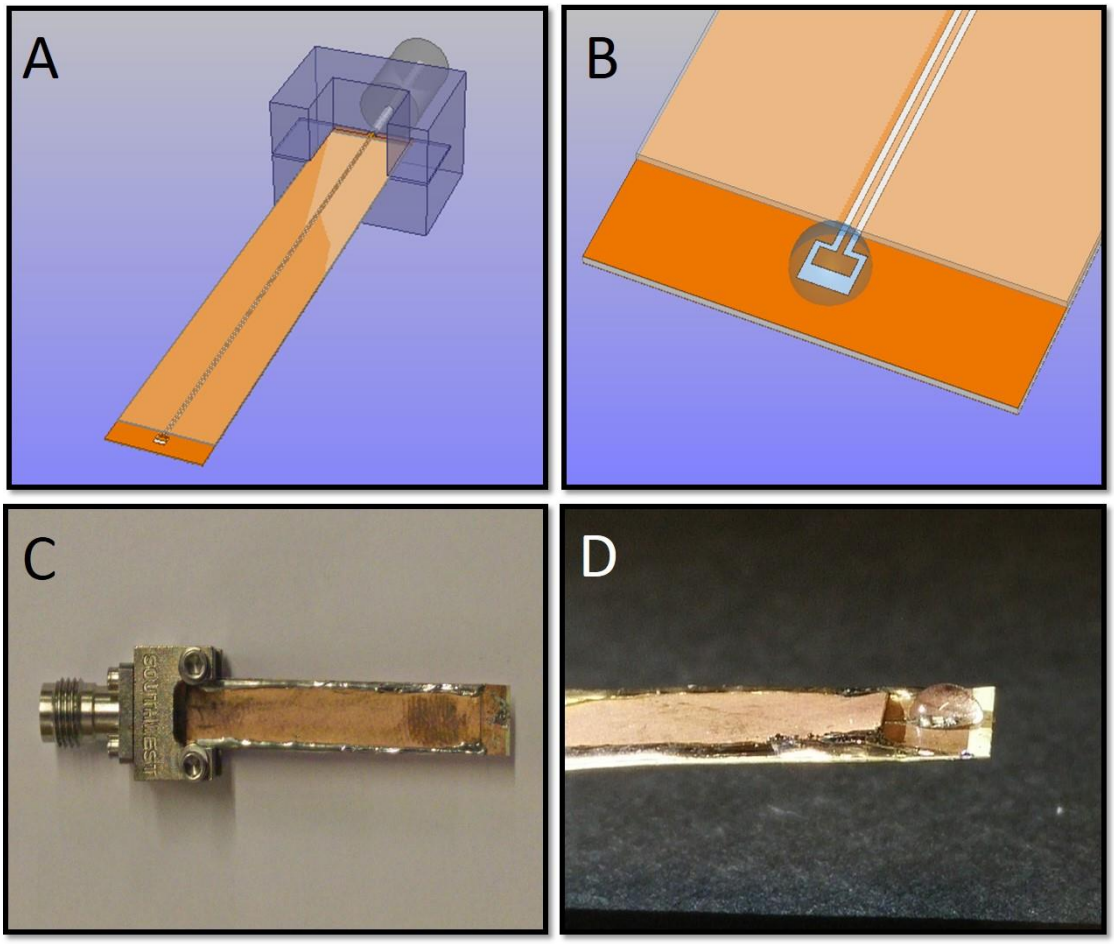

Figure 6.32 Buried transmission line geometry on the end launch connector. A) HFSS model of the end launch connector and the buried transmission line. B) Close-up view of the transmission line. C) Fabricated transmission line attached to the end launch connector. D) Close-up view of the water droplet on the buried transmission line.

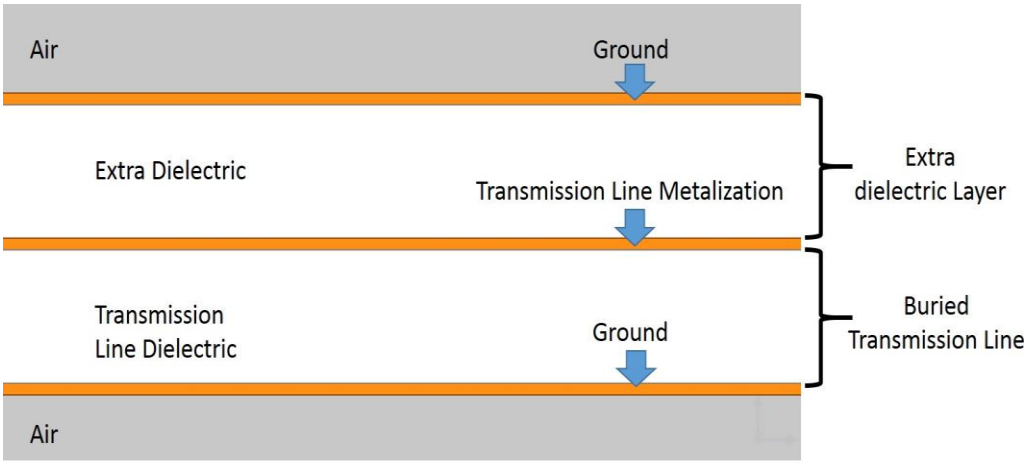

Figure 6.33 Profile view of buried transmission line.

To verify the effect of the extra dielectric layer, the gains of two transmission lines, one covered (buried) with the top dielectric and one uncovered, were measured. The transmission lines were placed directly below a transmitting antenna, and their gains were recorded between 0-8 GHz. As it can be seen in Figure 6.34, the covered transmission line has a lower gain between 2 - 4 GHz, and between 5 - 6 GHz, when compared with the uncovered one. This detail is important as, this way, the covered transmission line will have lower gain than then antenna at 2 GHz, and theoretically will not interfere with the antenna radiation pattern measurement.

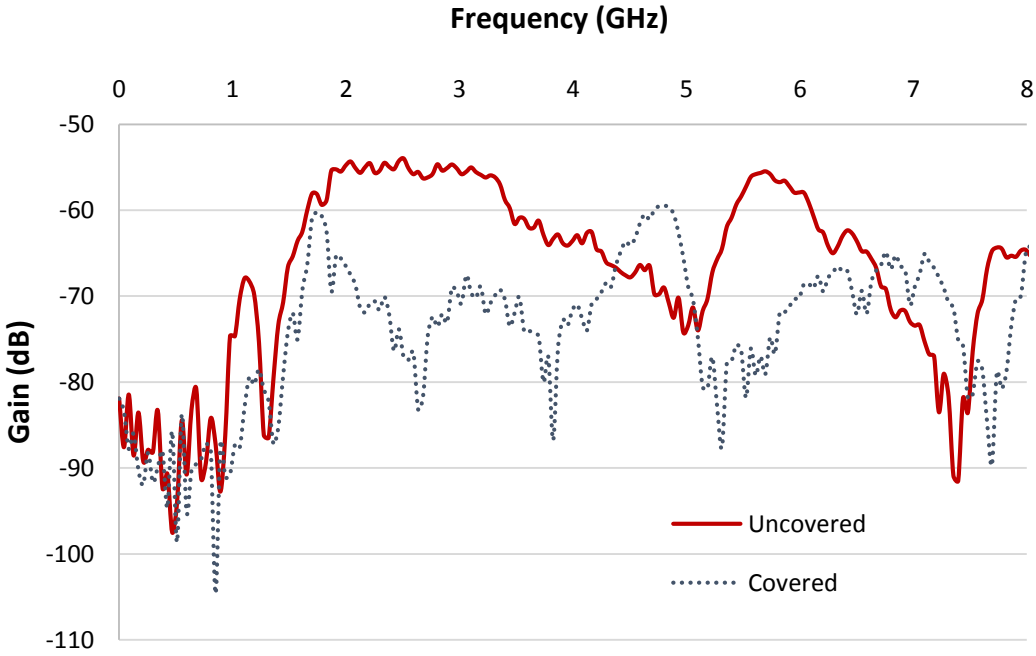

Figure 6.34 Measured gain of the uncovered and covered transmission lines.

6.1.5.1 S-Parameters

Control simulations and measurements were performed in order to study the connector and transmission line system, with and without the antenna and dispersive media. The S-parameters of the system without antenna are presented in Figure 6.35.

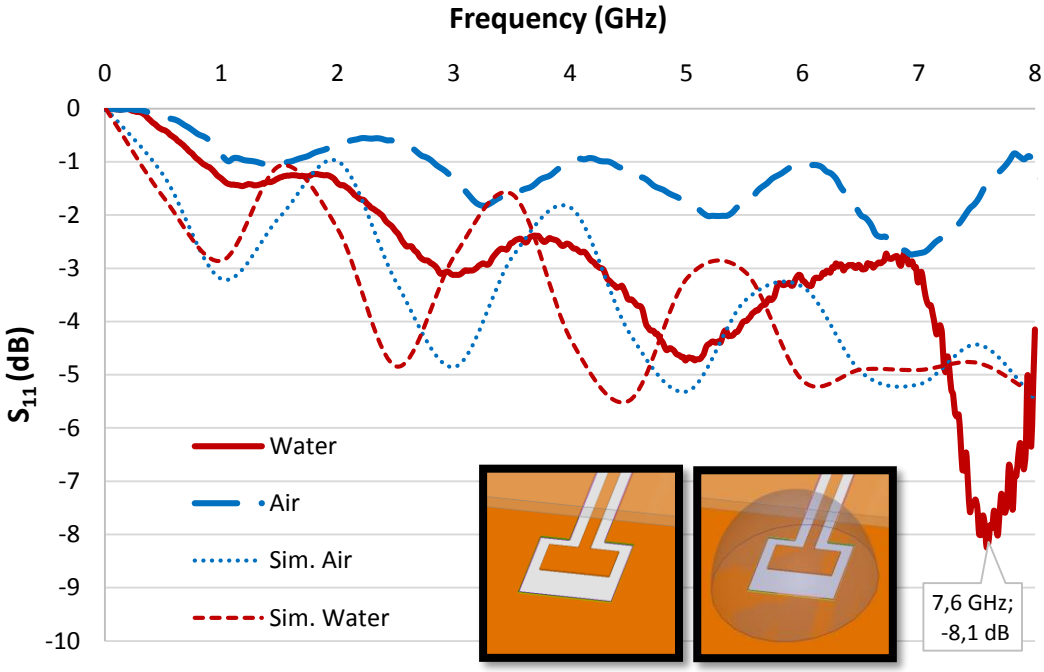

Figure 6.35 Simulated and measured S_{11} of buried transmission line without the micro antenna.

The S_{11} values above -10 dB mean that the line does not accept much of the injected power. However, and as seen before, the water phantom does terminate the line, contributing to a slightly lower S_{11} (-8.1 dB at 7.6 GHz). In general, the simulations show higher S_{11} values than the measurements, nonetheless there is an overall good agreement between them. Here, the differences between the measurements and simulation can be attributed to the noticeable structural differences between the HFSS model and the fabricated structures, as seen in Figure 6.32. A more detailed discussion regarding this issue will be given at the end of this chapter.

Figure 6.36 presents the S-parameters of the system composed of the transmission line and the micro antenna. In air, the system isn't able to accept much power. Here, the measured S_{11} is higher than the simulated, which never goes below -10 dB. However, when the water phantom is introduced, the systems accepts most of power at 2.2 GHz (-36 dB), in similarity to the results given by the simulation (2.0 GHz, -39 dB).

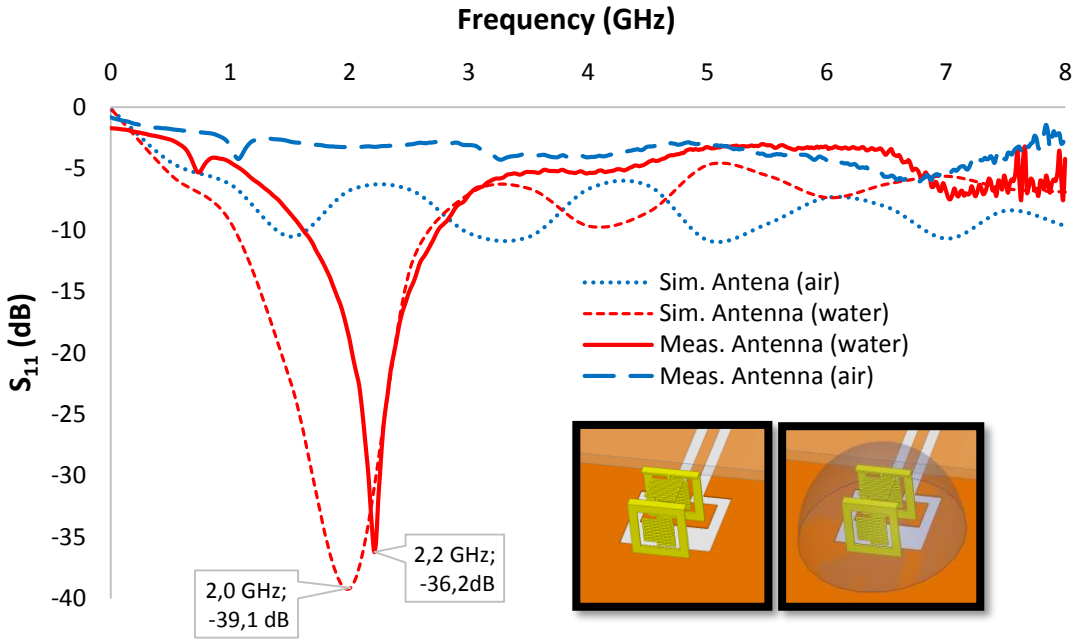

Figure 6.36 Simulated and measured S_{11} of the buried transmission line and micro antenna system.

6.1.5.2 Antenna Radiation Pattern

With the buried transmission line, the simulations provided, for the first time, a set of coherent radiation patterns for all tested conditions. The connector and transmission line system has the lowest gain, while the antenna and water systems the highest. The 3D radiation patterns and maximum gain values are presented in Figure 6.36 and Table 6.5, respectively. As it can be seen, the simulated radiation patterns and gain values are very close to those of the water and muscle embedded micro antenna of Figure 6.2 (-35.4 dB and -35.8 dB, respectively), so we can now proceed to the experimental measurement of the antenna radiation pattern.

Table 6.5 Simulated max. realized gains of connector of the system composed of the end launch connector, the buried transmission line and micro antenna. (SW – Southwest end launch connector, TL – Transmission line)

Tested Condition	Max. Gain (dB)
A) SW + TL (on air)	-48.5
B) SW + TL (on water)	-46.6
C) SW + TL + Antenna (on air)	-39.5
D) SW + TL + Antenna (on water)	-38

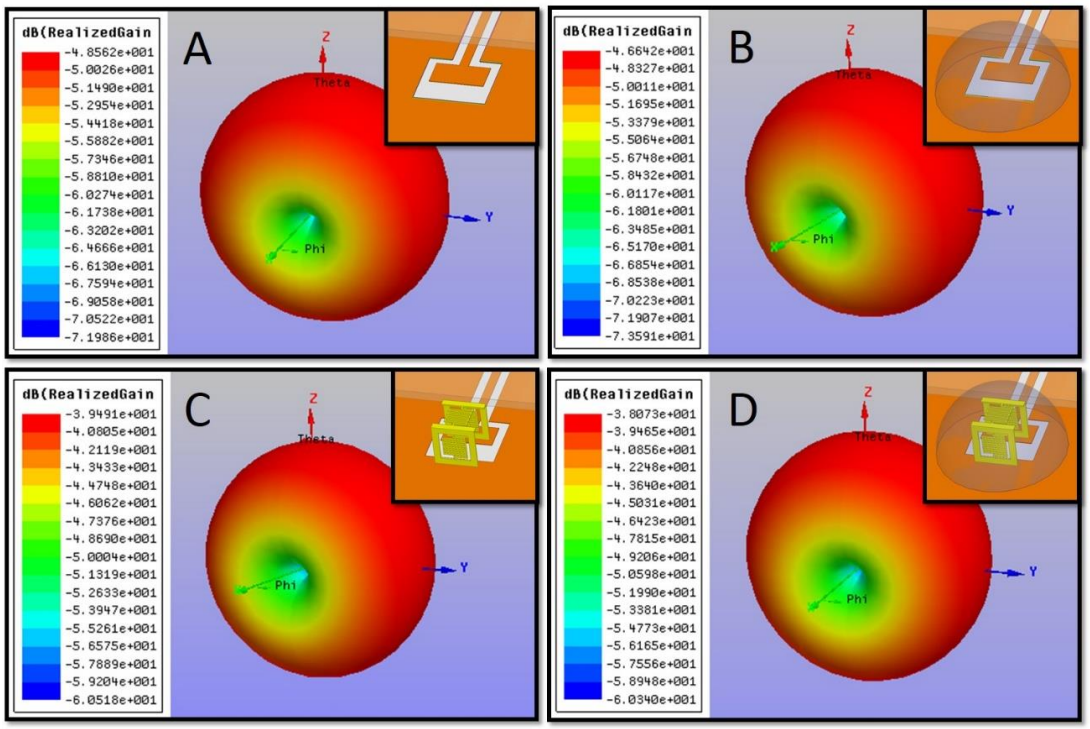

Figure 6.37 Simulated 3D radiation patterns of the system composed of the southwest end launch connector, the buried transmission line and micro antenna.

6.2 Antenna Radiation Pattern Measurement

The energy radiated from an antenna is a three dimensional problem, making what we call a radiation pattern. Its shape can be nearly spherical, as in the case of isotropic radiators, or extremely directional as in the case of antenna arrays. These are measured in special facilities that vary accordingly to the antenna purpose and the pattern it generates. Low-gain or electrically small antennas, such as the antenna we present in this work, can be measured in a simple rectangular anechoic chamber in the microwave frequency range [177].

6.2.1 Results and Discussion

The radiation pattern measurements were lineup in the same manner as for the S-parameters, i.e., comparing the buried transmission line with and without the micro antenna, and water phantom. As seen with HFSS, the radiation patterns usually exhibit a donut shape, with expected minimum gain values at 0 and 180 degrees in the azimuth plane, and at 90 and 270 degrees in the elevation plane. The maximum gain values were expected at 90 and 270 degrees in the azimuth plane, and in the elevation plane at 0 and 180 degrees. However, the measured radiation patterns showed slightly different outcomes when compared to the simulation (Figure 6.38).

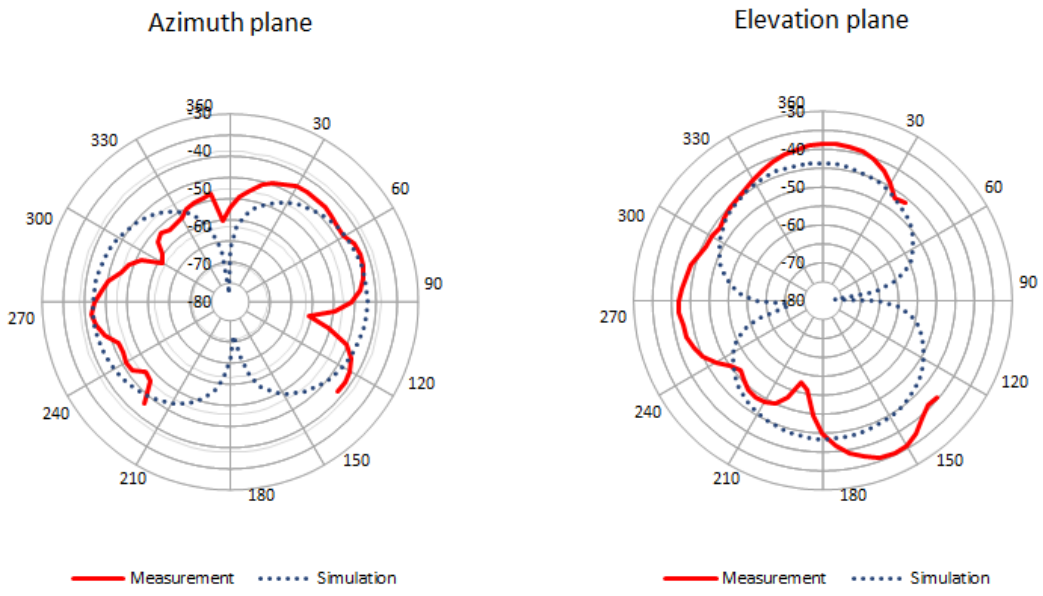

Figure 6.38 Radiation diagrams of the buried transmission line in air at 2 GHz.

Figure 6.38 shows the radiation patterns of the buried transmission line in air (without the water phantom), revealing some level of agreement between the measured and simulated radiation pasterns, but also some obvious discrepancies, as they do have similar shapes but do not share the same minimum gain values at the predicted angles. Also, the measured gains are generally higher than the simulated ones. In the azimuth plane (XY), the maximum measured gain, at a given direction, is of -41 dB while simulation shows a maximum gain of -48.5 dB (a 7.5 dB difference). In the elevation plane (XZ) the maximum measured gain at a given direction is of -35 dB while the simulation shows a maximum gain of -45 dB (a 10 dB difference).

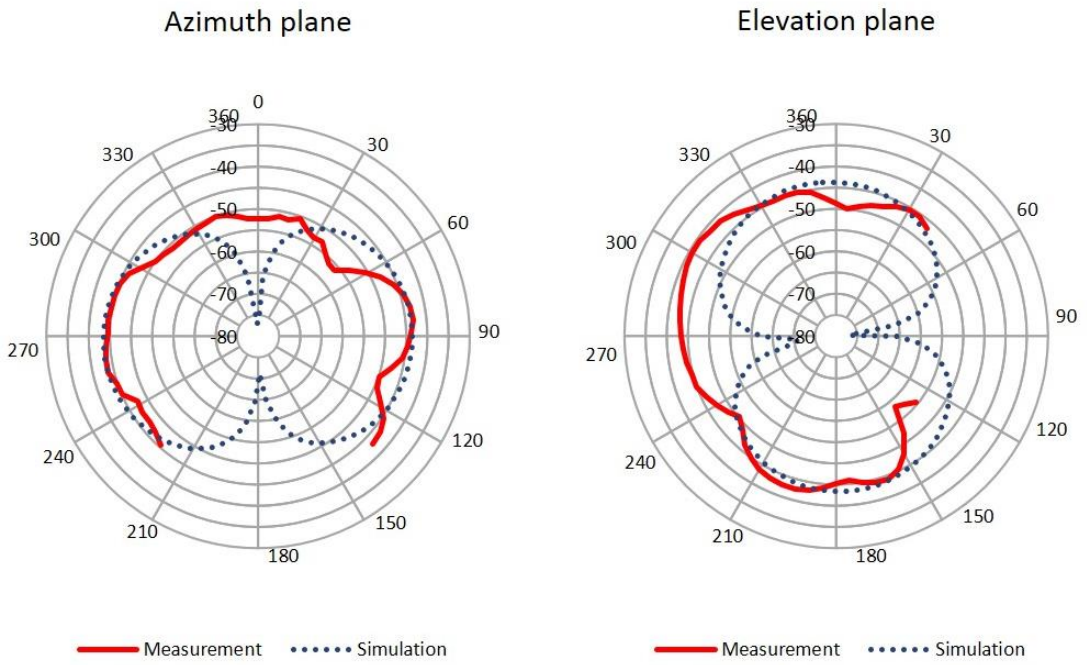

Figure 6.39 Radiation diagrams of the buried transmission line with the water phantom at 2 GHz.

Figure 6.39 illustrates the radiation patterns of the transmission line with the water phantom on the line's termination. In general, the simulated and measured radiation patterns shapes and gains show some level of agreement in spite the fact that the measurements show higher gains than the simulations. However, the main difference between them lies in the fact that, in both azimuth and elevation planes, the measured radiation patterns do not display the minimum gain values given by the HFSS. As it can be seen in the azimuth plane at 0 degrees, and in the elevation plane at 270

degrees, the measured patterns show relatively high gains when low gains were expected. As compared to the previous situation (Figure 6.38), the presence of the water phantom seems to have slightly reduced the maximum achievable gain, and changed the radiation patterns shape in both the azimuth and elevation planes.

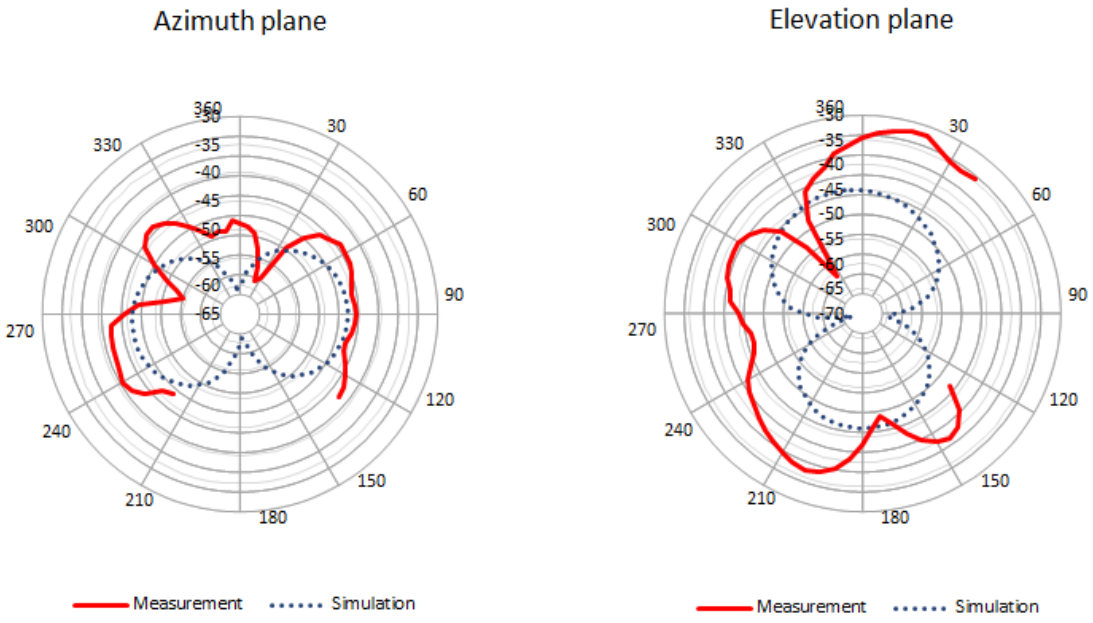

Figure 6.40 Radiation diagrams of the buried transmission line with the micro antenna in air at 2 GHz.

The radiation patterns of the transmission line and antenna system in air are presented in Figure 6.40. Here, the simulated and measured patterns do not agree as well as seen previously. The measured gains are generally higher than the simulated ones (up to 12.5 dB), with the exception of a few angles where the measured patterns have minimum gain values, which are lower than the simulated ones. However, and in spite of the noticeable gains differences, it is possible to spot anyway, that the measured patterns distribution follows the patterns' trend shown in the simulation, as it can be verified by the horizontally and vertically pattern distributions of the azimuth and elevation planes, respectively.

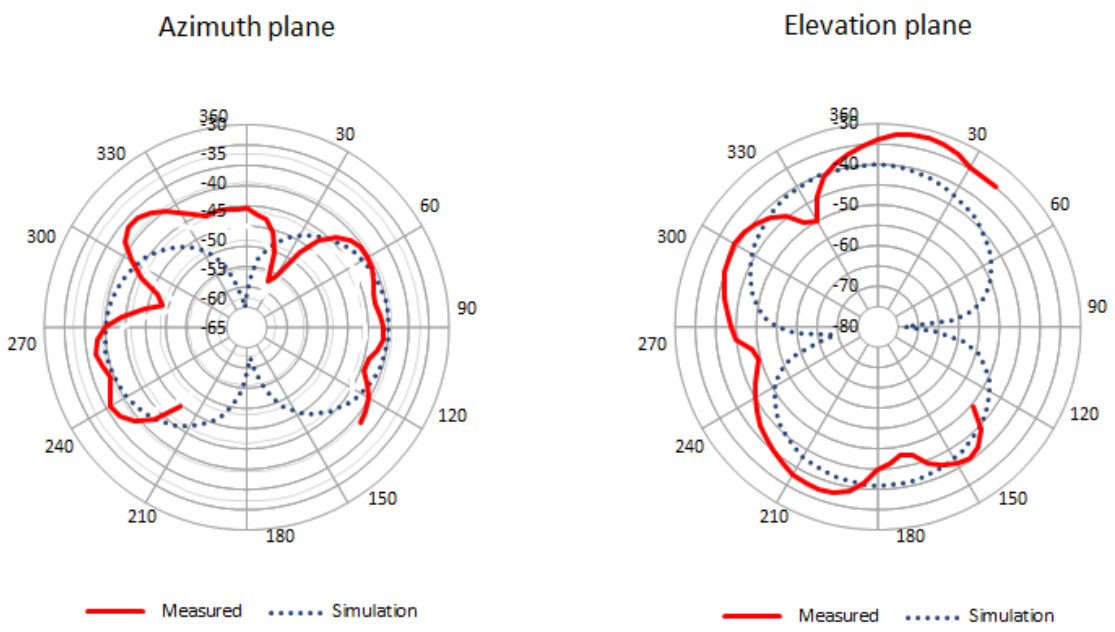

Figure 6.41 Radiation diagrams of the buried transmission line and micro antenna system with a water phantom at 2 GHz.

Finally, the radiation diagrams of the transmission line and antenna system with the water phantom are shown in Figure 6.41. Again, some level of agreement between the measured and simulated patterns is registered, regardless of the fact that at some angles the measured gains are almost 10 dB higher than the simulated gains. It is noteworthy that, as the simulated patterns illustrate, adding the water phantom to the system should increase the achievable gain. Yet, such effect is only verified experimentally by a slight gain increase (about 2 dB) in the fourth quadrant of both azimuth and elevation planes. Hence, the radiation patterns shapes are very similar to those of Figure 6.40, following the horizontal and vertical distributions on the azimuth and elevation planes respectively.

6.3 Measurements discussion

The differences between the measured and simulated radiation patterns can be rooted in a number of uncertainties and inaccuracies inherent to various aspects such as the experimental setup and utilized equipment, the materials and methods, and in the very challenging nature of measuring the radiation patterns of an extremely small antenna with small efficiency and gain. As mentioned earlier in this chapter, it is hard to measure the parameters of an antenna whose dimensions are countless times smaller

than the tools and the apparatus utilized for its characterization. These can produce significant interferences that mask the antenna radiation pattern and hence further add to the long list of uncertainties and inaccuracies that are about to be disclosed.

6.3.1 Setup Influence

As to the utilized setup, the classic bench test may not be the ideal solution the measurement sub-millimeter scale antennas due to the contrasting dimensions of DUT and the antenna used for the radiation patter measurement. With our setup, we are extremely vulnerable to misalignment issues between the transmitting antenna and the DUT, and problems related with the non-symmetry of the control measurements. Ideally, the radiation pattern would be characterized resorting to a probe system with mechanical harms as shown in [178][179] for greater measurement precision. Also we are measuring very small gains (approximately -40 dB, or smaller) and is vulnerable to signal reflections generated by cables and support structures as well as the asymmetries of the anechoic chamber caused by the necessary instrumentation inside the chamber.

Other major contributors for the observed discrepancies between the simulations and measured results are the structural differences between the 3D HFSS models and the fabricated structures, namely the transmission lines. HFSS does allow a great deal of detail and model complexity, but it isn't always possible to practically replicate the 3D models. It is important to refer that the simulation did not include all the necessary connectors and cables used in the practical measurements, it only considered the end launch connector, the transmission line, the micro antenna and the water phantom. Starting with the end launch connector model, that in spite of embodying a fair representation of the real connector, isn't free of small geometric inaccuracies that are very difficult to eliminate. Yet, more important sources of error are believed to have been created during the transmission line fabrication and assembly, the antenna soldering, and the water phantom positioning.

6.3.2 Fabrication

When compared to the HFSS models, the fabricated transmission lines have some structural differences that can affect the shape of the measured radiation patterns. While HFSS allows impeccably designed lines with extreme feature precision and positioning, the fabricated structures are, on the other hand, subjected to many design and implementation imperfections. These are generated during the transmission line fabrication, assembly and handling.

Throughout the fabrication stages, several causes of imprecision can be tracked down. First, the photomasks used for the transmission line fabrication were printed on translucent sheets, that are not the ideal medium for the patterning of features in the order the 100 µm. Secondly, the equipment used for pattern imprinting was not the most reliable one, as the vacuum system that holds the photomask unto the substrate was often not strong enough to assure the best contact between the two materials. Consequently, during exposure, the UV light scatters below the mask, widening features, destroying its critical dimension, such as the distance between the central feeding strip and the ground plane.

6.3.3 Interface Assembling

With HFSS, all structures are perfectly designed and positioned. However, such is extremely difficult to attain in practice. Significant structural differences between the HFSS transmission line model and the fabricated one can be clearly identified, as shown in Figure 6.32. The two RO3850HT substrates that compose the transmission line, were hand-assembled, and held together using solder (Figure 6.42), resulting in a structure that is fairly different from the one designed with the simulator. Also, assembling the lines by hand creates small gaps between the bottom and top substrates, as well as some misalignment between the two substrates, further adding to the structural differences between the 3D model and the fabricated structures.

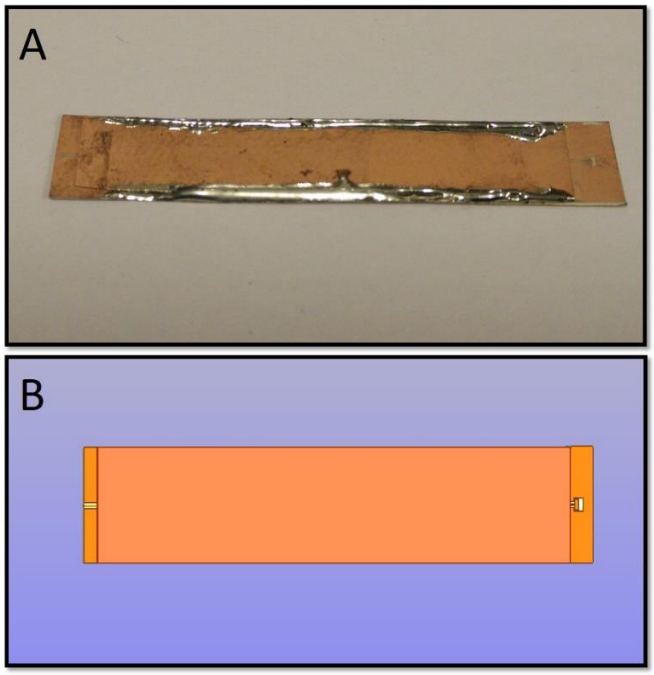

Figure 6.42 Transmission lines covered (buried) with an extra dielectric layer. A) Fabricated transmission line with solder on the edges connecting the top and bottom substrates. B) HFSS model of the buried transmission line.

Other details that might introduce variations in the system may be related to the attachment of the transmission line to the southwest connector, as the actual fitting is never as tight as in HFSS, and to the fact that, after repetitive use, the lines are not perfectly straight anymore as they tend to slightly bend.

6.3.4 Antenna Soldering

As mentioned previously, soldering the antenna to any structure is an extenuating task. Not only is it extremely difficult, but it is also a messy procedure that leaves unwanted tiny pieces of solder all over the transmission line (cf. Figure 6.27D), as well as bulky solder bumps between the antenna panels and the transmission line. This excess solder is not considered in HFSS models, and it may alter the way the antenna connects to the transmission line, affecting its input impedance, and therefore its performance. Another observed aspect is the warping (and even the destruction) of the 17 µm copper clad, caused by the soldering iron. The utilized solder paste needs temperatures between 300 and 400° Celsius for proper operation. At such temperatures, if the soldering iron tip touches the copper clad with enough pressure, it will certainly bend, warp and even be destroy the cladding and the dielectric substrate

as seen in Figure 6.27D. As many attempts were made to solder the antenna to the transmission line, the cladding was consequently fairly damaged.

Furthermore, another important aspect that may contribute with additional inaccuracies is the antenna orientation on the transmission line, as it is not perfectly aligned as seen in the HFSS model. Accurate antenna positioning is a very demanding task, and this is especially true if precise orientation is wanted. In HFSS models we can see the micro antenna orthogonality aligned with the nearby features. However, seeking a flawless alignment is an arduous chore, and if repeated many times in the pursuit of a perfect alignment, it translates in many soldering and desoldering cycles, thus inevitably harming the copper clad. Therefore, a compromise had to be achieved, in which an eventual slight antenna rotation was deemed acceptable. A small antenna rotation on the XY plane was occasionally noticed, and it was expected for the radiation pattern to be itself slightly rotated too, and therefore the expected radiation pattern minimum gain would not be perfectly aligned at 0 degrees. The soldering procedure can also alter the antenna's initial U-shape, and tilt it. As often times observed while soldering the antenna, the heat transfer across its structure would re-heat the hinges, causing either additional antenna folding or under-folding, or both at the same time in different hinges. This caused a slight antenna tilting that may also contribute for a slight radiation pattern shift.

6.3.5 Water Phantom

Another extremely important source of imprecision comes from the misplacement of the water phantom over the micro antenna. In order to guarantee the measurements reproducibility and reliability it is necessary to keep constant both the water droplet volume and its positioning. This was a laborious task and quite difficult to attain. Since the temperature inside the anechoic chamber if often high, it was noticed that water evaporation affects the measurements repeatability. Once evaporated, the water droplet had to be replaced, and difficulties to replicate exactly the same conditions, such as positioning and volume, were felt. The misalignment of the water droplet can be particularly significant. As the micro antenna rotates in the anechoic chamber, if the droplet is not perfectly aligned at the center (as seen in HFSS

simulations), it means that more water might exist in one side of the antenna than the other (Figure 6.43), hence causing asymmetries of the radiation pattern. This is particularly true for the measurements performed in the elevation places, as the only factors keeping the water stuck to the antenna are molecular adhesion and cohesion forces, which have to battle gravity. These forces are able to keep the water droplet on and around the antenna, but are not sufficiently strong to avoid the deformation of the droplet shape when measurements in the elevation plane are made.

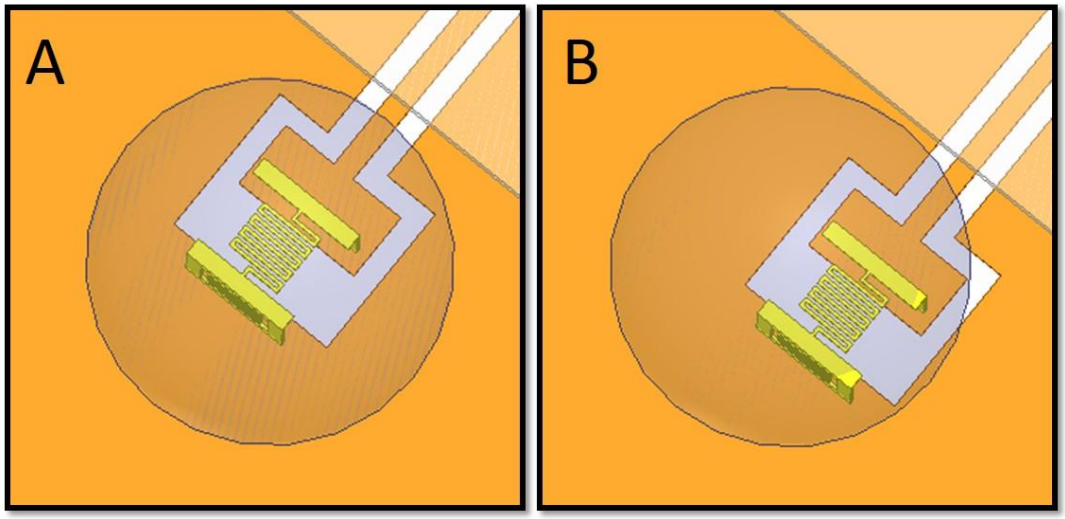

Figure 6.43 Water phantom surrounding the micro antenna. A) Perfectly aligned. B) Misaligned.

The combination of all the aforementioned issues regarding the setup, methods, equipment and materials must have deeply influenced the radiation pattern measurements. However, bearing in mind the antenna's dimension and its small gain we find these measurements to be somewhat satisfactory and worthwhile, thus providing relevant insights regarding the micro antenna characteristic as well as a good starting point future and more in depth work on radiation pattern measurement.

6.4 Wireless Power Transfer

To demonstrate the feasibility of using micro antennas in a practical application, we built a setup where a horn antenna transmitted an RF signal, which was received by the U-shaped antenna. The antenna was immersed in water, which is a dispersive media similar to that which would be encountered in a practical application of powering a biomedical implant within the body. The micro antenna was connected to a rectifying circuit, which was used to convert the received RF energy into a DC signal. Finally, at the end of the rectifying circuit, an LED was used to verify that enough power was successfully transmitted to the U-shaped antenna and converted to a DC signal. The wireless power transfer schematic is shown in Figure 6.44.

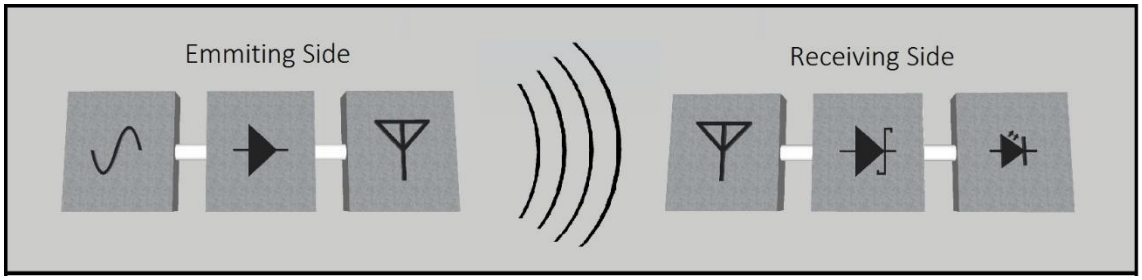

Figure 6.44 Schematic of the wireless power transfer setup. The transmitting side includes a VNA that serves as the RF signal source, the RF amplifier and the horn antenna which transmits the generated RF signal. The receiving side includes the U-shaped antenna, which acts as the RF signal receiver, a rectifying circuit and an LED.

The wireless power transfer experimental setup is composed of a horn antenna as the RF signal transmitter, and the micro antenna as the receiver. On the transmitting side, the horn antenna was connected to the VNA port 1 through a signal amplifier, (ZVE-3W-83+ Mini Circuits, Brooklyn, NY). The receiver side was composed of the test antenna with a rectifying circuit, to convert the received RF energy into a DC signal. The rectifying circuit was composed of a 1 µH inductor, a schottky diode (MADS-001317-1500AG Macom, MA) and a 1.2 pF capacitor. The LED (SML-A12UTT86T Rohm Semiconductor, Kyoto, Japan) was placed at the end of the circuit. The micro antenna was submerged into a water container approximately 1 cm deep, and the horn antenna was placed next to the container, aligning the polarization with the test antenna Figure 6.45.

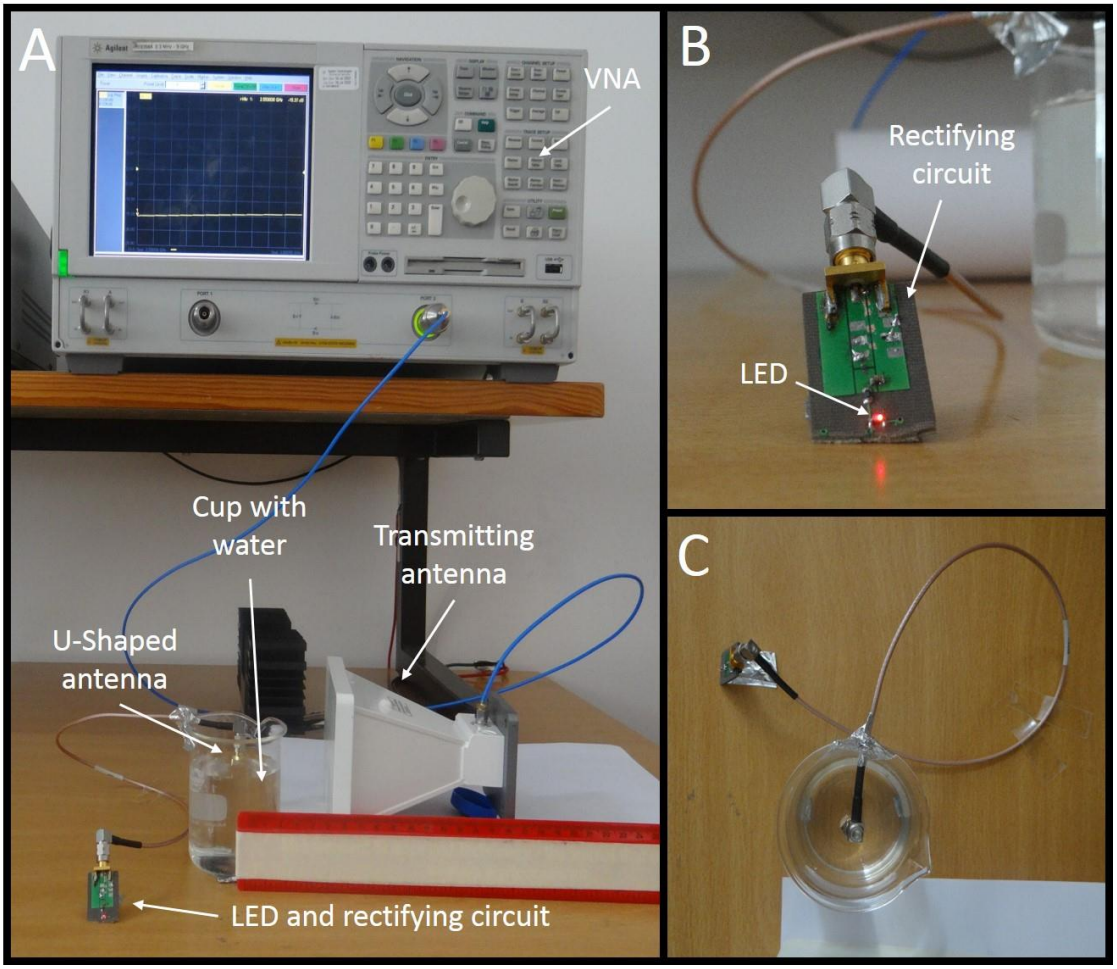

Figure 6.45 A) Wireless power transfer setup composed of the VNA, the RF amplifier, the transmitting antenna, the U-shaped antenna, a cup with water, and the rectifying circuit with an LED. B) Picture of the rectifying circuit and the LED. C) Top view picture of the receiving side.

The power transfer measurements were assessed for different distances between the transmitting and receiving antennas, namely 2.5, 5, 7.5, and 10 cm, and the received power was illustrated by the LED brightness when power was successfully transferred to the antenna. In order to determine the power transfer dependency on the angular orientation, the measurements were repeated as the horn antenna was kept at different spherical coordinates. Taking advantage of the symmetry, the measurements were done only at the 1st and 2nd octants. The wireless power transfer is best shown by the brightness of the LED as seen in Figure 6.46. Since the transferred power depends on the distance between the transmitter and receiver due to losses, both in the air and in the dispersive media, the LED brightness is highest when the horn and micro antenna are closest, 2.5 cm apart in this setup, and decreases with increasing

distance Figure 6.46A. The results also show that the fabricated U-shaped antenna is fairly insensitive to the direction of the incoming signal, which is a big advantage compared to other electromagnetic energy harvesting methods such as using inductive coupling. The LED in our setup stayed lit while we rotated the horn antenna in the 1st and 2nd octant of the micro antenna Figure 6.46B.

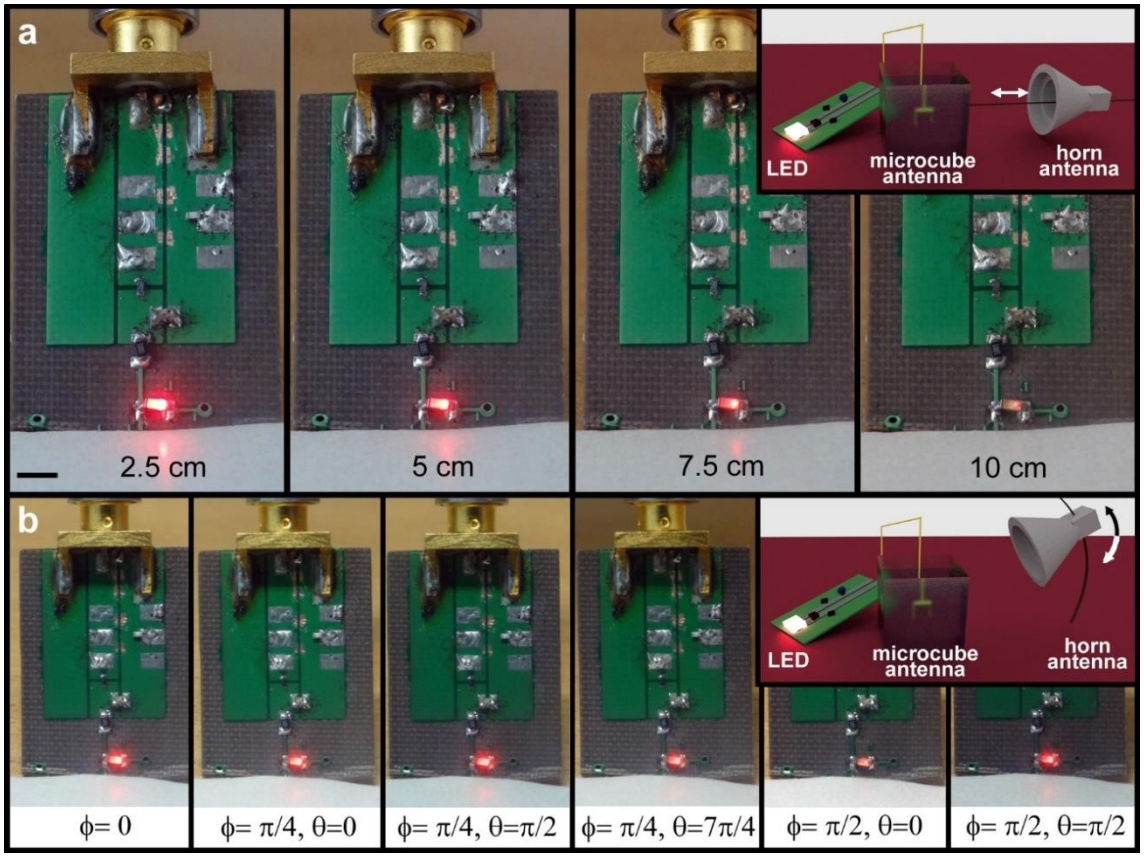

Figure 6.46 Wireless power transfer to the U-shaped antenna to power an LED. The bright field images show the RF to DC conversion circuit with an LED when power is successfully transferred from the transmitting horn antenna to the micro antenna (shown in the inset schematics). The transmitting and receiving antennas are kept at A) Different distances and B) Different angles. The LED brightness represents the amount of power transmitted from the horn antenna to the U-shaped antenna. While the power transfer drops regularly with increasing distance between two antennas, it is fairly independent from the angular orientation. The scale bar represents 2 mm.

7 Conclusions

7.1 Conclusions

The work accomplished in the framework of this thesis aimed at the development of miniaturized antennas for ultra-small implantable medical devices, and their application for wireless power transfer purposes. Important notions regarding the nature of IMDs, the fundamental limits and the performance of antennas in lossy media, and antenna miniaturization techniques were given. However, while it is not an original contribution, this analysis does revise some existing and critical knowledge for the design of implantable antennas, thus providing a solid base for the developments presented further on.

In this work, 3D micro antennas were fabricated using a methodology that combines conventional planar photolithography techniques and self-folding. In this approach, planar photolithography permitted the patterning of planar antenna panels with reproducible feature precision, and the flexibility to easily and quickly change the antenna geometry, which can be important to change the antenna characteristic according to the environment it is used in. This combined method offers ease of mass production, extreme control of size and shape, material versatility, and the ability to integrate electronic modules.

After fabrication, the antenna characterization was performed by measuring its S-Parameters and radiation pattern. Due to the antenna's reduced size, different mounting structures were engineered in order to allow it to be connected to a VNA. The development of these structures was a laborious process, involving the use of diverse elements such as connectors, CPWs, transmission lines and RF probes. After several iterations, it was concluded that a combination of an end launch connector and a transmission line system allowed a more accurate measurement of the antenna radiation pattern. However, difficulties were felt. As mentioned previously, the main problem with the characterization for such small antennas is that the measuring setup is itself composed of metallic elements, which are huge when compared with the DUT. This way, the measuring setup produces a masking effect which can difficult an accurate

measurement of the antenna radiation pattern. Nonetheless, throughout the antenna characterization steps, it was verified an acceptable level of agreement between measurements and simulations.

Finally, we have successfully developed a wireless power transfer application, where a micro antenna embedded in dispersive media (water) was capable of receiving enough energy from an external antenna to power an LED. The fabricated micro antenna demonstrated to be fairly insensitive to the angular orientation of the external horn antenna transmitting the RF signal. This is important in untethered implantable devices where it may not be possible to precisely control the orientation of the implant relative to the source.

Finally, our process's compatibility with the current photolithographic techniques, and the ability to engineer and mass-produce precise ultra-small 3D electrically interconnected structures by self-folding suggests that other packaged and RF powered devices of relevance to wireless sensor networks, smart dust and implantable medical devices could also be formed.

7.2 Future Work & Perspectives

As mentioned in the last chapter, the main difficulties felt during this work are related with the antenna extremely small size, which makes difficult its interconnection to other structures for measurement purposes. While the manual handling of a fabricated antenna was doable, its interconnection to other structures by soldering was a very tiring task, and an important source of inconsistencies between simulated and measured results. To avoid these issues, it would be extremely advantageous if, in future work, the antennas were to be fabricated and assembled on-chip, allowing direct interconnection to 50 Ω transmission lines as proposed in [176][180] (Figure 7.1). We believe that this approach has the potential to eliminate many of the imprecisions caused by the antenna's manual handling and assembly, and hopefully lead to a better antenna characterization.

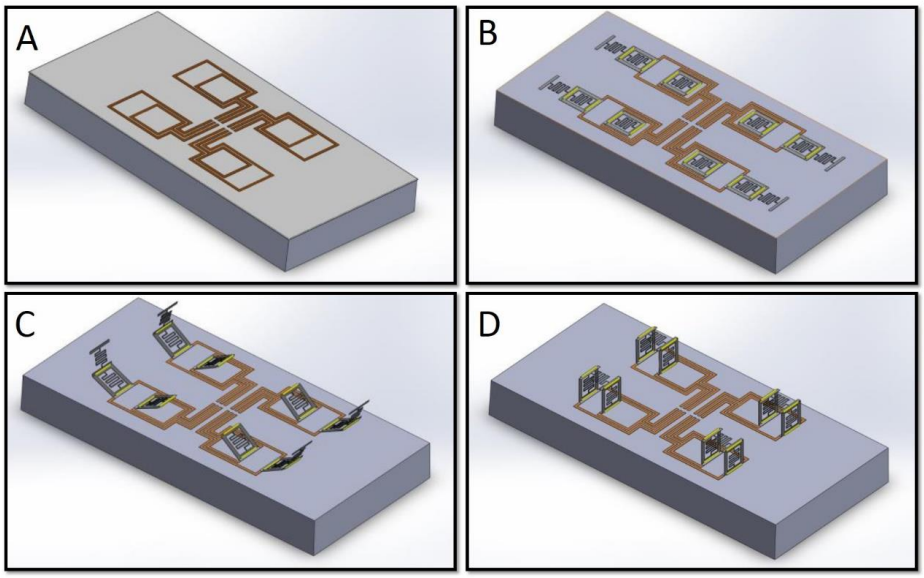

Figure 7.1 On chip antenna fabrication and assembly. A) Patterned 50 Ω transmission lines. B) Patterned antenna frames and solder hinges. C) On-chip self-folding. D) Antenna structures connected to 50 Ω transmission lines.

Other important issues that must be addressed in future work, is the use of a proper tissue mimic phantom, and a method to properly restrain it around the antenna. As seen in chapter four, simulations were performed with a micro antenna embedded in muscle tissue. However, in chapter six, the measurements were performed with a water phantom, for the sake of simplicity. Hence, to reach more realistic results, it is important to contemplate a more realistic phantom, and fortunately, the literature available is on this subject is dense [181-184]. It would be interesting to use a gel-based phantom, in order to avoid fluid evaporation issues thus keeping a steady phantom around the antenna.

As antennas require some kind of insulation in order to be implanted, the use of proper insulation is also crucial, and future most consider packaging solutions as these insulating/packaging layers can enhance antenna performance and power transmission in WPT application [185].

Another extremely important issue that must be addressed is related with the measurement setup, as the radiation pattern would be better characterized resorting to a probe system with mechanical harms. Nonetheless the difficulty of characterizing micro antennas is stressed throughout [178], where the authors point out that there aren't yet any setups capable of seamlessly measure antennas with such small dimensions.

Appendix 1: Protocol for the Fabrication of Self-Folded Micro Antennas

1. Prepare the masks as explained in 5.2.1. For fabrication of the micro antennas with 500 µm panel edge length, draw a panel mask such that the panels are spaced apart by 30 µm. Draw a hinge mask where folding hinges have dimensions of 400 µm x 100 µm.
2. Prepare a silicon wafer substrate as explained in 5.2.2.
3. Spin coat ~5 µm thick layer of 950 PMMA A11 at 1,000 rpm, on the silicon wafers. Wait for 1 min and then bake it at 180 °C for 60 sec.
4. Using a thermal evaporator, deposit 15 nm chromium (Cr) as an adhesion promoter and 100 nm copper (Cu) as the conducting layer.
5. Spin coat ~10 µm thick SPR220 at 1700 rpm onto the wafers. Wait for 1 min.
6. Perform a ramp-up softbake by placing the wafer on a hotplate at 60 °C for 30 sec. Then transfer the wafer onto another hotplate at 115 °C for 90 sec and then back to 60 °C for 30 sec.
7. Cool the wafers at room temperature and wait for a few minutes.
8. Expose the wafers to the panel mask using ~460 mJ/cm^2 of UV light (365 nm) and a mercury based mask aligner.
9. Develop in MF-26A developer for 2 min and change the developer solution and develop for another 2 min.
10. Calculate the total metallic panel area and use it to compute the current required to electrodeposit Ni from a commercial nickel sulfamate solution at a rate of approximately 1-10 mA/cm^2 up to a thickness of 10 µm. When immersed in the plating solution the back of the wafer must face the anode.
11. Dissolve the photoresist with acetone. Rinse the wafer with IPA, and dry with N^2 gas.
12. Spin coat ~10 µm thick SPR 220 at 1700 rpm onto the wafers. Wait for 3 min.
13. Perform a ramp-up softbake by placing the wafer on a hotplate at 60 °C for 30 sec. Then transfer the wafer to another hotplate at 115 °C for 90 sec and then back to 60 °C for 30 sec.

14. Cool the wafers at room temperature and wait for a few minutes.
15. Expose the wafers to the hinge mask using ~460 mJ/cm^2 of UV light (365 nm) and a mercury based mask aligner. Ensure that the registry marks are aligned so that the hinges are aligned with the panels.
16. Develop in MF-26A developer for 2 min and change the developer solution and develop for another 2 min.
17. Using a diamond cutter, cut the wafer into small pieces so they can fit into the plating solution recipient. Coat the edges of the pieces with nail polish.
18. Calculate the total exposed hinge area and use it to compute the current required to electrodeposit Pb-Sn solder from a commercial solder plating solution at a rate of approximately 20-50 mA/cm^2 up to a thickness of 15 µm. When immersed in the plating solution the back of the wafer must face the anode.
19. Dissolve the photoresist in acetone. Rinse the wafer pieces with IPA, and dry with N^2 gas.
20. Immerse the wafer piece in etchant APS 100 for 25-40 sec to dissolve the surrounding Cu layer. Rinse with DI water and dry with N^2 gas.
21. Immerse the wafer piece in etchant CRE-473 for 30-50 sec to dissolve the surrounding Cr layer. Rinse with DI water and dry with N^2 gas.
22. Immerse the wafer piece in ~2-3 ml of 1-Methyl-2-Pyrollidinone (NMP) and heat at 100 °C until the templates are released from the substrate.
23. Transfer the templates (20-40) into a small Petri dish and distribute them uniformly.
24. Add ~3-5 ml of NMP and ~5-7 drops of Indalloy 5RMA liquid flux.
25. Heat at 100 °C for 5 min. In this step, the Indalloy 5RMA liquid flux cleans and dissolves any oxide layer formed on the solder and thereby ensures good solder reflow on heating above melting point.
26. Increase the hotplate temperature to 150 °C for 5 min and then slowly increase it to 200 °C until folding occurs. When the temperature is increased to 200 °C folding starts after 5 min. When the panels start to fold reaching an angle close to 90 degrees, remove them from the hot plate. The mixture may turn brownish as it starts to burn.

27. When the antennas have folded, allow the dish to cool down. Add acetone to the dish, pipette out the liquid, and rinse the antennas in acetone and then ethanol.
28. Store the fabricated structures in ethanol.

Appendix 2: 3D vs 2D Antennas

In this section, we compare 2D and 3D micro antennas suitable to be used on miniaturized devices. Here, we intend to demonstrate that with a 3D antenna design, it is possible to increase the power transfer efficiency without increasing the occupied cross-sectional space on a miniaturized device. This comparison is made between the antennas geometries presented in Figure A2.1, both on the surface of a hypothetical cubic micro device (500 × 500 × 500 μm^3). As it can been seen, and in comparison with the 2D geometry, by adopting a 3D configuration, the cross-section occupied by the 3D antenna is kept constant, while its size and the radian sphere filling factor (in which the antennas are contained in) are increased. As it can be seen, the 2D antenna is composed of only one panel (500 × 500 μm^2), while 3D antenna is composed of three panels.

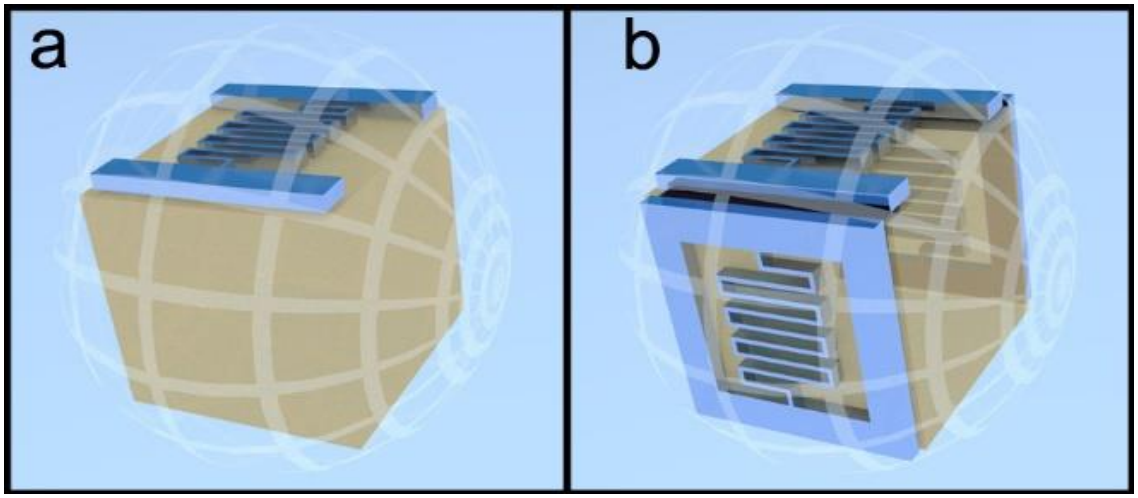

Figure A2.1 Concept of the 2D and 3D antennas on a micro device. Schematic representations of A) Planar antenna. B) 3D antenna on a hypothetical device with the same form factor (500 × 500 × 500 μm^3). The lines around the device indicate the radian sphere.

We simulated both antennas using air and water as surrounding media. When immersed in water, both 3D and 2D antennas operate in the low gigahertz range, at 3.7 GHz and 5 GHz, with S_{11} values of -35 dB and -26.2 dB respectively, thus confirming that the bigger antenna, even though it occupies the same radian sphere volume, operates at lower frequencies. We also simulated and compared the radiation efficiency of each antenna in air and in water (Figure A2.2). The radiation efficiency represents the

antenna ability to convert the absorbed signal into radiation and it is calculated by P_{rad}/P_{acc}, where P_{rad} and P_{acc} are the radiated and accepted powers respectively. For very small antennas, greater efficiencies are expected when high operating frequencies are used [62]. As demonstrated in the simulations, and as expected, the radiation efficiency of both 3D and 2D antennas increases with frequency. It can also be seen that the 3D antenna radiation efficiency is significantly higher than the planar one throughout the analyzed frequency range. This result, which was also verified in previous works, can be explained by the 3D nature of the U-shaped antennas which exhibit a higher effective volume occupancy within the radian sphere when compared to their 2D counterparts [54][60][69].

Another result that can be gathered from the simulations is that the presence of dispersive media, in this case water, enhances the antenna efficiency at lower frequencies, which leads to a better wireless link efficiency. Usually, lossy media such as water, adds losses to the total propagation loss path. However, the antenna resonant frequency also decreases when it is surrounded with high permittivity dispersive media like water or human muscle tissue. This feature becomes advantageous when the antenna operates in an electrically-small regime, i.e., when the antenna size is much smaller than the signal wavelength. This phenomenon is also known as dielectric loading and is used for antenna miniaturization and tuning [169][186]. Since these antennas were designed to operate in the low GHz range in order to decrease losses due to tissue attenuation, the dielectric loading helps increase the overall link efficiency. In air, both antennas operate at higher frequencies and consequently show high levels of reflected power in the analyzed frequency range.

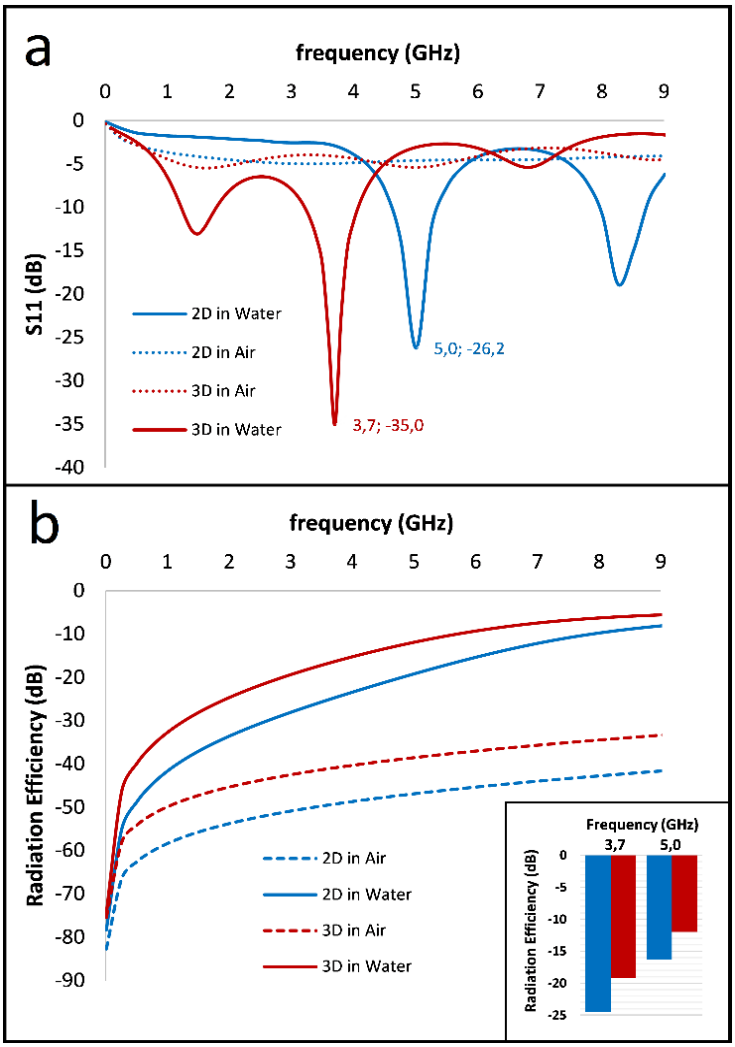

Figure A2.2 Simulations results illustrating the comparison between planar (2D) and U-shaped (3D) antennas that can fit on a 500 μm^3 device. HFSS simulations results show: A) The resonance frequency and S_{11}. B) The radiation efficiency of each antenna in air and in dispersive media. The inset graph shows the radiation efficiency for 2D and 3D antennas in water at their resonance frequencies.

For the S-parameter measurements, both antennas were soldered to the CPW. Measured results showed that the both antennas have the expected characteristics as predicted by the HFSS simulations (Figure A2.3). The measured resonant frequency of the 3D antenna with a resonant dip at 3.6 GHz shifted only 0.2 GHz from the simulated data, while the measured resonant frequency of the 2D antenna matched the simulation result at 4.8 GHz. The measured S_{11} values of the 3D and 2D antennas, at the resonance frequency, were -31.2 dB and -22.8 dB respectively (Figure A2.3).

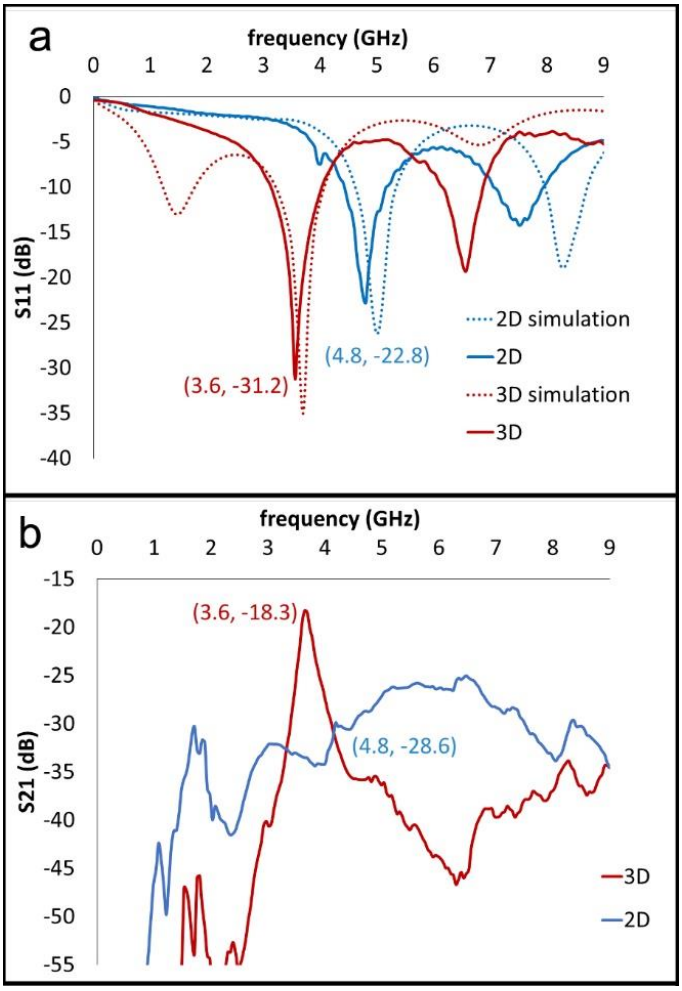

Figure A2.3 Experimentally measured S_{11} and power transfer characteristics (S_{21}) of the fabricated planar (control samples) and U-shaped antennas in dispersive media. The graphs show A) S_{11}. B) S_{21}, the power transfer characteristics of planar and U-shaped antennas. The 10.3 dB difference in the S_{21} data between the 2D and 3D antennas at their resonance frequencies shows an approximately 10-fold increase in the power transfer efficiency.

The S_{21} parameter, which is the scattering parameter representing the power transfer efficiency between the two antennas for a given distance was also measured. To this purpose, a broadband antenna was used as an RF transmitter, and the signal collected by the 3D and 2D antennas (Figure A2.3B). At their resonant frequencies, the S_{21} values of the 3D and 2D antenna are -18.3 dB and -28.6 dB respectively. The 10.3 dB difference in S_{21} values shows that approximately 10 times more power was transmitted to the 3D antenna than the 2D antenna. On the S_{21} graph, the amplitude variations represent the antenna's ability to receive energy as a function of frequency, while the smaller modulations represent the reflections created by the coplanar waveguide (CPW) interface and the SMA launcher.

Appendix 3: Micro Antenna Radiation Pattern Measurement Setup

Ideally, antenna measurements should be carried where no electromagnetic wave reflections can occur, and such environments can be found in anechoic chambers, which allow for all reflected waves from nearby objects to be suppressed. These chambers are designed to absorb reflections of either electromagnetic waves or sounds, and its insulation helps creating a virtual open space environment, free from exterior sources of noise [177]. In this work, the radiation pattern measurements were performed in the anechoic chamber shown in Figure A3.1.

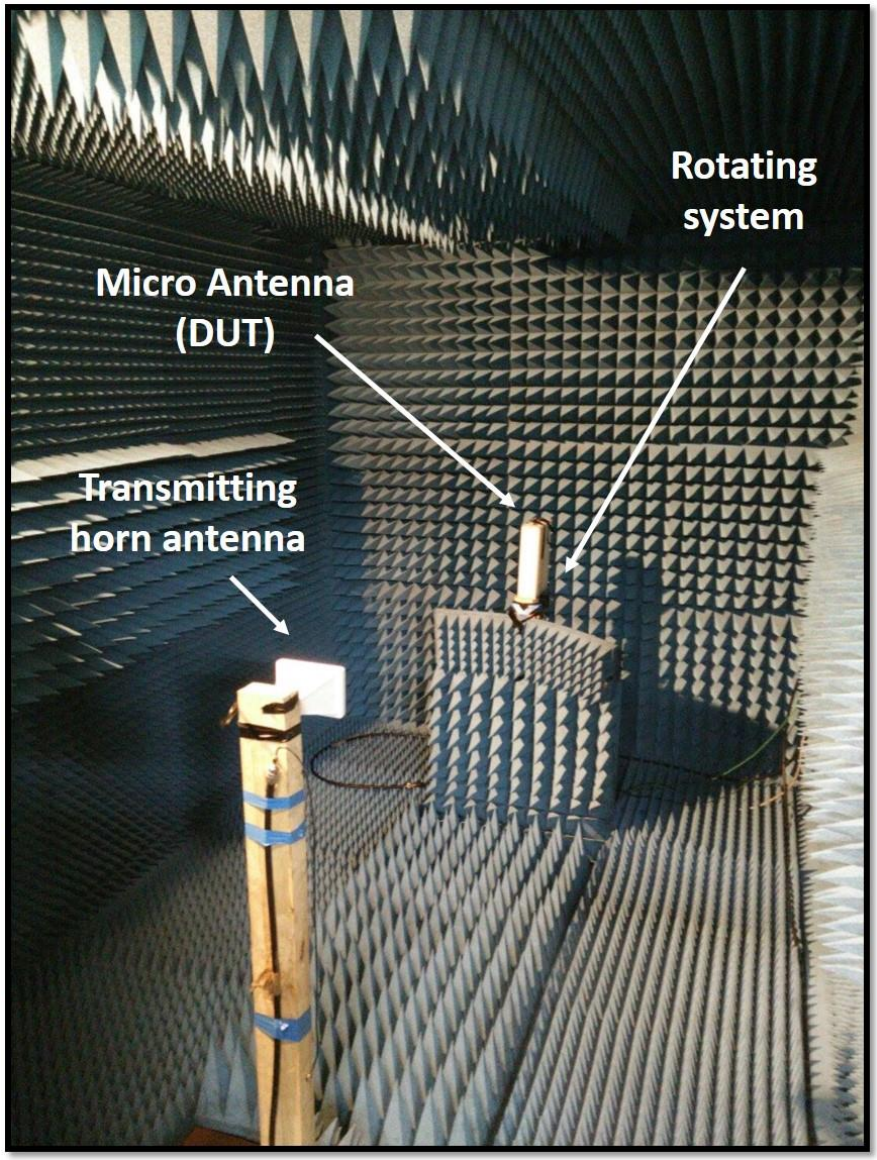

Figure A3.1 Measuring setup Inside of the anechoic chamber.

To measure the micro antenna radiation pattern we utilized a setup composed of a transmitting horn antenna, a micro antenna (device under test - DUT), and a VNA. If the DUT radiation pattern is to be measured, it is also convenient to use a positioning system to rotate it relatively to the transmitting antenna in order to record the gain at different angles, therefore generating a gain diagram. As mentioned in chapter six, the micro antenna was soldered to the transmission line which is connected the VNA via cables. This configuration does limit the radiation pattern measurement to a span of 270°, as structures such as the connector and cables would block the transmitting and receiving antennas' line of sight. The measurements were performed at 2 GHz, as this is the micro antenna operating frequency when the water phantom is used.

Setup Calibration

The available measurement setup is not an ideal one, and consequently losses are introduced in the system by the several transmission cables, free-space propagation and the utilized antennas. In order to have more accurate measurements, these losses must be accounted for. Using an antenna with known characteristics, namely its gain at 2 GHz, it is possible to determine the system's gain. In an ideal system, i.e. FSPL and cable loss = 0, and assuming the transmission antenna has 0 dB gain, the measured S_{21} in the horn antenna would be its gain at 2 GHz, 5 dB. As the system is not ideal, it won't be 5 dB. For example, if it measures -10 dB, it means that the system FSPL, cables and transmission antenna introduces a gain of -15 dB. Knowing this, it is possible to remove this effect from the DUT's measurements simply by adding 15 dB to counteract this contribution, as the system is the same in both the calibration and DUT measuring stages, thus allowing for a DUT-only S_{21} measurement.

Measurement Protocol

The following protocol was used to obtain the radiation patterns of fabricated transmission lines and micro antenna:

1. With the help of a laser, align the transmitting antenna with a receiving horn antenna of known properties for measurement in the azimuth plane. Make sure the antennas are at the same height.
2. At zero degrees (antennas directly pointed at each other), measure the S_{21} parameter of the receiving antenna.
3. Replace the receiving antenna with a transmission line without a micro antenna.
4. Rotate of the receiving setup from -135° to 135°, with a 5° step and record the S_{21} value for the measurement of the azimuth plane (XY plane).
5. Rotate all components by 90° (transmitting antenna and transmission line) in order to measure the radiation pattern in the elevation plane (XZ plane) and repeat step 4.
6. Place of the water phantom on the transmission line termination and repeat steps 4 and five.

The same procedure must be used for the measurement of the transmission line and antenna system. Figure A3.2 shows a schematic of the setup utilized for the radiation pattern measurements, a classic bench test, composed of an anechoic chamber housing two carefully aligned antennas, a transmitting one with known characteristics and the DUT on top of a rotating platform.

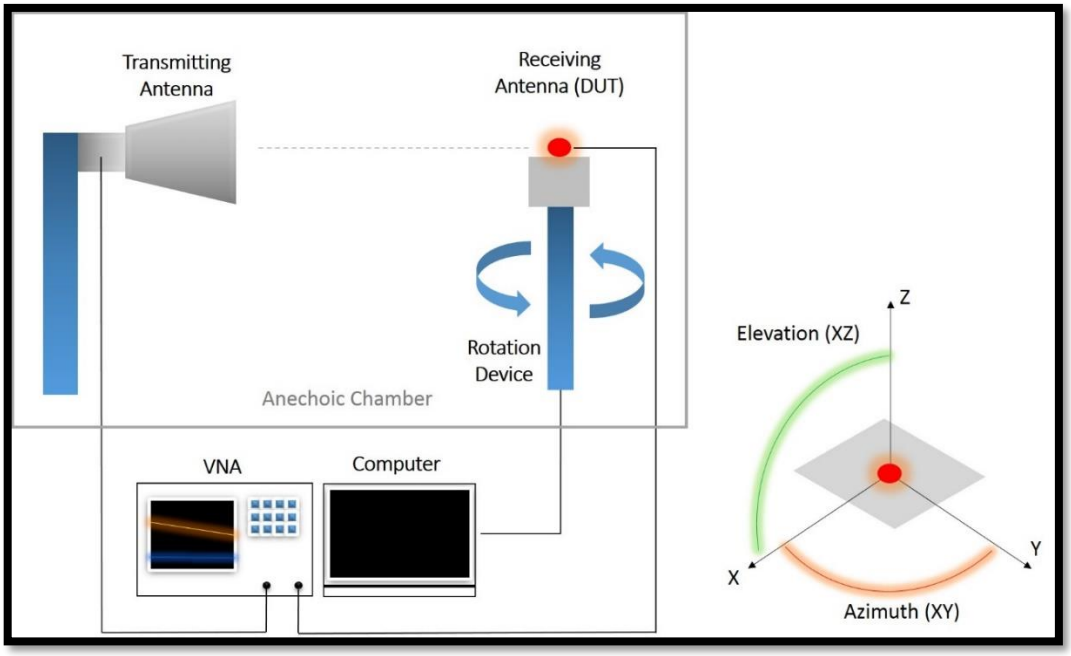

Figure A3.2 Representation of the utilized setup for the micro antenna radiation pattern measurements.

Bibliography

[1] F.M. Blanding, “New medical mevices get to patients too slowly.” Forbes, Aug-2015. http://www.forbes.com/sites/hbsworkingknowledge/2015/08/11/new-medical-devices-get-to-patients-too-slowly/#2b6b784a76c8

[2] E. Meng, R. Sheybani, “Insight: Implantable Medical Devices” Lab Chip, vol. 14, no. 17, pp. 3233-3240, 2014.

[3] T. Nguyen, S. Zupancic, D. Lie, “Engineering Challenges in Cochlear Implants Design and Practice” IEEE Circuits and Systems Magazine, vol. 12, no. 4, pp. 47-55, 2012.

[4] E. Zrenner, “Fighting Blindness with Microelectronics,” Science Translational Medicine, vol. 5, no. 210 2013.

[5] R. Farra, N. Sheppard Jr., L. McCabe, R. Neer, J. Anderson, J. Santini Jr., M. Cima, R. Langer, “First-in-Human Testing of a Wirelessly Controlled Drug Delivery Microchip,” Science Translational Medicine, vol. 4, no. 122, p. 122ra21, 2012.

[6] Y. T. Liao, H. Yao, A. Lingley, B. Parviz, B. P. Otis, “A CMOS Glucose Sensor for Wireless Contact-Lens Tear Glucose Monitoring” IEEE Journal of Solid-State Circuits, vol. 47, no. 1, pp. 335–344, 2012.

[7] M. Ahmadi, G. Jullien, “A Wireless-Implantable Microsystem for Continuous Blood Glucose Monitoring” IEEE Transactions on Biomedical Circuits and Systems, vol. 3, no. 3, pp. 169–180, 2009.

[8] O. Murphy, C. Toumazou et al., “Continuous in vivo blood pressure measurements using a fully implantable wireless SAW sensor” Biomedical Microdevices, vol. 15, no. 5, pp. 737–749, 2013.

[9] R. Levy R, T. Deer, J. Henderson, “Intracranial neurostimulation for pain control: a review” Pain Physician, vol. 13, pp. 157–165, 2010.

[10] E. Chow, Y. Ouyang, B. Beier, W. Chappell, P.Irazoqui, “Evaluation of Cardiovascular Stents as Antennas for Implantable Wireless Applications,” IEEE Transactions on Microwave Theory and Techniques, vol. 57, no. 10, pp. 2523-2532, 2009.

[11] W. Abraham, B. Jeffries, J. Yadav, “Wireless pulmonary artery haemodynamic monitoring in chronic heart failure: a randomised controlled trial” The Lancet, vol. 377, no. 9766, pp. 658–666, 2011.

[12] J. Jin, “Implantable spinal cord stimulator allows voluntary movement in individuals with lower-extremity paralysis” JAMA - Journal of the American Medical Association, vol. 312, no. 2, 2014.

[13] D. Pivonka, A. Yakovlev, A. S. Y. Poon, T. Meng, “A mm-Sized Wirelessly Powered and Remotely Controlled Locomotive Implant” IEEE Transactions on Biomedical Circuits and Systems, vol. 6, no. 6, pp. 523–532, 2012.

[14] F. Wiedbrauck, J. Albert, “Small Bowel Tumor Detection in Capsule Endoscopy: Balancing Preoperative Diagnosis Against Capsule Retention” Video Journal and Encyclopedia of {GI} Endoscopy, vol. 1, no. 1, pp. 278–280, 2013.

[15] Medtronic.Inc, “Reveal LINQ Insertable Cardiac Monitor", 2015. https://www.medtronic.com/patients/fainting/device/our-insertable-cardiac-monitors/reveal-linq-icm/

[16] Second Sight, “The Argus® II Retinal Prosthesis System" - http://www.2-sight.eu/ee/product.”

[17] Given Imaging, “PillCam Capsule Endoscopy" - http://www.givenimaging.com/en-int/innovative-solutions/capsule-endoscopy/pages/default.aspx

[18] K. Mountfort, “The Promise of Leadless Pacing” Arrhythmia Electrophysiol. Rev., vol. 3, pp. 51–55, 2014.

[19] A. Mohammadi, K. Chen, M. Ali, K. Takahata, “Radio aneurysm coils for noninvasive detection of cerebral embolization failures: A preliminary study” Biosensors and Bioelectronics, vol. 30, no. 1, pp. 300–305, 2011.

[20] M. Jamal, A. Zarafshar, D. Gracias, “Differentially photo-crosslinked polymers enable self-assembling microfluidics” Nature Communications, vol. 2, 2011.

[21] C. Randall, T. Leong, N. Bassik, D. Gracias, “3D lithographically fabricated nanoliter containers for drug delivery” Advanced Drug Delivery Reviews, vol. 59, no. 15, pp. 1547–1561, 2007.

[22] J. Park, Y. Kalinin, S. Kadam, C. Randall, D. Gracias, “Design for a Lithographically Patterned Bioartificial Endocrine Pancreas” Artificial Organs, vol. 37, pp. 1059-1067, 2013.

[23] E. Gultepe, J. Randhawa, S. Kadam, D. Gracias, “Biopsy with Thermally-Responsive Untethered Microtools” Advanced Materials, vol. 25, no. 4, pp. 514–519, 2013.

[24] K. Malachowski, M. Jamal, Q. Jin, B. Polat, C. Morris, D. Gracias, “Self-Folding Single Cell Grippers” Nano Letters, vol. 14, no. 7, pp. 4164–4170, 2014.

[25] Wang Xi, A. Solovev, A. Ananth, D. Gracias, S. Sanchez, O. Schmidtad, “Rolled-up magnetic microdrillers: towards remotely controlled minimally invasive surgery” Nanoscale, vol. 5, no. 4, pp. 1294–1297, 2013.

[26] S. Pandey, M. Ewing, A. Kunas, N. Nguyen, D. Gracias, G. Menonf, “Algorithmic design of self-folding polyhedra” Proceedings of the National Academy of Sciences, vol. 108, no. 50, pp. 19885-19890, 2011.

[27] A. Azam, K. Laflin, M. Jamal, R. Fernandes, D. Gracias, “Self-folding micropatterned polymeric containers” Biomedical Microdevices, vol. 13, no. 1, pp. 51–58, 2011.

[28] T. Leong, Randall, B. Benson, A. Zarafshar, D. Gracias, “Self-loading lithographically structured microcontainers: 3D patterned, mobile microwells” Lab Chip, vol. 8, p. 1621, 2008.

[29] T. Leong, C. Randall, B. Benson, N. Bassik, G. Stern, D. Gracias, “Tetherless thermobiochemically actuated microgrippers” Proceedings of the National Academy of Sciences, vol. 106, no. 3, pp. 703-708, 2009.

[30] K. Bazaka, M. Jacob, “Implantable Devices: Issues and Challenges” Electronics, vol. 2, no. 1, 2012.

[31] A. Yakovlev, S. Kim, A. Poon, “Implantable biomedical devices: Wireless powering and communication” IEEE Communications Magazine, vol. 50, no. 4, pp. 152–159, 2012.

[32] E. Katz, Implantable Bioelectronics. Wiley, 2014.

[33] Shashank Priya, Daniel J. Inman, "Energy Harvesting Technologies" Springer, 2009.

[34] W. Liu, W. Fink, M. Tarbell, M. Sivaprakasam, “Image processing and interface for retinal visual prostheses” in IEEE International Symposium on Circuits and Systems, Vol. 3, pp. 2927–2930, 2005.

[35] Q. Xu, X. Gao, H. Wang, J. He, Z. Mao, M. Sun, “Batteries Not Included: A Mat-Based Wireless Power Transfer System for Implantable Medical Devices As a Moving Target” IEEE Microwave Magazine, vol. 14, no. 2, pp. 63–72, 2013.

[36] S. N. Jain, “A pictorial essay: Radiology of lines and tubes in the intensive care unit” Indian J Radiol. Imaging., vol. 21, pp. 182–190, 2011.

[37] S. K. Kelly, J. F. Rizzo III et al., “A Hermetic Wireless Subretinal Neurostimulator for Vision Prostheses” IEEE Transactions on Biomedical Engineering, vol. 58, no. 11, pp. 3197–3205, 2011.

[38] K. Mountfort, “The Promise of Leadless Pacing” Arrhythmia Electrophysiol. Rev., vol. 3, pp. 51–55, 2014.

[39] A. Kim, M. Ochoa, R. Rahimi, B. Ziaie, “New and Emerging Energy Sources for Implantable Wireless Microdevices” IEEE Access, vol. 3, pp. 89–98, 2015.

[40] K. Sun, T.-S. Wei, B. YAhn, J. Seo, S. Dillon, J. Lewis, “3D Printing of Interdigitated Li-Ion Microbattery Architectures” Advanced Materials, vol. 25, no. 33, pp. 4539-4543, 2013.

[41] W. Lai, C. Erdonmez, C. Marinis, C. Bjune, N. Dudney, F. Xu, R. Wartena, Y. Chiang, “Ultrahigh-Energy-Density Microbatteries Enabled by New Electrode Architecture and Micropackaging Design” Advanced Materials, vol. 22, pp. E139–E144, 2010.

[42] L. Yin, X. Huang, H. Xu, Y. Zhang, J. Lam, J. Cheng, J. Rogers, “Materials, Designs, and Operational Characteristics for Fully Biodegradable Primary Batteries” Advanced Materials, vol. 26, pp. 3879-3884, 2014.

[43] M. Koo, K. Park, S. Lee, M. Suh, D. Jeon, J. Choi, K. Kang, K. Lee, “Bendable Inorganic Thin-Film Battery for Fully Flexible Electronic Systems” Nano Letters, vol. 12, no. 9, pp. 4810–4816, 2012.

[44] S. Li, Z. Guo, C. Wang, G. Wallace, H. Liu, “Flexible cellulose based polypyrrole-multiwalled carbon nanotube films for bio-compatible zinc batteries activated by simulated body fluids” Journal of Materials Chemistry A, vol. 1, no. 45, pp. 14300–14305, 2013.

[45] T. Arthur, B. Dunn et al., “Three-dimensional electrodes and battery architectures” MRS Bulletin, vol. 36, no. 07, pp. 523–531, 2011.

[46] G. Zhou, F. Li, H.-M. Cheng, “Progress in flexible lithium batteries and future prospect” Energy Environ. Sci., vol. 7, no. 4, pp. 1307–1338, 2014.

[47] J. Rabaey, M. Mark, D. Chen, C. utardja, C. Tang, S. Gowda, M. Wagner, D. Werthimer, “Powering and communicating with mm-size implants” Design, Automation Test in Europe Conference Exhibition (DATE), 2011.

[48] J. Kim, Y. Rahmat-Samii, “Implanted antennas inside a human body: simulations, designs, and characterizations” IEEE Transactions on Microwave Theory and Techniques, vol. 52, no. 8, pp. 1934–1943, 2004.

[49] K. Wong, G. Lee, T. Chiou, “A low-profile planar monopole antenna for multiband operation of mobile handsets” IEEE Transactions on Antennas and Propagation, vol. 51, no. 1, pp. 121–125, 2003.

[50] M. Sailor, J. Link, “Smart dust: nanostructured devices in a grain of sand” Chem. Commun., no. 11, pp. 1375–1383, 2005.

[51] S. R. Best, “The Radiation Properties of Electrically Small Folded Spherical Helix Antennas” IEEE Transactions On Antennas And Propagation, vol. 52, pp. 953–960, 2004.

[52] L. Chen, K. Parizi, H. Kosuge, K. Milaninia, M. McConnell, H. Wong, A. Poon, “Mass fabrication and delivery of 3D multilayer microTags into living cells” Scientific Reports, vol. 3, 2013.

[53] P.M. Mendes, A. Polyakov, M. Bartek, J.N. Burghartz, J.H. Correia, “Integrated chip-size antennas for wireless microsystems: Fabrication and design considerations” Sensors and Actuators, vol. 125, pp. 217–222, 2005.

[54] J. Adams, E. Duoss, T. Malkowsji, M. Motala, B. Ahn, R.Nuzzo, J. Bernhard, J. Lewis, “Conformal Printing of Electrically Small Antennas on Three-Dimensional Surfaces” Advanced Materials, vol. 23, pp. 1335–1340, 2011.

[55] C. Pfeiffer, X. Xu, S. Forrest, A. Grbic, “Direct Transfer Patterning of Electrically Small Antennas onto Three-Dimensionally Contoured Substrates” Advanced Materials, vol. 24, no. 9, pp. 1166–1170, 2012.

[56] X. Liu, S. Yao, S. Georgakopoulos, B.Cook, M. Tentzeris, “Reconfigurable helical antenna based on an origami structure for wireless communication system” in IEEE MTT-S International Microwave Symposium (IMS), 2014.

[57] D. Karnaushenko, D. Karnaushenko, D. Makarov, D.Schmidt, “Compact helical antenna for smart implant applications” NPG Asia Materials, vol. 7, 2015.

[58] M. Mannoor, Z. Jiang, T. James, Y. Kong, K. Malatesta, W. Soboyejo, N. Verma, D. Gracias, M. McAlpine, “3D Printed Bionic Ears” Nano Letters, vol. 13, no. 6, pp. 2634–2639, 2013.

[59] K. Kamata, Z. Piao, M. Hangyoc et al., “Spirulina-Templated Metal Microcoils with Controlled Helical Structures for THz Electromagnetic Responses” Scientific Reports, vol. 4, 2014.

[60] S. Best, “A discussion on the properties of electrically small self-resonant wire antennas” IEEE Antennas and Propagation Magazine, vol. 46, no. 6, pp. 9–22, 2004.

[61] C. Kruesi, R. Vyas, M. Tentzeris, “Design and Development of a Novel 3-D Cubic Antenna for Wireless Sensor Networks (WSNs) and RFID Applications” IEEE Transactions on Antennas and Propagation, vol. 57, no. 10, pp. 3293–3299, 2009.

[62] P. Gadfort, P. Franzon, “Millimeter-Scale True 3-D Antenna-in-Package Structures for Near-Field Power Transfer” IEEE Transactions on Components, Packaging and Manufacturing Technology, vol. 4, no. 10, pp. 1574–1581, 2014.

[63] S. Guo, F. Gosselin, N. Guerin, A. Lanouette, M. Heuzey, D. Therriaul, "3D Printing: Solvent-Cast Three-Dimensional Printing of Multifunctional Microsystems" Small, vol. 9, no. 24, pp. 4090–4090, 2013.

[64] A. Russo, B. Ahn, J. Adams, E. Duoss, J. Bernhard, J. Lewis, "Pen-on-Paper Flexible Electronics" Advanced Materials, vol. 23, no. 30, pp. 3426–3430, 2011.

[65] N. Oraon, P. Kumar M. K, C. Srivastava, Ma. Rao, "Self-assembly based 3D heatsink antenna for high density 3D integration" in International conference on Circuits, Controls and Communications (CCUBE), 2013.

[66] G. Hayes, L. Ying, J. Genzer, G. Lazzi, M. Dickey, "Self-Folding Origami Microstrip Antennas" IEEE Transactions on Antennas and Propagation, vol. 62, no. 10, pp. 5416–5419, 2014.

[67] P. Anacleto, P.M. Mendes, E. Gultepe, D. Gracias, "3D small antenna for energy harvesting applications on implantable micro-devices" in Loughborough Antennas and Propagation Conference (LAPC), 2012.

[68] A. Enayati, S. Brebels, W. De Raedt, G. Vandenbosch, "3D-Antenna-in-Package Solution for Microwave Wireless Sensor Network Nodes" IEEE Transactions on Antennas and Propagation, vol. 59, no. 10, pp. 3617–3623, 2011.

[69] I.T. Nassar, T. M. Weller, "Development of Novel 3-D Cube Antennas for Compact Wireless Sensor Nodes" IEEE Transactions on Antennas and Propagation, vol. 60, no. 2, pp. 1059–1065, 2012.

[70] A. Carlson, A. Bowen, Y. Huang, R. Nuzzo, J. Rogers, "Transfer Printing Techniques for Materials Assembly and Micro/Nanodevice Fabrication" Advanced Materials, vol. 24, no. 39, pp. 5284–5318, 2012.

[71] Sheng Xu, R. Nuzzo,Y. Huang, Y. Zhang, J. Rogers et al., "Assembly of micro/nanomaterials into complex, three-dimensional architectures by compressive buckling" Science, vol. 347, no. 6218, pp. 154–159, 2015.

[72] P. Anacleto, E. Gultepe, D. Gracias, J.H. Correia, P. M.Mendes, "Antenna operating frequency selection for energy harvesting on nano biomedical devices" in 41st European Microwave Conference (EuMC), pp. 64–66., 2011.

[73] J. Ho, S. Kim, A. Poon, "Midfield Wireless Powering for Implantable Systems" Proceedings of the IEEE, vol. 101, no. 6, pp. 1369–1378, 2013.

[74] R. F. Harrington, "Effect of Antenna Size on Gain, Bandwidth, and Efficciency" Journal of Research of the National Bureau of Standards-D Radio Propagation, vol. 51, 1960.

[75] A. Skrivervik, J. Zurcher, O. Staub, J. R. Mosig, "PCS antenna design: the challenge of miniaturization" IEEE Antennas and Propagation Magazine, vol. 43, no. 4, pp. 12–27, 2001.

[76] S. R. Best, D. L. Hanna, "A Performance Comparison of Fundamental Small-Antenna Design" IEEE Antennas and Propagation Magazine, vol. 52, pp. 47–70, 2010.

[77] E. Chow, A. Chlebowski, S. Chakraborty, W. Chappell, P. Irazoqui, "Fully Wireless Implantable Cardiovascular Pressure Monitor Integrated with a Medical Stent" IEEE Transactions on Biomedical Engineering, vol. 57, no. 6, pp. 1487–1496, 2010.

[78] E. Chow, M. Morris, P. Irazoqui, "Implantable RF Medical Devices: The Benefits of High-Speed Communication and Much Greater Communication Distances in Biomedical Applications" IEEE Microwave Magazine, vol. 14, no. 4, pp. 64–73, 2013.

[79] C. Randall, E. Gultepe, D. Gracias, "Self-folding devices and materials for biomedical applications" Trends Biotechnology, vol. 30, pp. 138–146, 2012.

[80] S. C. W. Burleson, Security and Privacy for Implantable Medical Devices. Springer, 2014.

[81] A. Cadei, A. Dionisi, E.Sardini, M. Serpelloni, "Kinetic and thermal energy harvesters for implantable medical devices and biomedical autonomous sensors" Measurement Science and Technology, vol. 25, no. 1, p. 012003, 2014.

[82] A. Harb, "Energy harvesting: State-of-the-art" Renewable Energy, vol. 36, pp. 2641–2654, 2011.

[83] C.-Y. Sue, N.-C. Tsai, "Human powered MEMS-based energy harvest devices" Applied Energy, vol. 93, pp. 390–403, 2012.

[84] N. Hudak, G. Amatucci, "Small-scale energy harvesting through thermoelectric, vibration, and radiofrequency power conversion" Journal of Applied Physics, vol. 103, no. 10, p. 101301, 2008.

[85] S. Cosnier, A. Le Goff, M. Holzinger, "Towards glucose biofuel cells implanted in human body for powering artificial organs: Review" Electrochemistry Communications, vol. 38, pp. 19–23, 2014.

[86] Y. Yang, X.-J. Wei, J. Liu, "Suitability of a thermoelectric power generator for implantable medical electronic devices" Journal of Physics D: Applied Physics, vol. 40, no. 18, p. 5790, 2007.

[87] C. Dagdevirena, John A. Rogers et al., "Conformal piezoelectric energy harvesting and storage from motions of the heart, lung, and diaphragm" Proceedings of the National Academy of Sciences - PNAS, vol. 111, no. 5, pp. 1927–1932, 2014.

[88] D. Leech, P. Kavanagh, W. Schuhmann, "Enzymatic fuel cells: Recent progress" Electrochimica Acta, vol. 84, pp. 223–234, 2012.

[89] P. Cinquin , C. Gondran, F. Giroud, S. Mazabrard, A. Pellissier, F. Boucher, J.-P. Alcaraz, K. Gorgy, F. Lenouvel, S. Mathe, P. Porcu, S. Cosnie, "A Glucose BioFuel Cell Implanted in Rats" PLOS One, vol. 4, 2010.

[90] E. Katz, "Implantable biofuel cells operating in vivo: Providing sustainable power for bioelectronic devices: From biofuel cells to cyborgs" in 6th IEEE International Workshop on Advances in Sensors and Interfaces (IWASI), pp. 2–13, 2015.

[91] Y. Yang, G. D. Xu, J. Liu, "A Prototype of an Implantable Thermoelectric Generator for Permanent Power Supply to Body Inside a Medical Device" Journal of Medical Devices, vol. 8, 2014.

[92] J. R. Lim, J. F. Whitacre, J.-P. Fleurial, C.-K. Huang, M. A. Ryan, N. V. Myung, "Fabrication Method for Thermoelectric Nanodevices" Advanced Materials, vol. 17, no. 12, pp. 1488–1492, 2005.

[93] J. Potkay, K. Brooks, "An Arterial Cuff Energy Scavenger for Implanted Microsystems" in 2nd International Conference on Bioinformatics and Biomedical Engineering, pp. 1580–1583, 2008.

[94] Z. Wang, “Towards Self-Powered Nanosystems: From Nanogenerators to Nanopiezotronics” Advanced Functional Materials, vol. 18, no. 22, pp. 3553–3567, 2008.

[95] X. Chen, D. Brox, B. Assadsangabi, Y. Hsiang, T. Kenichi, “Intelligent telemetric stent for wireless monitoring of intravascular pressure and its in vivo testing” Biomedical Microdevices, vol. 16, no. 5, pp. 745–759, 2014.

[96] L. Marnat, M. Ouda, M. Arsalan, K. Salama, A. Shamim, “On-Chip Implantable Antennas for Wireless Power and Data Transfer in a Glaucoma-Monitoring SoC” IEEE Antennas and Wireless Propagation Letters, vol. 11, pp. 1671–1674, 2012.

[97] T. Sun, X. Xie, Z. Wan, Wireless Power Transfer for Medical Microsystems. Springer, 2013.

[98] C. A. Balanis, Antenna Theory - Analysis and Design - Third Edition. John Wiley and Sons, Inc., 2005.

[99] J. Ho, A. Yeh, E. Neofytou, S. Kim, Y. Tanabe, B. Patlolla, R. Beygui, Ada S. Y. Poon, “Wireless power transfer to deep-tissue microimplants” Proceedings of the National Academy of Sciences, vol. 111, no. 22, pp. 7974–7979, 2014.

[100] M. Rasouli, L. Phee, “Energy Sources and their Development for Application in Medical Devices” Expert Rev. Med. Devices, vol. 7, pp. 693–709, 2010.

[101] S. Aldhaher, P. C. K. Luk, J. F. Whidborne, “Electronic Tuning of Misaligned Coils in Wireless Power Transfer Systems” IEEE Transactions on Power Electronics, vol. 29, no. 11, pp. 5975–5982, 2014.

[102] B. Flynn, K. Fotopoulou, “Rectifying loose coils: Wireless power transfer in loosely coupled inductive links with lateral and angular misalignment” IEEE Microwave Magazine, vol. 14, no. 2, pp. 48–54, 2013.

[103] K. Fotopoulou, B. Flynn, “Wireless Power Transfer in Loosely Coupled Links: Coil Misalignment Model” IEEE Transactions on Magnetics, vol. 47, no. 2, pp. 416–430, 2011.

[104] E. Kyungsik, J. Joonsoo, L. Tae Hyung, K. Jinhyung, K. Junghoon, L. Sung Eun, K. June, “A wireless power transmission system for implantable devices in freely moving rodents” Medical & Biological Engineering & Computing, vol. 52, no. 8, pp. 639–651, 2014.

[105] CardioMems, Inc., “CardioMems Wireless Sensing" - http://www.cardiomems.com/

[106] CardioMEMSTM, “HF System Patient System Guide" http://www.cardiomems.com/

[107] S. J. Medical, “CardioMEMSTM HF System" - http://health.sjm.com/heart-failure-answers/treatment-options/pulmonary-artery-pressure-monitoring/cardiomems.

[108] J. S. Yadav, “CardioMEMS ChampionTM Heart Failure Monitoring System" http://www.fda.gov/downloads/AdvisoryCommittees/CommitteesMeetingMaterials/MedicalDevices/MedicalDevicesAdvisoryCommittee/CirculatorySystemDevicesPanel/UCM284021.pdf, 2011.

[109] D. Andersen, S. Archer, J. Pearson, “Anatomically compliant antenna for implantable medical device.” Google Patents, Sep-2014.

[110] C. P. J. Soler J. Mumbru, “Wireless Implantable Medical Device.” Google Patents, Oct-2013.

[111] M. Meulmester, R. Imani, W. Lim, P. Li, “Inverted antenna with parallel plate capacitor formed along an Arm of the antenna for use with an implantable medical mevice.” Google Patents, Jan-2014.

[112] S. Vajha, K. Maile, D. Larson, D. Chizek, J. Edgell, “Folded Antennas For Implantable Medical Devices.” Google Patents, Aug-2014.

[113] Y. Zhao, Q. Denzene, “Implantable Medical Device Antenna.” Google Patents, Dec-2013.

[114] P. Rawat, J. Von Arx, “Implantable Medical Device With Fractal Antenna.” Google Patents, 2013.

[115] G. Haubrich, J. Yamamoto, D. Mateychuk, “High dielectric substrate antenna for implantable miniaturized wireless communications and method for forming the same.” Google Patents, Jul 2013.

[116] R. Ritter, J. Handwerker, T. Liu, M. Ortmanns, “Telemetry for Implantable Medical Devices: Part 1 - Media Properties and Standards” IEEE Solid-State Circuits Magazine, vol. 6, no. 2, pp. 47–51, 2014.

[117] L. Xu, Y. Guo, W. Wu, “Miniaturized Dual-Band Antenna for Implantable Wireless Communications” IEEE Antennas and Wireless Propagation Letters, vol. 13, pp. 1160–1163, 2014.

[118] Z. Duan, Y. X. Guo, M. Je, D. L. Kwong, “Design and in Vitro Test of a Differentially Fed Dual-Band Implantable Antenna Operating at MICS and ISM Bands” IEEE Transactions on Antennas and Propagation, vol. 62, no. 5, pp. 2430–2439, 2014.

[119] C. Liu, Y. X. Guo, S. Xiao, “Capacitively Loaded Circularly Polarized Implantable Patch Antenna for ISM Band Biomedical Applications” IEEE Transactions on Antennas and Propagation, vol. 62, no. 5, pp. 2407–2417, 2014.

[120] X. Meng, K. D. Browne, S. M. Huang, C. Mietus, D. K. Cullen, M. R. Tofighi, A. Rosen, “Dynamic Evaluation of a Digital Wireless Intracranial Pressure Sensor for the Assessment of Traumatic Brain Injury in a Swine Model” IEEE Transactions on Microwave Theory and Techniques, vol. 61, no. 1, pp. 316–325, Jan. 2013.

[121] M. K. Hosain, A. Kouzani, S. Tye, “Multi-layer implantable antenna for closed loop deep brain stimulation system” in International Symposium onCommunications and Information Technologies (ISCIT), pp. 643–648, 2012.

[122] F. J. Huang, C. M. Lee, C. L. Chang, L. K. Chen, T. C. Yo, C. H. Luo, “Rectenna Application of Miniaturized Implantable Antenna Design for Triple-Band Biotelemetry Communication” IEEE Transactions on Antennas and Propagation, vol. 59, no. 7, pp. 2646–2653, 2011.

[123] A. Vorobyov, C. Hennemann, A. Vasylchenko, J. D. Decotignie, J. Baumgartner, “Folded loop antenna as a promissing solution for a cochlear implant” in The 8th European Conference on Antennas and Propagation (EuCAP), pp. 1735-1738. 2014.

[124] C. Schmidt, F. Casado, A. Arriola, I. Ortego, P. D. Bradley, D. Valderas, “Broadband UHF Implanted 3-D Conformal Antenna Design and Characterization for In-Off Body Wireless Links” IEEE Transactions on Antennas and Propagation, vol. 62, no. 3, pp. 1433–1444, 2014.

[125] M. H. Ouda, M. Arsalan, L. Marnat, A. Shamim, K. N. Salama, "5.2-GHz RF Power Harvester in 0.18-/spl mu/m CMOS for Implantable Intraocular Pressure Monitoring" IEEE Transactions on Microwave Theory and Techniques, vol. 61, no. 5, pp. 2177–2184, 2013.

[126] S. H. Lee, J. Lee, Y. J. Yoon, S. Park, C. Cheon, K. Kim, S. Nam, "A Wideband Spiral Antenna for Ingestible Capsule Endoscope Systems: Experimental Results in a Human Phantom and a Pig" IEEE Transactions on Biomedical Engineering, vol. 58, no. 6, pp. 1734–1741, 2011.

[127] C. Liu, Y. X. Guo, S. Xiao, "Circularly Polarized Helical Antenna for ISM-Band Ingestible Capsule Endoscope Systems" IEEE Transactions on Antennas and Propagation, vol. 62, no. 12, pp. 6027-6039, 2014.

[128] P. M. Izdebski, H. Rajagopalan, Y. Rahmat-Samii, "Conformal Ingestible Capsule Antenna: A Novel Chandelier Meandered Design" IEEE Transactions on Antennas and Propagation, vol. 57, no. 4, pp. 900–909, 2009.

[129] Basari, D. C. Sirait, F. Y. Zulkifli, E. T. Rahardjo, "A helical folded dipole antenna for medical implant communication applications" in International Microwave Workshop Series on RF and Wireless Technologies for Biomedical and Healthcare Applications (IMWS-BIO), 2013.

[130] H. Huang, P. Zhao, P. Y. Chen, Y. Ren, X. Liu, M. Ferrari, Y. Hu, D. Akinwande, "RFID Tag Helix Antenna Sensors for Wireless Drug Dosage Monitoring" IEEE Journal of Translational Engineering in Health and Medicine, vol. 2, pp. 1–8, 2014.

[131] C. L. Yang, C. L. Tsai, S. H. Chen, "Implantable High-Gain Dental Antennas for Minimally Invasive Biomedical Devices," IEEE Transactions on Antennas and Propagation, vol. 61, no. 5, pp. 2380-2387, 2013.

[132] P. Poulichet, L. Fakri-Bouchet, C. Delabie, L. Rousseau, A. Fakri, A. Exertier, "Optimisation and realisation of a portable NMR apparatus and micro antenna for NMR" in Symposium on Design, Test, Integration and Packaging of MEMS/MOEMS (DTIP), pp. 193–196, 2011.

[133] P. Nenzi, F. Tripaldi, M. Balucani, F. Marzano, "Three-dimensional micro-antenna array for millimetre and sub-millimetre-wave remote imaging" in Proceedings of the 5th European Conference on Antennas and Propagation (EUCAP), pp. 2596-2600, 2011.

[134] S. Manafi, H. Deng, "Design of a Small Modified Minkowski Fractal Antenna for Passive Deep Brain Stimulation Implants" International Journal of Antennas and Propagation, 2014.

[135] E. Moradi, T. Björninen, L. Sydänheimo, J. M. Carmena, J. M. Rabaey, L. Ukkonen, "Measurement of Wireless Link for Brain-Machine Interface Systems Using Human-Head Equivalent Liquid" IEEE Antennas and Wireless Propagation Letters, vol. 12, pp. 1307–1310, 2013.

[136] A. Kiourti, K. A. Psathas, P. Lelovas, N. Kostomitsopoulos, K. S. Nikita, "In Vivo Tests of Implantable Antennas in Rats: Antenna Size and Intersubject Considerations" IEEE Antennas and Wireless Propagation Letters, vol. 12, pp. 1396–1399, 2013.

[137] H. Y. Lin, M. Takahashi, K. Saito, K. Ito, "Performance of Implantable Folded Dipole Antenna for In Body Wireless Communication" IEEE Transactions on Antennas and Propagation, vol. 61, no. 3, pp. 1363–1370, 2013.

[138] A. Poon, S. O'Driscoll, T. H. Meng, "Optimal Frequency for Wireless Power Transmission Into Dispersive Tissue" IEEE Transactions on Antennas and Propagation, vol. 58, no. 5, pp. 1739-1750, 2010.

[139] D.Andreuccetti, R.Fossi, C.Petrucci, "An internet resource for the calculation of the dielectric properties of body tissues in the frequency range of 10 Hz to 100 GHz" Italian Research Council - Institute Of Applied Physics, 1997.

[140] F. Ulaby, E. Michielssen, U. Ravaioli, Fundamentals of Applied Electromagnetics - 6th Edition. Prentice Hall, 2010.

[141] M. Kiani, A. Ibrahim, "Safe Inductive Power Transmission to Millimeter-Sized Implantable Microelectronics Devices" in 37th Annual International Conference of the IEEE Engineering in Medicine and Biology Society (EMBC), 2015.

[142] L. Lucke, V. Bluvshtein, "Safety considerations for wireless delivery of continuous power to implanted medical devices" in 36th Annual International Conference of the IEEE Engineering in Medicine and Biology Society (EMBC), pp. 286–289. 2014

[143] K. Chan, R. Cleveland, D. Means, "Evaluating Compliance with FCC Guidelines for Human Exposure to Radiofrequency Electromagnetic Fields - OET Bull. 65, Supp. C." FCC, Washington DC, 1997.

[144] H. A. Wheeler, "Fundamental Limitations of Small Antennas" Proceedings of the IRE, vol. 35, no. 12, pp. 1479–1484, 1947.

[145] L. J. Chu, "Physical Limitations of Omni-Directional Antennas" Journal of Applied Physics, vol. 19, no. 12, pp. 1163–1175, 1948.

[146] R. Collin, S. Rothschi, "Evaluation of antenna Q" IEEE Transactions on Antennas and Propagation, vol. 12, no. 1, pp. 23–27, 1964.

[147] R. Hansen, "Fundamental limitations in antennas" Proceedings of the IEEE, vol. 69, no. 2, pp. 170-182, 1981.

[148] J. McLean, "A re-examination of the fundamental limits on the radiation Q of electrically small antennas" IEEE Transactions on Antennas and Propagation, vol. 44, no. 5, p. 672, 1996.

[149] H. Thal, "New Radiation Q Limits for Spherical Wire Antennas" IEEE Transactions on Antennas and Propagation, vol. 54, no. 10, pp. 2757–2763, 2006.

[150] R. Hansen, R. Collin, "A New Chu Formula for Q" IEEE Antennas and Propagation Magazine, vol. 51, no. 5, pp. 38–41, 2009.

[151] M. Gustafsson, C. Sohl, G. Kristensson, "Physical Limitations on Antennas of Arbitrary Shape" Proceedings of the Royal Society of London A: Mathematical, Physical and Engineering Sciences, vol. 463, no. 2086, pp. 2589–2607, 2007.

[152] A. Yaghjian, H. Stuart, "Lower Bounds on the Q of Electrically Small Dipole Antennas" IEEE Transactions on Antennas and Propagation, vol. 58, no. 10, pp. 3114–3121, 2010.

[153] S. Best, "Low Q electrically small linear and elliptical polarized spherical dipole antennas" IEEE Transactions on Antennas and Propagation, vol. 53, no. 3, pp. 1047–1053, 2005.

[154] K. Fujimoto, H. Morishita, Modern Small Antennas. Cambridge University Press, 2014.

[155] W. Geyi, “Physical limitations of antenna” IEEE Transactions on Antennas and Propagation, vol. 51, no. 8, pp. 2116–2123, 2003.

[156] P. M. Mendes, “Microantenas Integradas em Microssistemas de Rádio-Frequência para Comunicações Sem Fios” Universidade do Minho - Escola de Engenharia, 2005.

[157] R. Chavez-Santiago, A. Khaleghi, I. Balasingham, “Matching layer for path loss reduction in ultra wideband implant communications” in 36th Annual International Conference of the IEEE Engineering in Medicine and Biology Society (EMBC), pp. 6989–6992, 2014.

[158] E. Chow, C.-Lung, Y. Ouyang, A. Chlebowski, P. Irazoqui, W. Chappell, Wireless Power Transfer - Chapter 9: Wireless Powering and Propagation of Radio Frequencies through Tissue. River Publishers, pp. 301–336, 2012.

[159] Gabriel, S., Lau, R.W., Gabriel, C.S. Gabriel, R. Lau, C. Gabriel, “The dielectric properties of biological tissues: I. Literature survey” Physics in Medicine and Biology, vol. 41, no. 11, p. 2231, 1996.

[160] K. Yazdandoost, R. Kohno, “Wireless Communications for Body Implanted Medical Device” in Asia-Pacific Microwave Conference, 2007.

[161] T. F. for Research on Information Technologies in Society, “Tissue Properties - Database: Dielectric Properties" http://www.itis.ethz.ch/itis-for-health/tissue-properties/database/dielectric-properties/, 2011.

[162] R. Chavez-Santiago, N. Cardona, “Experimental Path Loss Models for In-Body Communications Within 2.36-2.5 GHz” IEEE Journal of Biomedical and Health Informatics, vol. 19, no. 3, pp. 930-937, 2015.

[163] D. Kurup, W. Joseph, G. Vermeeren, L. Martens, “In-body Path Loss Model for Homogeneous Human Tissues” IEEE Transactions on Electromagnetic Compatibility, vol. 54, no. 3, pp. 556–564, 2012.

[164] J. Rashed-Mohassel, A. Mehdipour, H. Aliakbarian., “New schemes of size reduction in space filling resonant dipole antennas” in 3rd European Conference on Antennas and Propagation, pp. 2430-2432, 2009.

[165] J. Volakis, C.-C. Chen, K. Fujimoto, Small Antennas:Miniaturization Techniques and Applications. McGraw Hill Professional, 2010.

[166] R. Azadegan, K. Sarabandi, “A novel approach for miniaturization of slot antennas” IEEE Transactions on Antennas and Propagation, vol. 51, no. 3, pp. 421–429, 2003.

[167] G. T. Warren, L. Stutzman, Antenna Theory and Design - 3rd Edition. Wiley, 2007.

[168] K. Virga, Y. Rahmat-Samii, “Low-profile enhanced-bandwidth PIFA antennas for wireless communications packaging” IEEE Transactions on Microwave Theory and Techniques, vol. 45, no. 10, pp. 1879–1888, Oct. 1997.

[169] S. R. Best, “A discussion on electrically small antennas loaded with high permittivity and permeability materials” in International Workshop on Antenna Technology, pp. 90–93, 2011.

[170] T. Leong, P. Lester, T. Koh, E.Call, D. Gracias, "Surface Tension-Driven Self-Folding Polyhedra" Langmuir, vol. 23, no. 17, pp. 8747–8751, 2007.

[171] C. Wen, "Coplanar Waveguide: A Surface Strip Transmission Line Suitable for Nonreciprocal Gyromagnetic Device Applications" IEEE Transactions on Microwave Theory and Techniques, vol. 17, no. 12, pp. 1087–1090, 1969.

[172] M. Rizwan, A. Syed, "Characterization of a Coplanar Waveguide Open Stub-Based Discontinuity for MMICs and Filter Applications" International Journal of Antennas and Propagation, 2012.

[173] B. C. Wadell, Transmission Line Design Handbook. Boston,Mass. Artech House, 1991.

[174] Thomas Boutell, Boutell.Com Inc., "Coplanar Waveguide Analysis/Synthesis Calculator." http://wcalc.sourceforge.net/cgi-bin/coplanar.cgi

[175] D. Torrungrueng, A. Wongwattanarat, M. Rairiksh, "Magnitude of the voltage reflection coefficient of terminated reciprocal uniform lossy transmission lines" Microwave and Optical Technology Letters, vol. 49, no. 7, pp. 1516–1519, 2007.

[176] H. Dinis, P. Anacleto, J. Fernandes, P. M. Mendes, "Characterization of chip-size electrically-small antennas for smart wireless biomedical devices" in 9th European Conference on Antennas and Propagation (EuCAP), 2015.

[177] L. Hemming, Electromagnetic Anechoic Chambers. Wiley Interscope - John Wiley & Sons Inc, 2002.

[178] Y. Fu., "Development of a test setup for miniature antennas for millimeter frequencies" University of Grenoble, 2012.

[179] X. Y. Bao, Y. X. Guo, Y. Z. Xiong, "60-GHz AMC-Based Circularly Polarized On-Chip Antenna Using Standard 0.18- μ m CMOS Technology" IEEE Transactions on Antennas and Propagation, vol. 60, no. 5, pp. 2234–2241, 2012.

[180] H. Dinis, M. Zamith, J. Fernandes, J. Magalhaes, P.M. Mendes, "On-chip, efficient and small antenna array for millimeter-wave applications" in International Workshop on Antenna Technology (iWAT) pp. 227–228, 2015.

[181] J M. Urban, M. Lopera, S. Aristizabal, C. Amador, I. Nenadic, R. Kinnick, A. Weston, B. Qiang, Z. Xiaoming, J. Greenleaf, "Characterization of transverse isotropy in compressed tissue-mimicking phantoms" IEEE Transactions on Ultrasonics, Ferroelectrics, and Frequency Control, vol. 62, no. 6, pp. 1036–1046, 2015.

[182] J. Garrett, E. Fear, "Stable and Flexible Materials to Mimic the Dielectric Properties of Human Soft Tissues" IEEE Antennas and Wireless Propagation Letters, vol. 13, pp. 599–602, 2014.

[183] Y. Yuan, C. Wyatt, P. Maccarini, P. Stauffer, O. Craciunescu, J. MacFall, M. Dewhirst, S. Das, "A heterogeneous human tissue mimicking phantom for RF heating and MRI thermal monitoring verification" Physics in Medicine and Biology, vol. 57, no. 7, p. 2021, 2012.

[184] M. Lazebnik, E. Madsen, G. Frank, S. Hagness, "Tissue-mimicking phantom materials for narrowband and ultrawideband microwave applications" Physics in Medicine and Biology, vol. 50, no. 18, p. 4245, 2005.

[185] F. Merli, B. Fuchs, J.R. Mosig, A. Skrivervik, “The Effect of Insulating Layers on the Performance of Implanted Antennas” IEEE Transactions on Antennas and Propagation, vol. 59, no. 1, pp. 21–31, 2011.

[186] E. Altshuler, T. O'Donnell, “An Electrically Small Multi-Frequency Genetic Antenna Immersed in a Dielectric Powder” IEEE Antennas and Propagation Magazine, vol. 53, no. 5, pp. 33–40, 2011.